

UNIVERSITY OF CINCINNATI

Date: _____

I, _____,
hereby submit this work as part of the requirements for the degree of:

in:

It is entitled:

This work and its defense approved by:

Chair: _____

CORROSION PROTECTION OF METALS BY SILANE SURFACE TREATMENT

A dissertation submitted to the
Division of Research and Advanced Studies
Of the University of Cincinnati

In partial fulfillment of the
Requirements for the degree of

DOCTOR OF PHILOSOPHY (Ph. D.)

In the Department of Materials Science and Engineering
Of the College of Engineering

2005

by

Danqing Zhu

M. S. University of Science and Technology Beijing (Beijing, China) 1994

B. S. University of Science and Technology Beijing (Beijing, China) 1991

Committee Chair: Dr. W. J. van Ooij

Abstract

The need for toxic chromate replacements in metal-finishing industries has prompted an intensive search for replacement technologies in recent years. Among the replacements that have been proposed, those that are based upon the use of organofunctional silanes rank very high in terms of performance, broad applicability as well as ease of application.

This dissertation presents a four-part work: (1) structural characterization of silane films on metals, (2) mechanism studies of silane-treated metal systems, (3) development of water-based silane systems, and (4) measurements of other properties of silane films.

In part 1, silane films, i.e., bis-[triethoxysilylpropyl]tetrasulfide (bis-sulfur silane) and bis-[trimethoxysilylpropyl]amine (bis-amino silane) were deposited on AA 2024-T3 and were characterized mainly using reflection-absorption Fourier-transform infrared spectroscopy (FTIR-RA) and electrochemical impedance spectroscopy (EIS) techniques. The results showed that further hydrolysis and crosslinking occurs in the applied bis-sulfur silane films in the presence of water and moisture. This is because the bis-sulfur silane is difficult to hydrolyze completely in its water/ethanol solution. The remaining ester groups would hydrolyze to silanols when water or moisture presents (e.g., in the processes of curing in the atmosphere and immersion in an aqueous solution). The as-formed silanols would further condense either with themselves or with aluminum hydroxyl groups at the alloy surface, forming siloxanes and aluminum-siloxanes.

Three different regions were clearly detected by EIS in the bis-sulfur silane-treated AA 2024-T3 system, and were further observed in the SEM/EDX studies. According to these studies, the three regions are assigned to, from outside to inside,

outermost silane film dominated with siloxanes (SiOSi), interfacial layer with both siloxanes and aluminum-siloxanes (AlOSi), and innermost aluminum oxide.

In part 2, the mechanistic study of corrosion protection of AA 2024-T3 by bis-sulfur silane film was carried out. In summation, the following two factors play critical roles in the corrosion protection of AA 2024-T3: (1) the formation of a highly crosslinked interfacial layer, and (2) high water resistance of silane films. The former inhibits corrosion in the following two ways: (1) blocking favorable sites for water adsorption by the formation of AlOSi bonds at the interface which effectively reduces the tendency of aqueous corrosion; and (2) bonding tightly to the metal and thus restricting transportation of the existing corrosion products away from their original sites which hinders pit growth. It should be noted that a high density of AlOSi bonds can be obtained employing bis-silanes rather than mono-silanes. A high water resistance makes water penetration difficult in silane films. This is essential for preventing AlOSi bonds from hydrolysis.

The results also indicated that hydrophilic bis-amino silane can not provide a good corrosion protection for metals. This is because the bis-amino silane film tends to be positively charged due to the protonation of hydrophilic amino groups. As a result of electrostatic attraction, the transportation of detrimental anions like chloride (Cl^-) ions as well as water is promoted in the film. Without sufficient water resistance of the film, AlOSi bonds at the interface are readily hydrolyzed. Consequently, the interfacial adhesion is lost. Corrosion thus readily proceeds at the alloy surface.

Although bis-sulfur silane performs well on Al alloys, it fails on HDG. This is caused by poor film coverage on HDG due to the insufficient wetting of Zn oxide by bis-sulfur silane solution. A mixture at the bis-sulfur/bis-amino ratio of 3/1 enhances the

corrosion resistance of both AA 2024-T3 and HDG. A small portion of bis-amino silane makes the mixture solution hydrophilic enough to wet Zn oxide on HDG, which facilitates the formation of a homogenous film on HDG. On the other hand, a large portion of bis-sulfur silane enhances the hydrophobicity of the mixture film, which is the basis for good protective performance of the mixture.

In part 3, test results for newly-developed water-based silane systems were reported. The major advantage of these silane systems is that they are highly miscible with water, which makes them more industrially acceptable than alcohol-based silanes. Test results demonstrated that these silanes provide excellent corrosion protection as well as paint adhesion on a variety of metals including, Al alloys, Zn-coated steels, carbon steels, and stainless steels.

Part 4 reported several other properties of silane films, such as resistivity/conductivity, mechanical properties, and thermal stabilities of silane films.

Acknowledgments

I am very grateful to my academic advisor, Professor Wim J. van Ooij, for leading me to this exciting multi-disciplinary research field, for stimulating my research interest, and for so many invaluable advices and encouragements he gave me throughout the course of this work. I also thank my dissertation committee members, Prof. Jim. Borieo, Prof. D. Shi, Prof. D. Schaefer, and Dr. E. Pohl of OSi Specialties, for taking the time to review my dissertation, and for attending to my Ph. D. defense.

To all the members of our research group, present and past, Vijay, Prasanna, Guru, Senthil, Ning, Shijian, Jing, Adi, Kim, Fu, Matt, Anna, Vignesh, Anuj, Ram, Corinne, Madhu, Ernie, Pankaj, Rick, and Rebha, thank you for everything you have done to make the lab being such a nice place to work.

I would especially like to thank Mr. Adrian S. C. While and Dr. Terrie Child of Brent/Chemetall for all the heart-warming encouragements and support they gave me. I also wish to thank, Dr. Thomas Schmidt-Hansberg and Mr. Manfred Walter of Chemetall/GmbH, for coordinating my enjoyable stay at Frankfurt/Main in the summer of 2000.

I would also acknowledge the following people for their assistances to this work: Mr. G. Górecki of Brent America PLC for operation of salt spraying testing, Mr. W. D. Hasler of Chemetall/GmbH for TGA measurements, Mr. Thomas Rose of Chemetall/GmbH for far-IR measurement, Mr. D. Boving of CSEM of mechanical tests, Mr. D. Loudermilk and Dr. R. J. Comstock of Armco Inc. for Franklin and deep drawing tests, Mr. A. Franquet of Vrije Universiteit Brussel for ellipsometry, Dr. B. Kain of LaQue Center for Corrosion Technologies Inc. for seawater immersion test, Mr. S. van

Susteren of Weert Co. for Machu test, Tonya Shipp for SIMS analysis, and Srinivas, Marty, and Niloy for SEM/EDX operation. I also wish to thank OSi Specialties for free supply of silanes.

Finally, I would give the deepest thanks to my parents and brother for their love and support throughout their lives. Most importantly, I thank my dearest husband, Hongwen Cao, for his love, understanding, and support in all these days, without which I would not have accomplished this work.

Contents

Objectives and Outline of the Present Work ix

Lists of Figures xiii

Lists of Tables xxiv

Chapter 1. Literature Reviews 1

- 1.1. Corrosion control of metals by silane surface treatment 1
 - 1.1.1. Silane solution chemistry: hydrolysis and condensation 2
 - 1.1.2. Bonding mechanisms through silane coupling agents 7
 - 1.1.3. Corrosion protection of metals by silane surface treatment 10
- 1.2. Corrosion of Al and AA 2024-T3 19
 - 1.2.1. Corrosion of Al 19
 - 1.2.1.1. Pitting corrosion of Al 19
 - 1.2.1.2. Cathodic corrosion of Al 30
 - 1.2.2. Corrosion of 2024-T3 Al alloy 31
 - 1.2.2.1. Second-phase particles in AA 2024-T3 32
 - 1.2.2.2. Pitting associated with S phase in AA 2024-T3 34
 - 1.2.2.3. Pitting of AA 2024-T3 by acetone degreasing 37

Chapter 2. Experimental 40

- 2.1. Materials 40
- 2.2. Silane solution preparation 42
- 2.3. Silane surface treatment 43
- 2.4. Characterization techniques 44
 - 2.4.1. Fourier-Transform Infrared Reflection-Absorption (FTIR-RA) Spectroscopy 45
 - 2.4.2. Electrochemical Impedance Spectroscopy (EIS) 45
 - 2.4.3. Ellipsometry 49
- 2.5. Corrosion tests 50
 - 2.5.1. Electrochemical tests 50
 - 2.5.2. Performance tests 51
- 2.6. Measurements of other properties of silane films 52
 - 2.6.1. Resistivity/conductivity measurements of silane films 52
 - 2.6.2. Measurements of mechanical properties of silane films 54
 - 2.6.3. Thermogravimetric analysis (TGA) of silane films 58

Chapter 3. Electrochemical Impedance Spectroscopy of Bis-[triethoxy-silylpropyl]tetrasulfide Film on AA 2024-T3 59

- 3.1. Introduction 60
- 3.2. Results and discussion 61
 - 3.2.1. EIS results for bis-sulfur silane treated AA 2024-T3 system under different curing processes 62

| | |
|---|----|
| 3.2.1.1. Effect of immersion time on bis-sulfur silane-treated AA 2024-T3 in 0.5 M K ₂ SO ₄ | 62 |
| 3.2.1.2. Effects of curing time at 80°C and aging time in ambient condition on bis-sulfur silane-treated AA 2024-T3 | 69 |
| 3.2.2. Analysis of EIS for bis-sulfur silane-treated AA 2024-T3 | 72 |
| 3.2.2.1. Equivalent electrical circuit models | 72 |
| 3.2.2.2. Analysis of the fitted data for bis-sulfur silane-treated AA 2024-T3 | 79 |
| 3.2.3. Surface analysis by FTIR-RA | 85 |
| 3.2.4. Potentiodynamic polarization tests | 89 |
| 3.2.5. Salt Spray Test (ASTM B117) | 90 |
| 3.3. Conclusions | 91 |

Chapter 4. Structural Characterization of Bis-[triethoxysilylpropyl]-tetrasulfide and Bis-[trimethoxysilylpropyl]amine by FTIR-RA and EIS

93

| | |
|--|-----|
| 4.1. Introduction | 94 |
| 4.2. Results and discussion | 96 |
| 4.2.1. Structures of the bis-sulfur and bis-amino silane films on AA 2024-T3 | 96 |
| 4.2.1.1. Effect of hydrolysis time of bis-sulfur and bis-amino silane solutions | 96 |
| 4.2.1.2. Structural evolution of bis-sulfur and bis-amino silane films on AA 2024-T3 in the 100°C curing process | 101 |
| 4.2.1.3. Formation of new phase in bis-amino silane films in the ambient | |

aging process 111

4.2.2. Comparison of bis-sulfur and bis-amino silane treated AA 2024-T3 systems 115

4.3. Conclusions 120

Chapter 5. Surface Modification of Metals by Silanes 122

5.1. Introduction 122

5.2. Results and discussion 123

5.2.1. Effect of organic solvents on the film structure of bis-sulfur silane on AA 2024-T3 123

5.2.2. Effect of metal substrates on the film structure of bis-sulfur silane 129

5.2.3 Observation of the interfacial layer of silane/metal systems 135

5.3. Conclusions 138

Chapter 6. Corrosion Protection of AA 2024-T3 by Bis-[triethoxysilylpropyl]tetrasulfide in Neutral Sodium Chloride Solution– Part 1: Early Corrosion of AA 2024-T3 139

6.1. Introduction 139

6.2. Results 141

6.2.1. Identification of second-phase particles in AA 2024-T3 141

6.2.2. SEM/EDX observation of corrosion of AA 2024-T3 during immersion in a neutral NaCl solution 143

6.3. Discussion 150

6.3.1. Pitting associated with anodic S phase particles 150

| | |
|---|-----|
| 6.3.2. Corrosion behavior of cathodic Al-Cu-Fe-Mn-containing and Al-Si-containing phase particles | 151 |
| 6.3.3. Alternative mechanism of Al dissolution in the vicinity of S phase particles | 152 |
| 6.3. Conclusions | 156 |

Chapter 7. Corrosion Protection of AA 2024-T3 by Bis-[triethoxysilylpropyl]tetrasulfide in A Neutral Sodium Chloride Solution–Part 2: Mechanism of Corrosion Protection 157

| | |
|--|-----|
| 7.1. Introduction | 158 |
| 7.2. Results and discussion | 158 |
| 7.2.1. Electrochemical tests | 158 |
| 7.2.1.1. Potential transient measurements in a neutral 0.6 M NaCl solution | 158 |
| 7.2.1.2. Anodic and cathodic polarization tests of bis-sulfur silane-treated AA 2024-T3 in a neutral 0.6 M NaCl solution | 161 |
| 7.2.1.3. EIS measurements in a neutral 0.6 M NaCl solution | 164 |
| 7.2.2. SEM/EDX observation | 172 |
| 7.2.3. General discussion | 176 |
| 7.2.3.1. Mechanism for corrosion protection of AA2024-T3 by bis-sulfur silane | 176 |
| 7.2.3.2. Enhancement of interfacial adhesion: bis-silanes vs. mono-silanes | 179 |
| 7.2.3.3. Enhancement of water resistance of silane films | 182 |

7.3. Conclusions 182

Chapter 8. Enhanced Corrosion Resistance of AA 2024-T3 and HDG Using A Silane Mixture of Bis-[triethoxysilylpropyl]tetrasulfide and Bis-[trimethoxysilylpropyl]amine 184

8.1. Introduction 185

8.2. Results and discussion 186

8.2.1. Silane film thickness measurements 186

8.2.2. Electrochemical Studies of silane-treated AA 2024-T3 and HDG in a neutral 0.6 M NaCl solution 187

8.2.3. SEM observation of silane-treated AA 2024-T3 and HDG surfaces after immersion in a neutral 0.6 M NaCl solution 196

8.3. Conclusions 210

Chapter 9. Development of Water-based Silanes for Corrosion Protection of Metals 211

9.1. Introduction 211

9.2. Results and discussion 213

9.2.1. Corrosion performance of metals treated with bis-amino/VTAS silane mixtures 213

9.2.1.1. Bare corrosion protection 213

9.2.1.2. Corrosion protection and paint adhesion 215

9.2.2. Characterization of bis-amino/VTAS silane mixtures 222

9.2.2.1. Hydrolysis of bis-amino/VTAS silane mixtures 222

| | | |
|---------|---|-----|
| 9.2.2.2 | Solution stability of bis-amino/VTAS silane mixtures | 224 |
| 9.2.2.3 | Film thickness of bis-amino/VTAS silane mixture | 227 |
| 8.2.2.4 | DC polarization tests of bis-amino/VTAS mixtures | 228 |
| 9.2.2.5 | Structural characterization of bis-amino/VTAS silane mixtures on AA 2024-T3 and HDG by FTIR-RA | 230 |
| 9.2.3 | Other water-based silane systems | 233 |
| 9.2.3.1 | Salt immersion test for silane-treated metals | 234 |
| 9.2.3.2 | Improved adhesion of silane-treated metals to adhesives and paints | 235 |
| 9.3 | Conclusions | 237 |

Chapter 10. Other Properties of Silane Films 239

| | | |
|----------|---|-----|
| 10.1 | Resistivity/conductivity of silane films on AA 2024-T3 and CRS | 239 |
| 10.2 | Measurements of mechanical properties of silane films | 244 |
| 10.2.1 | Nano-indentation testing: modulus and hardness | 245 |
| 10.2.2 | Pin-on-Disk testing: friction coefficients | 249 |
| 10.3 | Stability of bis-sulfur silane film in water and ethanol | 252 |
| 10.3.1 | Stability of bis-sulfur silane film in water | 253 |
| 10.3.2 | Stability of bis-sulfur silane film in ethanol | 256 |
| 10.4 | Thermal stability of free silane films | 257 |
| 10.4.1 | TGA measurements of free silane films | 257 |
| 10.4.2 | Corrosion performance of silane-treated metals at different temperatures | 261 |
| 10.4.2.1 | Effect of 200°C-curing on the corrosion performance of silane- treated CRS | 261 |

10.4.2.2. Effect of -70°C -cooling process on the corrosion performance
of silane-treated AA 2024-T3 263

10.5. Conclusions 264

Chapter 11. General Conclusions and Suggested Future Work 266

11.1. General conclusions 266

11.2. Suggested future work 271

11.2.1. Study on silane/metal interface 271

11.2.2. Transferring silane technology into existing industrial systems 271

11.2.2.1. In-line quality control of silane solution 271

11.2.2.2. In-line detection of silane films on metals 272

11.2.3. “Self-healing” silane-based systems 272

Appendixes 273

A. Comparison of Corrosivity of K_2SO_4 and NaCl 273

B. Fitted EIS Data for Chapter 3 275

C. ToF-SIMS Mapping of Bis-[triethoxysilylpropyl]tetrasulfide Treated AA 2024-T3 279

References 281

Objectives and Scope of the Present Work

1. Objectives of the Present Work

Chromates, the most efficient within the current repertoire of inhibitors, are now facing to be terminated in the field of corrosion control due to the toxic and carcinogenic nature of hexavalent chromium [Cr(VI)]. In the Europe, for example, the “End-of Life Vehicle” directive issued in 2000 states that, “ Member States shall ensure that materials and components of vehicles put on the market after 1 July 2003 do not contain lead, mercury, cadmium or hexavalent chromium...”. As a result, a call for alternatives for chromate-based inhibitors has arisen. A number of candidates, so-called “green inhibitors”, have been explored with the hope of providing an alternative for chromates. Among them, organofunctional trialkoxysilanes (silanes from hereon), a group of silicon-based organic-inorganic hybrids, have emerged as a very promising alternative.

Silanes have been primarily used as adhesion promoters or “coupling agents” in glass/mineral-reinforced polymeric composites for a few decades. In this application, silanes are mainly used for surface modification to improve adhesion between reinforcements and the polymer matrix [1-2]. It is generally accepted [1-2] that hydrolyzed silane molecules are capable of reacting with glass/mineral surfaces as well as polymers, behaving as a bridge to link the two phases together.

Since early 1990s', silane application for corrosion protection of metals has been explored. A variety of performance tests have consistently demonstrated that some silanes provide excellent corrosion protection as well as paint adhesion for metals as

chromates do, yet the associated mechanism has not been fully understood. Therefore, **one main task of this work is to identify the mechanism of corrosion protection of metals by silanes.** Bis-[triethoxysilylpropyl]tetrasulfide (bis-sulfur silane) and AA 2024-T3 were extensively studied for this purpose.

With an increased concern of reduction of Volatile Organic Compounds (VOC), the research focus has shifted to **seeking water-based silanes.** Silanes such as bis-[triethoxysilyl]ethane (BTSE) and bis-sulfur silane provide good performance on metals, yet they are not miscible with water. A large quantity of alcohol is thus needed for silane solution preparation. This obviously poses a major obstacle in the transfer of this technology into existing industrial systems, as VOC reduction is also demanded for the sake of flammability and human safety concern.

In addition, the knowledge of some other film properties, such as thermal stabilities, mechanical properties, and conductivities, is also of industrial interest. Therefore, **the third objective of this work is to measure the properties of silane films.**

2. Scope of The Present Work

This dissertation merges 5 major sections: (1) literature reviews on silane surface treatment and corrosion of Al and 2024-T3 Al alloy; (2) structural characterization of silane films on metals, (3) mechanistic studies of silane-treated metal systems, (4) studies of water-based silane systems, and (5) measurements of other properties of silane films.

Chapters 1 and 2 review previous works on silane surface treatment and corrosion of Al and AA 2024-T3. It is hoped that with a fully understanding of the achievements that have already been reached, the author wishes to make new contributions in this field.

Chapters 3 to 5 deal with structural characterization of silane films on metals by means of FTIR-RA and EIS measured in a non-corrosive electrolyte. The knowledge of silane film structures on metals is essential for interpreting corrosion protective behavior of silanes. The following effects on the silane films structures were studied: (1) effect of different curing processes (i.e., curing time, curing temperature, and immersion in aqueous solution) (Chapters 3 and 4), (2) effect of hydrolysis time of silane solutions (Chapter 4), (3) effect of the type of organic solvents (Chapter 5), and (4) effect of metal substrates (Chapter 5).

The work then extends to mechanistic study of corrosion protection of silane-treated metals, which is included in Chapters 6 to 8. Electrochemical methods such as DC polarization tests and EIS measurements in a corrosive electrolyte of 0.6 M NaCl solution (pH 6.5) were employed. Scanning electron microscopy (SEM) and energy-dispersive X-ray spectroscopy (EDX) were also used to examine the silane-treated surfaces. In Chapter 6, a new version of mechanism of early corrosion of bare AA 2024-T3 was proposed. The study in Chapter 7 focused on the bis-sulfur silane-treated AA 2024-T3 system, and a mechanism of corrosion protection was proposed. Chapter 8 reported a silane mixture formulated on the basis of bis-sulfur and bis-amino silanes. This mixture provided a universal protection on AA 2024-T3 and hot-dip galvanized steel (HDG). The corrosion mechanisms of these three types of silanes on both metals were compared.

As mentioned earlier, water-based silanes are more acceptable to industry than alcohol-based silanes. Chapter 9 reported the studies on newly-developed water-based silanes such as mixtures of bis-amino silane and vinyltriacetoxysilane (bis-amino/VTAS), etc.

In Chapter 10, other properties of silane films such as mechanical properties, thermal stabilities, solvent resistance, and conductivities were measured and discussed.

Lists of Figures

Figure 1.1. A plot of the concentration of gamma-glycidoxypropylmethyldiol vs. time; empty dot=silane diol; solid dot=disiloxane [6] 5

Figure 1.2. Possible conformation of aminopropylsilane triol with total conformational energy of -26.3kcal/mol [8] 7

Figure 1.3. Schematic of condensation of silanol with hydroxyl groups on the glass/metal surface (Me stands for Si or metal) 8

Figure 1.5. Film thickness of bis-sulfur and bis-amino silanes on stainless steel vs. solution concentration [28] 15

Figure 1.6. Pourbaix diagrams for pure Al. Shaded areas indicate corrosion susceptibility. Labels 0, -2, -4, and -6 are the log of soluble ion activity for the indicated lines [36] 20

Figure 1.7. Time series showing the effect of potential on anodic current spikes associated with metastable pitting [41] 22

Figure 1.8. Time series showing the effect of concentration of Cl^- ions on the anodic current spikes associated with metastable pitting (polarized at -0.6 V) [41] 23

Figure 1.9. Potentiodynamic polarization curve of AA 2024-T3 in 1M aqueous NaCl solution [60] 34

Figure 1.10. S phase particles after potentiodynamic polarization to -0.69V/SCE , the potential was maintained at -0.69V/SCE for 5 min [60] 35

Figure 2.1. Schematic EIS plots of a polymer coated metal system (solid curve-impedance plot; dashed curve-phase angle plot) (a), and equivalent electric circuit model (ECM) for EIS data fitting (b) 47

Figure 2.2. Apparatus of Franklin tester (a), and Diagram of connections for contracts and resistors (b) 53

Figure 2.3. Apparatus of nano-indentation tester (a), and indentation hysteresis curve (b) 56

Figure 2.4. Apparatus of Pin-on-Disk tester 58

Figure 3.1. Bis-sulfur silane treated AA 2024-T3 panels after 10 days of immersion in a naturally-aerated neutral 0.6 M NaCl solution; (a) cured for 17 hrs at 100°C in air, (b) cured for 10 min at 100°C in air, (c) cured in ambient conditions for 24 hrs, and (d) untreated, alkaline-cleaned only (bis-sulfur silane solution, 5%, pH 6.5) 60

Figure 3.2. Bode plots for bare AA 2024-T3 during immersion in 0.5 M K₂SO₄ solution for 0 to 8 hrs 62

Figure 3.3. Bode plots for bis-sulfur silane-treated Al 2024-T3 panels during immersion in 0.5 M K₂SO₄ solution for 0 to 24 hrs 64

Figure 3.4. Schematic of a plausible interfacial structure between bis-sulfur silane film and AA 2024-T3 alloy 69

Figure 3.5. Bode plots for bis-sulfur silane-treated AA 2024-T3 panels cured at 80°C in air for 10 min. to 370 min., then tested by EIS in 0.5 M K₂SO₄ 70

Figure 3.6. Bode plots for bis-sulfur silane-treated AA 2024-T3 panels aged in ambient conditions and then tested by EIS in 0.5 M K₂SO₄ 71

Figure 3.7. Equivalent circuits and their corresponding physical structures for bis-sulfur silane-treated AA 2024-T3 at initial stages (without unknown phase); (a) EC, and (b) the physical structure 73

Figure 3.8. Equivalent circuits (EC) and their corresponding physical structures for bis-sulfur silane-treated AA 2024-T3 at later stages (with unknown phase); (a) the complete-nested EC, (b) the physical structure corresponding to (a), (c) the half-serial EC, and (d) the physical structure corresponding to (c) 75

Figure 3.9. Fitted Bode plots for bis-sulfur silane-treated AA 2024-T3 after immersion in 0.5 M K_2SO_4 solution for various times (a) 0.16 hr, (b) 2 hrs, (c) 4 hrs, and (d) 8 hrs 78

Figure 3.10. Capacitances and resistances as a function of immersion time in 0.5 M K_2SO_4 solution for bis-sulfur silane-treated AA 2024-T3; n and n' are for silane film and unknown phase, respectively 79

Figure 3.11. Capacitances and resistances as a function of curing time at 80°C for bis-sulfur silane-treated AA 2024-T3; n and n' are for silane film and unknown phase, respectively 82

Figure 3.12. Capacitance and resistance as a function of ambient aging time on AA 2024-T3 substrate 83

Figure 3.13. FTIR-RA spectra of bis-sulfur silane-treated AA 2024-T3 aged in air at RT from 0 hr to 72 hrs (a) 4000 – 2700 cm^{-1} ; (b) 1200 – 825 cm^{-1} 86

Figure 3.14. FTIR-RA spectra of bis-sulfur silane-treated AA 2024-T3 immersed in 0.5M K_2SO_4 solution from 0 hr to 20 hrs (a) 4000 – 2700 cm^{-1} ; (b) 1200 – 800 cm^{-1} 88

Figure 3.15. Potentiodynamic polarization curves of bis-sulfur silane-treated AA 2024-T3 panels in 0.5M NaCl solution at pH 6 89

Figure 4.1 FTIR-RA spectra of bis-type silane films on AA 2024-T3 obtained from the silane solutions with different hydrolysis times, and followed by 10 min of curing at 100°C; (a) bis-sulfur silane, and (b) bis-amino silane 98

Figure 4.2. Area ratio of 963 cm^{-1} and 1246 cm^{-1} as a function of hydrolysis time of the bis-sulfur silane solution 100

Figure 4.3. FTIR-RA spectra of bis-type silane films on AA 2024-T3 after curing at 100°C in air for various times; (a) bis-sulfur silane, and (b) bis-amino silane 103

Figure 4.4. Bode plots of bis-sulfur silane coated AA 2024-T3 after curing at 100°C in air for various times, measured in 0.5 M K_2SO_4 solution (pH 6.5); (a) impedance plot, and (b) phase angle plot 106

Figure 4.5. Schematic of structural evolution of bis-sulfur silane system upon curing; (a) before curing, and (b) after curing 108

Figure 4.6. Bode plots of bis-amino silane coated AA 2024-T3 after curing at 100°C in air for various times, measured in 0.5M K_2SO_4 solution (pH 6.5); (a) impedance plot, and (b) phase angle plot 110

Figure 4.7. FTIR-RA spectra of bis-amino silane film on AA 2024-T3; (a) cured at 100°C for 24 hrs, before aging, (b) aged in air for 8 days;, and (c) the sample (b) after immersing in water for 24 hrs 112

Figure 4.8. Bode plots of 12-day aged bis-amino silane coated AA 2024-T3, after immersed in 0.5M K_2SO_4 solution for 2 hrs; (a) impedance plot, and (b) phase angle plot 114

Figure 4.9. FTIR-RA spectra of bis-amino silane film (a), and bis-sulfur silane film (b) on AA 2024-T3 after curing at 100°C for 24 hrs 116

Figure 4.10. Bode plots of bis-sulfur silane and bis-amino silane coated AA 2024-T3, measured in 0.5M K₂SO₄ (pH 6.5); (a) impedance plot, and (b) phase angle plot 117

Figure 5.1. FTIR-RA spectra of ethanol- and dioxane-based bis-sulfur silane films on AA 2024-T3 125

Figure 5.2. Schematic of molecular structures of these two types of bis-sulfur silane films on Al alloy; (a) ethanol-based, and (b) dioxane-based 127

Figure 5.3. 7-day seawater immersion test on different types of bis-sulfur silane films on AA 2024-T3; (a) ethanol-based bis-sulfur silane film on AA 2024-T3, and (b) dioxane-based bis-sulfur silane film on AA 2024-T3 128

Figure 5.4. FTIR-RA spectra of ethanol-based bis-sulfur silane films on different metals; (a) HDG, (b) AA 2024-T3, (c) CRS, and (d) AZ 91B 129

Figure 5.5. Schematic of the interfaces between metals and bis-sulfur silane water/ethanol solution; (a) MgO/silane-solution, and (b) Al₂O₃/silane-solution 132

Figure 5.6 Schematic of the interfacial regions between metals and bis-sulfur silane film; (a) Mg /silane film, and (b) Al/silane film 134

Figure 5.7. FTIR-RA spectra of untreated and silane-treated AA 2024-T3; (a) untreated, (b) treated with bis-sulfur silane (5%, natural pH 6.5), and (c) treated with bis-amino silane (5%, pH 7) 136

Figure 5.8. FTIR-RA spectra of bis-sulfur silane films on AA 2024-T3 from silane solutions with different concentrations; (a) 0.1%, (b) 0.5%, (c) 1%, and (d) 5% 137

Figure 6.1. Distribution of second-phase particles on the matrix of AA 2024-T3 142

Figure 6.2. SEM images of 4 types of second-phase particles in AA 2024-T3; (a) Al-Cu-Mg, (b) Al-Cu-Fe-Mn-Si, (c) Al-Si, and (d) Al-Cu 142

Figure 6.3. SEM images of AA 2024-T3 sample immersed in a neutral 0.6 M NaCl solution; (a) before immersion, (b) 3.5 hrs of immersion, and (c) 72 hrs of immersion 145

Figure 6.4. Composition of elements of the S phase particle at “A₁” 146

Figure 6.5. SEM images of two adjacent S phase remnants at “A₁” after immersion in 0.6M NaCl solution (pH 6.5) for various times; (a) 3.5 hrs, and (b) 72 hrs (Note: the compositions of the top one are reported in Figure 6.4) 147

Figure 6.6. SEM images of the cathodic particles after 72 hrs of immersion in 0.6 M NaCl solution (pH 6.5) ; (a) Al-Cu-Fe-Mn-containing particle (at “B₁” in Figure 6.3), and (b) Al-Si-containing particle (at “C₁” in Figure 6.3) 148

Figure 6.7. Schematic of early corrosion process of AA 2024-T3 in 0.6M NaCl solution; (a) dealloying and local alkalization, and (b) cathodic dissolution of the surrounding Al matrix 153

Figure 7.1. Potential transient curves of AA 2024-T3 treated with and without bis-sulfur silane (a), SEM images of bis-sulfur silane treated AA 2024-T3 after 8 hrs of immersion in a neutral 0.6 M NaCl solution (b) 160

Figure 7.2. Anodic polarization curves of AA 2024-T3 treated with and without bis-sulfur silane 162

Figure 7.3. Scanned images of AA 2024-T3 with and without bis-sulfur silane; (a) untreated; and (b) silane-treated 162

Figure 7.4. Cathodic polarization curves of AA 2024-T3 treated with and without bis-sulfur silane 163

Figure 7.5. Bode plots of bis-sulfur silane treated AA 2024-T3 during immersion in a neutral 0.6 M NaCl solution for 30 days (exposed area: 3.14 cm²); (a) impedance plot, and (b) phase angle plot 165

Figure 7.6. ECM's of EIS data fitting for bis-sulfur silane treated AA 2024-T3 for 30 days of immersion in 0.6M NaCl; (a) before water penetration into the film, (b) after water saturation of the film, (c) after pit formation-model 1, and (d) after pit formation – model 2 168

Figure 7.7. Fitted EIS plots of different immersion time with the ECMs in Figure 7.6, (a) 0 day, (b) 6 days, (c) 10 days, and (d) 30 days 170

Figure 7.8. Resistances of silane film, interfacial layer, and pit as a function of immersion time in a neutral 0.6 M NaCl solution of the bis-sulfur silane treated AA 2024-T3 system 172

Figure 7.9. SEM image of the pit formed in the bis-sulfur silane treated AA 2024-T3 system after 15 days of immersion in 0.6M NaCl; (a) younger pit; and (b) older pit 173

Figure 7.10. Structures of bis-silane molecule (a), and mono-silane molecule (b) 179

Figure 7.11. Schematic of bonding mechanism in mono-type silane/Al system; (a) bonding of bis-silane to Al; and (b) bonding of mono-silane to Al 181

Figure 8.1. DC polarization curves of the silane-treated AA 2024-T3 panels, measured in a neutral 0.6 M NaCl solution; (a) anodic polarization, and (b) cathodic polarization 189

Figure 8.2. Bode plots of silane-treated AA 2024-T3 panels in a neutral 0.6 M NaCl solution after 32 days of exposure; (a) impedance plot, and (b) phase angle plot (exposed area: 5.06 cm²) 191

Figure 8.3. DC polarization curves of silane treated HDG panels, measured in 0.6 M NaCl solution; (a) anodic polarization, and (b) cathodic polarization 193

Figure 8.4. Bode plots of silane-treated HDG panels measured in 0.6 M NaCl solution (pH 6.5) after 8 days of exposure; (a) impedance plot, and (b) phase angle plot (exposed area: 5.06 cm²) 195

Figure 8.5. AA 2024-T3 panels after 32 days of immersion in 0.6 M NaCl solution; (a) untreated, (b) bis-sulfur silane treated, (c) mixture-treated, and (d) bis-amino silane-treated 197

Figure 8.6. HDG panels after 8 days of immersion in 0.6 M NaCl solution; (a) untreated, (b) bis-sulfur silane treated, (c) mixture-treated, and (d) bis-amino silane treated 197

Figure 8.7. SEM images of silane-treated AA 2024-T3 surfaces after 32 days of immersion in a neutral 0.6 M NaCl solution; (a) bis-sulfur silane-treated, (b) bis-amino silane-treated, and (c) mixture-treated 199

Figure 8.8. Attraction of Cl⁻ ions in the electrolyte by a positively-charged bis-amino silane film on Al alloy 203

Figure 8.9. Bis-amino silane-treated AA 2024-T3 (in 5% bis-amino silane solution at pH 4), after immersion in a neutral 0.6 M NaCl solution for 4 days; (a) SEM image, and (b) EDX spectrum of bis-amino silane piece (site A in Figure 8.9(a)) 204

Figure 8.10. SEM images of silane-treated HDG surfaces after 8 days of immersion in a neutral 0.6 M NaCl solution; (a) bis-sulfur silane-treated, (b) bis-amino silane-treated, and (c) mixture-treated 206

Figure 8.11. Poorly-coated HDG surface with the bis-sulfur silane, and local corrosion occurring at defects 209

Figure 9.1. Individual silanes, silane mixture, and diluted aqueous silane solution used in this work (Note: silane 1 = unhydrolyzed bis-amino silane, silane 2 = unhydrolyzed VTAS, silane mixture = unhydrolyzed mixture at the bis-amino/VTAS ratio of 3/1 (v/v)) 212

Figure 9.2. AA 6061 panels after 336 hrs of SST; (a) untreated (20 hrs of exposure), (b) chromated (Alodine-series), and (c) silane-treated (Bis-amino/VTAS=1.5/1, 5%, pH 3.7) 214

Figure 9.3. AA 2024-T3 panels after 168 hrs of SST; (a) untreated, (b) chromated (CHEM-CODE 105[®]), and (c) silane-treated (bis-amin/VTAS = 1.5/1, 5%, pH 3.7) 214

Figure 9.4. PU powder-painted AA2024-T3 after 1008 hrs of SST; (a) untreated, (b) chromated (CHEM CODE 105[®]), and (c) silane-treated (bis-amino/VTAS=1.5/1, 2%) 216

Figure 9.5. PET powder-painted AA2024-T3 after 1008 hrs of SST, (a) untreated, (b) chromated (CHEM CODE 105[®]), and (c) silane-treated (bis-amino/VTAS =1.5/1, 2%) 216

Figure 9.6. PET-powder-painted AA 5005 after 240 hrs of CASST; (a) untreated, (b) chromated (Chromicoat 103[®]), and (c) silane-treated (bis-amino/VTAS = 1.5/1, 2%, pH 4)

217

Figure 9.7. PU-powder-painted AA 5005 after 240 hrs of CASST; (a) untreated, (b) chromated (chromicoat 103[®]), and (c) silane-treated (bis-amino/VTAS = 1.5/1, 2%, pH 4)

218

Figure 9.8. 1000-hr exposure of PET powder painted delta Zn panels; (a) silane-treated (bis-amino/VTAS = 5/1, 2%, pH 6), and (b) chromated (Granodine 108B[®])

Figure 9.9. Machu testing results of PET-painted HDG panels, (a) untreated, (b) silane-treated (bis-amino/VTAS = 5/1, 2%, pH 6), and (c) conventional chromate-treated (Granodine 108B[®])

Figure 9.10. Representative view of 3-month immersed panels; (a) epoxy-coated only, (b) silane-treated only, and (c) silane-pretreated (bis-amino/VTAS = 5/1, 2%, pH 6), followed by Cu-antifouling painted

Figure 9.11. Hydrolysis in the mixture of bis-amino and VTAS

Figure 9.12. Film thicknesses of silanes as a function of the corresponding silane solution concentrations

Figure 9.13. DC polarization of AA 2024-T3 treated with and without silane; (a) anodic polarization, and (b) cathodic polarization

Figure 9.14. FTIR-RA spectra of bis-amino/VTAS silane films on AA2024-T3; (a) bis-amino/VTAS (5%, 1/2, pH 3.0), (b) bis-amino/VTAS (5%, 1.5/1, pH 3.7), and (c) bis-amino/VTAS (5%, 5/1, pH 6)

Figure 9.15. FTIR-RA spectra of silane films on HDG (a) bis-amino/VTAS (5%, 1/2, pH 3.0), (b) bis-amino/VTAS (5%, 1.5/1, pH 3.7), and (c) bis-amino/VTAS (5%, 5/1, pH 6)

233

Figure 9.16. A 7-day immersion test in 0.6M NaCl solution (pH 6.5, open to air); (a) untreated, (b) treated with bis-UPS/VTAS (5%, 6/1, pH 4), and (c) treated with bis-diamine/bis-UPS/VTAS (5%, 1/5/1, pH 5) 234

Figure 10.1. Loading-depth curves of silane films deposited on BSS; (a) bis-amino silane film; (b) bis-sulfur silane film, (c) bis-sulfur/amino mixture silane film, and (d) uncoated BSS substrate (reference) 247

Figure 10.2. Friction curves of silane films deposited on BSS; (a) bis-amino silane film, (b) bis-sulfur silane film, (c) bis-sulfur/amino mixture silane film, and (d) uncoated BSS substrated (reference) 251

Figure 10.3. FTIR-RA spectra of bis-sulfur silane film on AA 2024-T3 after dried in the ambient for various times and followed by immersed in DI water for 30 min 254

Figure 10.4. FTIR-RA spectra of bis-sulfur silane film on AA 2024-T3 after drying in the ambient for various times and followed by immersed in ethanol for 30 min 257

Figure 10.5. TGA curves of free silane films; (a) bis-amino silane film, (b) bis-amino/VTAS (1.5/1) mixture silane film, (c) bis-sulfur silane film, and (d) bis-sulfur/bis-amino (9/1) silane film 260

Figure 10.6. I_{corr} of silane-treated CRS panels as a function of curing time at 200°C 262

Figure 10.7. Corrosion rates (I_{corr}) of AA 2024-T3 treated with and without silanes 263

Figure 11.1. A schematic of the interfacial layer formed in a silane-treated Al system 267

Figure A1. Potentiodynamic polarization curves of AA 2024-T3 blank in 0.5M K_2SO_4 and 0.5 M NaCl solutions at pH 6 272

Figure A2. Potentiodynamic polarization curves of bis-sulfur silane-treated AA 2024-T3
in 0.5 M K_2SO_4 and 0.5 M NaCl solutions at pH 6 273

Figure C1. Positive mapping (resolution $1\mu m \times 1\mu m$) 278

Figure C2. Negative mapping (resolution $1\mu m \times 1\mu m$) 279

List of Tables

| | |
|---|-----|
| Table 1.1. Representative commercial silane coupling agents | 2 |
| Table 1.2. A guide of compatible silanes to polymers | 10 |
| Table 1.3. Silanes suitable for corrosion protection of metals | 12 |
| Table 1.4. Corrosion potentials of second phases in AA 2024-T3 [62] | 33 |
| Table 2.1. Silanes used in this study and their chemical structures | 41 |
| Table 3.1. Assignments of characteristic absorption bands for bis-sulfur silane film on AA 2024-T3 [33,88,89] | 87 |
| Table 3.2. Corrosion evaluation of AA 2024-T3 blank, treated by bis-sulfur silane and Chromicoat103 [®] after 360 hrs of SST | 90 |
| Table 4.1. IR band assignments for Figure 4.1(a) [83,88,89] | 99 |
| Table 4.2. EDX results (in wt.%) for bis-amino silane film on AA 2024-T3 before and after immersed in 0.5M K ₂ SO ₄ | 119 |
| Table 4.3. EDX results (in wt.%) for bis-amino and bis-sulfur silane films on AA 2024-T3 after 15 days of immersion in a 0.6 M NaCl solution (pH 6.5) | 120 |
| Table 5.1 Assignments of absorption bands for bis-sulfur silane films [88,89] | 125 |
| Table 6.1. Chemical composition (in at. %) of second-phase particles in AA 2024-T3 | 142 |
| Table 7.1. Comparison of chemical compositions (in wt %) of regions A, B and C in Figure 7.9, and bare AA 2024-T3 | 174 |
| Table 8.1. Film thickness of three silanes deposited on SS | 187 |

| | |
|---|-----|
| Table 8.2. Compositions (wt. %) of three regions in silane-treated AA 2024-T3 systems | 200 |
| Table 8.3. Compositions of bis-sulfur silane-treated HDG, shown in Figure 8.10 (a) | 207 |
| Table 8.4. Compositions of bis-amino silane-treated HDG, shown in Figure 8.10 (b) | 207 |
| Table 8.5. Compositions of mixture silane-treated HDG, shown in Figure 8.10(c) | 207 |
| Table 9.1. pH and stability of 5% bis-amino/VTAS mixture solutions as a function of the content of bis-amino silane in the bis-amino/VTAS silane mixture | 225 |
| Table 9.2. Adhesion strength of silane-treated metals | 235 |
| Table 9.3. Testing result for carbon epoxy-painted steel after GM 9505P Environmental Cycle J-5 cycles | 236 |
| Table 9.4. Adhesion strength of acrylic-adhered CoCr samples, after subjection to various pretreatments and followed by 5000 thermal cycles between 5°C to 55°C | 237 |
| Table 10.1. Conductivities and resistivities of silanes films on AA 2024-T3 | 241 |
| Table 10.2 Conductivities and resistivities of silanes films on CRS | 242 |
| Table 10.3 Berkovich Hardness and Young's modulus of silane films on BSS | 248 |
| Table 10.4. Frictional coefficient and distance before failure of silane films on BSS | 251 |
| (c) | 206 |
| Table B1. Summary of fitted EIS data for the immersion process | 274 |
| Table B2. Summary of fitted EIS data for the curing process | 275 |
| Table B3. Summary of fitted EIS data for the aging process (c) | 276 |
| Table B4. Dielectric constants ϵ of sulfane silane film in the curing process at 80°C (c) | 277 |

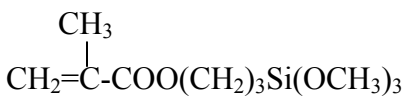
Chapter 1. Literature Reviews

1.1. Corrosion Protection of Metals by Silane Surface Treatment

Trialkoxysilanes (silanes hereon), are a class of environmentally-benign organic-inorganic hybrids which have shown a great potential in replacing toxic chromates in a variety of industries, such as aerospace, marine, automotive and construction industries. A silane-based surface treatment has the following attractive advantages: environmental and human compliance, economical application, and providing corrosion protection performance and paint adhesion for a number of metals comparable to chromating and phosphating.

Silanes have a general formula of $R'(CH_2)_nSi(OR)_3$, where R' represents an organofunctional group and OR is a hydrolyzable alkoxy group such as methoxy (OCH_3), ethoxy (OC_2H_5) and acetoxy ($OCOCH_3$). They have been widely used in paints, adhesives, sealants in plastics and composites as adhesion promoters or coupling agents for decades. A small amount of silanes (e.g., a 0.1 to 0.5 % silane aqueous solution) offers a great enhancement in adhesion of polymeric matrices to glass fibers. As a result, the mechanical properties of the polymer/glass composites are dramatically improved. Further, the as-formed composites can withstand a wet environment for a quite long time period without showing any significant loss in mechanical properties. A very good literature review exists, dealing with associated silane theories and applications [1]. Table 1.1 lists some representative commercial silane coupling agents [1].

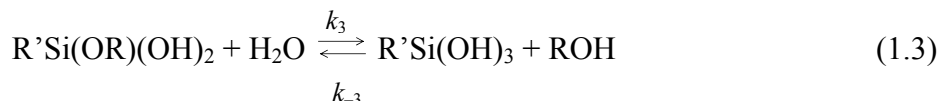
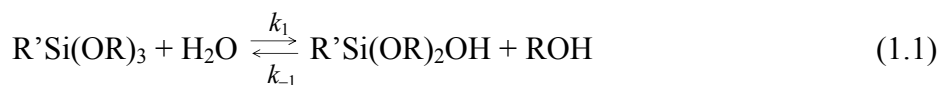
Table 1.1. Representative commercial silane coupling agents [1]

| Organofunctional group | Chemical structure | Abbreviations |
|------------------------|---|---------------|
| Vinyl | $\text{CH}_2=\text{CHSi}(\text{OCH}_3)_3$ | VS |
| Chloropropyl | $\text{Cl}(\text{CH}_2)_3\text{Si}(\text{OCH}_3)_3$ | CPS |
| Epoxy |  $\text{CH}_2\text{CHCH}_2\text{O}(\text{CH}_2)_3\text{Si}(\text{OCH}_3)_3$ | GPS |
| Methacrylate |  $\text{CH}_2=\text{C}(\text{CH}_3)\text{-COO}(\text{CH}_2)_3\text{Si}(\text{OCH}_3)_3$ | MPS |
| Primary amine | $\text{H}_2\text{N}(\text{CH}_2)_3\text{Si}(\text{OCH}_3)_3$ | APS |
| Diamine | $\text{H}_2\text{N}(\text{CH}_2)_2\text{NH}(\text{CH}_2)_3\text{Si}(\text{OCH}_3)_3$ | AEAPS |
| Mercapto | $\text{HS}(\text{CH}_2)_3\text{Si}(\text{OCH}_3)_3$ | MGPS |

1.1.1. Silane solution chemistry: hydrolysis and condensation

In most cases, the hydrolyzable alkoxy groups (OR) of silanes need to be converted to active silanols (SiOH) in the presence of water or moisture before application. This process usually takes place in a diluted silane solution. The following section discusses silane solution chemistry. Critical phenomena such as hydrolysis and condensation in a silane solution have been studied extensively [1].

Hydrolysis of alkoxy groups (esters) of organotrialkoxysilanes in their aqueous solutions occurs in a stepwise manner, as is shown as follows [2].



Pohl et al. [2] monitored each step of the hydrolysis reaction of vinyltrialkoxysilane solution using an NMR technique. They found that the ratios of the rate constants k_1/k_2 and k_1/k_3 are small. This indicated that the first step of the hydrolysis is slow, and thus becomes the rate-determining step in the process of silane hydrolysis.

The kinetic of hydrolysis of alkoxy silane esters in organic solvent/water mixture is generally expressed by [3]

$$\begin{aligned} -d[S]/dt = & k_{\text{spon}} [\text{H}_2\text{O}]^n [S]^m + k_{\text{H}} [\text{H}^+]^n [\text{H}_2\text{O}]^n [S]^m \\ & + k_{\text{HO}} [\text{HO}^-]^n [\text{H}_2\text{O}]^n [S]^m + k_{\text{B}} [\text{B}]^n [\text{H}_2\text{O}]^n [S]^m \end{aligned} \quad (1.4)$$

where $[S]$ = the concentration of the alkoxy silane, $-d[S]/dt$ = hydrolysis rate, and $[B]$ = the concentration of any basic species other than hydroxide anion (OH^-). Expression (1.4) contains all possible factors that affect silane hydrolysis.

The first term on the right is the spontaneous reaction rate without catalysis. This term is not of great interest to researchers. The reason is that the spontaneous hydrolysis

occurs so slowly that the corresponding contribution to the observed rate of hydrolysis is negligibly small under most conditions.

The second, third and fourth terms on the right of Expression (1.4) describe the contributions of acids and bases to silane hydrolysis. It is seen that both acids and bases accelerate silane hydrolysis but in different ways. Pohl reported [4] that, “acid-catalyzed hydrolysis involved attack on an alkoxy oxygen by a hydronium ion (H^+) followed by bimolecular SN_2 -type displacement of the leaving groups by water. Alkali-catalyzed hydrolysis involved attack on silicon by a hydroxyl ion (OH^-) to form a pentacoordinate intermediate followed by a bimolecular displacement of alkoxy by hydroxyl. Rates of hydrolysis by both mechanisms were influenced by the nature of the alkyl group on silicon as well as the leaving alkoxy group”. Osterholtz and Pohl [3] further stated that the hydrolysis of trialkoxysilanes is the slowest at around neutral pH (pH 7); while at pH 4, the hydrolysis is about 1000 times faster than at pH 7.

The final hydrolysis product, monomeric silanetriols in the form of $R'Si(OH)_3$, however is not stable in concentrated aqueous solutions. These silanetriols tend to condense with themselves to form oligomeric siloxanols, $R'(SiOSi)_n(OH)$. It was found [5] that only very dilute silane solutions, e.g., 0.15% for γ -aminopropyltriethoxysilane (γ -APS) and 1% for vinyltriethoxysilane (VS), remain as monomeric silanetriols. Therefore, it should be kept in mind that, in most practical cases, the employed silane solutions contain oligomeric siloxanols rather than monomeric silanetriols, as the practical silane concentration is normally above 1%. Thus, another critical concern on silane solution chemistry is condensation of silanols in aqueous solutions.

Condensation of silanols and rehydrolysis in difunctional silane aqueous solutions is in equilibrium with an equilibrium constant of condensation $K=210$ (Figure 1.1), as observed by Pohl et al [6].

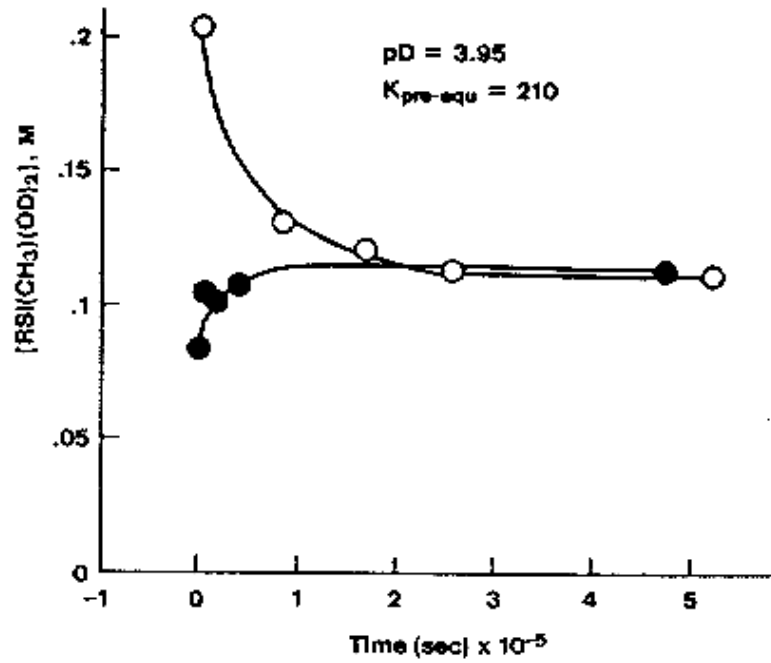


Figure 1.1. A plot of the concentration of gamma-glycidoxypropylmethylsilanediol vs. time; empty dot=silane diol; solid dot=disiloxane [6]

A kinetic expression describing the rate of silanol condensation to disiloxane is given as [3],

$$-d[S']/dt = k_H [H^+] [S']^2 + k_{HO} [HO^-] [S']^2 + k_B [B] [S']^2 \quad (1.5)$$

where S' = SiOH groups, $-d[S']/dt$ = rate of silanol condensation, and B = any basic species other than OH^- .

It is seen in Expression (1.5) that both acids and bases also catalyze the condensation reaction in silane solutions. The rate minimum for tri-functional silanes is found at about pH 4. A high pH favors the condensation of SiOH groups, leading to a premature gelatin before all alkoxy groups are hydrolyzed [3].

HCl-catalyzed propyltrimethoxysilane hydrolysis in the aqueous solution was studied using HPLC [7]. It was observed that the formation of dimeric species proceeds much faster than that of trimeric species, and the appearance of haze or onset of phase separation in the solution is coincident with the occurrence of branching or cyclic formation (i.e., tetramer). In addition to acids and bases, other factors that influence both hydrolysis and condensation reactions in silane solutions are summarized as follows.

Steric effect The rates of hydrolysis of alkoxy groups are generally associated with their steric bulk: $\text{CH}_3\text{O} > \text{C}_2\text{H}_5\text{O} > \text{t-C}_4\text{H}_9\text{O}$. That is, the smaller the size of the alkoxy groups, the faster the hydrolysis rate. A methoxysilane, for instance, hydrolyzes at 6-10 times the rate of an ethoxysilane [7].

Organic substitution (alkyl substitution) The hydrolysis rate increases with the increase of organic substitution: $\text{Me}_3\text{SiOMe} > \text{Me}_2\text{Si}(\text{OMe})_2 > \text{MeSi}(\text{OMe})_3$ [7]. It was also reported that increasing size of alkyl group on silicon would increase the stability of intermediate silanols and a tendency for cyclic siloxane formation upon condensation [1].

Organic solvents The condensation of silanols in protic solvents, such as water, methanol, ethanol, etc, approach equilibrium rather than completion, due to the competition between silane hydrolysis and alcoholysis. On the contrary, the condensation in non-protic solvents such as dioxane, tends to completion [3].

Solution concentration Silanols are stable in a very diluted solution, during which the silanols would be relatively isolated from one another and stabilized by hydrogen bonding to water. Thus, the diluted silane aqueous solution would retain much silane-triol ($R'Si(OH)_3$), or low-molecular oligomeric siloxanol structure.

Hydrophilic organofunctional group (amines) It was found that a relatively concentrated γ -APS aqueous solution has a good stability. The phenomenon has been explained by the bonding of silanol hydrogen to amino groups preventing the crosslinking between silanols [8]. A possible conformation is shown in Figure 1.2 [8].

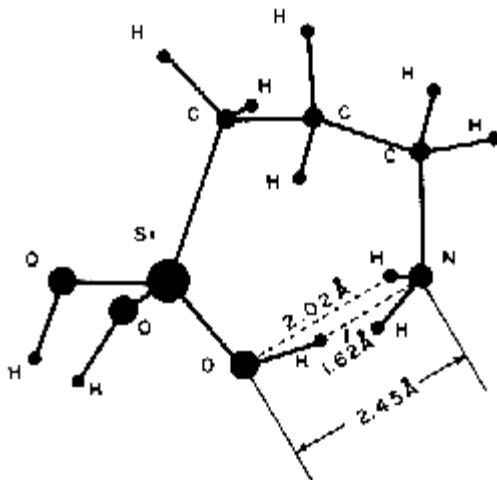


Figure 1.2. Possible conformation of aminopropylsilane triol with total conformational energy of -26.3kcal/mol [8]

1.1.2. Bonding mechanisms through silane coupling agents

Bonding to glass/metal surface via silane coupling agents has been extensively studied, and effects of glass/metal surface conditions and organofunctional groups (e.g., amino groups) of silanes have been investigated [9-13]. A generally-accepted bonding

mechanism to date states that silanols (SiOH) deposited on silica/mineral surface would react with hydroxyl groups (MeOH) on a hydrated glass/metal surface, forming covalent bonds of siloxanes/metallo-siloxanes (SiOMe) and releasing water. Figure 1.3 schematically shows the resultant interface with SiOMe bonds.

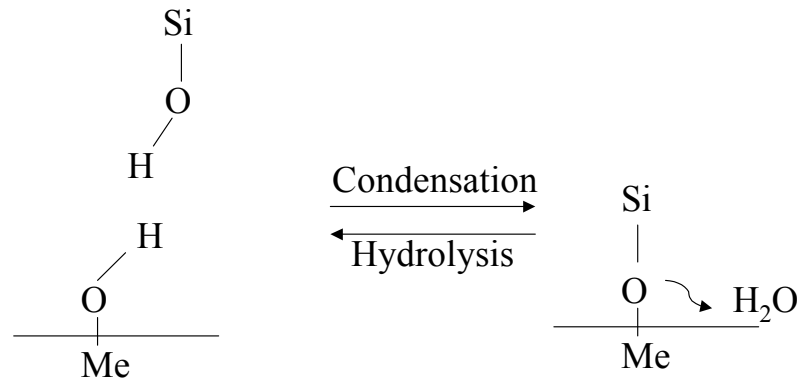


Figure 1.3. Schematic of condensation of silanol with hydroxyl groups on the glass/metal surface (Me stands for Si or metal)

Although SiOMe bond at the interface has not been clearly identified detected due to the limitations of current analytical techniques, a great deal of indirect evidence obtained from performance testing for silane modified glass/polymer compositions supported this bonding mechanism [6]. According to Plueddemann et al [1], a well-bonded interface should meet the following requirements:

Equilibrium conditions at the interface It is known that siloxane bonds formed at the interface are hydrolyzable during long-term exposure to water and re-formable when dried. Again, no direct evidence has been available so far for the equilibrium conditions

at the interface, but such reversible natures of the siloxane-bonded interface has been demonstrated in performance testing. Bonding of a trialkoxysilane $R'Si(OH)_3$ to silica has a much greater improvement in water resistance than a simple alkoxy bond between a hydroxyl functional polymer and silica [1].

Maintaining equilibrium conditions across the interface The favorable conditions for bonding across the interface are, (1) a maximum initial formation of MeOSi; (2) a minimum equilibrium concentration of water at the interface; and (3) polymer structures that hold silanols at the interface.

Plueddemann further concluded that “the bond between a silane-modified resin and a hydrophilic mineral surface is pictured as existing under equilibrium conditions of oxane bond formation and hydrolysis to silanols in the presence of water”; and that “most favorable bonding in the presence of water is obtained with a hydrophobic interphase region that is highly cross-linked” [1].

Bonding to polymers via silane coupling agents has also been studied [14-19]. However, the mechanism by which silanes bonding to various polymers is still not fully understood. The basic understanding on this aspect is that a good adhesion of silanes to polymers is attributed to, (1) chemical reactions occurring between organofunctional groups in the silanes and reactive groups in the polymers, and/or (2) interpenetrating networks (IPN) formed at the silane/polymer interface. Table 1.2 [20] gives a guide of compatible silanes to polymers, mostly on the basis of empirical experiences.

Table 1.2. A guide of compatible silanes to polymers

| <u>Class</u> | <u>Reactivity/product class</u> |
|--------------------------------|--|
| Vinyl | Peroxide activated cure (heat cured rubber) |
| Hydride | Vinyl addition (platinum cure) |
| Silanol | Dehydrogenative coupling (metal salt cure) (foamed silicones, water repellent coatings) |
| Alkoxy/Polymeric Alkoxide | Moisture cure 1-part RTVs Condensation cure 2-part RTVs Sol-gel (ceramics, ormosil) |
| Amine | Polyureas, polyimides |
| Epoxy | Epoxy addition Cationic UV |
| Carbinol | Polyester Polyurethane |
| Methacrylate/Acrylate | Radical (including UV) cure |
| Mercapto | Thiol-one UV cure Thermal cure |
| Acetoxy/Chlorine/Dimethylamine | Moisture cure |

1.1.3. Corrosion protection of metals by silane surface treatment

The use of silanes for corrosion protection of metals was expected a long time ago [1], but an intensive research on this aspect has only been carried out within the past few years. This is mostly a response to the request of seeking an alternative for conventional chromating processes in metal-finishing industries. So far, chromates are still the most efficient within the current repertoire of inhibitors. Nevertheless, the well-recognized toxicity and carcinogenicity of hexavalent chromium ions (Cr^{6+}) leads to the high

restriction of the continued use of chromates. In Europe, for example, the “End-of Life Vehicle” directive issued in 2000 states that, “ Member States shall ensure that materials and components of vehicles put on the market after 1 July 2003 do not contain lead, mercury, cadmium or hexavalent chromium...”.

As a result, a number of candidates (also called “green inhibitors”) have been explored with the hope of providing an alternative for chromates [21-23]. In summation, these studies showed that, (1) most individual alternatives cannot provide equivalent anticorrosive performance on metals as chromates; in most cases, the mixtures of several types of “green inhibitors” are used to achieve a desired performance, and (2) most alternatives do not give comparable paint adhesion as chromates do. In comparison to the others, the performance of silanes is more promising, and is comparable to that of chromates in most cases. As consistently demonstrated by performance testing, silane surface treatment provides not only corrosion protection but also paint adhesion as well for a broad range of metals. Van Ooij and his coworkers pioneered in this field [24-29]. Their previous efforts are summarized as follows.

Selection of silanes for corrosion protection of metals Numerous silanes were tested on a variety of metals with and without topcoats. Silanes that are suitable for corrosion protection of metals are divided into two categories in terms of their chemical structures: mono-trialkoxysilanes (mono-silanes hereon) and bis-trialkoxysilanes (bis-silanes hereon). Examples are listed in Table 1.3. Mono-silanes, with the general formula of $R'(CH_2)_nSi(OR)_3$, are actually silane coupling agents mentioned above. Bis-silanes have been mainly used as crosslinkers for the silane coupling agents [1], which has a general formula of $(RO)_3Si(CH_2)_nR'(CH_2)_nSi(OR)_3$. Obviously, a major difference

between these two types of silanes is the number of Si atoms per molecules. Mono-silanes only contain one Si atom per molecule, attached by 3 OR groups, while bis-silanes have two Si atoms per molecule, attached by 6 OR groups in total. Assuming all OR groups hydrolyze for both silanes, the mono-silanes would then obtain maximum 3 SiOH groups per molecule while the bis-silanes would have maximum 6 SiOH groups per molecule. After fully condensation of SiOH groups, a bis-silane film is then expected to be much denser than a mono-silane film.

Table 1.3. Silanes suitable for corrosion protection of metals

| Name (abbreviations) | Chemical structure |
|---|---|
| <i>Mono-silane: $R'(CH_2)_nSi(OR)_3$</i> | |
| Vinyltriethoxysilane (VS or VTES) | $CH_2=CHSi(OC_2H_5)_3$ |
| γ -ureidopropyltriethoxysilane (γ -UPS) | $N_2HCNH(CH_2)_3Si(OC_2H_5)_3$ O |
| <i>Bis-silane: $(RO)_3Si(CH_2)_nR'(CH_2)_mSi(OR)_3$</i> | |
| Bis-[triethoxysilyl]ethane (BTSE) | $(C_2H_5O)_3Si(CH_2)_2Si(OC_2H_5)_3$ |
| Bis-[triethoxysilylpropyl]tetrasulfane (Bis-sulfur silane) | $(C_2H_5O)_3Si(CH_2)_3S_4(CH_2)_3Si(OC_2H_5)_3$ |
| Bis-[trimethoxysilylpropyl]amine (Bis-amine silane) | $(CH_3O)_3Si(CH_2)_3NH(CH_2)_3Si(OCH_3)_3$ |

Performance tests demonstrated that although mono-silanes protect metals to a certain extent under the painted state, bis-silanes usually provide a better performance on a broader range of metals. The metals and alloys that are protected by bis-silanes include: Al and Al alloys, Fe and steels, Zn and Zn-coated steels, Cu and Cu alloys, and Mg and Mg alloys [24-30].

Optimization of process parameters Process parameters, such as silane solution concentration, solution pH, dipping time, curing temperatures and aging time, have been studied [26]. Based upon this, a typical procedure of silane surface treatment is made. The metal to be treated is degreased by organic solvents like ethanol and alkaline cleaners, followed by tap water rinsing and blow-air drying. The metal is then dipped into a silane solution for 30 sec., followed by drying in air either at ambient temperature or at elevated temperatures. It should be noted that the cleaned metal surface should be completely wettable to water, i.e., a “water-break-free” surface. Otherwise, any contaminants will affect silanol adsorption during immersion.

Some other important results are summarized as follows [26]. (1) A 5% by volume silane solution is needed for depositing a relatively thick silane film on metals for bare corrosion protection (without topcoats), while 2% by volume is used as pretreatment of metals prior to topcoating. (2) Dipping time does not significantly affect the performance of the resulting silane films, as the equilibrium of the adsorption of silanols onto metals achieves very quickly. It was found that dipping time of 5 sec. and 30 min makes no difference in corrosion protection performance of silane films. (3) An elevated-temperature curing process is optional, which all depends on the end use of the treated metals. No curing is recommended if silane-treated surfaces are to be painted. In this

way, reactivity of organofunctional groups of silanes can be retained for reacting with paints. A curing process at a high temperature (e.g., 100°C) for a long time period (e.g., several hours) greatly accelerates the crosslinking process in silane films, and is usually used to obtain an extensively crosslinked structure. (4) A two-step process was proposed. BTSE provides good bare corrosion protection on metals, but it is not compatible with paints since it has no organofunctional groups. Thus the other silane layer with proper functionalities (e.g., γ -APS) is applied on top of BTSE. Such multiple-silane system has proven to process both corrosion protection and paint adhesion [27].

Another important parameter which has often been ignored in these studies is the hydrolysis time of silane solutions. The study on this aspect, however, has not been explored sufficiently. As is known, hydrolysis and condensation of silane solution is a time-dependent process. A “workable” silane solution should contain a sufficient number of SiOH groups for the subsequent condensations during silane surface treatment. Without sufficient hydrolysis, an oily silane film is obtained. Such film cannot provide corrosion protection due to the lack of a crosslinked structure and a good adhesion to substrates. Ogarev and Selector [31] pointed out in a review on silanes for corrosion protection that the published results were poorly reproducible in most cases. This may be also due to the ignorance of the hydrolysis time by these investigators.

Structural characterization of silane films on metals Silane film characterizaion has been conducted using the following surface characterization techniques, such as FTIR-RA, XPS, ToF-SIMS, AFM, ellipsometry, SEM/EDX, etc [28]. The results showed that: (1) a nearly linear relationship was found in ellipsometric measurements between silane solution concentrations and the silane film thicknesses and their corresponding

solution concentrations; the thicknesses of bis-amino and bis-sulfur silane films on stainless steel as a function of their solution concentrations are shown in Figure 1.5 [28]; and (2) the structure of γ -APS film deposited on Fe and Zn were characterized with FTIR-RA as a function of pH, the results indicating the effect of pH on the film structure by showing the significant changes in the ranges between 1700-1300 cm^{-1} due to amine salts and 1100- 800 cm^{-1} due to siloxanes [28].

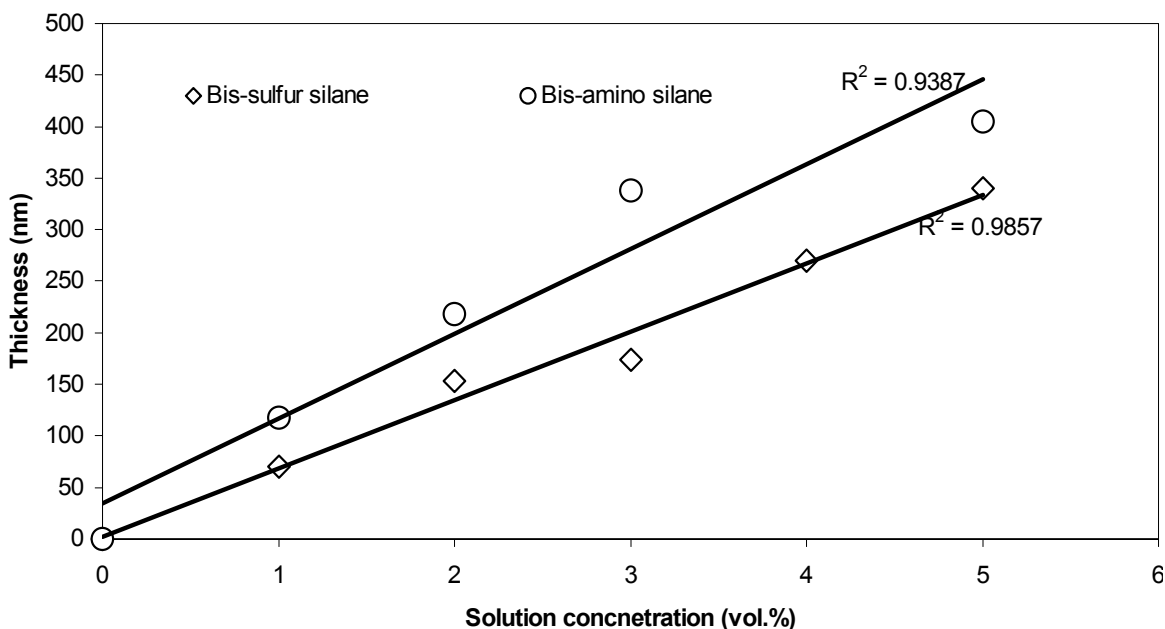


Figure 1.5. Film thickness of bis-sulfur and bis-amino silanes on stainless steel vs. solution concentration [28]

Electrochemical impedance spectroscopy (EIS), commonly used for monitoring organic coating degradation in aqueous environment, also found its application as a powerful characterization technique for silane films on metals [24, 27]. Non-corrosive electrolytes, such as potassium sulfates (0.5M K_2SO_4 solution) were used for

characterization purpose. The major benefit of EIS measurements in a non-corrosive electrolyte is that the information on film structures can be extracted without interference of corrosion information from corroding metal substrates usually caused by corrosive electrolytes such as NaCl. Subramanian [27] used EIS to characterize BTSE films on 1100 Al alloy (AA 1100) to investigate the effects of process parameters such as curing time on the structure of BTSE film.

Mechanism studies of corrosion protection of metals by silanes The effect of hydrophilic amino groups on the corrosion performance of γ -APS deposited on Fe was studied [30]. It was found that γ -APS film does not protect Fe from corrosion, as the amino groups in γ -APS film would compete with silanols to bond to the Fe surface, resulting in a hydrophilic interface which shows no water resistance in the DC polarization test. The study also found that amino groups would accelerate the ingress of aggressive chloride ions (Cl^-) into the film, which primarily accounts for the poor corrosion performance of γ -APS film on Fe.

The effect of silane solution pH on the corrosion rate of BTSE-treated Fe was also investigated [30]. The lowest corrosion rate was found at pH below 5, the mechanism for which was not proposed further. It is noted in ref. 30 that all the silane solutions with different pHs only hydrolyzed for 1 hr before application, thus, the effect of pH on the hydrolysis of BTSE should be pronounced. When catalyzed by acids, the silane solutions at pH 4-5 hydrolyzes faster than the others. As a result, more SiOH groups are obtained, and the resulting BTSE film should be more crosslinked than the others. This could be the direct contribution of low solution pH to a better corrosion performance of BTSE at pH <5.

Petrinin and his coworkers [32] studied the formation mechanism and anticorrosive properties of siloxane monolayers on Al surfaces using different silanes (VS, GPS, and APS, etc.) with ellipsometry and the quartz microbalance technique. They reported that the covalent bonding of silanes with the surface (AlOSi bonds) occurs in the presence of adsorbed water on the Al surface. The presence of a silane monolayer on Al decreases water adsorption on the surface, and inhibits hydration of the oxide metals film, and that a positively charged layer, such as γ -APS, activates local metal corrosion in chloride containing media by promoting the adsorption of chloride ions on the metal surface.

Beccaria and Chiaruttini [33] reported that methacryloxypropyltrimethoxysilane (MAOS) showed a good inhibitive action on aluminum corrosion in sodium chloride solutions due to the synergistic effect of aluminum oxides and of Al-siloxane compounds (formed by chemical condensation reactions between silanols and aluminum oxides) which form a polymeric passive film hindering ion diffusion.

Underhill and Duquesnay [34] measured corrosion resistance of 7075-T6 and 2024-T3 aluminum alloys treated with various silane coupling agents, such as GPS, MGPS, and BTMSE (bis(trimethoxysilyl)ethane), using the EIS technique. They found that MGPS exhibited the best improvement, compared to the others.

However, it should be pointed out that, as compared with chromates, the major downside of silanes is a lack of “self-healing” effect that is very important in service. In reality, such mechanical damage as scratches and pin-points on metal surfaces is common. In the case of chromating, chromate ions can diffuse to the damaged area in an aqueous medium and reform protective compounds with the metal in-situ. The damaged

area is thus “healed”. A current study conducted by Van Ooij and his coworkers is focusing on eliminating this shortcoming by incorporating certain inhibitors into silane films. A similar work has also been done by Aramaki [34]. In this work, a chromate-free inhibitor, sodium octylthiopropionate ($C_8H_{17}S(CH_2)_2COONa$, or NaOTP), was incorporated into a BTSE film on Fe. It was reported that NaOTP behaved effectively for corrosion inhibition of Fe in an aerated 0.1 M NaCl solution. The BTSE film was then crosswise scratched with a knife-edge, and the healing ability of the film was observed during polarization and impedance measurements in the NaCl solution.

1.2. Corrosion of aluminum and 2024-T3 aluminum alloy

Due to the increasing use of Al alloys in aerospace and automotive industries, the studies related to corrosion of Al and Al alloys have been performed intensively in the last few decades. This review intends to summarize these works, especially focusing on corrosion of Al and 2024-T3 Al alloy (AA 2024-T3). AA 2024-T3, as a major aerospace alloy, is a hot topic in the current corrosion field. Despite of its excellent mechanical properties, the alloy suffers different forms of corrosion due to its intrinsic electrochemical properties.

1.2.1. Corrosion of Al

1.2.1.1. Pitting corrosion of Al

It is well known that Al and its alloys have a high corrosion resistance in noncomplex aqueous solutions due to the protection of the passive Al oxide film formed on the surfaces. The passive Al oxide film exhibits both low solubility and electronic conductivity in the aqueous media over a pH range of 4 to 9 (as shown in Figure 1.6 [36]), which blocks redox reactions on the oxide film. In halogen environments (e.g., chloride-containing solutions), however, both Al and its alloys suffer severe pitting corrosion, as the passive Al oxide film tends to be broken down by the local attack of chloride ions and thus no longer protects the bare Al underneath.

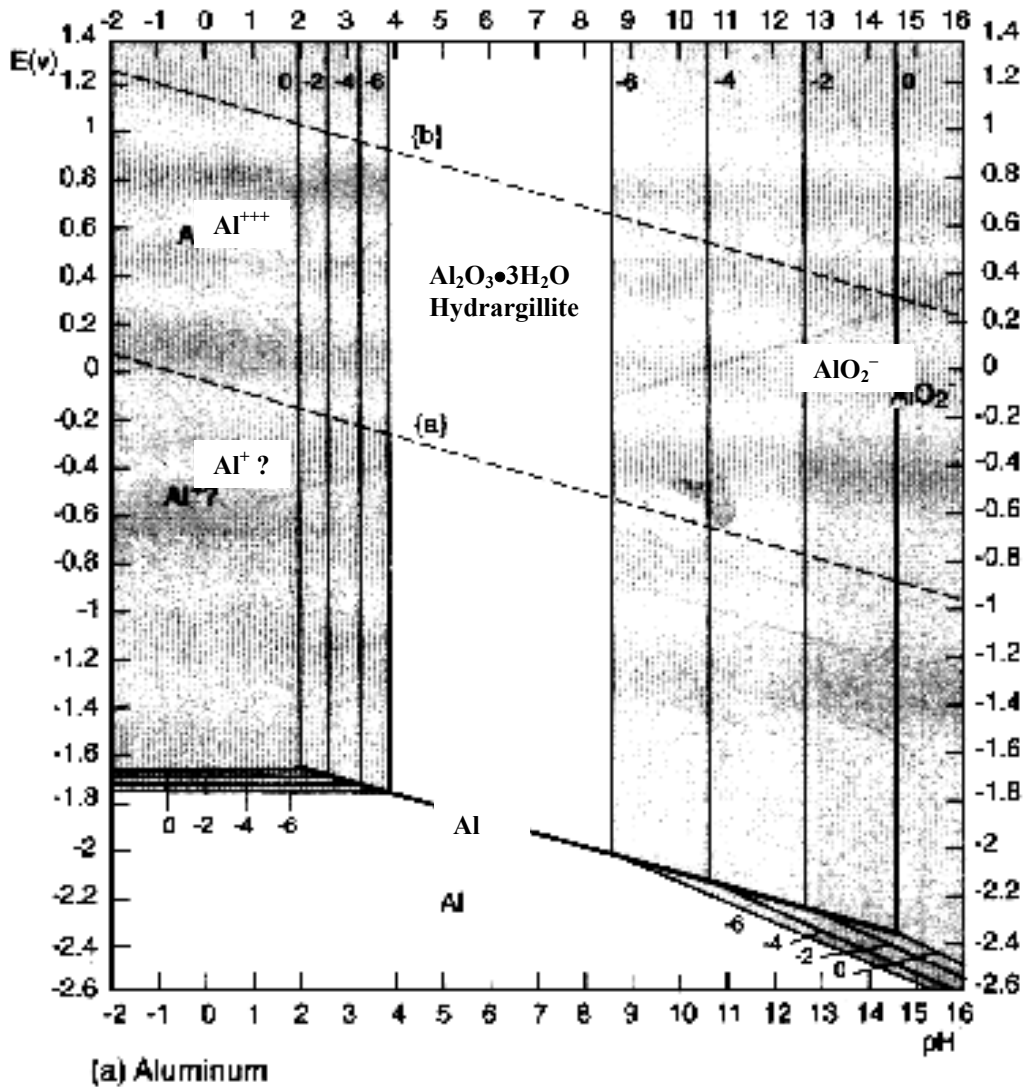


Figure 1.6. Pourbaix diagrams for pure Al. Shaded areas indicate corrosion susceptibility. Labels 0, -2, -4, and -6 are the log of soluble ion activity for the indicated lines [36]

Four stages have been proposed for the pitting process of Al in a halogen solution [37]: (1) processes at oxide/solution interface; (2) processes in the oxide film; (3) formation and repassivation of metastable pits below the critical pitting potential; and (4) growth of stable pits above the critical pitting potential. Among these stages, (3) can be

regarded as an intermediate step in pitting. A large number of works have focused on the latter two stages; the first two stages associated with the interactions between corrosive species (e.g., Cl^-) and oxide films, however, have not been fully understood.

Adsorption of chloride ions on Al oxide It is believed that Al pitting in halogen aqueous media is initiated by the local attack of halogen ions, e.g., Cl^- ions, on Al passive oxide films. Although the early stages of the pitting process have not been fully understood, many studies did conform that Cl^- ions adsorbed at certain sites on passive Al oxide films [38-40], by using autoradiography, SIMS, and X-ray photoelectron spectroscopy. Such sites usually are considered as the defects on the Al surface initially, and the corresponding pit sites later on. Berzing [38] measured the amount of chloride adsorbed (w_{cl}) as a function of the chloride concentration (Cl) and time using Cl^{36} as a radioactive tracer:

$$\log w_{\text{cl}} = 0.64 (\log(\text{Cl}) + \log t) - 7.8 \quad (1.6)$$

where w_{cl} is expressed as g cm^{-2} , (Cl) as mol^{-1} and t in min. They concluded that a corroding Al surface has a variety of adsorption sites with different adsorption properties; only a minority of these sites is active for pitting corrosion; and the presence of an inhibitor will delay but not prevent the onset of pitting.

Pitting initiation Szklarska-Smialowska observed current oscillations on anodic polarization curves at a constant potential below the pitting potential for various metals and alloys in chloride solutions [41]. This phenomenon was believed to be associated with the consecutive formation and repassivation of metastable pits, which is an

intermediate step in the pitting process. The metastable pits are in microsize and grow and repassivate in less than a few seconds. Further work made by Pride et al [42] has shown that the number of metastable pits on pure aluminum increase when increasing the anodic potential (up to the pitting potential) and/or the concentration of Cl^- ions (Figures 1.7 and 1.8 [42]). It is clear that the current spikes (or the rate of metastable pit nucleation) increase with the applied anodic potential and the concentration of Cl^- ions.

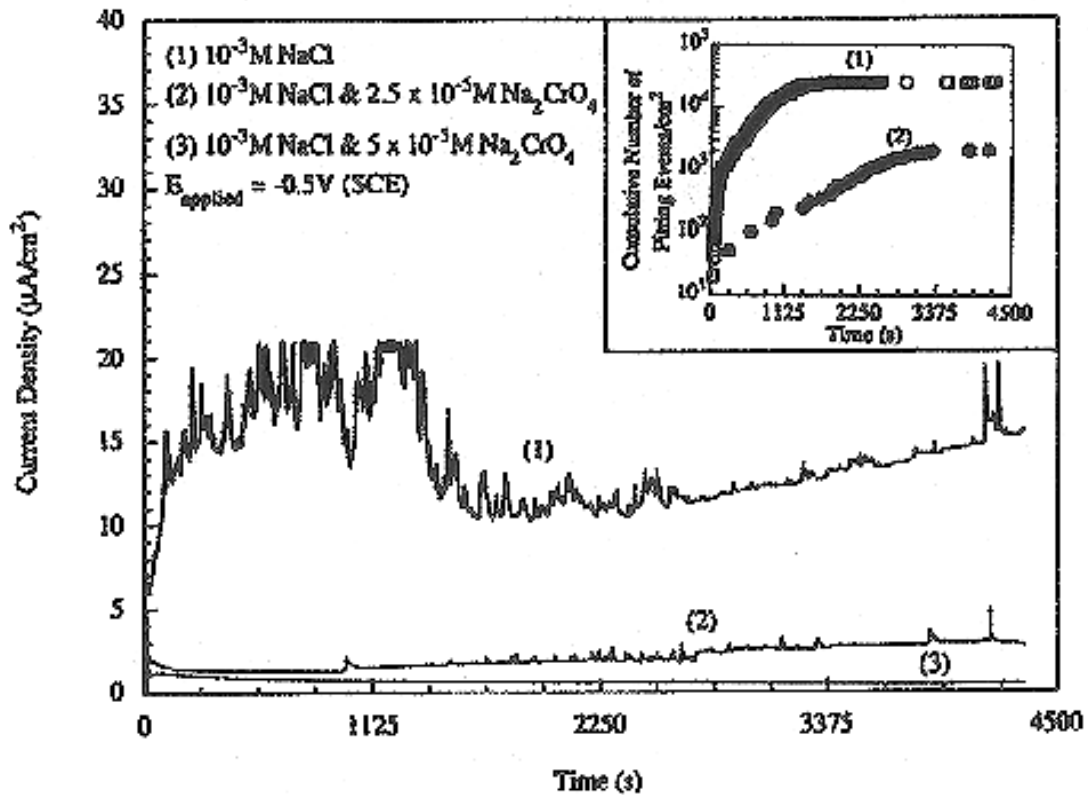


Figure 1.7. Time series showing the effect of potential on anodic current spikes associated with metastable pitting [42]

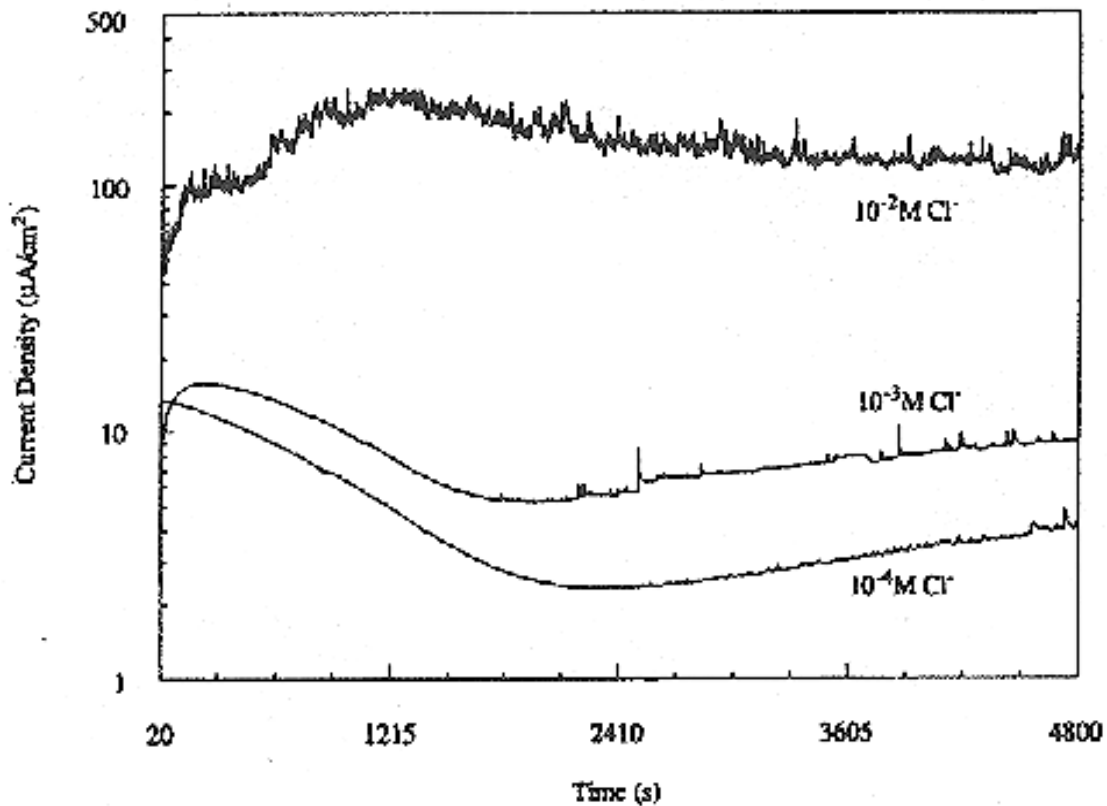


Figure 1.8. Time series showing the effect of concentration of Cl^- ions on the anodic current spikes associated with metastable pitting (polarized at -0.6 V) [42]

A necessary condition for pit growth is to stabilize metastable pits. Buzza and Alkire [43] suggested that an active pit requires a critical concentration adjacent to the pit surface at a certain applied potential. Frankel et al [44] reported that metastable pitting on stainless steel is stabilized by the ohmic drop associated with the porous pit cover and that repassivation is expected to occur if the pit cover ruptures. When the cap on the pit is broken the pit solution is diluted and repassivation occurs. According to Galvele [45], a stable pit would grow if the critical value of $x \cdot i$ (pit depth times pit current density) were

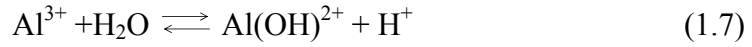
exceeded. The pH of the pit solution is intimately associated with the concentration of Cl^- ions. A higher Cl^- concentration in the pit solution would lower the pH until a solid metal salt is formed in the form of MeCl_x and/or MeOH_xCl_y (Me refers to metal cation). The chloride salts are only stable in a high acidic solution.

Kinetics of pit growth The work done by Godard [46] on Al showed that the pit depth was proportional to $t^{1/3}$. Hunker and Boehni studied the time required for pits to perforate Al foils of different thickness in chloride solutions and in a chloride solution containing different anions at a constant potential [47]. They reported that the pit growth is ohmically controlled because the rate of pit growth is related to the conductivity of the bulk electrolyte. The pit depth is a function of time ($d \approx t^{1/2}$) as is pit current density ($i \approx t^{-1/2}$), which are consistent with both a diffusion controlled and an ohmic controlled pit growth rate.

Pitting chemistry A chloride salt film forms at the bottom of a pit, as a result of rapid dissolution of Al. In the literature, two types of salts in terms of the chemical composition have been identified [48]: aluminum chloride (AlCl_3) and aluminum oxychlorides $\text{Al}(\text{OH})_2\text{Cl}$ and $\text{Al}(\text{OH})\text{Cl}_2$. The pH of the pit solution is highly dependent upon the salt type: The pH could be 1 in the presence of AlCl_3 ; while the pH of a saturated solution of $\text{Al}(\text{OH})_2\text{Cl}$ is around 3. In a pure Al pit, the solution pH was found to be between 3 to 4, even when the bulk solution pH was 11 [48]. Hoch [49] measured a pH 1 at the active heads of the filiform corrosion.

According to Hagyar and Williams [50], a pitting process in a chloride-containing aqueous solution can be generally expressed as the following sequence of reactions:

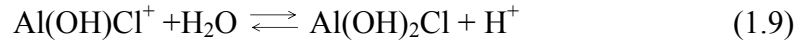
(1) Ionization of Al, followed by a rapid hydrolysis to form Al hydroxide



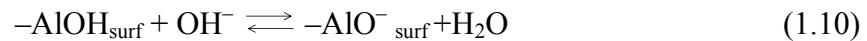
(2) Al hydroxide reacts with chloride ions to form chloride salts



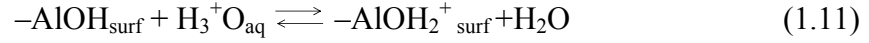
(3) Hydrolysis of chloride salts to acidify the pit solution



E. McCafferty et al [51] has proposed a pitting model by taking into account the effect of isoelectric point (IEP) of surface oxides. When immersed in aqueous solutions, the hydroxyl groups on the outermost surface of Al oxide will remain undissociated if the solution pH is equal to the IEP of the oxide (i.e., “pH of zero charge”). If the pH is greater than the IEP, the surface will acquire a negative charge due to dissociation of the surface hydroxyl group,



and if the pH is less than the isoelectric point, the surface will acquire a positive charge due to attraction of a proton,



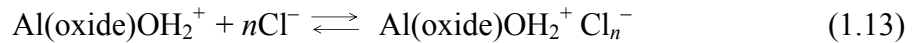
In a neutral aqueous solution, the oxide-covered Al surface acquires a positive charge. This is because the as-reported IEP of Al oxide film is 9.5 [52], greater than 7.0.

Based on the above considerations, the following sequence of reactions is suggested to describe pit initiation due to the adsorption of Cl^- ions, transport of chloride through the oxide film by means of oxygen vacancies [53, 54], and local dissolution of Al atoms at the metal/oxide interface in three consecutive one-electron transfer reaction in a chloride-containing aqueous solution:

(1) Positive charging of Al surface hydroxide



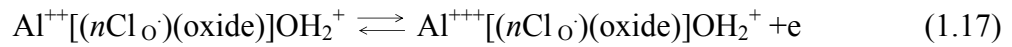
(2) Adsorption of Cl^- ions on positively-charged Al hydroxide



(3) Transport of chloride through the oxide film by means of oxygen vacancies



(4) Local dissolution of Al atoms at the metals/oxide interface in three consecutive one-electron transfer reaction

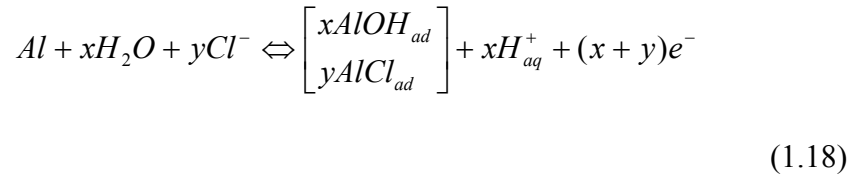


where Al(oxide)OH refers to a substrate Al atom located beneath the oxide, the surface of which is positively charged (OH_2^+); V_{O}^- represents an oxygen vacancy in the oxide film; and Cl_{O} is a Cl^- ion occupying an oxygen lattice site. Al^+ , Al^{++} , and Al^{+++} , respectively, represent mono-, di-, and trivalent Al ions at the metals/oxide interface, i.e., at the pitting site. It is noted that the adsorption of chloride ions is non-uniformly distributed, and Cl^- ions accumulate in clusters on the oxide surface where pits are to initiate.

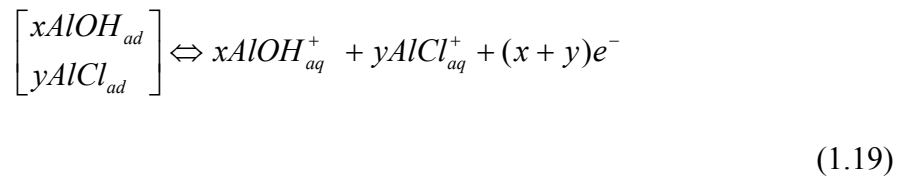
Pyun et al [55] studied the formation and repassivation of Al pitting in different halide aqueous solutions with the concentration ranging from 0 to 0.5 M by measuring potentiostatic current transients using an abrading electrode technique. A 0.5 M Na_2SO_4 solution was used as a buffer solution. They found that the anodic behavior of Al-1 wt.% Si-0.5 wt.% Cu alloy was highly dependent upon the concentration of halide ions in the solutions, and hence could be divided into the following three groups. (1) In low concentrations (0 – 0.01 M), only repassivation occurs due to the formation of

passivating oxide. (2) In intermediate concentrations (0.05 – 0.3 M), a competition occurs between oxide repassivation and film breakdown, and the stable pit grows after an induction time of t_m . (3) In high concentrations (> 0.3 M), only a uniform metal dissolution proceeds through the Al salt film. Based on these measurements and the facts that both oxygen and halide ions have an affinity for adsorption sites on the bare Al surface, and that competition exists between oxide repassivation by oxygen adsorption and film breakdown by halide ions adsorption, Pyun et al [55] suggested a pitting model in a chloride-containing solution, as expressed by the following consequence of reactions:

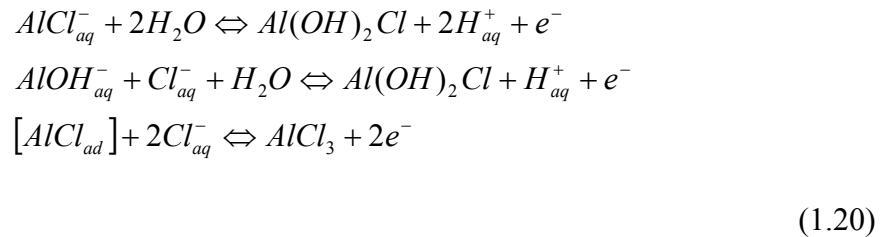
(1) Hydrolysis of bare Al surface and adsorption of Cl^- ions



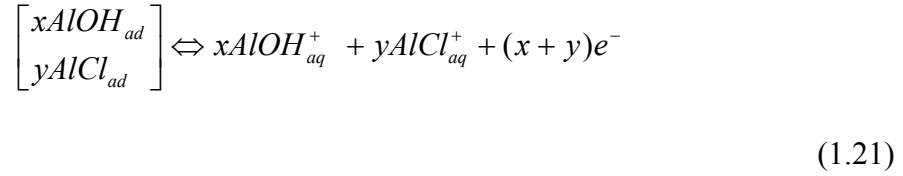
(2) Acceleration of dissolution



(3) Precipitation of chloride salt layers

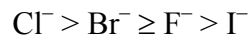


(4) Formation of the passivating oxide

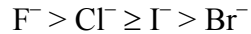


In the case of low concentrations of Cl^- ions, most adsorption sites on Al surface would be occupied by oxygen rather than Cl^- ions. In other words, Cl^- ions hardly accumulate at the adsorption sites to achieve a critical amount that is required for pitting initiation, and hence pitting is inhibited. In the case of high concentrations of Cl^- ions, adsorption of Cl^- would prevail on Al surface, resulting in Cl^- clusters at certain sites. Pitting would initiate at these sites, once the critical concentration of Cl^- ions is exceeded.

In addition to the above pitting model, they also determined the relative adsorption tendency of various halide ions. In the case of bare Al surface, halide ions have the following adsorption tendency,

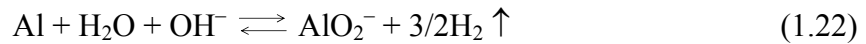


Whereas on an oxide-covered Al, the adsorption tendency is in the following order,



1.2.1.2. Cathodic corrosion of Al

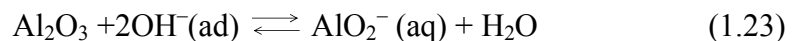
Al corrosion also occurs in highly alkaline aqueous media, starting with chemical dissolution of Al oxide. This type of Al corrosion is called cathodic corrosion of Al. The most detrimental species in this case is hydroxide ions (OH^-) other than Cl^- ions in neutral media. Van de Ven and Koelmans [56] proposed that cathodic corrosion of Al in aqueous solutions proceeds via a chemical dissolution reaction of aluminum by hydroxide ions and water,



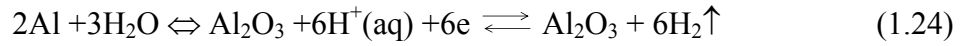
During the cathodic corrosion, the reduction of water results in hydrogen gas evolution (H_2) and formation of soluble aluminate ions (AlO_2^-) on the Al surface.

Moon and Pyun [57] conducted a detailed study on corrosion of pure Al during cathodic polarization in de-aerated aqueous solutions. They found that the corrosion of Al increased during cathodic polarization, accompanied by hydrogen evolution and that the oxide film is spontaneously formed and still exists at the Al surface even under cathodic polarization in aqueous solutions. Thus, they concluded that cathodic corrosion of Al proceeds by chemical dissolution of the oxide film at the oxide/electrolyte interface and by simultaneous oxide formation at the Al/oxide interface, as expressed as follows:

(1) Chemical dissolution of Al surface oxide at the oxide/electrolyte interface



(2) Simultaneous formation of Al oxide at the Al/oxide interface



Note that processes (1) and (2) occur simultaneously. Process (1) is simply a chemical reaction; while process (2) is an electrochemical reaction which involves an electron transfer.

1.2.2. Corrosion of 2024-T3 Al alloy

The microstructure of AA 2024 is characterized by a uniform distribution of second-phase particles in the Al matrix. These embedded second-phase particles, on one hand, lead to good mechanical properties of the alloy by the strengthening of the Al matrix; on the other hand, some particles undesirably make the alloy being highly corrosion-prone. In general, AA 2024 suffers corrosion such as pitting, intergranular corrosion and stress corrosion. Additionally, T3 condition was found to worsen the corrosion resistance of the alloy [58]. T3 condition indicates that AA 2024 alloy is solution heat-treated, cold-worked and naturally aged. With the hope of finding an efficient solution to improve its corrosion behavior, it is essential to understand corrosion phenomena of AA 2024-T3.

1.2.2.1. Second-phase particles in AA 2024-T3

In the literature [59-62], two major kinds of second-phase particles have been reported: Al-Cu-Mg-containing (Al_2CuMg or S phase) and Al-Cu-Fe-Mn-containing particles. In some cases, Si with a trace amount is also presented in these particles.

Al-Cu-Mg-containing second-phase particles (Al_2CuMg , or S phase) are characterized by a round or spherical shape with a high contents of Cu and Mg, i.e., 44 to 46% by weight Cu and 4 to 16% Mg [59]. It was also found that 2.7% of the total surface area of AA 2024-T3 was covered by S phase particles. S phase is anodic or active towards Al matrix, thus acting as an anode in aqueous corrosion of AA 2024-T3.

Al-Cu-Fe-Mn-containing second-phase particles are the other major kind found in a large quantity in AA 2024-T3. The average ratio among Cu: Fe: Mn is 2: 1: 1; the general chemical formula is suggested to be $Al_6(Cu, Fe, Mn)$ by SEM and TEM analysis [59,60]. These particles are more irregular or geometric, and rather large in size. In most cases, they display as clusters in the Al matrix of AA 2024-T3. The Al-Cu-Fe-Mn-containing phase is cathodic or noble towards Al matrix, and thus being an cathode during aqueous corrosion of AA 2024-T3.

In addition, some other types of second-phase particles with a small quantity have also been reported for AA 2024-T3. Such particles include Al-Cu-Mn, Al-Cu-Fe, and Al-Cu-Mn-Si-containing [59-61].

Table 1.4 lists corrosion potentials of some intermetallic compounds similar to the above second phases in NaCl aqueous solutions [62]. These values can be regarded as a reference to evaluate the susceptibility of these phases to corrosion.

Pryor et al [63] reported that the corrosion potential of Al-Cu alloy shifted to the more noble direction with an increase of Cu content, i.e., from -0.88 to -0.26 V/SCE in a 0.5 M NaCl solution. This indicates that corrosion resistance of Al-Cu is actually enhanced by a high Cu content, if Cu dissolves into Al matrix forming one uniform phase rather than presents in second-phase particles.

Table 1.4. Corrosion potentials of second phases in AA 2024-T3 [62]

| Phase | Stoichiometry | Corrosion potential (V/SCE) | Environment | Aeration | Other data reported* |
|----------|-------------------------------|-------------------------------------|--------------|---------------------|----------------------|
| θ | Al_2Cu | $-0.76, -0.64, -0.59$ | 1.0 M NaCl | N_2 spurge | AP, CP, RRDE |
| θ | Al_2Cu | $-0.70, -0.62, -0.49, -0.36, -0.32$ | 0.5 M NaCl | Open to air | -- |
| θ | Al_2Cu | -0.68 | 0.2 M NaCl | -- | AP, CP |
| S | Al_2CuMg | -0.89 | 1.0 M NaCl | Open to air | AP |
| S | Al_2CuMg | -0.92 | 0.5 M NaCl | N_2 spurge | -- |
| -- | $\text{AlCu}_{18}\text{Fe}_5$ | -0.67 | 0.6 M NaCl | N_2 spurge | GC |
| -- | $\text{AlCu}_{24}\text{Fe}_5$ | -0.67 | 0.6 M NaCl | N_2 spurge | GC |
| | Al Matrix of AA 2024-T3 | -0.65 | 0.6 M NaCl | Opent to air | AP, CP |

* AP: anodic polarization; CP: cathodic polarization; GC: galvanic couple; RRDE: rotating ring disk electrochemistry

1.2.2.2. Pitting associated with S phase in AA 2024-T3

Figure 1.9 shows the potentiodynamic polarization curve of AA 2024-T3 in a 1 M NaCl aqueous solution [61]. Two breakdown potentials are shown in the curve in Figure 1.9: the active one is close to -0.72 V/SCE (E_{b1}), corresponding to the dissolution of S phase; and the other noble one is close to -0.62 V/SCE (E_{b2}), due to the dissolution of Al matrix of AA 2024-T3.

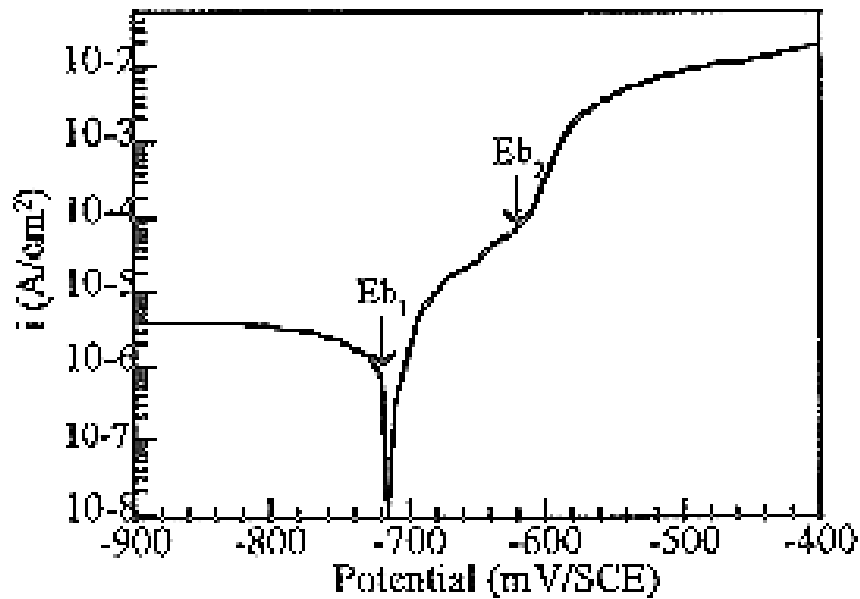


Figure 1.9 Potentiodynamic polarization curve of AA 2024-T3 in a 1 M aqueous NaCl solution [61]

S phase particles were found to dissolve preferentially in the early stages of immersion or when polarized the alloy at a more active potential in NaCl solutions [59,61,65]. From Table 1.4, it is seen that the corrosion potential of S phase is around -0.93 V/SCE, 0.30 V/SCE negative to that of the Al matrix of AA 2024-T3. In the case of immersion in an aqueous NaCl solution, S phase as an anode is subjected to a severe

galvanic attack. In general, the corrosion associated with S phase is accomplished by: (1) dealloying of Mg and Al of S phase particles; and (2) dissolution of the surrounding Al matrix. Figure 1.10 shows the SEM images of S phase particles after polarization to -0.69 V/SCE for 5 min. It is also noted that cathodic Al-Cu-Fe-Mn-containing particles and the Al matrix remain unattacked at this moment. Moreover, it was also found in the later corrosion stages that a large number of Cu nano-particles distributed uniformly on the corroding alloy surface.

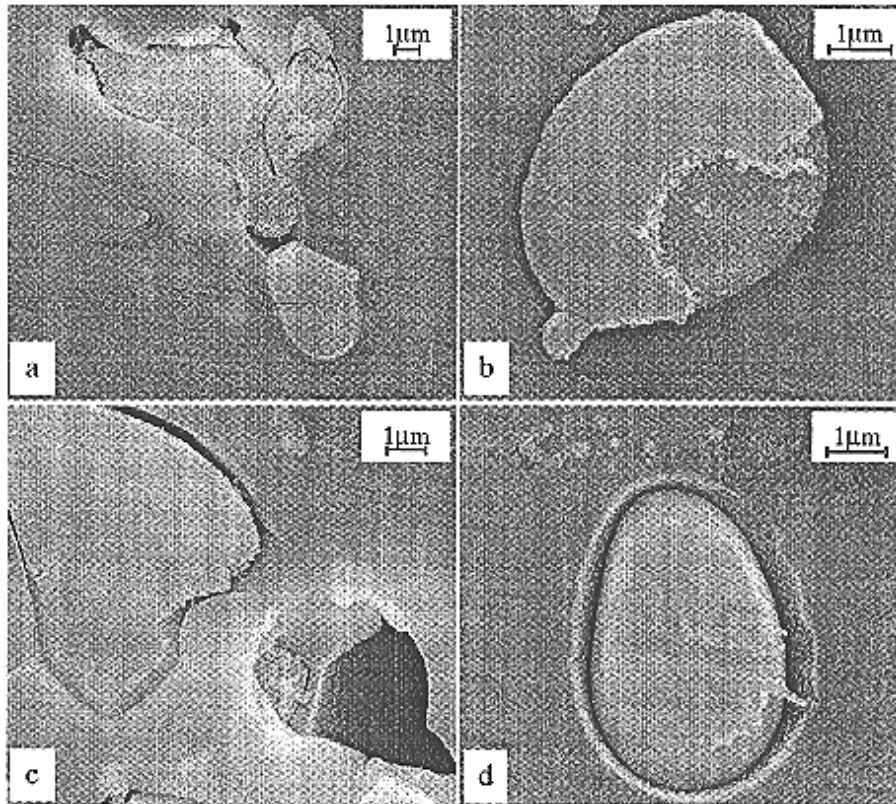


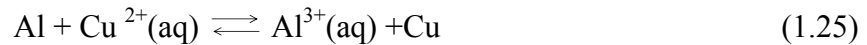
Figure 1.10 S phase particles after potentiodynamic polarization to -0.69 V/SCE, the potential was maintained at -0.69 V/SCE for 5 min [61]

In summation, two major versions exist of the mechanism concerning pitting corrosion associated with S phase and Cu redistribution. Buchheit et al [59] proposed that S phase particles are initially active with respect to the surrounding Al matrix. This leads to the S phase preferentially dissolve through dealloying of Al and Mg, leaving the Cu-rich remnants behind. With the continuing of dealloying, these Cu-rich remnants eventually turn out to be cathodes, resulting in a galvanic attack on the surrounding Al matrix (shown in Figure 1.9). As for Cu redistribution, Buchheit et al [59] speculated that the dealloyed Cu-rich S phase remnants with sponge-like structure are not stable, and tend to decompose into nano-particles to reduce the large surface area. These nano-particles detach from the alloy surface and are readily dispersed by mechanical action of growing corrosion product or solution movement.

Chen and Gao et al [65] studied the early corrosion of AA 2024-T3 by immersing the alloy in NaCl solutions at different pHs. A preferential dissolution of S phase was observed in both neutral (~ pH 6) and acid (~ pH 2) NaCl solutions, and a general corrosion of Al matrix in the alkaline NaCl solution (~pH 11). They explained that in principle, foreign particles with passive oxide films would have been protected against galvanic attack, even if the particles were active with respect to the matrix. The occurrence of galvanic corrosion of S phase is obviously due to the lack of a passive oxide film on the S phase.

Obispo and Murr et al [60] focused on Cu deposition during AA 2024-T3 corrosion in NaCl solutions at different pH values. After 5 days of immersion in 0.6 M NaCl solutions, they found that a propensity of large Cu particle clusters located at some cathodic second-phase particles, such as Al-Cu-Fe-Mn-containing particles. The

morphologies of these Cu particle clusters were highly dependent upon the solution pH. The Cu clusters exhibited microdendritic morphologies in basic and neutral environments, while botryoidal (or nodular) morphologies in acidic environments. They further concluded that the Cu deposition phenomenon associated with pitting of AA 2024-T3 is a result of an electrochemical displacement reaction:



This reaction can take place at some preferential sites, like cathodic Al-Cu-Fe-Mn-containing second-phase particles, on the alloy surface.

1.2.2.3. Pitting of AA 2024-T3 by acetone degreasing

Acetone is commonly used as a degreasing agent for metal cleaning. Kagwade et al [66] found that acetone remaining on the Cu-bearing second-phase particles after degreasing can react slowly with water vapor under ambient light to form acetic acid and together with chloride ions cause severe corrosion. They also observed the redeposition of dissolved copper onto the alloy matrix under conditions that induced pitting. A two-step mechanism was suggested as follows:

- (1) A photochemical process wherein copper promotes the reaction of acetone with water vapor to form acetic acid.



Hence, acetic acid is formed only on the Cu-bearing particles contained in AA 2024-T3.

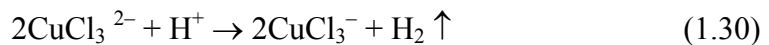
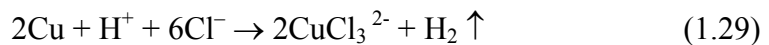
(2) A reaction of Al and Cu with acetic acid to form aluminium acetate and copper acetate.



And



The aluminum acetate film so formed was found to be highly insulating. This prevents further attack on the aluminum matrix and renders the Cu-bearing particles no longer galvanically coupled. Hence, a highly localized attack only occurs at the second-phase particles. Thermodynamically, copper does not reduce acetic acid spontaneously. But the study showed that Cu does react with acetic acid in the presence of oxygen and forms Cu(II) acetate. Furthermore, a localized attack of the intermetallic particles by chloride together with localized acidity could be expected to induce pitting.



Therefore, the aqueous medium along with chloride ions served to facilitate transportation of Cu through inducing pitting. Finally, metallic Cu is reduced and deposited on the surface of the ultrathin Al passive film, according to



Chapter 2. Experimental

2.1. Materials

Silanes Two groups of silanes, alcohol-based and water-based, were investigated in this work. The former is highly hydrophobic. Therefore, a high amount of alcohol is needed for the solution preparation. The latter is hydrophilic or infinitely miscible with water due to the hydrophilic functionalities (e.g., amino groups and acetoxy groups) carried by these silane molecules. Table 2.1 displays these silanes and their chemical structures. All the silanes listed here were provided by OSi Specialites (Tarrytown, NY), except for vinyltriacetoxysilane (VTAS) and aminopropylsilsequioxane-methylsilsequioxane (AMME), which were purchased from Gelest Co. (Tullytown, PA). The silanes were used without further purification.

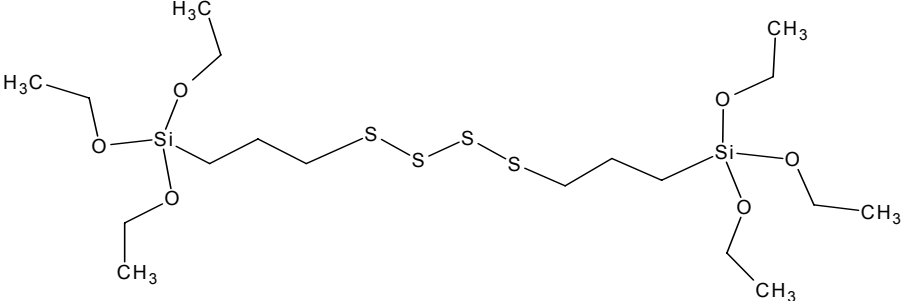
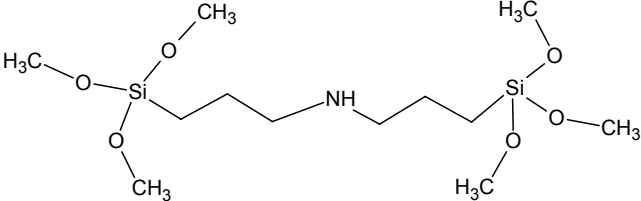
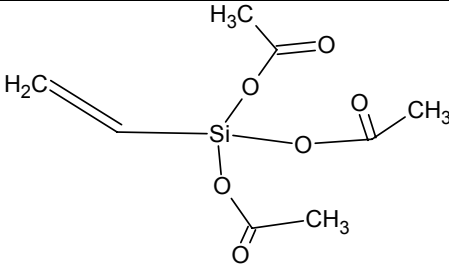
Alloys A variety of metals/alloys were tested with silanes in this work, as listed in the following:

- Al alloys: 2xxx series (AA 2024-T3), 5xxx series (AA 5005), 6xxx series (AA 6061), and 7xxx series (AA 7075-T6)
- Zn-coated steel: Hot-dip galvanized steel (HDG, the Zn coating is typically 20 μm)
- Carbon steel: Cold-rolled carbon steel (CRS)
- Mg alloy: AZ 91B

Al alloys except for AA 5005, HDG, and CRS were purchased from ACT Laboratories (Hillsdale, MI). AA 5005 and AZ 91B were provided by Chemetall/GmbH

(Frankfurt/Main, Germany). AA 2024-T3 (cleaned, not polished) was used extensively as a major metal substrate for silane film characterization as well as corrosion study.

Table 2.1. Silanes used in this study and their chemical structures

| Silane structure/Fomula/Trade name |
|--|
|  <p>Bis[3-(triethoxysilyl)propyl]tetrasulfide (Bis-sulfur silane, $C_{18}H_{42}O_6S_4Si_2$, <i>alcohol-based</i>) (Trade name: Silquest A-1289[®])</p> |
|  <p>Bis-[trimethoxysilylpropyl]amine (Bis-amine silane, $C_{12}H_{31}NO_6Si_2$, <i>water-based</i>) (Trade name: Silquest A-1170[®])</p> |
|  <p>Vinyltriacetoxysilane (VTAS, $C_8H_{12}O_6Si$, <i>water-based</i>) (Catalog No.: SIV 9098.0)</p> |

2.2. Silane solution preparation

Two typical solution concentrations investigated in this work were: 2% by volume for silane pretreatment of metals and 5% by volume for bare corrosion protection of metals. The former is primarily used in a surface pretreatment to improve paint adhesion and the latter is a finishing treatment intending to protect metals against corrosion in the unpainted state [26,27].

As mentioned above, solution preparation of alcohol-based silanes requires organic solvents. A 5 vol.% bis-sulfur silane solution, for example, was prepared by adding the silane into a mixture of deionized (DI) water and ethanol. The ratio of bis-sulfur silane/DI water/ethanol was 5/5/90 (v/v/v). The solution was aged continuously in the ambient for at least 2 days to ensure that the solution was “workable”, from which a solid rather than oily film would be obtained. It was found that stirring did not actually accelerate the hydrolysis of the solution, since the stagnant silane solution also became “workable” after 2 days of aging under the same condition. The natural pH of the solution was around 6.5. Lowering the solution pH to 4 is a common way to accelerate the hydrolysis process. However, in considering the stability of metal oxides (e.g., Al oxide is stable between pH 4 to 9), it is recommended to use the silane solution at its natural pH.

A 5 vol. % bis-amino silane solution was made in a similar way as the bis-sulfur silane solution. The organic solvent used for the bis-amino silane solution was methanol rather than ethanol. The reason is that it was observed in practice that a methanol-based bis-amino solution has a longer shelf life than an ethanol-based solution. The solution was aged in the ambient for 1 day before application for the same reason mentioned

above. The natural pH of the 5% bis-amino silane solution is above 10. The solution is not stable at this pH, and premature gelatin occurs within a few minutes. Thus, acetic acid (HAc) was added to lower the pH down to a neutral range, ~7.5.

Most water-based silanes were mainly used for surface pretreatment before painting. 2% solutions were prepared by simply adding 2 parts of the silanes into 98 parts of DI water. The as-prepared solutions were stirred for some time until the solutions become clear. A clear water-based solution is then ready for use.

2.3. Silane surface treatment

The following 5-step protocol of silane surface treatment was normally used in this work:

Alkaline degreasing of metal surfaces → tap water rinsing → blow air-drying → dipping or immersion of the metals into silane solutions (1 to 5 seconds) → drying of the treated metal surfaces (either at RT or at elevated temperatures, e.g., 100°C for 2 to 5 mins)

It is essential that the metal surface be thoroughly “water-break-free” after alkaline degreasing, as the remaining contaminants would block some of the active sites on the metal surface from reacting with SiOH groups.

In our previous work [26], it was found that immersion time or contact time for a metal in a silane solution does not influence silane adsorption or the silane film thickness. A film obtained by 5 sec-dipping shows no difference from the one from 30 min-dipping in terms of their film thickness and their corrosion protection performance. This is

understandable, as it is known [1] that SiOH groups adsorb instantaneously onto metal, forming hydrogen bonds with metal hydroxyls (MeOH) at the metal surface. Upon drying or curing, SiOH groups and MeOH groups further condense to form metallo-siloxane (MeOSi) or siloxane (SiOSi) covalent bonds on the metal surface. In other words, a silane film only forms during a drying/curing process rather than in an immersion process. Accordingly, the curing step rather than the immersion step is viewed as a key step during in silane surface treatment. This is totally different from a conventional chromating process where a chromate layer is formed on metal during the immersion step, and thus the layer thickness is determined by contact time. It should also be pointed out that in addition to dipping or immersion, silane solutions can also be sprayed or wiped onto metals.

2.4. Characterization techniques

Two major characterization techniques, Fourier-Transform Infrared Reflection-Absorption (FTIR-RA) spectroscopy and Electrochemical Impedance Spectroscopy (EIS), were employed extensively in this work. The FTIR technique is well known as a powerful tool in the field of polymer surface characterization. EIS has been known as one of the most valuable techniques in corrosion field, yet its function as a characterization tool has not been identified until very recently [2,5].

2.4.1. Fourier-Transform Infrared Reflection-Absorption (FTIR-RA) Spectroscopy

FTIR-RA measurements were conducted on a Bio-Rad FTS-40 spectrophotometer in the mid-IR range from 4000 to 400 cm^{-1} . All IR spectra were obtained at an incident angle of 75° normal to the surfaces of specimens, with a spectral resolution of 4 cm^{-1} . The number of scans was 100.

2.4.2. Electrochemical Impedance Spectroscopy (EIS)

EIS measurements on silane-coated metals (mainly AA 2024-T3) were carried out in a non-corrosive 0.5 M K_2SO_4 neutral aqueous solution, using an SR 810 frequency response analyzer and a Gamry CMS 100 potentiostat. Impedance data were recorded at frequencies ranging from 10^{-2} to 10^5 Hz, with an alternating current (AC) voltage amplitude of ± 10 mV. A commercial Saturated Calomel Electrode (SCE) served as the reference electrode, coupled with a graphite counter electrode. An area of 3.14 cm^2 of the specimen was exposed to the electrolyte during the measurement.

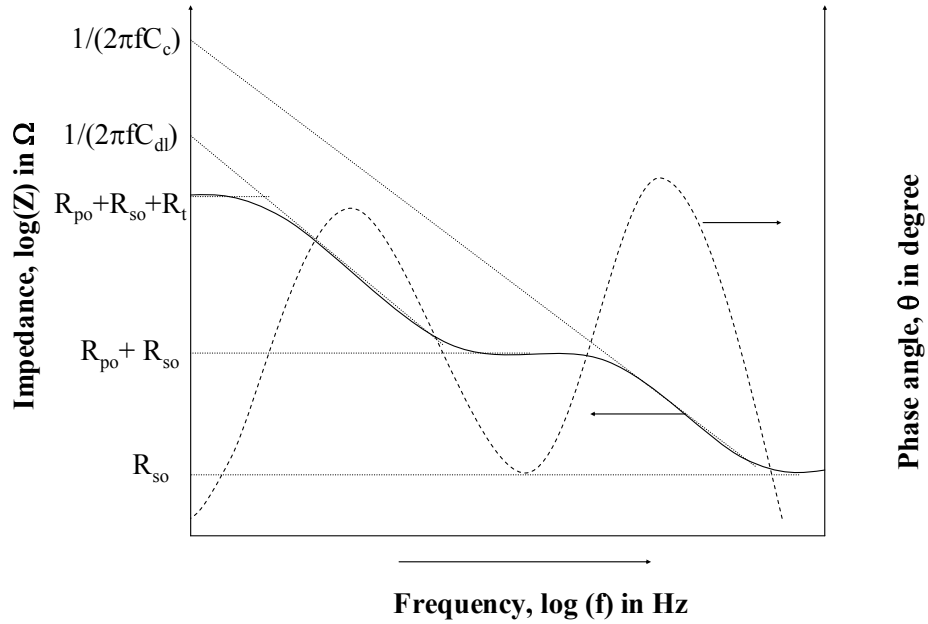
Background of Electrochemical Impedance Spectroscopy (EIS) In the field of aqueous corrosion science, EIS is commonly used as one of the most valuable techniques to investigate the degradation of polymer coated metal systems in chloride-containing aqueous media. An abundant of literature on this technique exists [67-70], providing information about theories and applications of EIS. In EIS measurements, a frequency-dependent impedance, $Z(f)$ (in Ω), is obtained by applying a sinusoidal alternating

potential signal to tested systems (e.g., epoxy-coated steel) in a range of frequencies. The expression for $Z(f)$ is as follows,

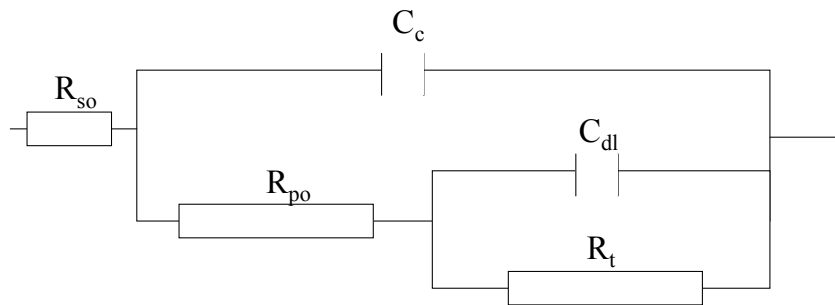
$$Z(f) = V(t)/I(t) \quad (2.1)$$

where, f = frequency, t = time, $V(t) = \text{sinusoidal alternating potential signal, } V_0 \sin(2\pi ft)$; $I(t) = \text{time-dependent current response, } I_0 \sin(2\pi ft + \theta)$; and $\theta = \text{phase angle between } V(t) \text{ and } I(t)$. EIS measurements are carried out in a conducting solution (or electrolyte). A sodium chloride (NaCl) solution is commonly used for the EIS monitoring of an organic coated metal substrate. A schematic of the EIS plots (in the form of Bode plots) for a polymer-coated metal system is shown in Figure 2.1(a). Two distinct steps (time constant, or RC) are observed in the impedance plot and two maxima in the phase angle plot. The one at high frequencies is believed to contain information about the coating; the other one at low frequencies is related to corrosion occurring at the metal surface under the coating. The associated EIS parameters shown in the figure are usually used to describe the coating properties and corrosion kinetics at the metal surface. These EIS parameters can either be roughly read from the graph, as illustrated in Figure 2.1 (a), or can be precisely found by regressing (or fitting) the associated mathematical equation to the experimental EIS data [68]. The fitting process can be easily done on a personal computer (PC), by inputting a proper equivalent electric circuit model (ECM) into commercial-available software. The ECM shown in Figure 2.1(b) is commonly used to fit the data in Figure 2.1(a). Two EIS parameters related to the coating properties are the coating capacitance

(C_c), and its pore resistance (R_{po}), the changes in which are used as a measure of the coating performance during exposure to the electrolyte.



(a)



(b)

Figure 2.1. Schematic EIS plots of a polymer coated metal system (solid curve-impedance plot; dashed curve-phase angle plot) (a), and equivalent electric circuit model (ECM) for EIS data fitting (b)

Coating capacitance (C_c) in the unit of farad (F) for a non-defect coating is given by,

$$C_c = \epsilon_0 \epsilon (A/d) \quad (2.2)$$

where, ϵ_0 = permittivity of free space (8.85419×10^{-12} F/m); ϵ = dielectric constant of the coating; A = the total area exposed to the electrolyte (m^2); and d = coating thickness (m). A typical ϵ value for a dried polymer is 3- 4, 8.5 for an oxide layer, and 80 for water. It is noted that ϵ of water is much greater than that of a dried polymer. Thus, ϵ of the polymer changes significantly when water penetrates into the polymer. For a given coating, the changes in C_c are often taken as a measure of water uptake in the coating [66, 68].

If the specific conductivity of a polymeric coating is negligible with respect to that of the electrolyte, R_{po} of the coating containing cylindrical defects/pores with the same length is expressed as,

$$R_{po} = \rho (d/A_p) \quad (2.3)$$

where, ρ = specific electrolyte resistivity in the defects/pores ($\Omega \cdot m$), which is constant for a given electrolyte system; d = the length of the cylindrical defects (m) or coating thickness; and A_p = the defect/pore area in the coating (m^2). For a given coating, R_{po} is inversely proportional to A_p . Once the electrolyte (water and ions) penetrates into the coating through defects and pores, conducting shortcuts develop between the electrolyte

and the metal substrate. This would cause a decrease in the value of R_{po} . Thus, R_{po} is another EIS parameter that is used to evaluate the coating performance in an aqueous environment.

It should be noted that the time constant mentioned above is the product of resistance (R) and capacitance (C), in the unit of seconds. The time constant for a polymeric coating is thus given as $R_{po}C_c$. When a silane film is crosslinked, a majority of the pores in the film would be sealed and water as condensation product would evaporate. This “pore sealing” would decrease the total pore area (A_p), resulting in an increase in R_{po} . In the meantime, “water removal” would cause a reduction in C_c .

The other EIS parameters shown in Figure 2.1(a) are, R_{so} = uncompensated solution resistance (Ω), the value of which is small (only several tens of Ω) and has no effects on the coated system; R_t = charge transfer resistance polarization resistance (Ω); and C_{dl} = capacitance of the double layer formed at the coating-metal interface (F). The latter two parameters are often observed when corrosion starts on the metal substrate under the coating. It should also be noted that the phase angle plot, in some cases, is more valuable than the impedance plot. It has been reported [71] that some subtle changes in coating structures are clearly reflected in the phase angle plot but not in the impedance plot.

2.4.3. Ellipsometry

Ellipsometry measurements were carried out to determine silane film thickness on a mirror-like surface of stainless steel. The measurement conditions are as follows:

wavelength range: 230 – 1700 nm (step size: 5 nm), incident angles: 65 – 85° (step size: 5°).

2.5. Corrosion tests

2.5.1 Electrochemical tests

DC polarization test and EIS are two commonly-used experimental methods in modern corrosion study. Unlike conventional weight loss measurements which require many days or more to determine corrosion rate, these two tests simply need a few minutes.

DC polarization tests were carried out on silane-treated panels in a neutral 0.6 M NaCl solution. The silane-treated panels were pre-immersed in the electrolyte for some time before testing, in order to achieve a steady state. The bare panels were tested immediately after exposure to the electrolyte. On average, 3 – 5 replicates were tested for each condition. The data were recorded at potentials $E_{\text{corr}} \pm 250$ mV (where, E_{corr} = corrosion potential or Open Circuit Potential (OCP)), with a scan rate of 1 mV/s. SCE and a platinum mesh were used as the reference and counter electrodes, respectively. The exposed area was fixed at 0.78 cm².

Electrochemical Impedance Spectroscopy measurements (EIS) were employed to monitor corrosion performance of the silane-treated metal systems as a function of immersion time in a neutral 0.6 M NaCl solution. The EIS measurements were carried out using an SR810 frequency response analyzer connected to a Gamry CMS100

potentiostat. The measured frequency range was from 10^{-3} to 10^5 Hz, with an AC excitation amplitude of 10 mV. SCE was used as the reference electrode and coupled with a graphite counter electrode. The distance between the electrodes and the tested area was around 6 cm. Per decade, 7 experimental points were collected during the measurement around E_{corr} of the tested system.

2.5.2. Performance tests

A variety of performance tests [72] were also used to evaluate corrosion performance of silane-treated metals under different conditions.

ASTM B117 (Salt spray (fog) test, SST) This test was employed to evaluate bare corrosion protection of silane-treated metals without topcoats. According to the specification, 5% salt solution (NaCl) is atomized in a salt spray chamber at 35°C with the solution pH around 7. The tested panels shall be placed at an angle of 45° in the chamber, exposing to the salt fog for a certain period.

ASTM 1654-92 (Corrosion test for painted or coated metals and alloys) This test provides a method to evaluate the corrosion performance and paint adhesion of painted alloys with silane pretreatment. The testing conditions are similar to that for ASTM B117, except that the painted metal surfaces need to be scribed prior to salt spray testing. Delamination area is measured along the scribe line after exposure, the value of which is often used as a measure for the corrosion performance and paint adhesion of the painted systems.

ASTM B368 (Copper-accelerated acetic acid-salt spray testing, CASST) This test is derived from ASTM B117. 0.25 g/liter copper chloride ($\text{CuCl}_2 \cdot 2\text{H}_2\text{O}$) is added into 5% NaCl solution. The pH of the salt copper solution is adjusted to the range of 3.0 to 3.3 by the addition of glacial acetic acid. The temperature in the salt spray chamber is 49°C.

Machu test This accelerated test is designed to evaluate corrosion performance of painted metals. The painted panels are cross-scribed on the surfaces, and then immersed in the solution of 5% NaCl + 10% $\text{Zn}(\text{OH})_2$ at 37 °C for 1 day. In the next day, another 10% $\text{Zn}(\text{OH})_2$ is added into the original solution. After 2 days of immersion, the panels are taken out and tapes are used to pull off the delaminated paints along the scribe lines. The delamination distance is taken as a measure of paint adhesion and corrosion performance of the whole system.

2.6. Measurements of other properties of silane films

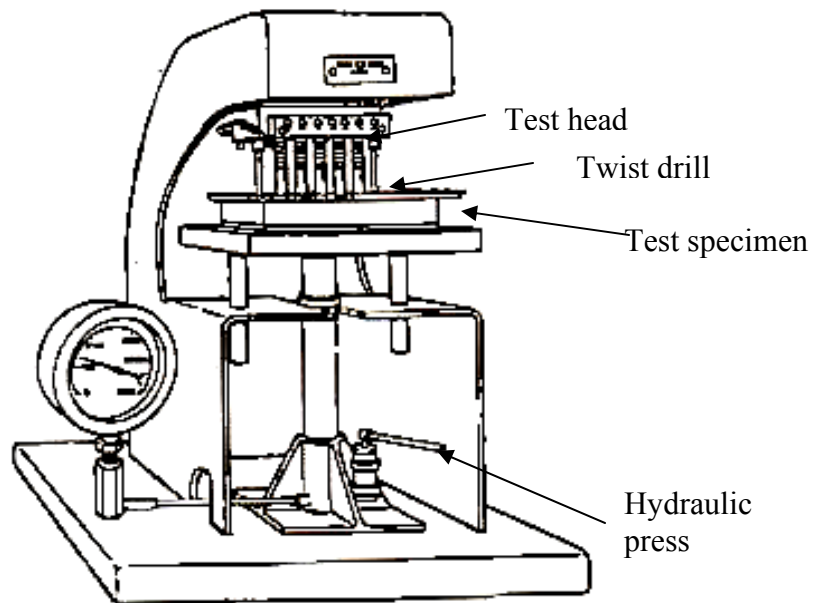
2.6.1. Resistivity/conductivity measurements

Specific resistivities of silane-treated metal surfaces were carried out in accordance with the specifications of ASTM A717M-95 (Standard Test Method for Surface Insulation Resistivity of Single-Strip Specimens, or “Franklin Test”) [72].

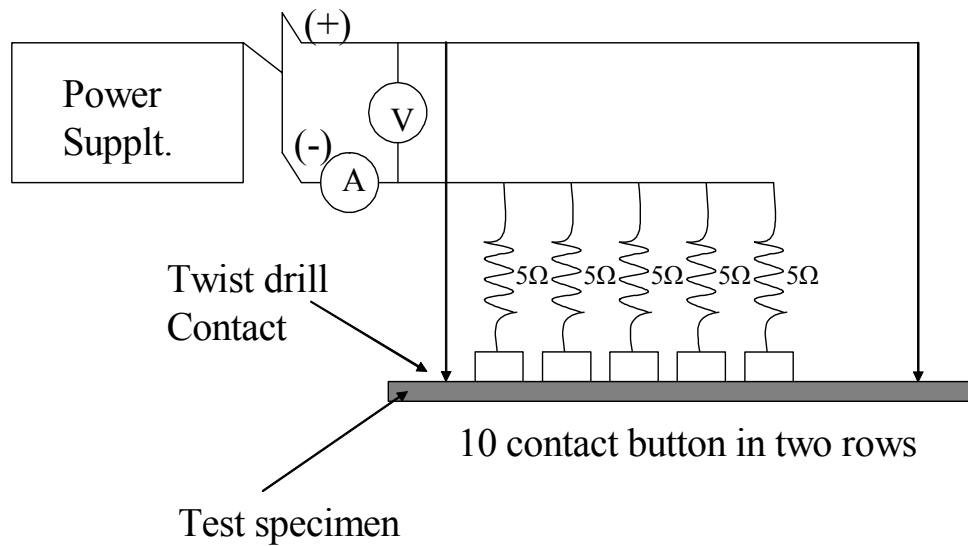
Figure 2.2 schematically shows the apparatus of this measurement [72]. Ten metallic contacts of fixed areas were applied to one of the silane treated surfaces of the specimen and electrical contact was made with the base metal by two drills. An average electrical current flowing between the contacts and the base metal (I in A) is measured

under a specified applied voltage. The recommended standard testing conditions are: (1) pressure – 0.0435 Pa; (2) testing temperature – room temperature (25°C); (3) applied voltage – 0.5 V; and (4) short-cut current – 0.99 V. The measured current values (I) are then converted to resistivity (R_j in $\Omega\cdot\text{cm}^2$). The calculation of R_j from I is given as follows [72],

$$R_j = 6.45 [(1/I)-1] \text{ in } \Omega\cdot\text{cm}^2/\text{lamination} \quad (2.4)$$



(a)



(b)

Figure 2.2. Apparatus of Franklin tester (a), and Diagram of connections for contracts and resistors (b)

2.6.2. Measurements of mechanical properties of silane films

Nano-Hardness Test (or Nano-indentation test): modulus and hardness The apparatus of the indentation method for harness and modulus measurements and the corresponding indentation hysteresis curve are shown in Figures 2.3 (a) and (b). An indenter tip with a known geometry is driven into the tested area of the sample surface by applying an increased normal load. When the preset maximum value (e.g., 0.5 mN) is reached, the normal load is reduced until partial or complete relaxation. The procedure is performed repetitively. For each loading/unloading cycle, the applied load value is plotted as a function of the corresponding position of the indenter (Figure 2.3 (b)). The

values of hardness and modulus of the material can be derived from the curve shown in Figure 2.3 (b) with the use of the established models.

To simplify the situation here, the hardness (H) is given as follows,

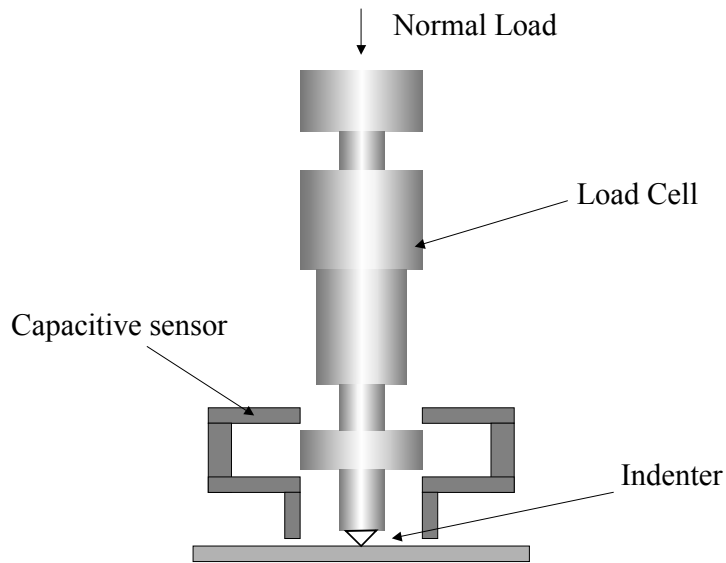
$$H = P_{\max}/A_c \quad (2.5)$$

where, P_{\max} = the maximum load. A_c = the projected contact area, which is dependent upon the type of the indenter used. For a Berkovich diamond indenter, $A_c = 24.5 h_c^2$, (where h_c is contact depth). The reader may refer to the paper by Oliver and Pharr for more details [73].

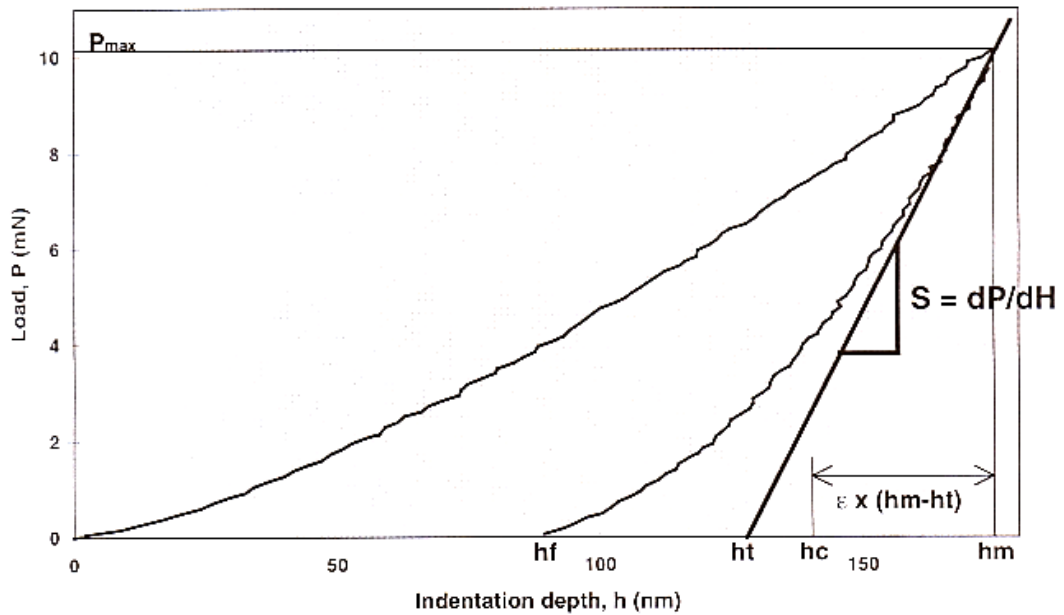
The Young's Modulus, E , is given by,

$$1/E_r = (1-\nu^2)/E + (1-\nu_i^2)/E_i \quad (2.6)$$

where E_r is the reduced modulus, which can be calculated after having derived the stiffness (S) and A_c from the indentation curve [73].



(a)



(b)

Figure 2.3. Apparatus of nano-indentation tester (a), and indentation hysteresis curve (b)

Silane-treated samples were measured under the following conditions: (1) preset maximum force: 0.35-0.50 mN; (2) loading rate: 1 mN/min; (3) unloading rate: 1

mN/min; and (4) indenter type: Berkovich diamond No.2. 5 measurements were applied for each sample.

Pin-on-Disk testing: Friction coefficient and distance before failure Another important mechanical property of silane films is their friction and wear behavior, which is also a critical concern on moving machine parts in manufacturing industry. Pin-on-Disk tribometer is usually used to determine friction coefficient and wear resistance of materials. The apparatus and the resulting curve are shown in Figure 2.4. In the measurement, a flat or a sphere-shaped indenter is loaded onto the tested sample with a precisely known weight. A pin is mounted on a stiff lever (or a frictionless force transducer). As the sample is either rotating or sliding, resulting frictional forces acting between the pin and the sample are measured by very small deflections of the lever. Wear coefficients for both the sample and material are calculated from the volume of the material lost during a specific friction run. The measuring conditions were: (1) load: 1.0 N; (2) speed: 5.0 cm/s; (3) ball radius: 6.0 mm.

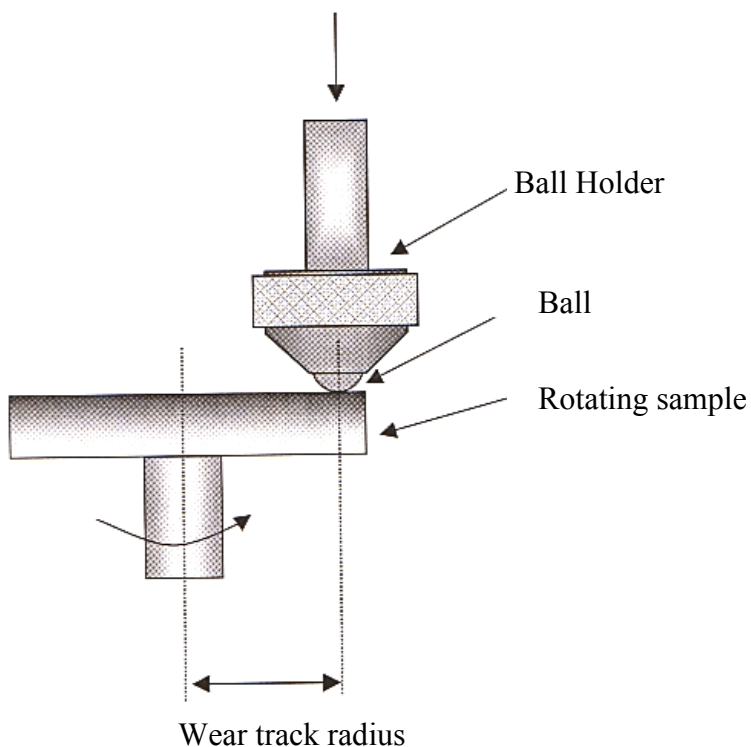


Figure 2.4. Apparatus of Pin-on-Disk tester

2.6.3 Thermogravimetric Analysis (TGA) of silane films

The thermal stability of free silane films was investigated on a METTER TOLEDO STAR[®] System conducted at Chemetall/GmbH, Germany. Unlike the others, the silane films used for this measurement were free-stand films, i.e., prepared without metal substrates. Free silane films were made by the following procedure: plastic dishes (no surface oxide, therefore is inert to adsorption of SiOH groups) that contained a small amount of these 5% silane solutions were placed in a hood for 1 day to drive the solvents (both alcohol and water) out of the solution and to make the silane components crosslinked. The obtained dried silane films were further ground to fine powders for the TGA measurements.

Chapter 3. Electrochemical Impedance Spectroscopy of Bis-[triethoxysilyl-propyl]tetrasulfide silane Film on AA 2024-T3¹

Abstract Thin films of bis-[triethoxysilylpropyl]tetrasulfide (“bis-sulfur silane”) were deposited on alkaline-cleaned AA 2024-T3 panels and investigated by Electrochemical Impedance Spectroscopy (EIS) using a non-corrosive electrolyte 0.5 M K₂SO₄ aqueous solution. The effects of continuous immersion of the films in this electrolyte and curing the films at room temperature or at 100°C in air were studied. Three equivalent circuits were proposed that fitted the experimental data very well. A continuous increase of impedance and the appearance of an additional time constant with respect to time in EIS spectra during immersion, curing, and aging processes were explained by: (1) the hydrolysis of the ester groups to silanol groups and condensation of the latter to siloxane bonds in the film; and (2) the formation of an unknown interfacial phase between the crosslinked silane film and the aluminum oxide. Reflection-Absorption Fourier-transform Infrared Spectroscopy (FTIR-RA) was used to enhance the interpretation of the EIS results. It is concluded that EIS in a non-corrosive electrolyte is a useful method for studying the stability of silane films formed on metals and can contribute to the determination of the optimum conditions for depositing silane films on metals for corrosion protection. The results of potentiodynamic polarization tests and a salt spray test (ASTM B117) confirmed the conclusion drawn from EIS that a fully cured bis-sulfur silane film provides an excellent corrosion protection on AA 2024-T3.

¹ This chapter has been published on Corrosion, 157(5), 413 (2001)

3.1. Introduction

Bis-sulfur silane provides excellent bare corrosion protection as well as paint adhesion for AA 2024-T3 alloy. However, it was also found that different curing processes affected remarkably the corrosion performance of the resulting bis-sulfur silane films. Figure 3.1 shows a typical example of corrosion protection of AA 2024-T3 alloy afforded by a bis-sulfur silane film during salt water immersion. The panel with the fully cured film (Figure 3.1(a)) is virtually free of any corrosion, whereas those that are not fully cured (Figures 3.1(b) and (c)) show some signs of corrosion after 10 days. Therefore, it is of great importance to understand the structural evolution of the silane film during different curing processes.

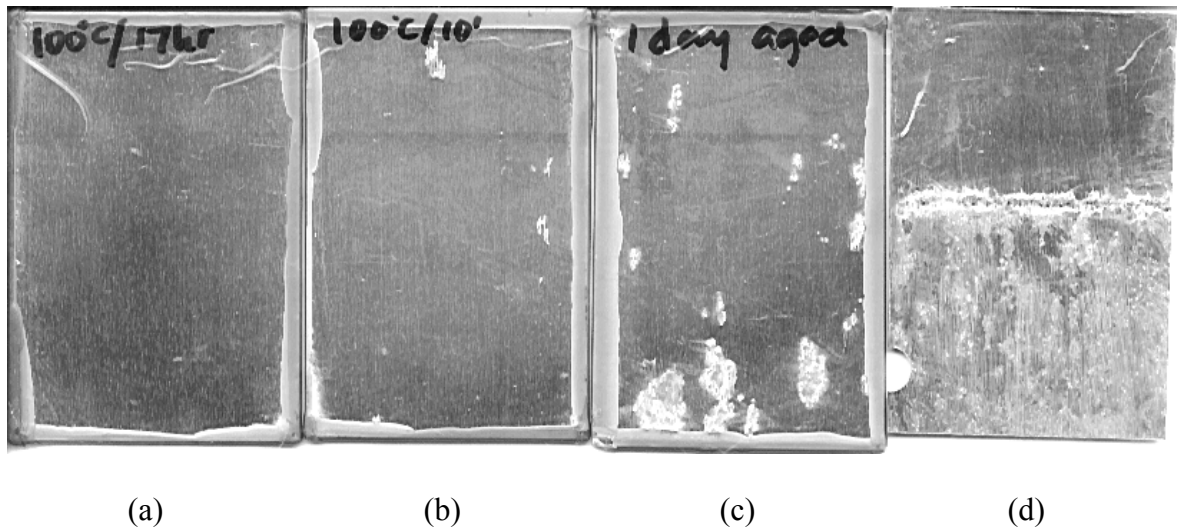


Figure 3.1. Bis-sulfur silane treated AA 2024-T3 panels after 10 days of immersion in a naturally-aerated neutral 0.6 M NaCl solution; (a) cured for 17 hrs at 100°C in air, (b) cured for 10 min at 100°C in air, (c) cured in ambient conditions for 24 hrs, and (d) untreated, alkaline-cleaned only (bis-sulfur silane solution, 5%, pH 6.5)

Electrochemical Impedance Spectroscopy (EIS) has been known for many years as a powerful tool in corrosion research of metals coated with organic films, such as paints. Mansfeld et al. and others have pioneered this technique [75-79]. Most of the initial work emphasized the use of EIS for continuous monitoring of the degradation process in coated metal systems in a corrosive environment such as 0.5 M NaCl solution. The technique can also be used to study the properties of the coating-metal interface rather than the coating degradation [80,81]. Only a few authors have described the characterization of properties of organic coated metal system other than corrosion inhibition using a non-corrosive electrolyte [82].

This chapter reports EIS measurements in a neutral 0.5 M K_2SO_4 solution for the bis-sulfur silane-treated AA 2024-T3 system. By using K_2SO_4 as electrolyte, it is hoped that concurrent corrosion reactions can be avoided, so that only the information of the silane film structure on AA 2024-T3 will be obtained and analyzed.

A 5% bis-sulfur silane water/ethanol solution (pH 6.5) was used here in this work.

3.2. Results and Discussion

Prior to the study on the bis-sulfur silane treated AA 2024-T3, EIS data were collected for bare AA 2024-T3 panels (untreated) during immersion in 0.5 M K_2SO_4 solution for various times, as shown in Figure 3.2. The purpose of this experiment was to determine any changes in the change of natural oxide film when exposed to the non-corrosive 0.5 M K_2SO_4 solution. As can be seen in Figure 3.2, only one time constant corresponding to the oxide film appears, and very little change occurred during 8 hrs of immersion. EIS measurements for bare AA 2024-T3 panels cured at 100°C for 0.16 hr and 8 hrs were also done (results not

shown here). Again, no significant differences were observed with curing time. Thus, the conclusion can be drawn that the natural oxide film remained stable during immersion and curing (100°C) processes. Any changes observed in the EIS spectra of the silane-coated Al 2024-T3 must be the result of specific interactions with or by the silane film.

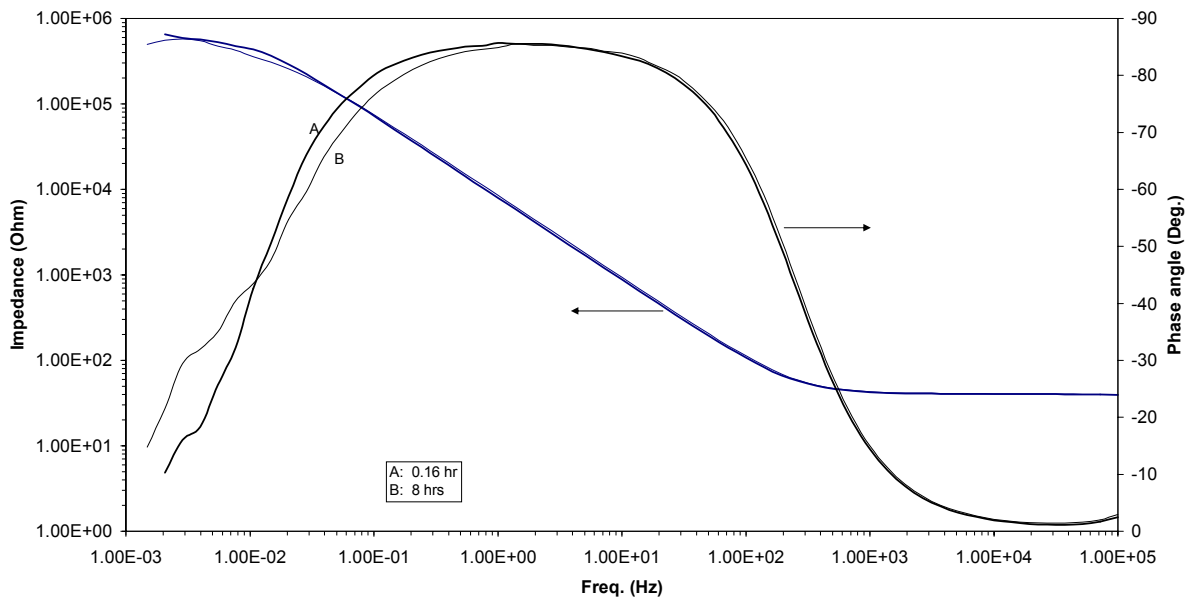


Figure 3.2. Bode plots for bare AA 2024-T3 during immersion in 0.5 M K_2SO_4 for 0 to 8 hrs

3.2.1. EIS results for bis-sulfur silane treated AA 2024-T3 system under different curing processes

3.2.1.1. Effect of immersion time of bis-sulfur silane -treated AA 2024-T3 in 0.5 M K_2SO_4

Figure 3.3 shows the Bode plots for the bis-sulfur silane-treated and cured (0.16 hr at 80°C) AA 2024-T3 as a function of immersion time in the 0.5 M K_2SO_4 solution. It can be

seen that the total impedance of the system increases with immersion time throughout most of the measured frequency range, with the appearance of a distinctive additional time constant after 4 hours of immersion. The additional time constant is shown more clearly in the phase angle plot than in the impedance plot.

At the initial immersion stages (0.16-2 hrs), only two time constants are observed, one (RC1) located at high frequencies ($\sim 10^4$ Hz), and the other (RC2) at low frequencies (~ 0.1 Hz). Since the bis-sulfur silane film was coated uniformly on the AA 2024-T3 surface, these two time constants can be assigned to the silane film (RC1) and the aluminum oxide (RC2), respectively.

As the immersion process continues (after 4 hrs of immersion), the impedance of the silane film (RC1) increases remarkably and, correspondingly, the time constant RC1 is shifted to lower frequencies. It is interesting to notice that an additional time constant (RC3) occurs in the phase angle plot in the medium frequency range between RC1 and RC2. It is also noticed that the low frequency impedance keeps increasing even after 24 hrs of immersion (curve 5 in Figure 3.3), but instead of two distinctive time constants, only one broadened time constant appears in the medium frequency range. This is probably due to the overlap of the two time constants (RC3 and RC1).

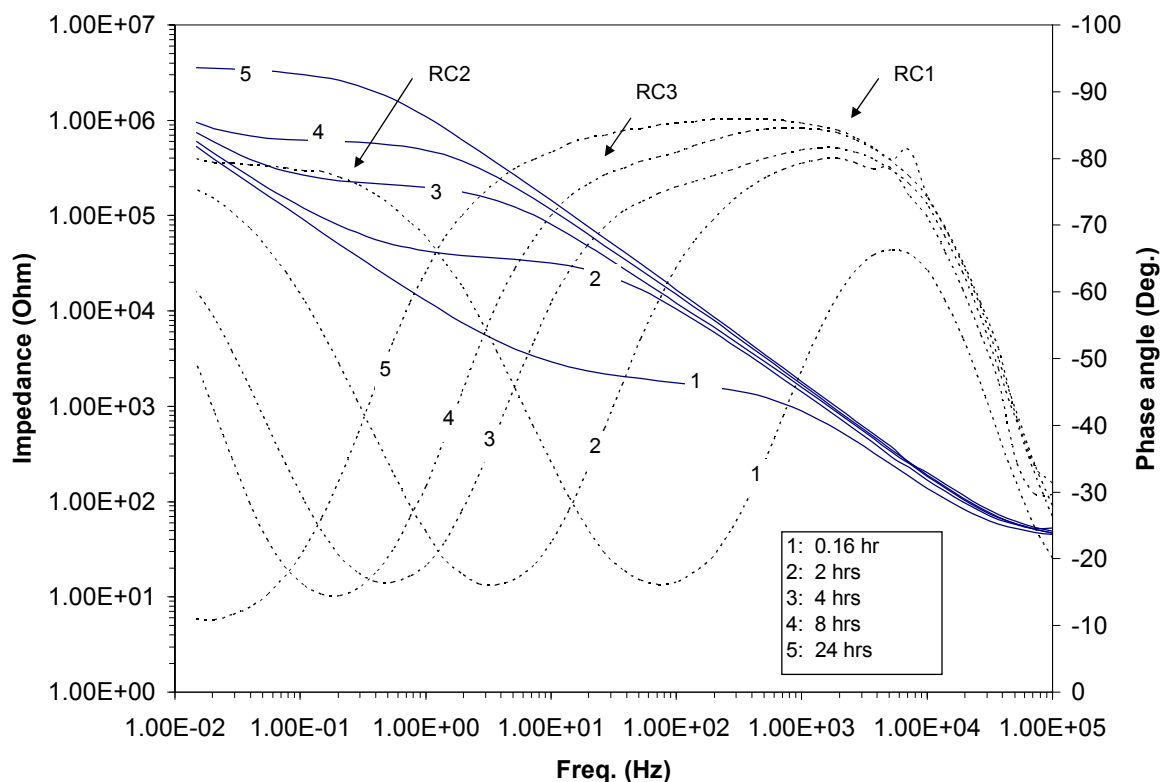


Figure 3.3. Bode plots for bis-sulfur silane-treated AA 2024-T3 panels during immersion in 0.5 M K_2SO_4 solution for 0 to 24 hrs

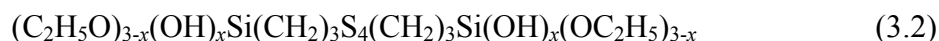
In general, the increase in the total impedance and the appearance of an additional time constant (RC3) may indicate the formation(s) of some new, highly water-resistant structure(s) in the bis-sulfur silane film and/or at the interface of the silane film and the aluminum oxide layer. A better understanding of these observations could shed more light on the mechanism of the silane film formation on metal substrates. Plausible mechanisms associated with the changes in EIS are discussed here.

(a) The formation of crosslinked silane film

As is well-known, the formation of a crosslinked silane film containing siloxane bonds SiOSi is the result of the condensation/crosslinking of silanol groups (SiOH) which are initially formed by the hydrolysis of ester groups ($-\text{SiOC}_2\text{H}_5$) in the dilute water/alcohol silane solution [1,26]. It was observed in practice that the bis-sulfur silane cannot be hydrolyzed completely in the 5% water/ethanol solution at pH 6.5. Therefore, some nonhydrolyzed ethoxy ester groups still remain in the applied silane film on the metal substrate [83]. This effect is a consequence, in part, of the low solubility of the silane ester in water. It can only be dissolved in 90/10 alcohol/water mixtures. This high alcohol content drives the hydrolysis equilibrium:



to the left, resulting in a film of the type:



rather than $(\text{HO})_3\text{Si}(\text{CH}_2)_3\text{S}_4(\text{CH}_2)_3\text{Si}(\text{OH})_3$ which would be obtained if the silane would be highly water-soluble. Here, x in subscript is the number of hydrolyzed ester groups.

When this partially hydrolyzed silane film on AA 2024-T3 is immersed in the 0.5 M K_2SO_4 aqueous solution for a certain time, it is likely that these remaining ester groups in the silane film slowly hydrolyze further to generate SiOH groups and these groups condense or crosslink to form siloxane (SiOSi) structures in the existing film. As a result, the amount of

the siloxane units in the film increases slowly during immersion. It is known that in pure water condensation of silanol groups always occurs slowly [1]. It is also known that siloxane structures are fairly resistant to hydrolysis by water, at least at room temperature. A conclusion thus can be drawn that the further formation of siloxane-like structures in the partly hydrolyzed sulfane silane film is likely to be one of the major causes of the increase of the total impedance seen in Figure 3.3.

There is an analogy here with solid-state dielectric spectroscopy where state-of-cure of resins is measured by recording the impedance of the polymer using a two-electrode system [84]. In this study, however, the traditional three-electrode approach is used with the bis-sulfur silane film fully immersed in electrolyte. This allows comparing the EIS response with that obtained from a corrosive electrolyte, e.g., NaCl, where the protective properties of the silanes can be evaluated.

It should now be clear why the bis-sulfur silane film was pre-cured at moderate conditions prior to immersion them into the electrolyte. This step condensed most of the free silanol groups that were present in the film as a result of the hydrolysis reaction in the water/alcohol mixture of pH 6.5. Therefore, what is observed in EIS will be mainly the hydrolysis and condensation of the remaining ester groups in the film that were not hydrolyzed in the water/alcohol mixture. It will also be obvious that there is an advantage of performing EIS in the non-corrosive electrolyte, as concurrent corrosion reactions due to the presence of Cl^- ions would obscure the effects observed in Figure 3.3. The equivalent circuit would become too complex to extract the data on the silane crosslinking reliably.

It should also be pointed out that although the initial bis-sulfur silane films are not stable with respect to time, they are still smooth enough to be fitted with the equivalent electrical circuit, which will be discussed later. The initial bis-sulfur silane films could be

considered as an open, non-barrier structure, as the lack of purely capacitive response is seen in the EIS spectra (curve 1, Figure 3.3).

(b) The formation of an interfacial phase

Another contribution to an increase in the total impedance shown in Figure 3.3 might be made by the formation and growth of a new interfacial phase, corresponding to the additional time constant (RC3) shown in Figure 3.3. Presently, there is still lack of detailed knowledge on the chemistry of this phase, but the phase may be a product formed by reaction between bis-sulfur silane film and aluminum hydroxide similar to that observed with other silanes in the previous silane work [1,33]. In Ref. 33, evidence by XPS and FTIR was presented for the formation of Al-siloxane compounds formed by condensation reactions between silanol groups and aluminum oxides when 99.9% Al was treated with methacryloxypropyltrimethoxysilane. This polymeric passive film hinders ion diffusion and, hence improved general and localized corrosion of pure aluminum. Two plausible interfacial structures are discussed as below.

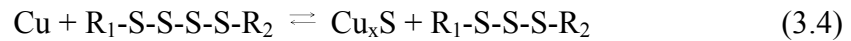
Al-siloxane structure (AlOSi) The condensation reaction between aluminum hydroxide and silanol groups in the bis-sulfur silane film is as follows [1],



The resultant Al-siloxane bond, AlOSi, is known as a strong covalent bond that gives excellent adhesion of silane film to Al substrate [1,33]. If the aluminum hydroxide is porous,

the silane can penetrate into and react with the oxide film and a three-dimensional structure containing these bonds is formed.

Sulfide compounds (Cu_xS) As is well known, AA 2024-T3 alloy contains a considerable amount of Cu-rich phase as strengthening phase throughout the Al matrix. Recent work with the bis-sulfur silane, on the other hand, has shown that sulfides is likely to be formed from the reaction between the bis-sulfur silane and metals such as Zn, Cu, and Ni with high affinity for S [85]. The reaction of S in organic sulfides with Cu is [86],



Cu_xS is non-stoichiometric copper sulfide. It is very likely that the Cu-rich phase reacts with the bis-sulfur silane in the same way.

Thus, a plausible interfacial structure between sulfane silane and AA 2024-T3 may consist of two types of structures, as shown in Figure 3.4. Al-siloxane structure is mainly formed between bis-sulfur silane film and Al oxide layer, while the Cu_xS-like compound may be located at the cathodic sites of Cu-rich phase.

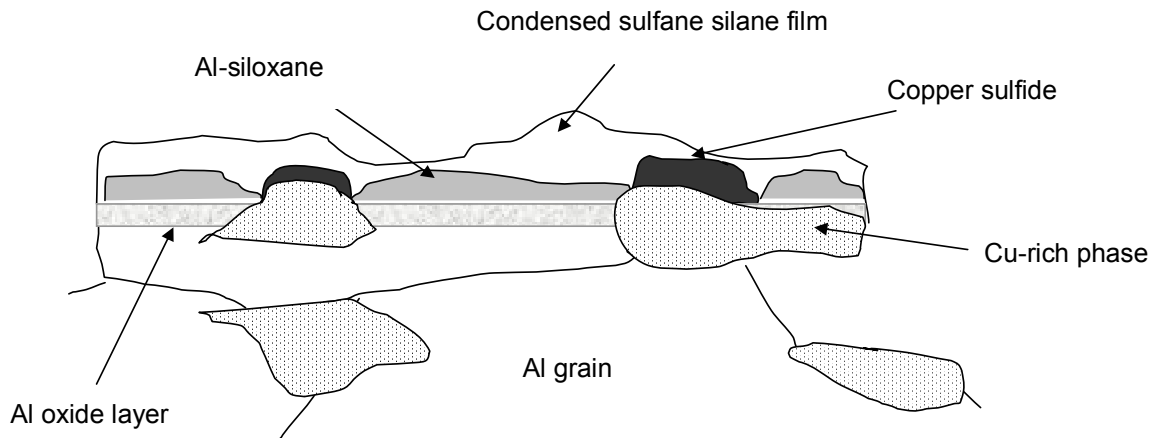


Figure 3.4. Schematic of a plausible interfacial structure between bis-sulfur silane film and AA 2024-T3 alloy

3.2.1.2. Effects of curing time at 80°C and aging time in ambient condition on bis-sulfur silane-treated AA 2024-T3

EIS behavior similar to that shown in Figure 3.3 was observed for the effect of the curing time (0.16 hr to 6 hrs at 80°C in air) on bis-sulfur silane-treated AA 2024-T3 alloy (Figure 3.5), except that the changes in the spectra developed faster for the curing time effect than for the immersion time effect. The new time constant RC3 is also formed here. This result is in agreement with the interpretation of the effects of Figure 3.3, as during the thermal cure the film will adsorb sufficient atmospheric moisture for hydrolysis of the remaining ethoxy ester groups. The ethanol molecules will evaporate immediately, driving the reaction (3.1) to the right. The silanol groups will condense readily under these circumstances and the water released in the condensation reaction is then available again for the further hydrolysis.

In other words, the effects during thermal cure are autocatalytic and the films crosslink quickly, requiring only a small amount of atmospheric humidity.

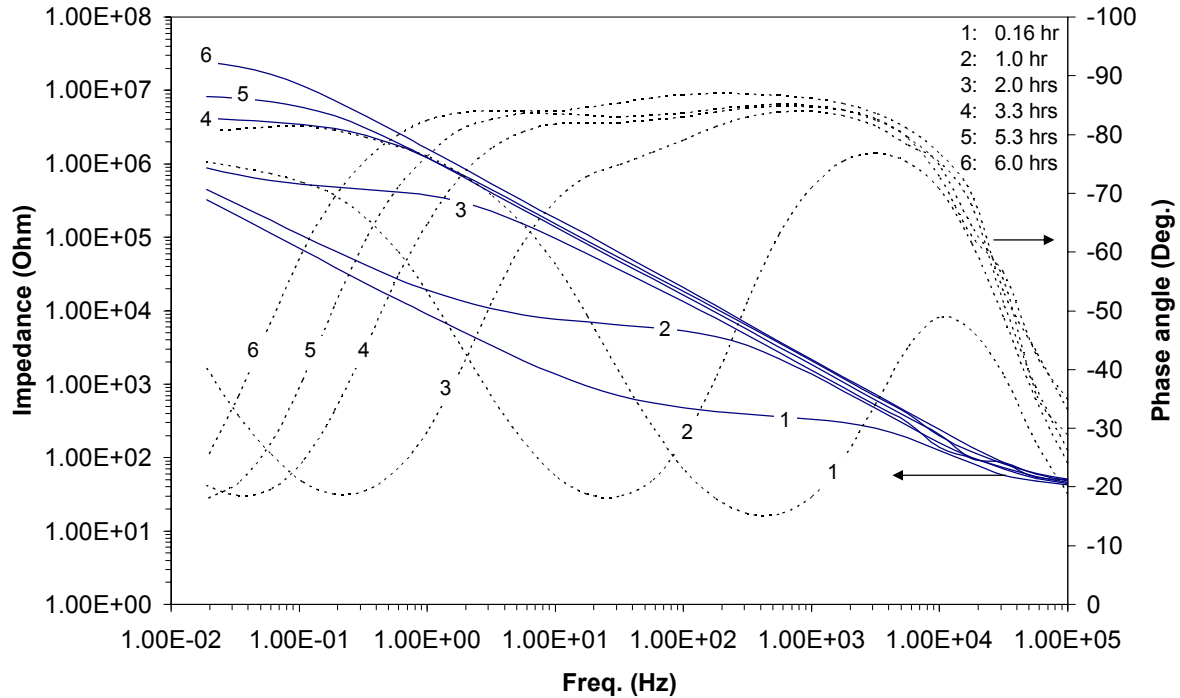


Figure 3.5. Bode plots for bis-sulfur silane-treated AA 2024-T3 panels cured at 80°C in air for 10 min. to 370 min., then tested by EIS in 0.5 M K₂SO₄

The changes in the EIS spectra of the bis-sulfur silane-treated AA 2024-T3 with aging time in air under ambient conditions are shown in Figure 3.6. After aging, each sample was immersed in the electrolyte and the EIS spectrum was recorded. The total impedance increases with aging time throughout the entire exposure period, with only two observed time constants corresponding to the bis-sulfur silane film (RC1) and the aluminum oxide (RC2), as in Figure 3.3. However, the additional time constant (RC3) indicative of a new interfacial phase formed in the immersion process is not observed during 120 hrs of aging. Apparently this phase can form during continuous immersion in electrolyte at room temperature, or

during curing at 80°C, but not easily during short-term aging in ambient conditions. It has been noticed, however, that after 840 hrs of aging, the low frequency impedance has increased significantly, while one broadened time constant appeared in the phase angle plot, which is probably due to the overlap of the two time constants for the unknown phase and outer silane film. The tendency in Figure 3.6 indicates that the partly crosslinked bis-sulfur silane film of is moisture-sensitive and hydrolyzes and crosslinks readily during storage in the ambient. As stated before, the bis-sulfur silane cannot easily be hydrolyzed fully, so the final hydrolysis followed by crosslinking has to be done on the deposited film. This process could be speeded up by storing the films conditions of high humidity.

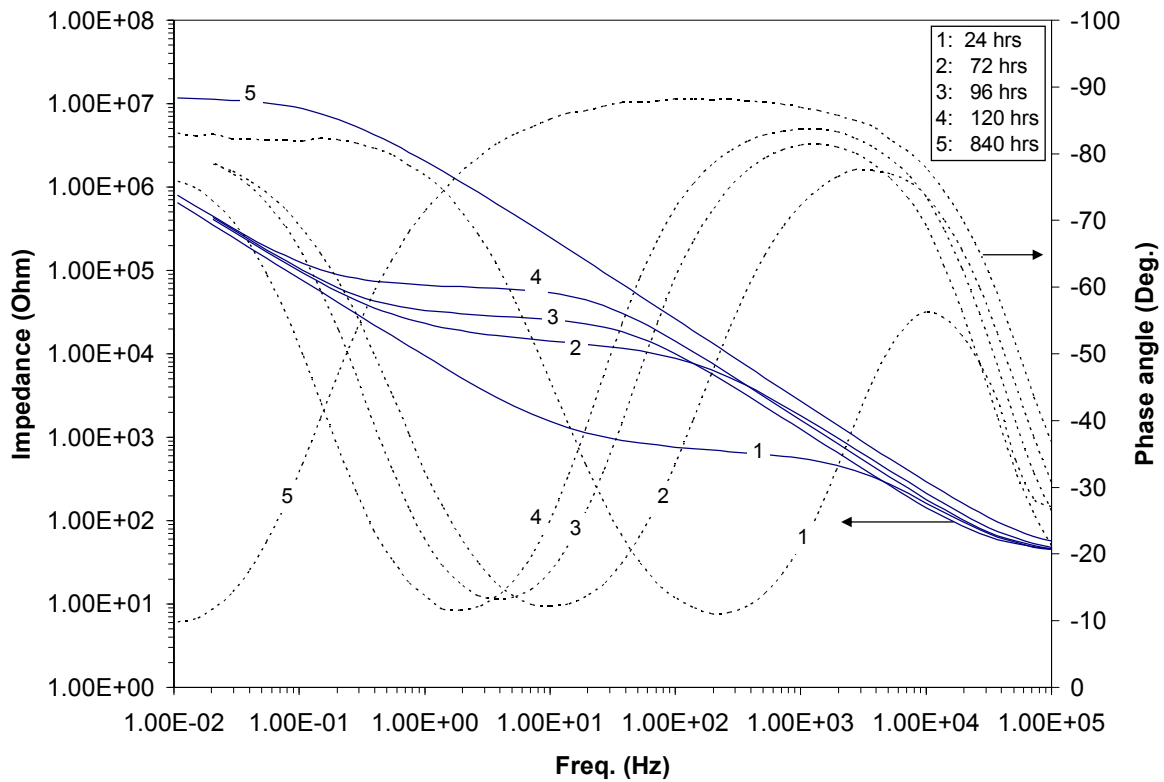


Figure 3.6. Bode plots for bis-sulfur silane-treated AA 2024-T3 panels aged in ambient conditions and then tested by EIS in 0.5 M K_2SO_4

3.2.2. Analysis of EIS for bis-sulfur silane-treated AA 2024-T3

3.2.2.1. Equivalent electrical circuit models

Several configurations of equivalent electrical circuits (EC) concerning the bis-sulfur silane-treated AA 2024-T3 were tested. Figures 3.7 and 3.8 exhibit three general circuits and their possible corresponding physical structures. It is noted that these models were suggested primarily based on the information extracted from the phase angle plots, which gave more details on the structural changes in the silane-treated system over time and which more clearly indicated the presence of a new phase (“unknown phase” hereon). Constant Phase Elements (CPE) instead of ideal capacitor is used in these models, as none of the films formed can be expected to be perfect capacitors. With CPE’s the fit was considerably better than with capacitances.

As Figure 3.7 shows, the data obtained for the earlier stages were fitted with an EC consisting of 2 time constant units (Figure 3.7 (a)). At this stage, the bis-sulfur silane film is very porous and readily permeable to the electrolyte, as no significant structural change is observed in EIS caused by hydrolysis and crosslinking inside.

At a later stage of the development of the film properties, when the new time constant has become apparent, a third RC element (‘unknown phase’) is added (Figures 3.8(a) and (c)). The bis-sulfur silane film has become condensed and pores being closed by the extensive crosslinking of silanol groups during this period. The film is less permeable to the electrolyte. Furthermore, the formation of the unknown phase improves the water resistance of the entire system. Figures 3.8(a) and (c) show two EC models suggested for EIS data fitting at the later stages. No significant difference can be found in the EIS fitted data between these two ECs.

Two possible structures correspond to these two EC models are shown in Figures 3.8(b) and (d). The structure associated with the EC in Figure 3.8(a) consists of a condensed bis-sulfur silane film at the topside, followed by an unknown phase layer covering uniformly on aluminum oxide layer (Figure 3.8(b)). The structure corresponding to the EC in Figure 3.8(c), however, demonstrates that the unknown phase may mix with aluminum oxide to some extent. The determination of the exact structure of the system will be subjected to further characterization work instead of EIS.

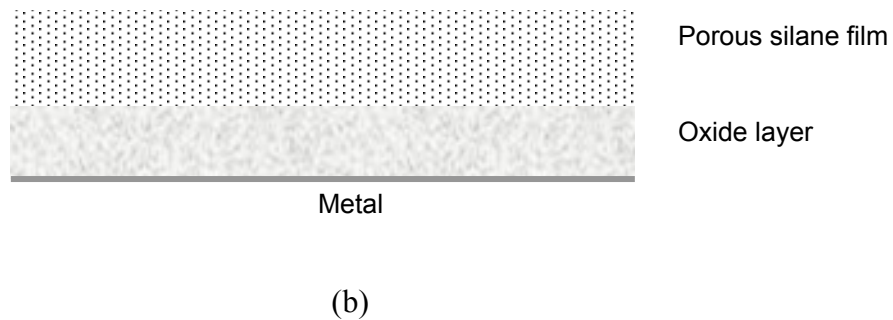
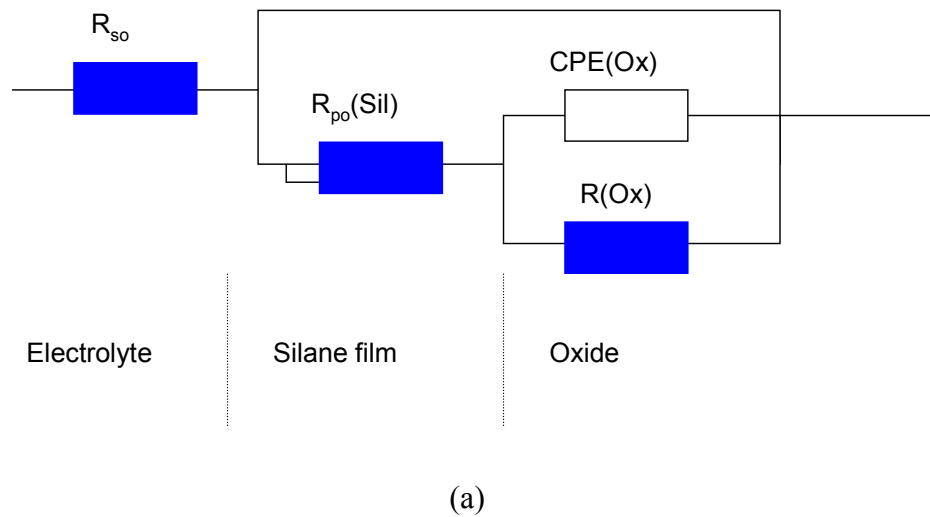
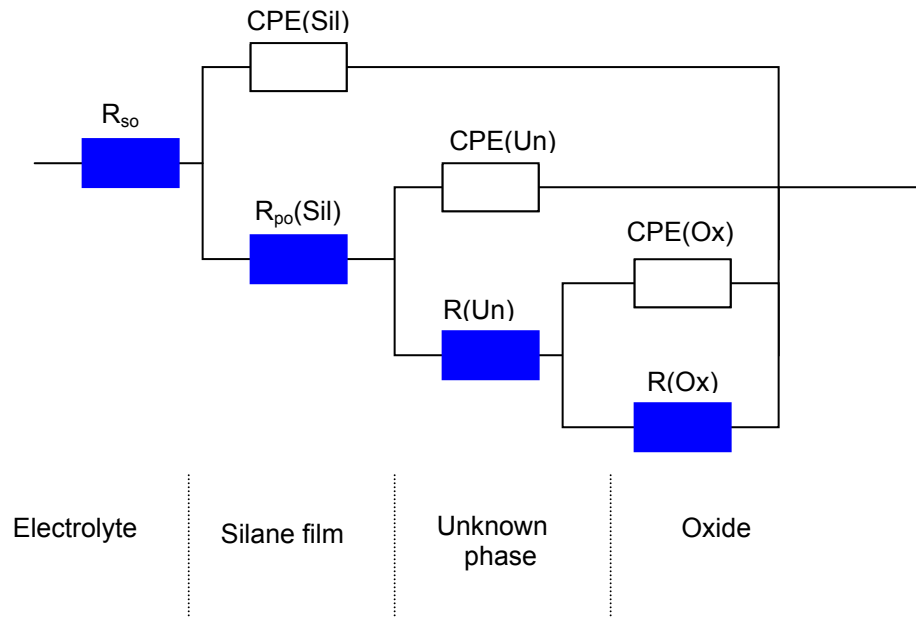
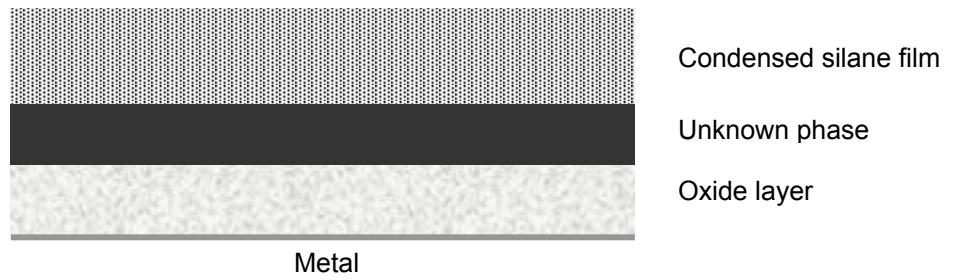


Figure 3.7. Equivalent electrical circuits and their corresponding physical structures for bis-sulfur silane-treated AA 2024-T3 at initial stages (without unknown phase); (a) EC, and (b) the physical structure

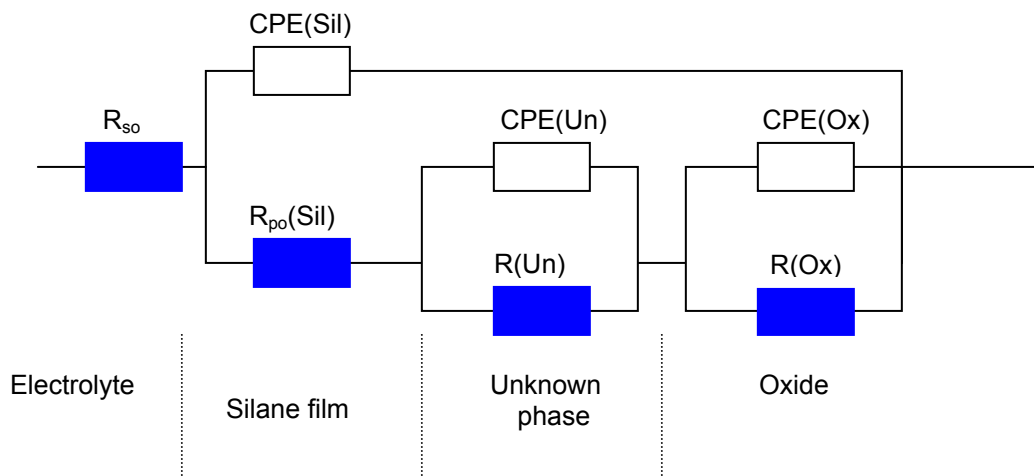


(a)

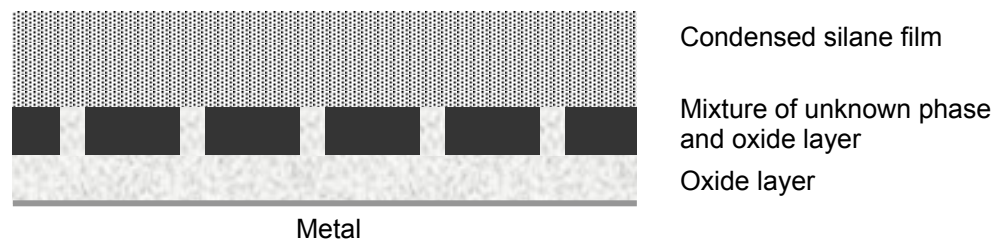


(b)

Fig. 3.8(a) and (b)



(c)



(d)

Figure 3.8. Equivalent electrical circuits (EC) and their corresponding physical structures for bis-sulfur silane-treated AA 2024-T3 at later stages (with unknown phase); (a) the complete-nested EC, (b) the physical structure corresponding to (a), (c) the half-serial EC, and (d) the physical structure corresponding to (c)

Figures 3.9(a)–(d) show the fitted Bode plots representing the changes in EIS spectra of the bis-sulfur silane-treated AA 2024-T3 with immersion time in 0.5 M K_2SO_4 solution. An excellent agreement can be observed between the experimental data (points) and the fitted curve (solid line). Since the properties of the bis-sulfur silane-treated AA 2024-T3 alloy with

time change so rapidly, a deviation from ideal dielectric properties is possible, i.e., the sample may have changed during the time required to record the entire EIS spectrum. Therefore, constant phase elements (CPE) rather than capacitances were used in the models, which have been shown to be the better way to describe the dielectric properties in non-ideal organic coated system. CPE is usually defined as [70],

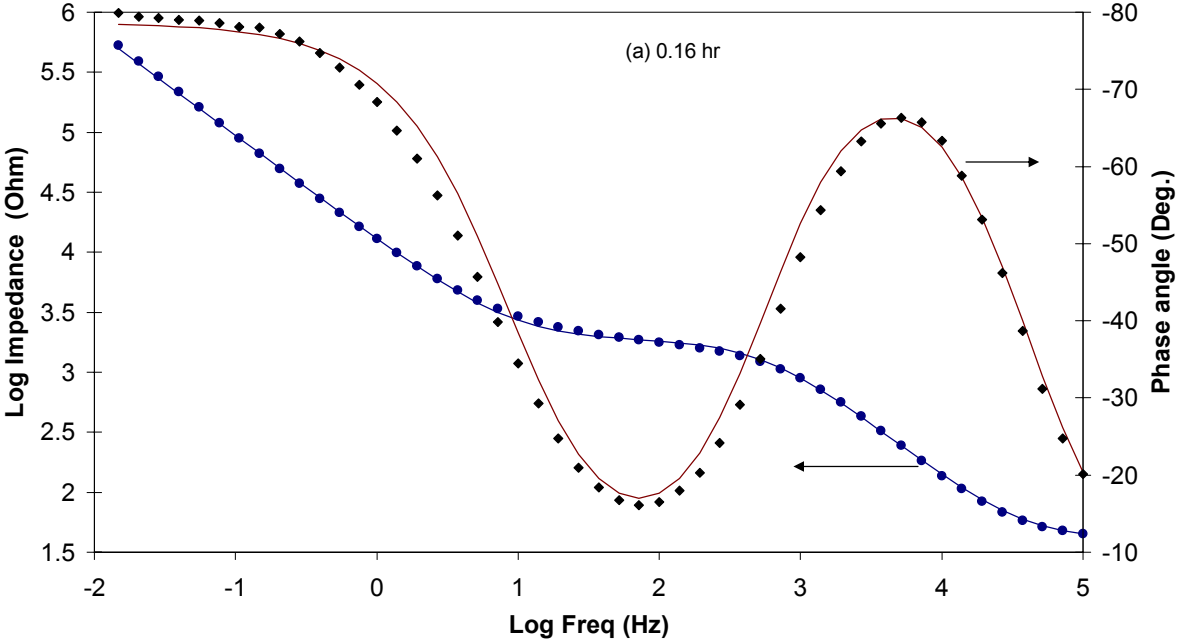
$$Z(CPE) = \frac{(j\omega)^{-n}}{Y_0} \quad (3.5)$$

where Z is the impedance of the CPE in Ω ; ω is the angular frequency in rad s^{-1} ; n and Y_0 the CPE parameters; n is also the deviation from ideal behavior. For $n = 1$, the element is an ideal capacitor and Y_0 is then equal to C . For $n = 0$, the CPE becomes a pure resistor with $R = 1/Y_0$. The capacitance can be calculated from the experimentally found CPE parameters n and Y_0 by the equation [70, 87],

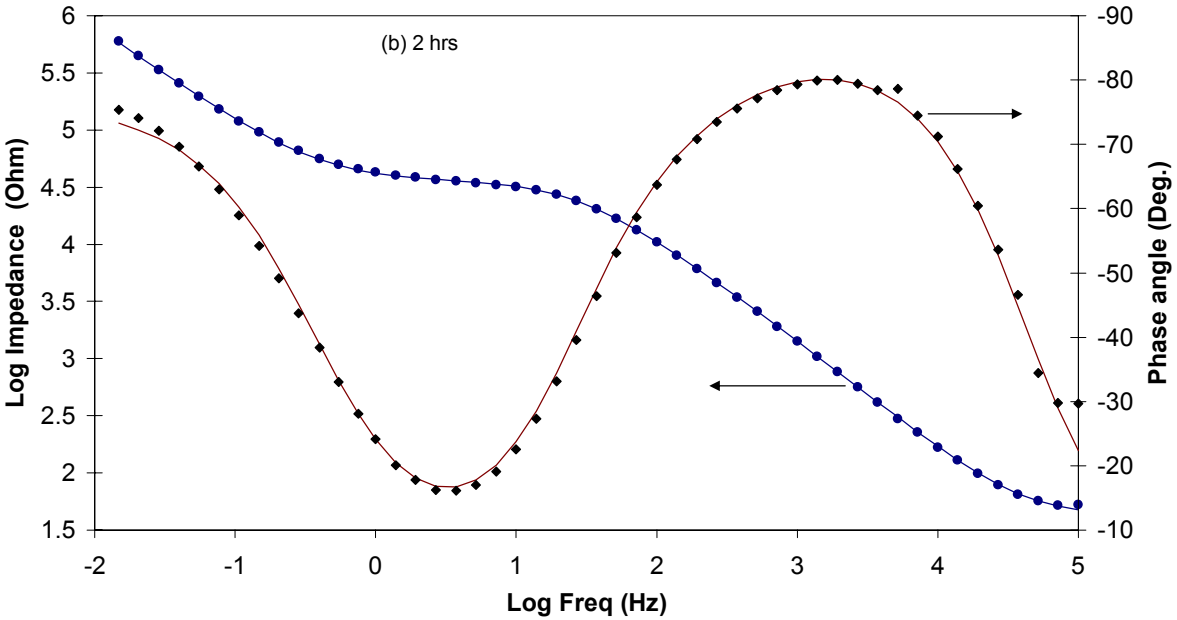
$$C = \frac{Y_0 \omega^{n-1}}{\text{Sin}(n \frac{\pi}{2})} \quad (3.6)$$

In Figure 3.9(a), the fit for the $t = 0$ sample is slightly poorer with the EC in Figure 3.7(a). The two-time-constant circuit was preferred here, as the phase angle plot did not indicate the presence of the time constant RC3 yet. The reason for the slight misfit in Figure 3.9(a) is most

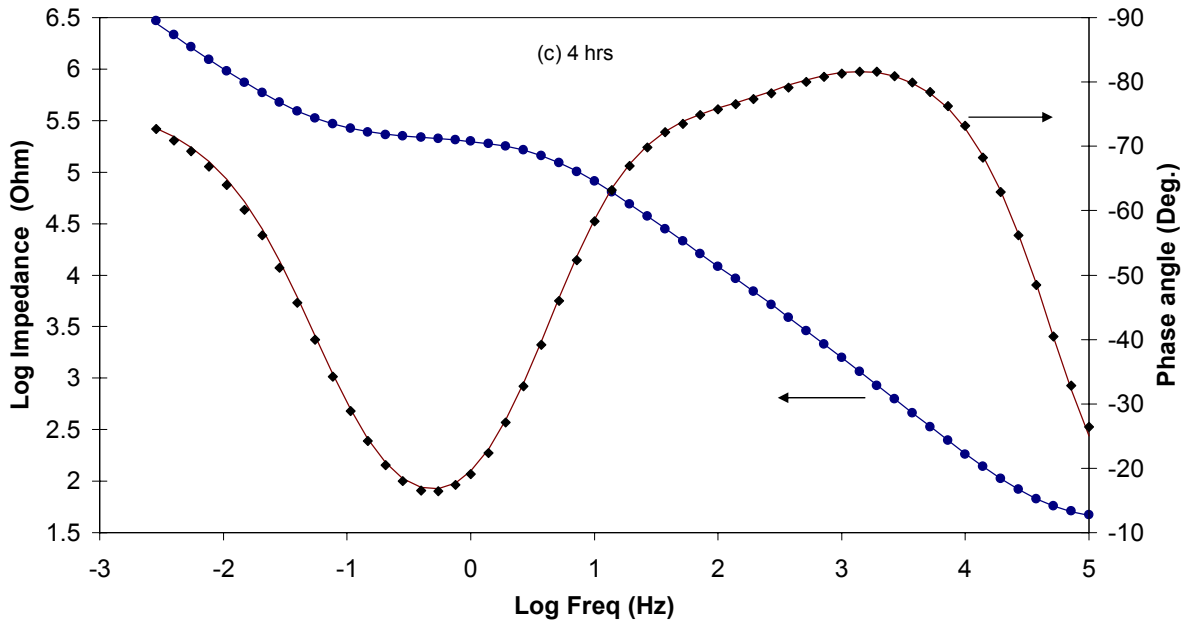
likely a time factor. The EIS analysis took approximately 40 min. In that time period, changes had already taken place in the film.



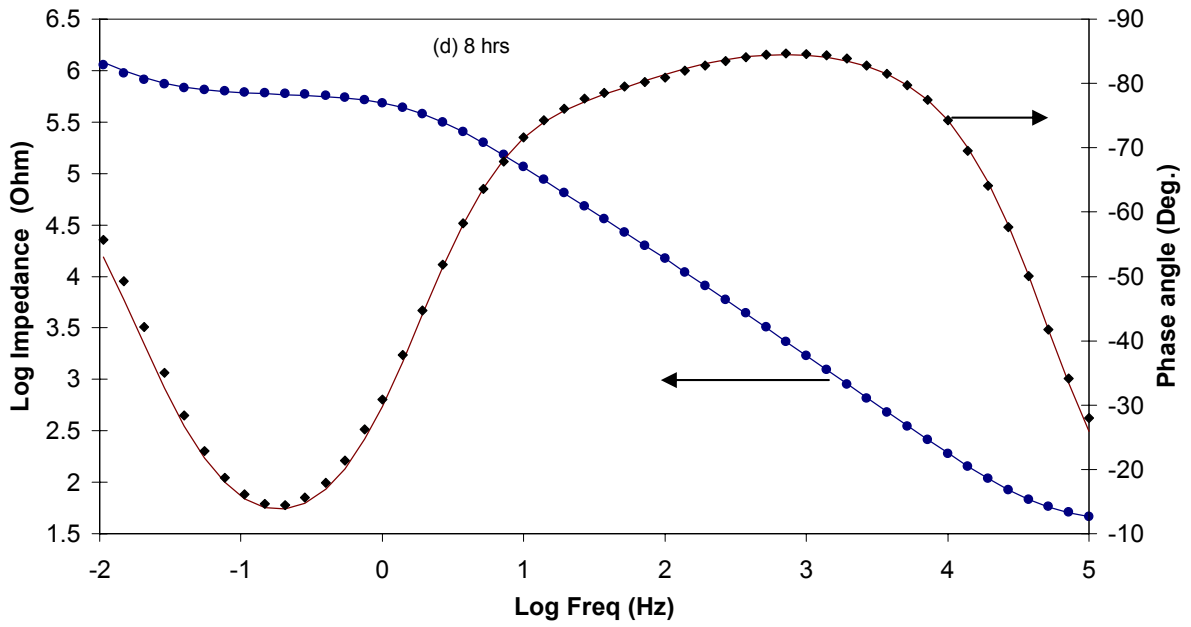
(a)



(b)



(c)



(d)

Figure 3.9. Fitted Bode plots for bis-sulfur silane-treated AA 2024-T3 after immersion in 0.5 M K_2SO_4 for various times (a) 0.16 hr, (b) 2 hrs, (c) 4 hrs, and (d) 8 hrs

3.2.2.2. Analysis of the fitted data for bis-sulfur silane--treated AA 2024-T3

Figure 3.10 shows the resistances and capacitances as a function of immersion time of the bis-sulfur silane-treated samples in the electrolyte. The capacitances were calculated from the fitted Y_0 and n values using Equation (3.2). The figure also shows the values of n , the deviation from ideal capacitive behavior.

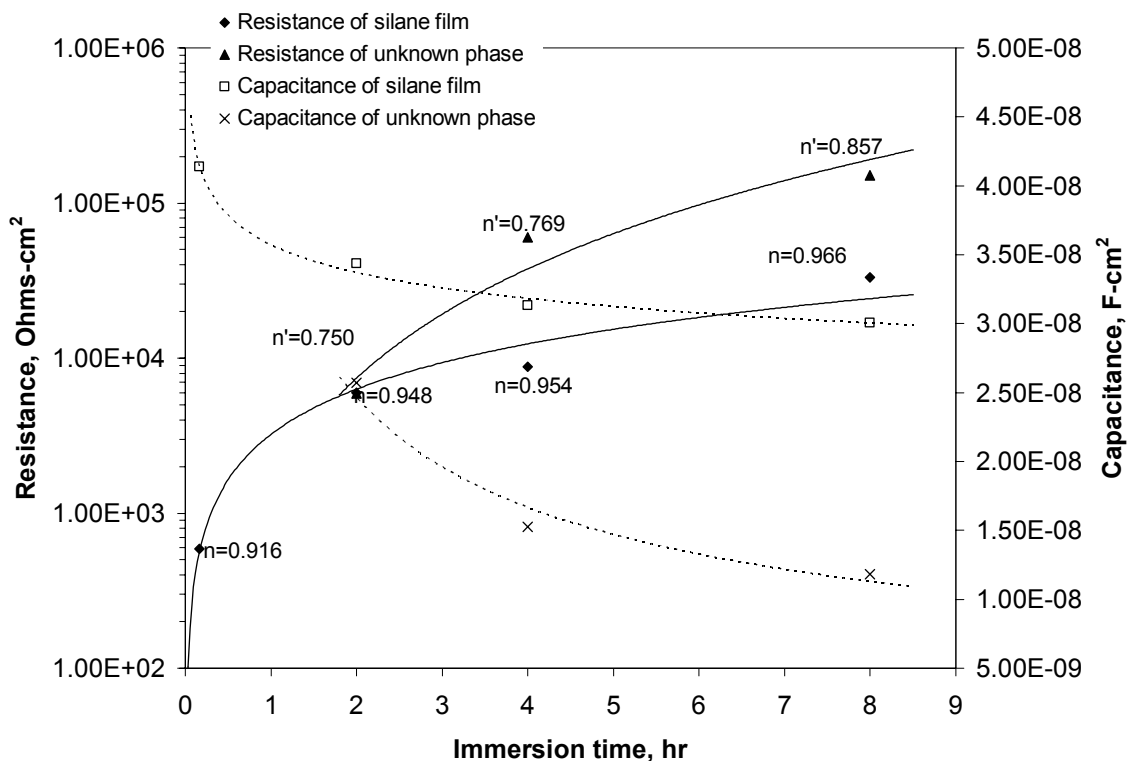


Figure 3.10. Capacitances and resistances as a function of immersion time in 0.5 M K_2SO_4 solution for bis-sulfur silane-treated AA 2024-T3; n and n' are for silane film and unknown phase, respectively

The values of the resistances for both the silane film and the unknown phase (starting after two hours) increase with immersion time. A stationary situation is not reached during the measuring period, in other words, the formation of the siloxane structures in the silane film continues and the increased crosslinking leads to a higher resistance. The resistance increase of the unknown phase may be the result of the growth of this film. On the other hand, the capacitances for both bis-sulfur silane films and the unknown phase decrease with immersion time. This phenomenon is unusual for common organic coatings such as paints. The capacitance of a paint coating always tends to increase with immersion time, even in a non-corrosive electrolyte, as a result of water uptake [81]. The reason for the increase in capacitance of such coatings is due to a significant increase of the dielectric constant (ε) of the coating, which is influenced strongly by water penetration into the coating. This conclusion is valid if we assume that the coating thickness remains constant during water penetration, since the capacitance of a coating can be defined as [70, 87],

$$C = \varepsilon_0 \varepsilon \frac{A}{d} \quad (3.7)$$

where the parameters have their usual meanings: A = surface area, d = coating thickness, ε_0 = dielectric constant of the free space; ε and d are usually considered as the important factors for the change of capacitance.

In the case of the bis-sulfur silane-treated AA 2024-T3 panels, the observed decrease in the capacitances vs. immersion time could be explained as follows.

1. For the silane film the increase of the siloxane concentration (crosslink density) in the film is associated with a reduction of the swelling capacity of the film. This effect will reduce the ε of the bis-sulfur silane film since the water content will become lower as the crosslink density increases. Another way of putting it is that the film becomes more hydrophobic or less polarizable as it crosslinks more and the number of hydrophilic SiOH groups reduces. Again, the water content decreases.

2. For the unknown phase, the decrease of capacitance can most likely be attributed to the increase of the film thickness d as the film keeps growing with time, although it cannot be excluded that the ε for the unknown phase may be somewhat lower than for the silane film.

The n values show an interesting trend. For the silane film they start at 0.92 and then increase to 0.96, so the silane film appears to be of good quality and becomes even denser as it cures. The n of the new phase (n' in the Figures) starts considerably lower, and then increases to 0.85. This observation is associated with crosslinking in the film. The values of n and n' increase with crosslinking density.

Figures 3.11 and 3.12 show the change of the resistances, capacitances and n values with time for the bis-sulfur silane-treated AA 2024-T3 samples observed in the 80°C curing and ambient aging experiments, respectively. Behaviors similar to that in the immersion experiment are observed here, except that the progress in the 80°C curing case (Figure 3.11) is much faster than in the immersion experiment. The values for the unknown phase could not be obtained in the ambient aging experiment, since no new RC element was found, i.e., this unknown phase does not seem to be formed in this short-term and low-temperature aging process.

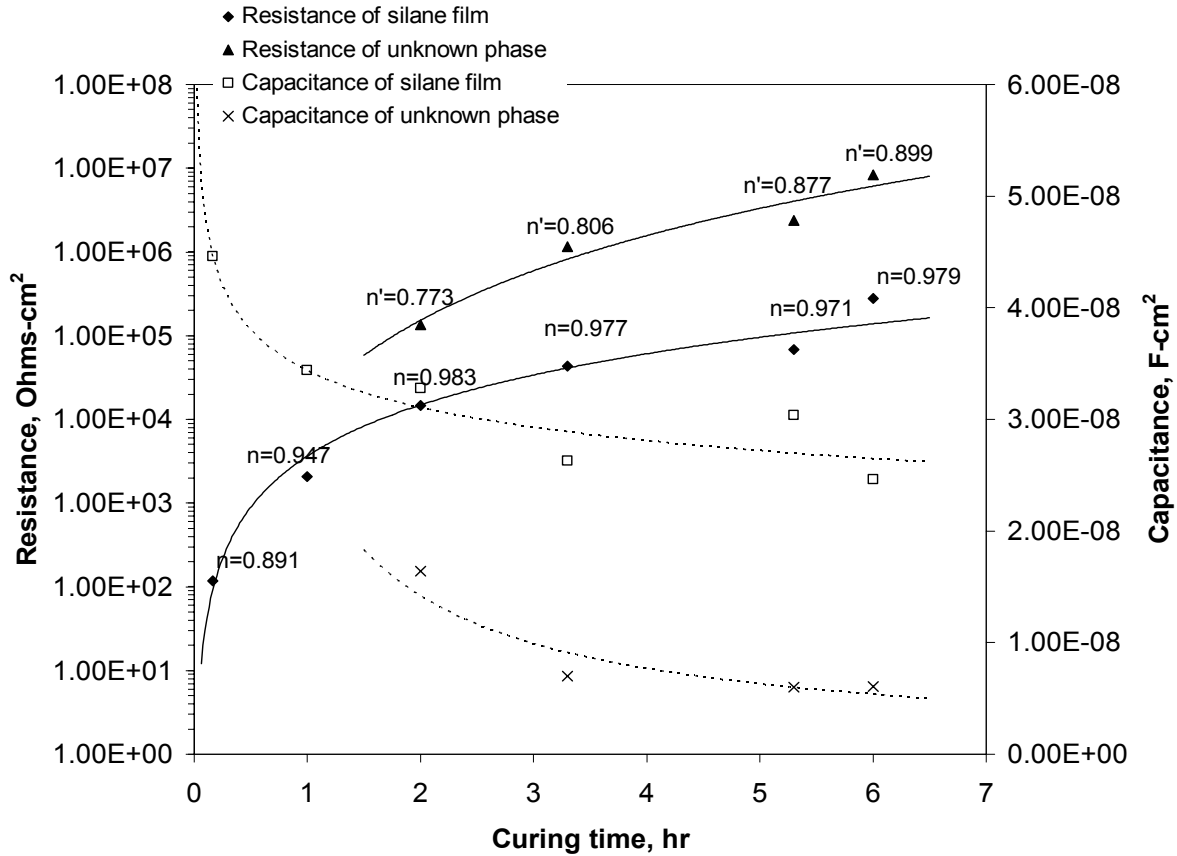


Figure 3.11. Capacitances and resistances as a function of curing time at 80°C for bis-sulfur silane-treated AA 2024-T3; n and n' are for silane film and unknown phase, respectively

The resistance values in the 80°C curing experiment are considerably higher than those observed in the other two experiments. Thus, the degree of crosslinking that can be attained in thermal aging at elevated temperature is higher than that observed in the other experiments. This in itself is not surprising, but it is remarkable to notice in Figure 3.11 that the silane film cannot be fully cured even after 6 hrs of curing at 80°C, as the resistance and capacitance of the silane film still tends to increase or decrease afterwards. However, higher temperatures can be expected to accelerate the curing process. In practice, it has been found

that a fully cured silane film can be obtained by curing at 100°C for 4 hrs. This conclusion is of paramount importance for the successful and reproducible application of this silane for corrosion protection in the field. It explains why unpredictable and sometimes erratic behavior of the same silane/metal system was observed previously, as hitherto there was no method available to determine the state of cure of the film. This state is determined not only by the curing temperature and time, but also by the relative humidity, as the ester groups have to be removed by hydrolysis first.

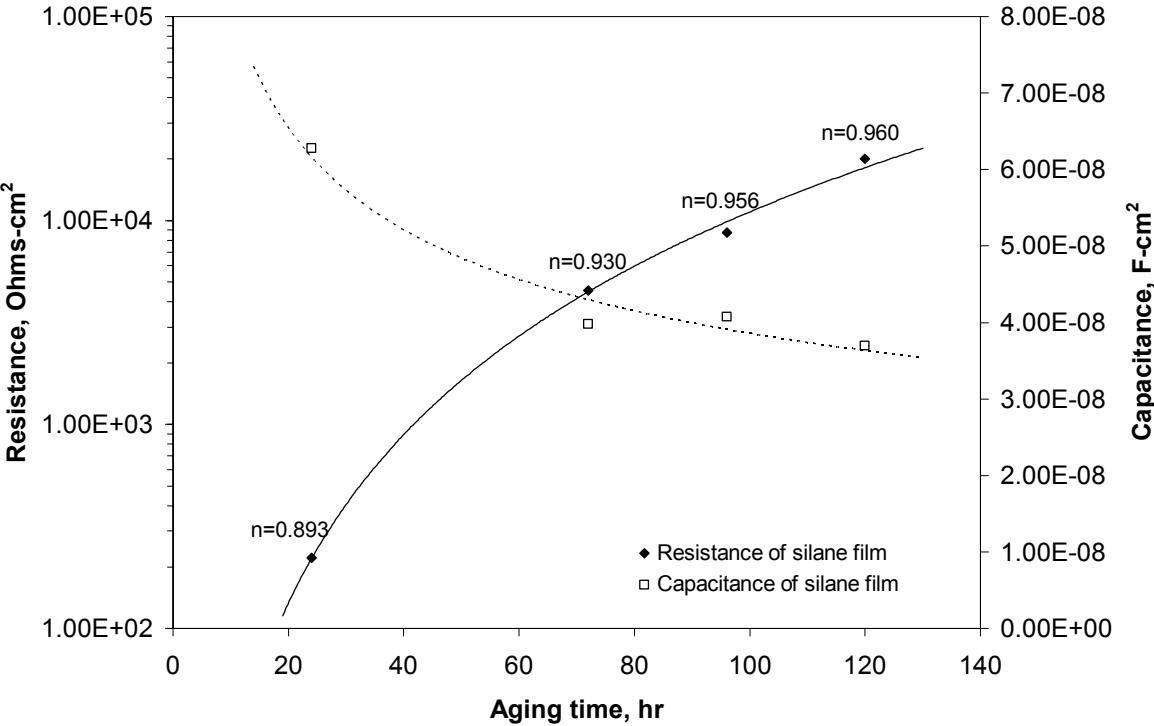


Figure 3.12. Capacitance and resistance as a function of ambient aging time on AA 2024-T3

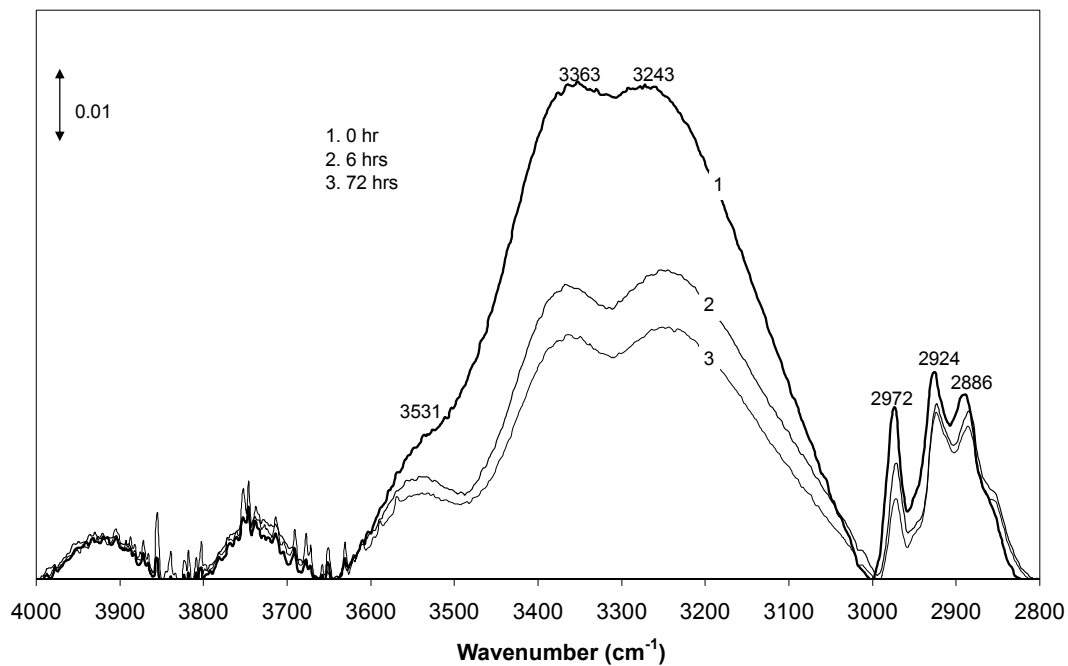
The n values show the same trends as in Figure 3.10: for the bis-sulfur silane film, a slight increase with aging is observed; for the unknown phase (Figure 3.11 only), a steeper increase is found. The final values for both the silane film and the unknown phase are the same in all tests.

It should also be noted that the value of the resistance of the new phase between the silane film and the aluminum oxide is always of the same or higher order of magnitude as that of the silane film, while its capacitance is always lower. This is an important finding, as it suggests that this unknown phase may provide a major contribution to the overall corrosion protection of the treated metal.

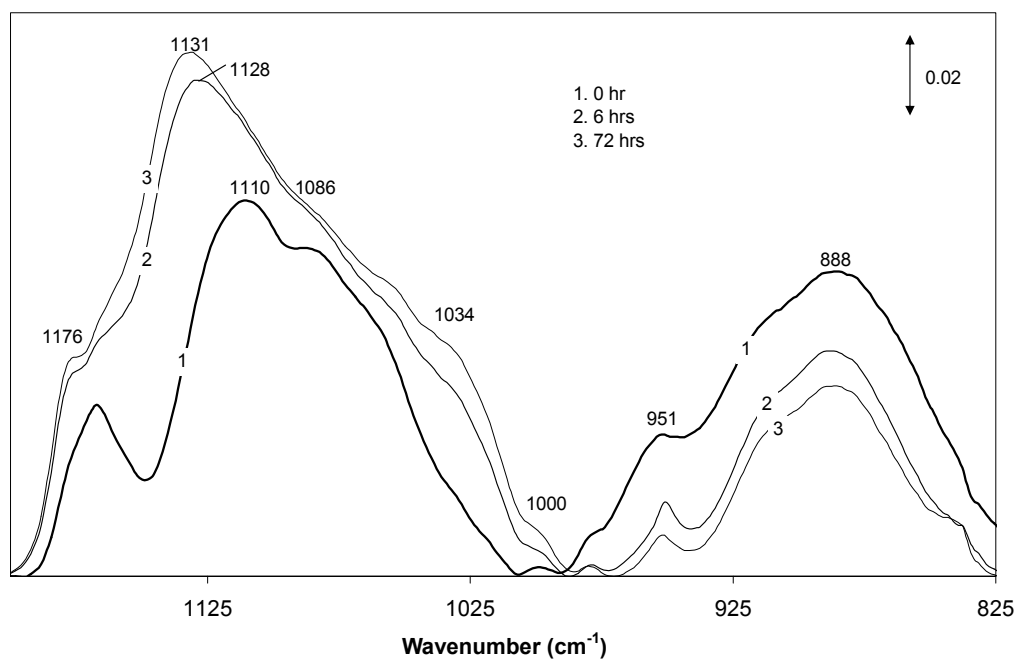
The fitted EIS data for both aluminum oxide and electrolyte are listed in the Appendix B. The CPE parameter of the aluminum oxide, $Y_0 (1/Q)$, decreases with time in all processes. This may indicate that the properties of aluminum oxide have changed, though the causes are still unknown. Possibly, the properties could be influenced by the reaction of silanol groups and aluminum hydroxide. In addition, the dielectric constants of bis-sulfur silane film in the curing process have been calculated using Equation (3.3) to make an internal check for the validity of the EIS analysis (Appendix B, Table B4).

3.2.3. Surface analysis by FTIR-RA

Figure 3.13 compares the absorption spectra of bis-sulfur silane-treated AA 2024-T3 aged in the ambient from 0 hr to 72 hrs. The assignments of characteristic absorption bands are given in Table. 3.1 [33, 88, 89]. As can be seen in Figures 3.13(a) and (b), the intensities of the absorption bands corresponding to silanols (SiOH) at 3531, 3363, 3243 and 888 cm^{-1} decrease with aging time, in the meanwhile, the ones to siloxane bonds (SiOSi) in the region of 1176 to 1000 cm^{-1} increase during the aging period. This indicates the occurrence of further crosslinking in the bis-sulfur silane film. It is noticed that the band of SiOSi at 1110 cm^{-1} shows a 20 cm^{-1} shift in the direction to high frequencies after 72 hrs of aging in the ambient. The shift may be associated with the formation of long siloxane chains during crosslinking. The bands of CH stretching in unhydrolyzed ester groups ($\text{SiOCH}_2\text{CH}_3$) at 2972, 2924, 2886 and 951 cm^{-1} decrease with time, as a result of further hydrolysis of esters to silanols in the bis-sulfur silane film. The same effects can be observed during immersion and curing processes with FTIR-RA.



(a)



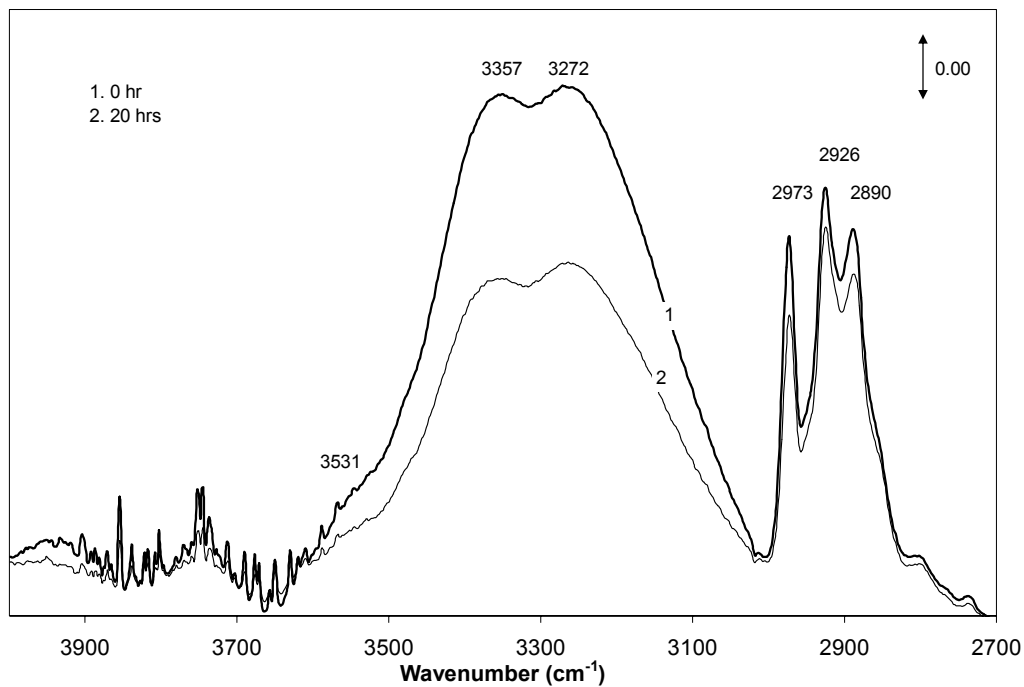
(b)

Figure 3.13. FTIR-RA spectra of bis-sulfur silane-treated AA 2024-T3 aged in air at RT from 0 hr to 72 hrs (a) $4000 - 2700 \text{ cm}^{-1}$; (b) $1200 - 825 \text{ cm}^{-1}$.

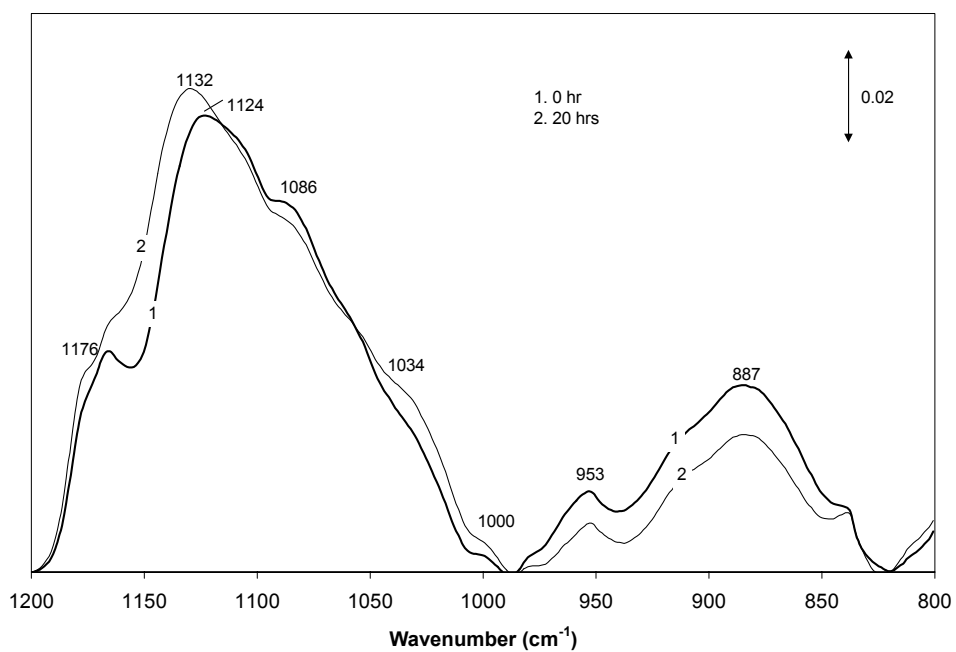
Table 3.1. Assignments of characteristic absorption bands for bis-sulfur silane film on AA 2024-T3 [33,88,89]

| Absorption band (cm⁻¹) | Assignment |
|--|--|
| 3531, 3363, 3243 | SiOH (H-bonded) |
| 2972, 2924, 2886 | SiOCH ₂ CH ₃ (C-H str.) |
| 1176 ~ 1000 | SiOSi, SiOC, and SiOAl region (Si-O asym.str.) |
| 951 | SiOCH ₂ CH ₃ (Si-O asym. str.) |
| 888 | SiOH (H-bonded) |

Figures 3.14(a) and (b) present the spectra of bis-sulfur silane-treated AA 2024-T3 immersed in 0.5M K₂SO₄ solution from 0 hr to 20 hrs. The specimen was pre-cured at 80°C for 10 min before immersion. In general, FTIR-RA results in Figures 3.13 and 3.14 confirmed that the bis-sulfur silane film undergoes further hydrolysis and crosslinking in the above-discussed processes, and hence supported the interpretations of the EIS results presented in the earlier sections. The formation of the unknown phase, however, is not evidenced by FTIR-RA. This is mostly because the major Si-O region between 1200 cm⁻¹ to 1000 cm⁻¹ is so broad that the peak differentiation becomes very difficult.



(a)



(b)

Figure 3.14. FTIR-RA spectra of bis-sulfur silane-treated AA 2024-T3 immersed in 0.5M K_2SO_4 solution from 0 hr to 20 hrs (a) $4000 - 2700 \text{ cm}^{-1}$; (b) $1200 - 800 \text{ cm}^{-1}$

3.2.4. potentiodynamic polarization tests

The potentiodynamic polarization curves measured in 0.5 M NaCl solution at pH 6 for AA 2024-T3 blank (untreated), treated by the bis-sulfur silane without and with curing (80°C for 20 hrs) are shown in Figure 3.15. Compared with these curves, it is obvious that both cathodic reduction reaction and anodic reaction on AA 2024-T3 are inhibited efficiently by the treatment with the bis-sulfur silane. Furthermore, the extensively cross-linked bis-sulfur silane film (curve 1, 80°C, 20 hrs) provides even better corrosion protection on AA 2024-T3 than the porous silane film (curve 2, not cured). Again, the results of potentiodynamic polarization tests are consistent with the conclusion drawn from the EIS study, i.e., a fully crosslinked structure with a high impedance in EIS spectrum provides an appreciable reduction in both cathodic and anodic currents in potentiodynamic polarization tests.

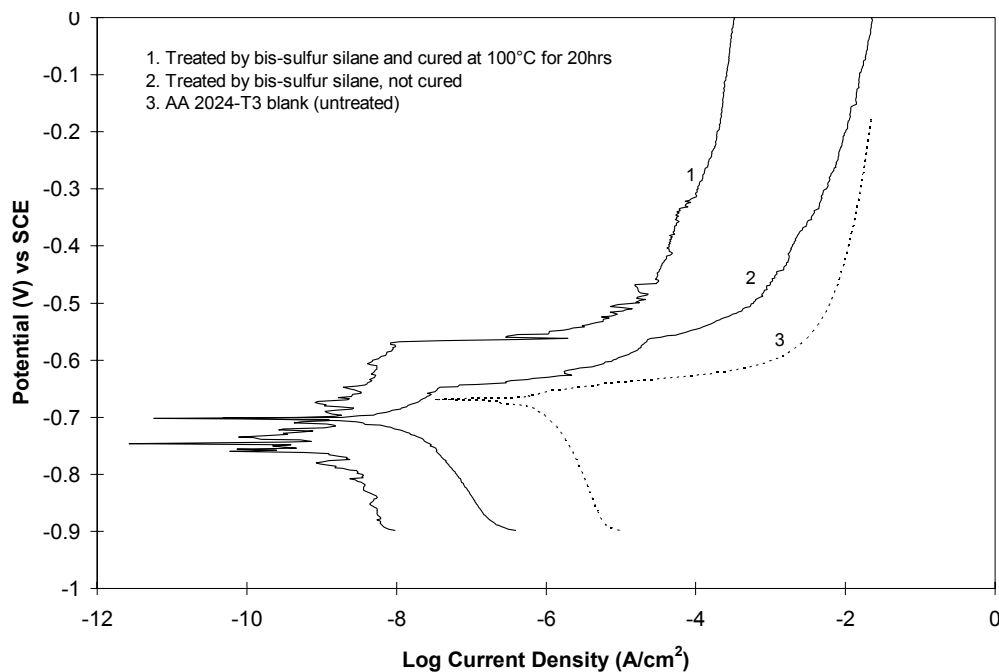


Figure 3.15. Potentiodynamic polarization curves of bis-sulfur silane-treated AA 2024-T3 panels in 0.5 M NaCl solution at pH 6

3.2.5. Salt Spray Test (ASTM B117)

A Salt Spray Test (SST) was employed for comparing the corrosion behavior of AA 2024-T3 blank, treated by bis-sulfur silane, and by chromate (Chromicoat103[®]). In order to obtain a fully crosslinked structure, bis-sulfur silane-treated AA 2024-T3 was cured at 100°C for 10 min., and then aged in air at RT for 336 hrs before exposure to SST for 360 hrs. The results (Table 3.2) show that the corrosion behavior of AA 2024-T3 treated by bis-sulfur silane and by Chromicoat103[®] is comparable, i.e., only a few small pits were observed after testing. This strongly demonstrates bis-sulfur silane treatment can be a promising replacement of chromating.

Table 3.2. Corrosion evaluation of AA 2024-T3 blank, treated by bis-sulfur silane and Chromicoat103[®] after 360 hrs of SST

| Treatment | Rust coverage on the tested surface (%) | Rust mark |
|---|--|------------------|
| A1050 alkaline cleaned | 100 | WR10 |
| Chromated (Chromicoat103 [®]) | A few pits on the surface | WR-spot |
| Bis-sulfur silane-treated | A few pits on the surface | WR-spot |

* WR- White Rust on the surface of Al alloy.

3.3. Conclusions

1. Three effects were studied in EIS of bis-sulfur silane-treated AA 2024-T3 alloy panels: *(i)* the effect of continuous immersion time in 0.5 M K_2SO_4 solution; *(ii)* the effect of curing time in air at 80°C prior to EIS analysis, and *(iii)* the effect of aging time at room temperature prior to EIS analysis. In all cases, the total impedance of the system increased markedly.

2. The phase angle plot is more sensitive to the structural changes in the system than the impedance plot. An additional time constant, most likely indicative of a new phase between the silane film and the aluminum oxide, was observed in the phase angle plot in two of the three experiments.

3. The significant increase of the total impedance of the system was attributed to: *(i)* the formation of siloxane structures -Si-O-Si- in the existing silane film by condensation of silanol groups SiOH generated from the hydrolysis of residual ester groups $-SiOC_2H_5$ in the 0.5 M K_2SO_4 electrolyte; and *(ii)* the formation and growth of the unknown phase between the silane film and the aluminum oxide. The conclusion has been partly conformed by FTIR-RA surface analysis.

4. Three successful equivalent circuits for the modeling of the observed changes in the EIS spectra vs. time were presented. These circuits fitted the data very well.

5. EIS in a non-corrosive electrolyte has been demonstrated to be a useful tool for determining the conditions for depositing silane films on metals with optimum conditions for corrosion protection. A fully crosslinked bis-sulfur silane film with a higher impedance in EIS

spectrum shows excellent corrosion protection on AA 2024-T3 in potentiodynamic polarization test as well as a 360-hr salt spray test (ASTM B117).

6. The barrier properties of the unknown phase observed in EIS is possibly the origin of the high corrosion protection performance.

Chapter 4. Structural Characterization of Bis-[triethoxysilylpropyl]tetrasulfide and Bis-[trimethoxysilylpropyl]amine Silanes by Fourier-transform Infrared Spectroscopy and Electrochemical Impedance Spectroscopy¹

Abstract Bis-[triethoxysilylpropyl]tetrasulfide (or bis-sulfur silane) and bis-[trimethoxysilylpropyl]amine (or bis-amino silane) were deposited on 2024-T3 aluminum alloy (AA 2024-T3). The film structures were characterized using Fourier-Transform Infrared Spectroscopy (FTIR) and Electrochemical Impedance Spectroscopy (EIS) techniques. The results showed that: (1) The silane structures are affected significantly by the hydrolysis time of the silane solutions. A minimum hydrolysis time is required to obtain a crosslinked silane film. (2) Hydrolysis progresses more readily and faster in the bis-amino silane system than in the bis-sulfur silane system. This is probably due to the catalytic action of the amine of the bis-amino silane. (3) Both silane systems experienced significant crosslinking upon curing at 100°C, during which an interfacial layer was formed via crosslinking in the interfacial region. This interfacial layer may be a major contribution to the corrosion protection of AA 2024-T3. (4) A new phase was observed in a fully cured bis-amino silane film after long-term aging in the atmosphere. This new phase is likely to be carbamates and bicarbonates formed via a reaction between the secondary amino groups in the bis-amino silane, carbon dioxide, and moisture absorbed from the atmosphere.

¹ The chapter has been published on J. of Adhesion Sci. and Technol., 16, 1235 (2002)

4.1. Introduction

In corrosion tests, bis-sulfur silane consistently exhibited excellent anticorrosive performance on metals, especially on Al and Al alloys. Bis-sulfur silane treated AA 2024-T3 panels, for example, survived a 360-hr salt spray test [24]. Bis-amino silane was also tested with metals such as AA 2024-T3 and hot-dip galvanized steel (HDG). The corrosion testing results, however, showed a poor corrosion protective performance by the bis-amino silane. Obviously, silane type is an important factor that influences the subsequent corrosion performance of silane-treated metal systems. Subramanian and Van Ooij [30] compared the corrosion behavior of BTSE and γ -APS films deposited on Fe using potentiodynamic polarization tests. They found that γ -APS showed no protection at all on Fe, while the BTSE-treated Fe exhibited no visible signs of corrosion after the test. They explained this difference by taking into account the effects of amine in γ -APS. Two detrimental effects of the amine on the corrosion performance are that, (1) amino groups can be adsorbed onto the Fe substrate by competing with the silanols, resulting in a hydrophilic interface between the γ -APS film and the substrate; and (2) the protonated amine ($-\text{NH}_3^+$) in the γ -APS film promotes the ingress of corrosive chloride ions (Cl^-) into the film. In the case of the bis-amino silane, its poor corrosion performance may also be associated with the similar actions of the secondary amine contained in the silane. Although the bis-amino silane alone is not suitable for corrosion protection of metals in the unpainted state, it still performs well when used as a paint promoter.

In addition to the silane type, it has also been found in practice that the hydrolysis time of silane solutions is another critical factor that considerably affects the silane film

structure, especially the crosslinking degree. This aspect, however, has not been explored in detail. Generally speaking, a functional or “workable” silane solution should generate enough silanols for the subsequent condensations between silanols and metal hydroxide and among silanols themselves. It was observed that a bis-sulfur silane solution without sufficient hydrolysis gave an oily rather than a solid film. The associated IR results showed that the oily film still contained a larger amount of unhydrolyzed esters than the solid film. As a consequence, the oily film had been poorly crosslinked and could not adhere to the metal substrate tightly due to the lack of sufficient silanols. Accordingly, such oily film is not expected to protect metals against corrosion effectively.

In this chapter, we report the results of the following investigations: (1) the effect of hydrolysis time of both bis-sulfur and bis-amino silane solutions on the resulting silane films structures; and (2) the structural changes in these two films under different conditions, i.e., curing at an elevated temperature and aging in the ambient. A comparison of these two types of silane films are also presented at the end of this chapter.

The silane solutions used here were all 5% water/alcohol solutions, with ethanol for the bis-sulfur silane solution and methanol for the bis-amino silane solution.

4.2. Results and Discussions

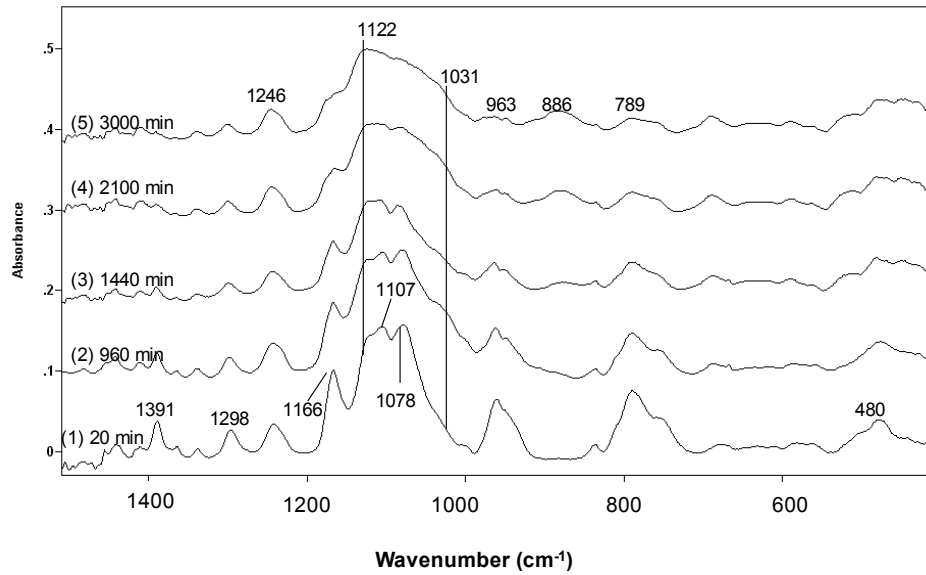
4.2.1. Structures of the bis-sulfur and bis-amino silane films on AA 2024-T3

4.2.1.1. Effect of hydrolysis time of bis-sulfur and bis-amino silane solutions

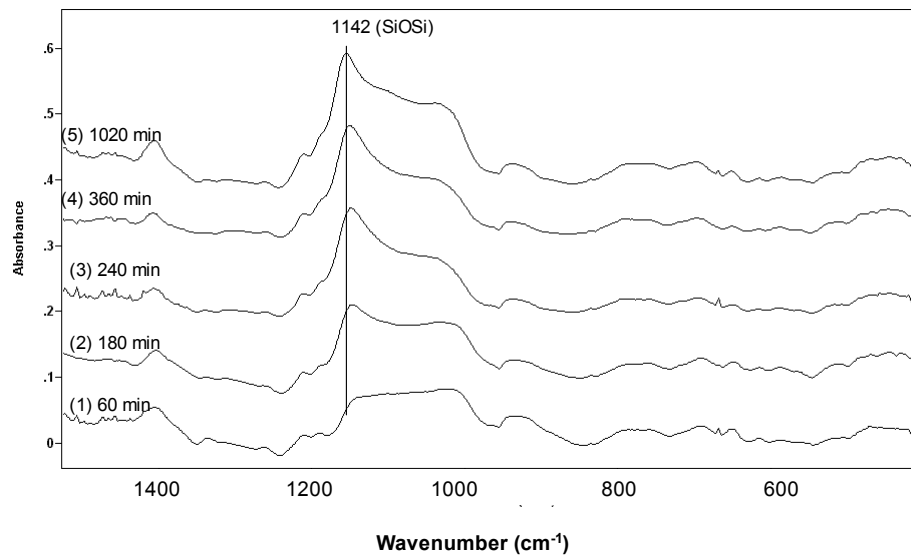
The FTIR-RA spectra of bis-sulfur and bis-amino silane films deposited on AA 2024-T3 from the silane solutions that were hydrolyzed for different times are shown in Figures 4.1(a) and (b), respectively. All the films were cured at 100°C for 10 min before IR measurements. In Figure 4.1(a), significant changes in the intensity of the bands in the range from 1500 cm^{-1} to 400 cm^{-1} are seen for the bis-sulfur silane films. The assignments of all bands in Figure 4.1(a) are listed in Table 4.1 [83,88,89]. After 20 min of hydrolysis, an oily film was obtained and its corresponding spectrum still showed many bands related to the unhydrolyzed ester groups (SiOC_2H_5), meaning that the extent of hydrolysis within 20 min was insignificant. As the hydrolysis time increases, the intensity of these bands decreases gradually, and in contrast, the SiOSi band at 1122 cm^{-1} becomes more noticeable. After 2100 min (35 hrs), a uniform and solid bis-sulfur film on AA 2024-T3 was observed visually. Correspondingly, the 1122 cm^{-1} band at this point becomes much more pronounced, and in the meanwhile, the region between 1000 cm^{-1} to 1200 cm^{-1} also broadens. This broadening is very likely due to the overlap of the SiOSi or SiOAl bands formed in the later curing stage. These SiOSi bands, however, are too obscured to be differentiated from one another. All of these changes suggest that more silanols (SiOH) were generated in the solution with increasing hydrolysis time, and that

these silanols condensed significantly during the following curing process forming SiOSi bonds. In addition, it is also noticed that a band at 886 cm^{-1} due to hydrogen-bonded SiOH gradually emerges and increases in the intensity with hydrolysis time. The appearance of this band was also reported in our previous work [24]. The explanation is as follows. Upon curing, the SiOH groups convert to SiOSi bonds by releasing the by-product water. This water would, in turn, participate in the hydrolysis of SiOC_2H_5 , producing more SiOH groups, evidenced by the band at 886 cm^{-1} . Ethanol ($\text{C}_2\text{H}_5\text{OH}$) as the by-product of the hydrolysis can be removed quickly from the film at higher temperatures, driving the hydrolysis reaction to completion.

In Figure 4.1(b), the effect of hydrolysis time on the structure of the bis-amino silane film on AA 2024-T3 is shown. After 60 min of hydrolysis, a solid bis-amino silane film was observed on AA 2024-T3. This solid film, however, did not cover the substrate uniformly. Some of the substrate area was still covered by a patch-like film, the formation of which is not well understood. The corresponding IR spectrum in Figure 4.1(b) shows no distinct bands due to unhydrolyzed ester groups and the band at 1142 cm^{-1} due to SiOSi asymmetric stretching is already noticeable after 60 min. This indicates that the hydrolysis of the bis-amino silane is fast; the generated silanols condense also quickly during the following curing process. As the hydrolysis continued, a uniform and solid bis-amino silane film was obtained on AA 2024-T3 after 240 min (i.e., 4 hrs), at which the 1142 cm^{-1} band due to SiOSi has become more pronounced. The band at 880 cm^{-1} due to hydrogen-bonded SiOH shown for the bis-sulfur silane film, however, is not seen in Figure 4.1(b), suggesting that no additional silanols are generated in the bis-amino silane film upon curing as does in the bis-sulfur silane film.



(a)



(b)

Figure 4.1 FTIR-RA spectra of silane films on AA 2024-T3 obtained from the silane solutions with different hydrolysis times, and followed by 10 min of curing at 100°C; (a) bis-sulfur silane, and (b) bis-amino silane

Table 4.1. IR band assignments for Figure 4.1(a) [83,88,89]

| Band position (cm ⁻¹) | Band assignment |
|-----------------------------------|--|
| 1391 | SiOCH ₂ CH ₃ (CH ₃ asymmetric stretch) |
| 1298 | SiOCH ₂ CH ₃ (CH ₂ wag) |
| 1246 | CH ₂ wagging in -CH ₂ -S- |
| 1166 | CH ₂ CH ₃ rock of SiOCH ₂ CH ₃ |
| 1122 | SiOSi (Si-O asymmetric stretching) |
| 1107 | SiOCH ₂ CH ₃ (Si-O asymmetric stretching) |
| 1031 | SiOSi (Si-O asymmetric stretching) |
| 1078 | SiOCH ₂ CH ₃ (Si-O asymmetric stretching) |
| 960 | SiOCH ₂ CH ₃ (Si-O asymmetric stretching) |
| 886 | Hydrogen-bonded SiOH |
| 789 | Si-C stretching |
| 480 | Si(OCH ₂ CH ₃) ₃ symmetric deformation |

The areas of the SiOC band at 963 cm⁻¹ for SiOC₂H₅ groups in the bis-sulfur silane films were measured using the “curve-fit” function included in the Bio-Rad IR analytical software, and were normalized to the areas of the band at 1246 cm⁻¹ due to CH wagging in -CH₂-S-, which are not supposed to change in the entire hydrolysis period. The results are plotted as a function of hydrolysis time in Figure 4.2. The normalized band area for 963 cm⁻¹ decreases continuously with hydrolysis time, and has not yet reached a constant value even after 3000 min (50 hr). This suggests that the hydrolysis of the bis-sulfur silane is relatively slow, and needs more than 3000 min (50 hr) to achieve

its hydrolysis equilibrium. Similar results were also reported [24, 90]. Such analysis has not been done with the bis-amino silane, since there is a difficulty in finding out a typical band for the unhydrolyzed ester groups in the bis-amino silane spectra (Figure 4.1(b)). Qualitatively speaking, the hydrolysis of the bis-amino silane is much faster than that of the bis-sulfur silane in their water/alcohol solutions.

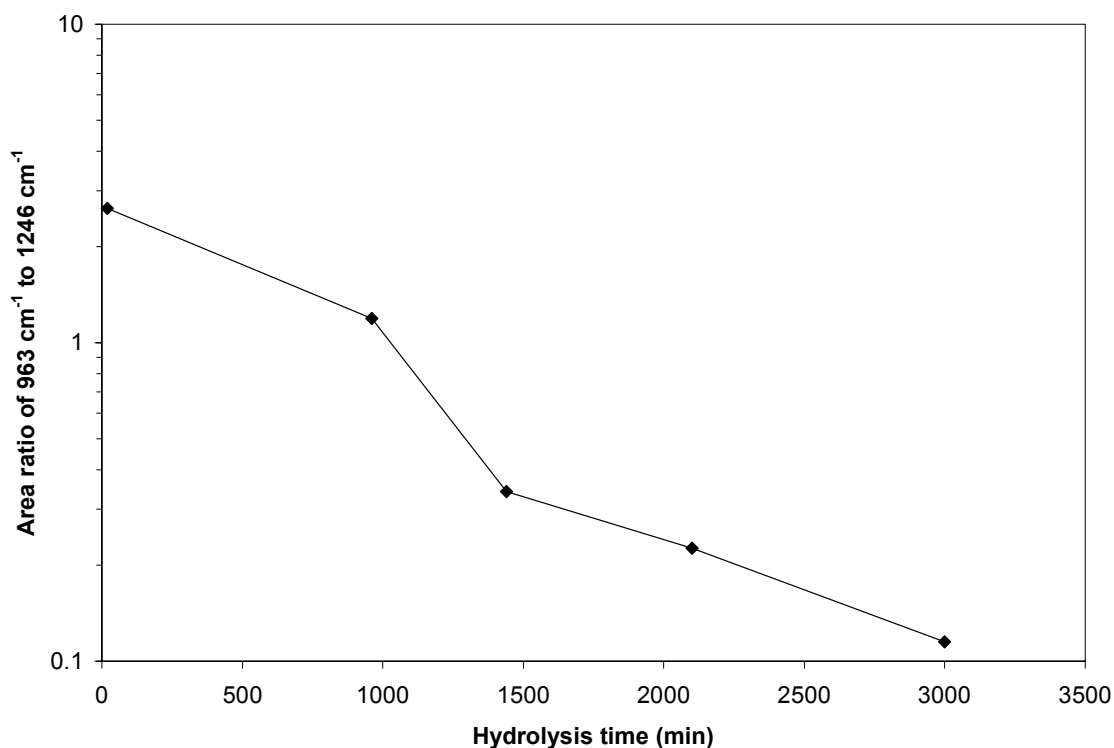


Figure 4.2. Area ratio of 963 cm⁻¹ and 1246 cm⁻¹ as a function of hydrolysis time of the bis-sulfur silane solution

As was mentioned above, a 5% bis-amino silane solution at its natural pH (10.8) gels within a few minutes. This simultaneous hydrolysis and the subsequent condensation in the bis-amino silane solution is very likely due to the catalytic action of the secondary amine (-NH-) contained in the bis-amino silane [3]. The solution pH is, thereby, lowered

to 7.5 using acetic acid (HAc). Correspondingly, the rates of both hydrolysis and condensation are reduced, as a considerable amount of secondary amines have been protonated by hydrogen ions (H^+) from acetic acid, and thus lose their activity as a catalyst. However, some remaining free secondary amines are still expected which may act as a catalyst for hydrolysis of the neutral bis-amino silane solution. In contrast, the bis-sulfur silane solution hydrolyzes slowly at its natural pH 6.5 due to the lack of catalytic species like amines.

4.2.1.2. Structural changes in bis-sulfur and bis-amino silane films on AA 2024-T3 in the 100°C curing process

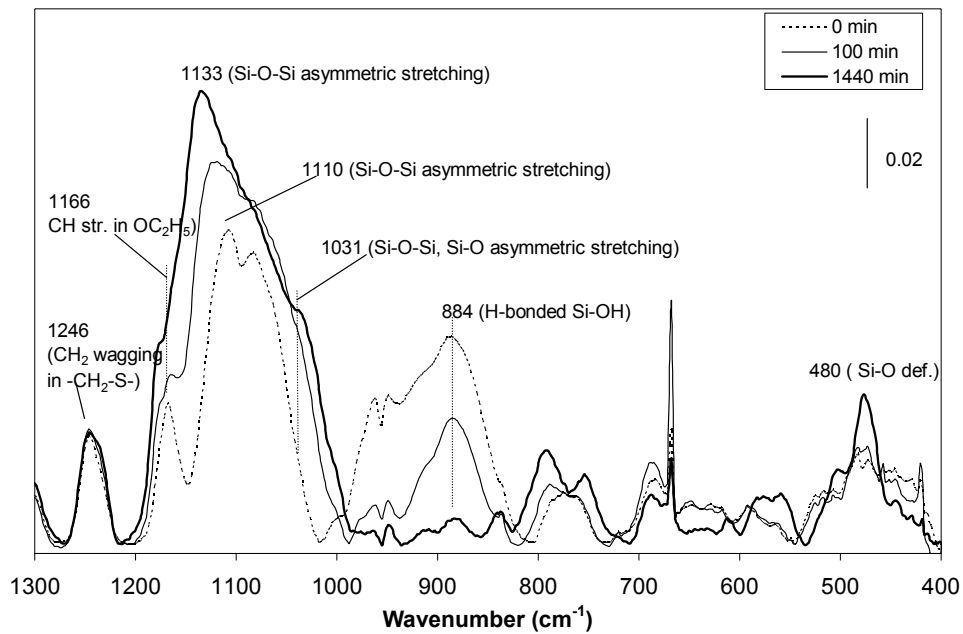
(a) FTIR-RA results

Once the silane solutions became “workable”, i.e., 2 days of aging for the bis-sulfur silane solution and 1 day for the bis-amino silane solution, the solid silane films were deposited on AA 2024-T3 substrate from these solutions. Further structural changes in both silane films upon curing at 100°C were monitored using FTIR-RA and EIS.

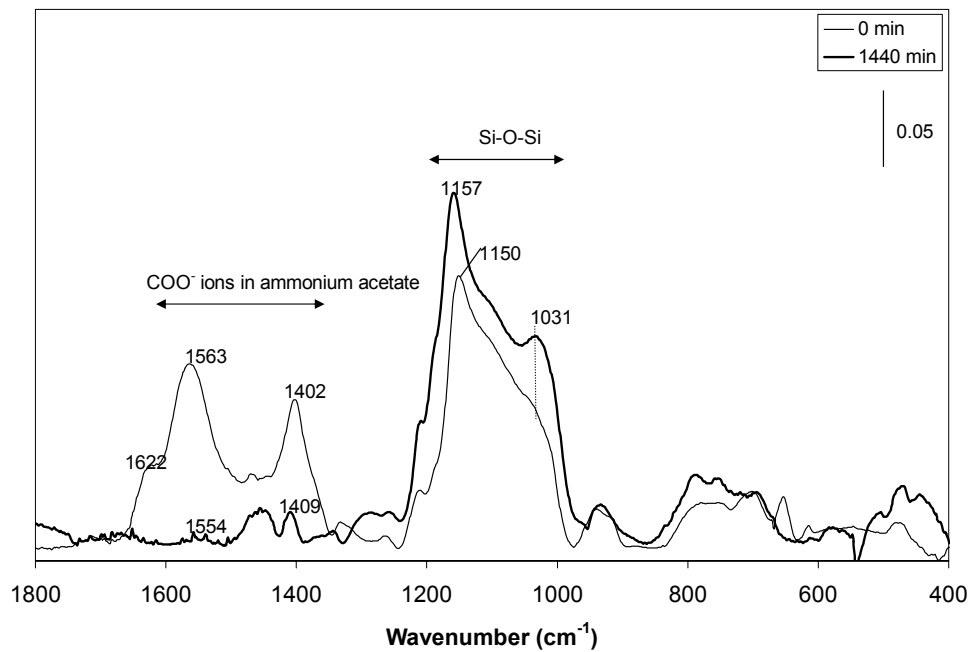
The FTIR-RA spectra of the bis-sulfur and the bis-amino silane films after curing at 100°C for different times are shown in Figures 4.4(a) and (b), respectively. The band assignments are also shown in the figures. As is seen in Figure 4.4(a), the bands centered at 1100 cm^{-1} due to SiOSi become more intensive as the curing time increases. The whole region becomes broader as compared to that without curing. In addition, the major band for SiOSi has shifted to higher frequencies from 1110 cm^{-1} at 0 min to 1133 cm^{-1} at

1440 min (24 hr). All of these changes indicate that the bis-sulfur silane film has experienced an extensive crosslinking forming a siloxane network during the curing period. Besides, it is also noticed that the band at 885cm^{-1} due to hydrogen-bonded SiOH decreases in intensity with curing time, confirming that the siloxanes have formed via the consumption of the silanols. It should be noted that, although some amount of silanols are expected to generate in the same curing process, the rate of condensation seems much quicker than that of hydrolysis. In other words, condensation rather hydrolysis dominates the whole curing process. This is reflected by a continuous decrease in the intensity of SiOH band at 886 cm^{-1} in the curing process, as shown in Figure 4.4 (a).

The FTIR-RA spectra of the bis-amino silane film on AA 2024-T3 after curing at 100°C for various times are shown in Figure 4.3(b). The bands at 1622 cm^{-1} , 1563 cm^{-1} , and 1402 cm^{-1} at 0 min (not cured) are due to the carboxylate ions (COO^-) in the ammonium acetates formed between the secondary amines and the acetic acid [88]. The possible form of the acetates is $-\text{NH}_2^+\text{COO}^-$. After curing at 100°C for 120 min (not shown), these acetates bands have almost diminished, indicating that the acetates have been removed (possibly by decomposition) from the film. The SiOSi band at 1150 cm^{-1} before curing has shifted to 1157 cm^{-1} after curing for 1440 min, along with the increase in the intensity. This means that a further crosslinking has occurred, resulting in a denser siloxane network. The band near 880 cm^{-1} due to hydrogen-bonded SiOH, is not observed for the bis-amino silane even before curing (0 min). This implies that the SiOH groups in the bis-amino silane film have already been consumed even before curing. Further curing only results in maturing of the siloxane network.



(a)



(b)

Figure 4.3. FTIR-RA spectra of bis-type silane films on AA 2024-T3 after curing at 100°C in air for various times; (a) bis-sulfur silane, and (b) bis-amino silane

It should be pointed out that although FTIR-RA is sensitive enough to identify chemical reactions (i.e., siloxane formation here) in the silane films, it is still hard for IR to differentiate the locations where these reactions may actually occur. EIS, on the other hand, CAN provide such information. Therefore, on combining the IR and EIS results together, a clearer picture of the overall progress in the silane systems will be obtained.

(b) EIS results

In summarizing the above IR results, it should be kept in mind that the major event occurring in the curing is crosslinking. Thus, the changes in the following EIS plots should be intimately associated with the crosslinking in both silane systems.

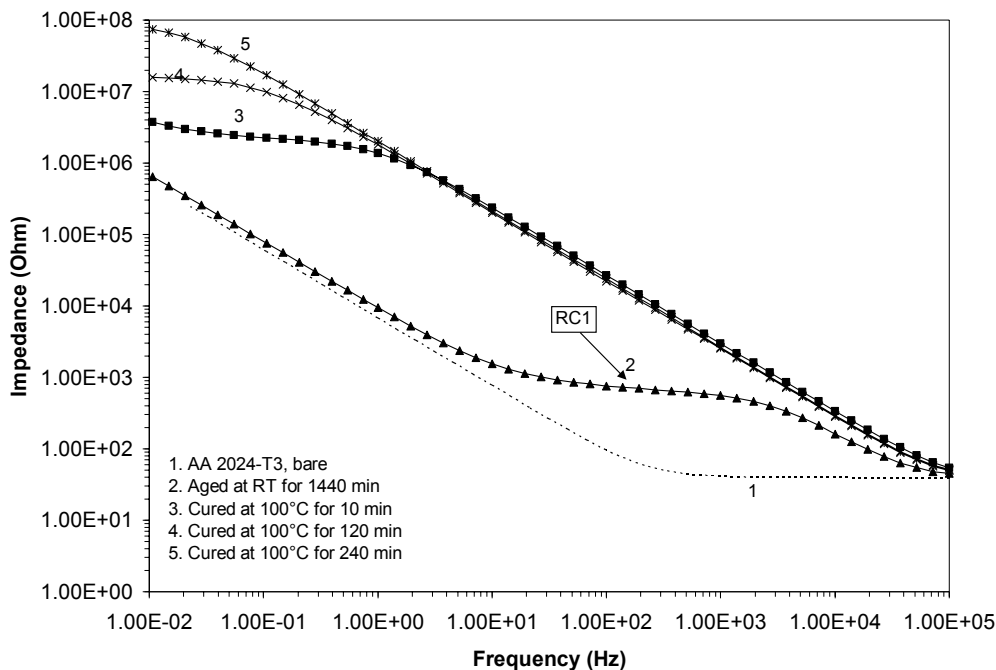
A simplified structure of a silane-coated AA 2024-T3 system is a silane film covering the Al oxide layer on the alloy substrate, so there are two distinct dielectric layers. It should be noted that the EIS measurements in this work were carried out in a non-corrosive electrolyte, i.e., a neutral 0.5 M K_2SO_4 aqueous solution, in which the Al oxide layer is stable due to the absence of detrimental species such as chloride ions. In a chloride-containing electrolyte, the Al oxide layer would be destabilized by chloride ions. This leads to corrosion of the Al matrix underneath. In this case, the information on the corrosion of the alloy should be reflected in the corresponding EIS models. Obviously, this would complicate the interpretation work.

Figures 4.4(a) and (b) show the EIS plots for the bis-sulfur silane coated AA 2024-T3 after curing at 100°C for various times. The EIS data are presented in the form of Bode plots, i.e., the impedance plot in Figure 6(a) and the phase angle plot in Figure

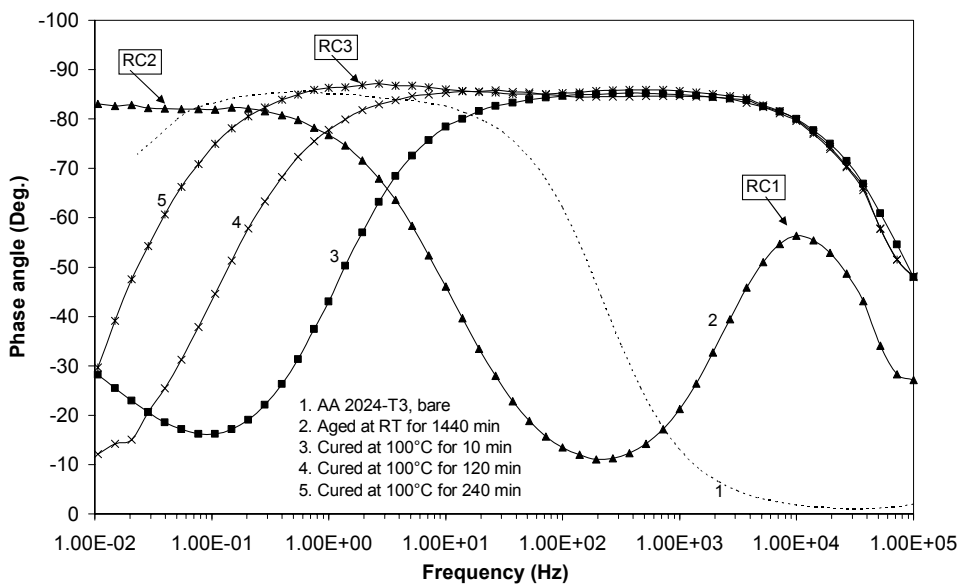
6(b). The curves for the bare AA 2024-T3 (untreated) are also shown in the figures as references. To clarify the structural changes in the system, the one simply aged for 1440 min (24 hr) under ambient conditions is also presented.

It is seen in Figure 4.4 that the EIS plots for the bare AA 2024-T3 (curve 1) show one time constant, with the peak maximum centered at < 1 Hz in the phase angle plot. This time constant obviously corresponds to the Al oxide layer on the bare AA 2024-T3.

After 1440 min of aging at the room temperature (curve 2), a new time constant, indicated as RC1, has been formed in the high-frequency range between 10^2 Hz to 10^4 Hz. The appearance of RC1 is due to the crosslinking in the film upon aging, as confirmed by our previous IR analysis in Chapter 3. Hence, the 1440 min-aged bis-sulfur silane film is expected to be denser and hydrophobic. The other time constant (RC2) located at lower frequencies (< 1 Hz) still correspond to the Al oxide layer. As compared to its original position (curve 1), RC2 has shifted nearly 1 order of magnitude to low frequencies. This shift is reasonable and can be explained as follows. Upon aging, the silanols in the interfacial region are likely to condense with themselves and with Al hydroxyls of the Al oxide layer, forming SiOSi and SiOAl units. As a result, the surface oxide layer becomes denser by reducing the pores. This is reflected by the shift of RC2 to lower frequencies on curve 2 in Figure 4.4.



(a)



(b)

Figure 4.4. Bode plots of bis-sulfur silane coated AA 2024-T3 after curing at 100°C in air for various times, measured in a neutral 0.5 M K_2SO_4 solution; (a) impedance plot, and (b) phase angle plot

After curing at 100°C for 10 min (curve 3 in Figures 4.4(a) and (b)), the impedance at 0.02 Hz increases sharply, as compared with that for the uncured one. RC1 in Figure 4.4(b) has been broadened, the peak maximum of which has shifted from 10^4 Hz to 10^3 Hz. This is caused by the further crosslinking in the silane film. A tail shown in the low frequency range, i.e. < 0.1 Hz is a part of RC2, since RC2 has further shifted to lower frequencies for the reason mentioned above. The major part of RC2 could be located at frequencies < 0.01 Hz, which is, however, beyond the measuring range (i.e., 0.01 Hz to 10^5 Hz in this work) and cannot be seen in Figure 4.4.

In the remainder of the curing period (curves 4 and 5), the low-frequency impedance at 0.02 Hz increases continuously in Figure 4.4(a), along with the further broadening of RC1 in Figure 4.4(b). After 120 min (curve 4 in Figure 4.4(b)), an additional time constant indicated as RC3 has become noticeable in the frequency region around 1 Hz to 10 Hz. The appearance of RC3 is thought to be due to the formation of a reaction product between silane and oxide (called “interfacial layer” hereon) [24]. This interfacial layer is the “unknown phase” discussed in Chapter 3. In considering the possible condensations in the interfacial region, this interfacial layer is plausibly comprised of large amounts of siloxanes (SiOSi) and Al-siloxanes (AlOSi). The former is formed via the condensation among silanols and the latter is produced via the condensation between silanols and Al hydroxyls. It is also noted that RC3 is more noticeable in the phase angle plot (Figure 4.4(b) than in the impedance plot (Figure 4.4(a)), showing that the former is more sensitive to the subtle changes in the systems than the latter. Thus, the phase angle plot is more valuable when tracking down different structures in the systems.

Based on the above results, the changes in the structures of the bis-sulfur silane treated AA 2024-T3 system during the curing is illustrated schematically in Figures 4.5(a) and (b). Before curing (Figure 4.5(a)), the system has a porous outermost silane film covering the Al oxide layer. This porous structure is mainly due to the lack of crosslinking, which could not offer good corrosion protection on AA 2024-T3, as demonstrated in Chapter 3. This is understandable, as such porous structure is highly permeable to water and the dissolved detrimental species such as Cl^- ions. Corrosion occurs once sufficient amount of water/ Cl^- ions reaches the metal surface. When curing the film, SiOC_2H_5 groups remained in the film undergo hydrolysis and condensation. This would result in a much denser film as well as an interfacial layer, as shown in Figure 4.5(b). Since the interfacial layer directly anchors to the substrate, thus it is expected that this interfacial layer rather than the outermost silane film may be a major contributor in the corrosion protection of AA 2024-T3.

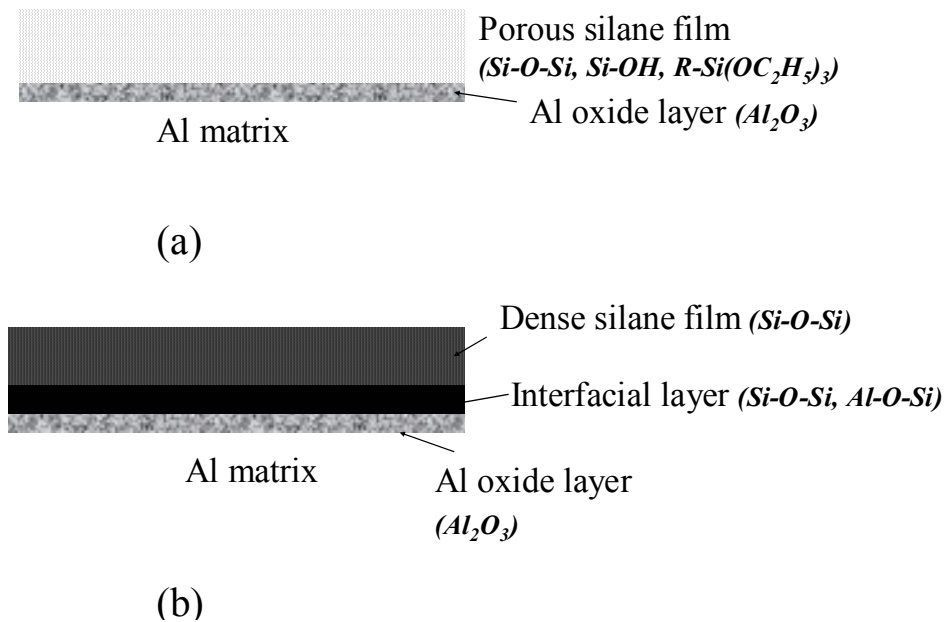
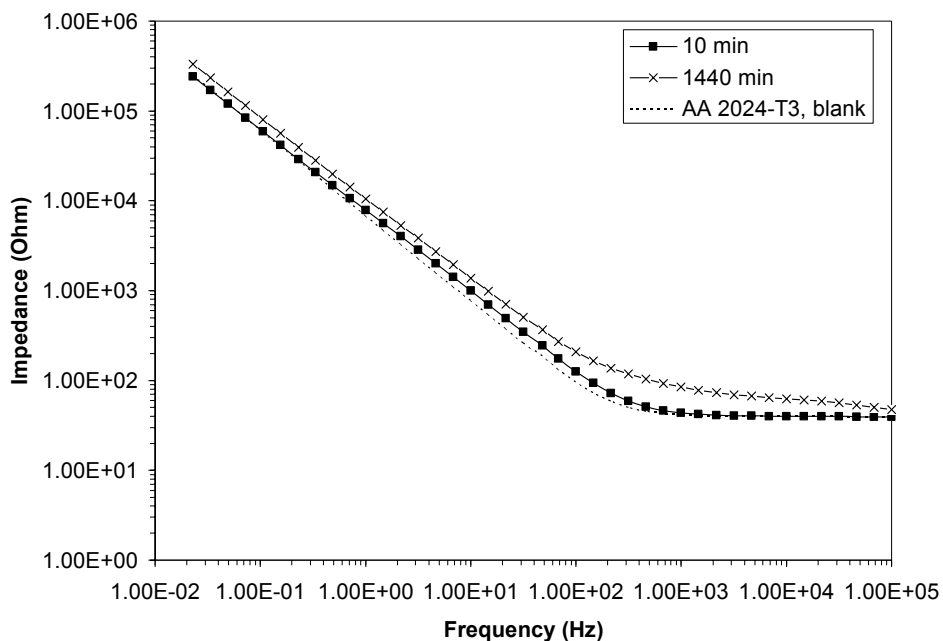


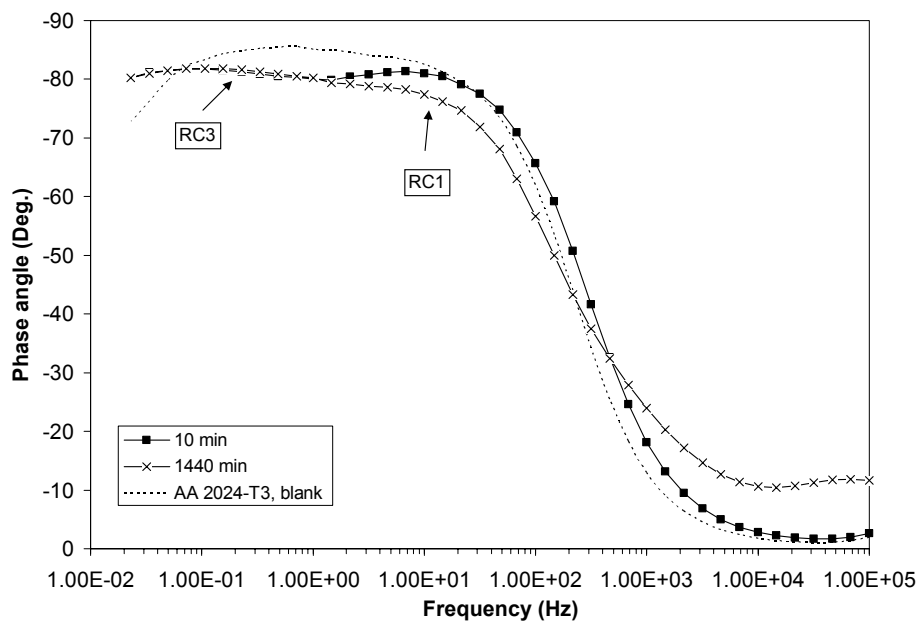
Figure 4.5. Schematic of structural evolution of bis-sulfur silane system upon curing; (a) before curing, and (b) after curing

As might be noted, a similar EIS behavior was also observed for the bis-sulfur silane coated AA 2024-T3 system during immersion in aqueous media in Chapter 3. The condensation rate in water is much slower than that in the curing process at 100°C, but the changes in RC3 are very obvious and can be easily identified (Figure 3.3).

Figures 4.6(a) and (b) compare the Bode plots of the bis-amino coated AA 2024-T3 after curing at 100°C for different times. In general, no significant changes are seen for the bis-amino coated AA 2024-T3 system, as compared with the bis-sulfur silane system. In Figure 4.6(a), the impedance of the bis-amino system after 10 min of curing is only a slightly higher than that of the bare AA 2024-T3; and the one after 1440 min of curing also only shows a little increase. In Figure 4.6(b), two time constants are differentiated. By referring to the analysis for the bis-sulfur silane system above, the one centered at 10 Hz (RC1) is due to the crosslinked bis-amino silane film; and the other at low frequencies is very likely to correspond to the bis-amino interfacial layer (RC3). The time constant for the Al oxide layer (RC2) is not seen, due to its quick shift to lower frequencies beyond the frequency range of interest. Compared with the bis-sulfur silane system, we can conclude here that the crosslinking occurs more readily and much faster in the bis-amino silane system. On the other hand, it might be noticed that the low-frequency impedance of the bis-sulfur silane system at 0.02 Hz is much higher than that of the bis-amino silane system. A detailed discussion on this difference will be presented in Section 4.2.2.



(a)



(b)

Figure 4.6. Bode plots of bis-amino silane coated AA 2024-T3 after curing at 100°C in air for various times, measured in 0.5 M K_2SO_4 solution (pH 6.5); (a) impedance plot, and (b) phase angle plot

4.2.1.3. Formation of new phase in bis-amino silane films in the ambient aging process

In practice, silane-coated metals are usually stored in the ambient for some time before application or testing. Thus, it is also important to understand the possible structural changes during the storage. The bis-sulfur silane film is normally stable. Only a slight crosslinking is observed if the film has not been fully cured before storing. When storing a fully crosslinked bis-amino silane film under the ambient conditions for some period, a new phase had formed in the bis-amino silane film, which was detected by both FTIR-RA and EIS techniques. The results are discussed here.

(a) FTIR-RA results

Figure 4.7 shows the IR spectra of the bis-amino silane film deposited on AA 2024-T3 before and after aging in the ambient conditions. The bis-amino silane film on AA 2024-T3 was cured at 100°C for 1440 min (24 hr) before aging. It is seen in Figure 4.7 that after aging for 8 days (spectrum b), the new bands at 1630 cm⁻¹ and 1591 cm⁻¹, and 1344 cm⁻¹ have emerged. In the meanwhile, the region between 3000 cm⁻¹ to 2000 cm⁻¹ has become broader. All of these changes indicate that there is a new phase formed in the bis-amino silane film. The band assignments are shown in the figure [91-94]. Battjes et al. [91] reported that the IR absorptions near 1630 cm⁻¹ and 1591 cm⁻¹ were associated with the carbonylate ions of carbamate salts of the amines due to the reaction between carbon dioxide and the amines. Boerio and Williams found [92] that bicarbonates could form in the γ -APS film during aging in the atmosphere. The weak

band at 1344 cm^{-1} appeared after 8 days of aging can be attributed to the bicarbonates. The broadness of the region between 3000 cm^{-1} to 2000 cm^{-1} is also believed to be associated with the salts of amines [94].

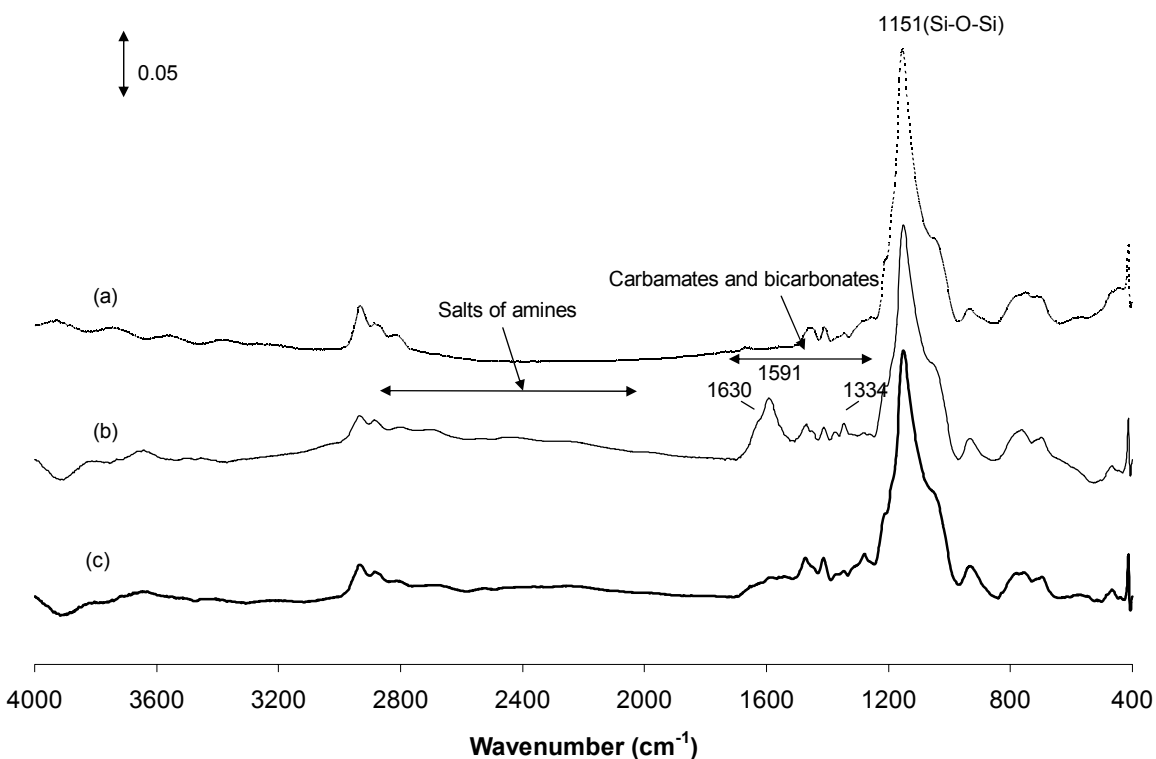


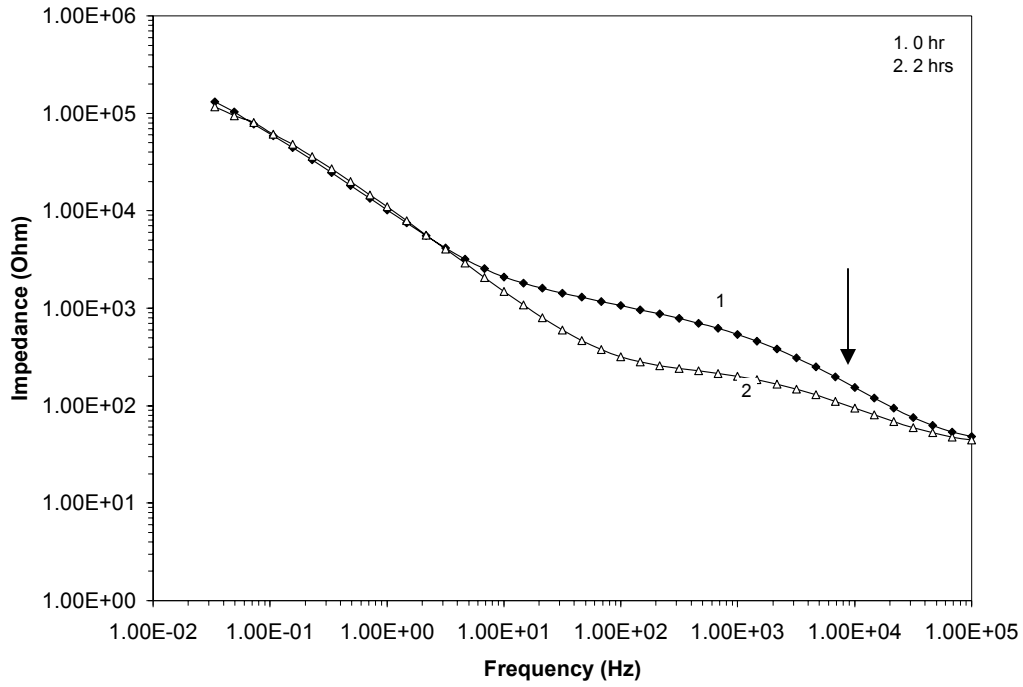
Figure 4.7. FTIR-RA spectra of bis-amino silane film on AA 2024-T3; (a) cured at 100°C for 24 hrs, before aging, (b) aged in air for 8 days, and (c) the sample (b) after immersing in water for 24 hrs

When immersing the aged bis-amino silane-coated AA 2024-T3 sample into water for 24 hrs, these new bands due to the carbamates and/or bicarbonates diminished gradually (spectrum c in Figure 4.7). This suggests that this new-formed phase during the ambient aging is water-soluble.

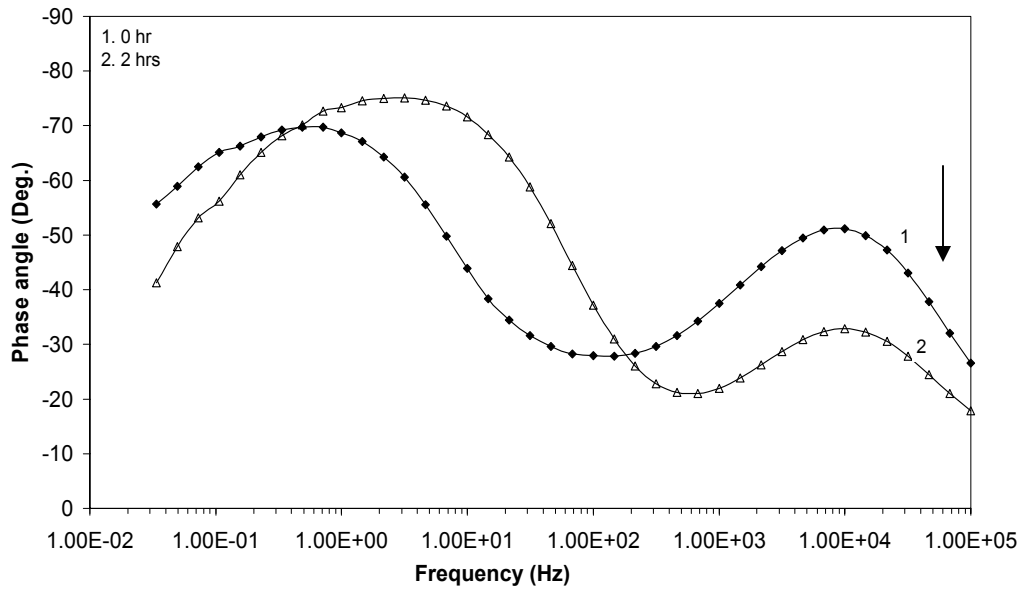
(b) EIS results

EIS was also used to monitor the similar process. The bis-amino silane coated AA 2024-T3 panel was cured at 100°C for 1440 min and then aged in the ambient conditions for 12 days before the EIS measurements in the 0.5M K₂SO₄ solution. As is shown in Figure 4.8, a new time constant is seen at high frequencies between 10² Hz and 10⁵ Hz after 12-day aging. The appearance of this time constant corresponds to the new phase discussed above. As the immersion continued in the 0.5 M K₂SO₄ aqueous solution for 2 hrs, the time constant reduced significantly (curve 2). The corresponding peak minimum for the time constant decreased from about -50° to -30°, as shown in Figure 4.8(b). This again confirms that the new phase is water-soluble, and gradually dissolves in the 0.5 M K₂SO₄ solution. It is also noticed that the total impedance of the system is not affected.

Combining the IR and EIS results, we thus conclude that this new phase is likely to be carbamates and/or bicarbonates due to the reaction between the secondary amines (-NH-) and the carbon dioxide in the presence of moisture under ambient conditions. The so-formed new phase is water-soluble. The EIS results also showed that the formation and the following dissolution of the new phase have little influence on the total impedance of the system. This implies that the new phase does not affect the film performance afterwards.



(a)



(b)

Figure 4.8. Bode plots of 12-day aged bis-amino silane treated AA 2024-T3, after immersed in 0.5 M K_2SO_4 solution for 2 hrs; (a) impedance plot, and (b) phase angle plot

4.2.2. Comparison of bis-sulfur and bis-amino silane treated AA 2024-T3 systems

Figure 4.9 compares the IR spectra of bis-sulfur and bis-amino silane films deposited on AA 2024-T3. The samples were cured at 100°C for 24 hrs to make sure that both systems have been extensively crosslinked. By comparing the bands in the SiOSi regions between 1000 cm^{-1} to 1200 cm^{-1} in both IR spectra, some differences are clearly seen: (1) the most intensive SiOSi band in the bis-amino silane system is at 1159 cm^{-1} , whereas that in the bis-sulfur silane system is at 1133 cm^{-1} ; (2) another SiOSi band at 1031 cm^{-1} is observed for both silane systems, but that for the bis-amino silane system is much more pronounced. It should be noted that the SiOSi band at higher frequencies is due to the formation of cyclic siloxane units. This band usually shifts in the high frequency direction when the silane films are further crosslinked [95]. The appearance of the SiOSi band at 1031 cm^{-1} for both silane systems is indicative of the formation of the long SiOSi chains [95]. Since the 1031 cm^{-1} band in the bis-amino system is more noticeable than that in the bis-sulfur silane system, this may indicate that the structure of the bis-amino system could be dominated with longer siloxane chains as compared with the bis-sulfur silane system.

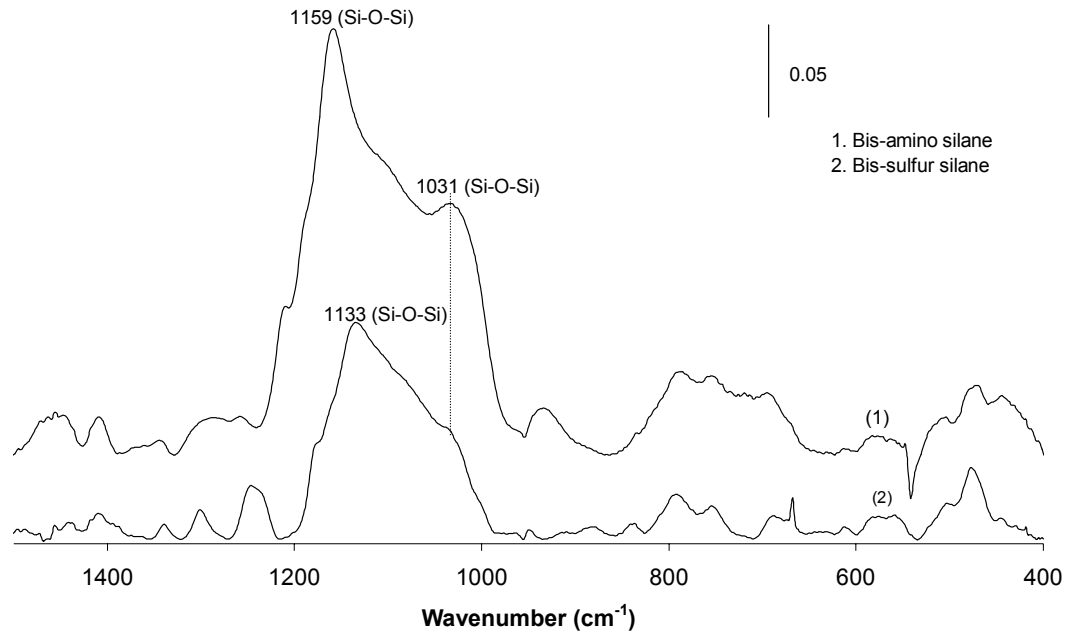
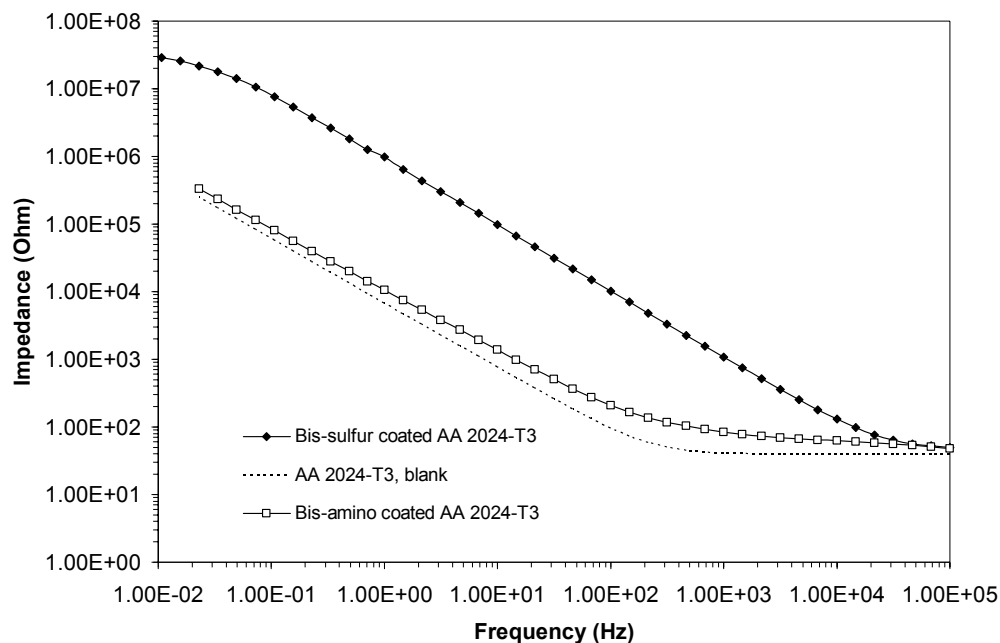
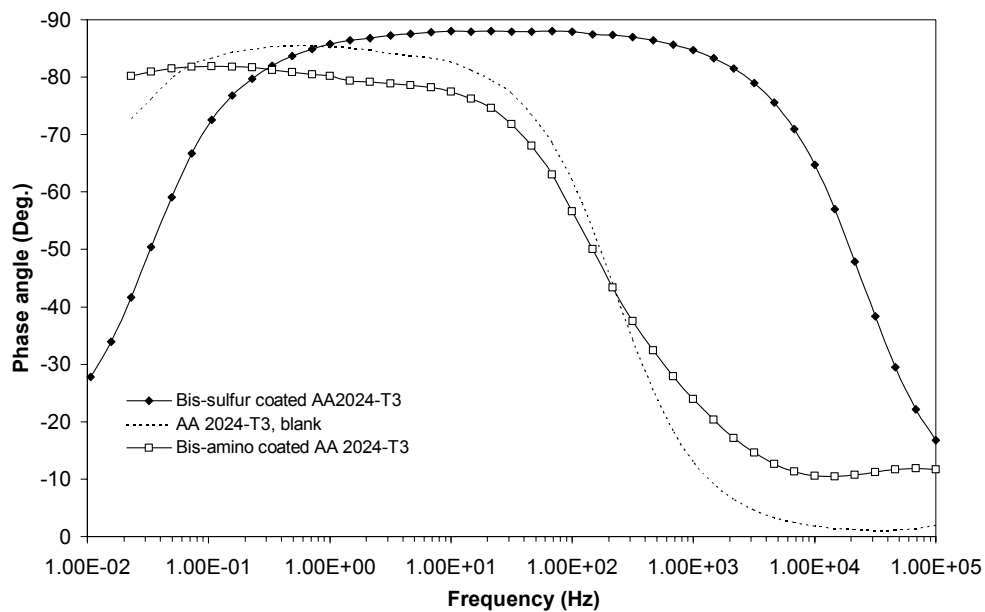


Figure 4.9. FTIR-RA spectra of bis-amino silane film (a), and bis-sulfur silane film (b) on AA 2024-T3 after curing at 100°C for 24 hrs

The Bode plots of the above bis-sulfur and bis-amino silane coated AA 2024-T3 are shown in Figures 4.10(a) and (b), along with the bare AA 2024-T3 as a reference. From the figure, it is clearly seen that the 0.02 Hz-impedance of the bis-sulfur silane coated AA 2024-T3 is much higher than those of the bis-amino silane coated and the untreated (Figure 4.10(a)). The time constant of the bis-sulfur silane system is also broader than the other two (Figure 4.10(b)). In Figure 4.10(a), the impedance of the bis-sulfur silane system approaches to $2 \times 10^7 \Omega$ at 0.02 Hz; while that of the bis-amino silane system only reaches $10^6 \Omega$ at 0.02 Hz, only showing a slight increase as compared with that of the bare AA 2024-T3. Since the thicknesses of both silane films are similar (350 nm for the bis-sulfur silane and 450 for the bis-amino silane [28]), the thickness effect is negligible. Therefore, some other factors responsible for this difference should be explored.



(a)



(b)

Figure 4.10. Bode plots of bis-sulfur silane and bis-amino silane coated AA 2024-T3, measured in 0.5 M K_2SO_4 (pH 6.5); (a) impedance plot, and (b) phase angle plot

A plausible hypothesis concerning the above difference is as follows. The bis-amino silane film deposited on AA 2024-T3 contains a considerable amount of protonated secondary amino groups ($-\text{NH}_2^+$); while the bis-sulfur silane film obtained from a solution at its natural pH (6.5) is expected to be neutral. In the EIS measurement, the positively charged bis-amino silane film would promote the diffusion of SO_4^{2-} anions into the film by electrostatic attraction. As a result, the conductivity of the whole system would increase. To further verify this hypothesis, Energy-Dispersive X-ray Spectroscopy (EDX) was performed here. Table 4.2 shows the EDX results for a fully cured ($100^\circ\text{C}/24\text{hr}$) bis-amino silane film on AA 2024-T3 before and after immersing in a K_2SO_4 solution for 40 min and 20 days. For comparison, the composition of bare AA 2024-T3 alloy is also listed in Table 4.2 [96]. It is seen that the signals for sulfur (S) and oxygen (O) have increased after immersion. Since both bis-amino silane and AA 2024-T3 alloy do not contain the element S (seen in Table 4.2), the detected S signal is solely from SO_4^{2-} ions. In addition, a slight increase in the percentage of O compared to that without immersion might also be from the SO_4^{2-} ions. The weight percentage of S increases with immersion time. After 40 min of immersion (i.e., a normal duration for an EIS measurement), 0.63% of S was detected. When continuing the immersion up to 20 days, the percentage of S has increased to 1.08%. This result strongly supports the hypothesis presented above. Similarly, the bis-amino film was also found to contain a detectable amount of Cl^- ions after immersed in a neutral 0.6 M NaCl solution for 15 days, while the bis-sulfur system did not. The corresponding EDX results are compared in Table 4.3. This, again, confirms that the positively charged bis-amino silane system attracts anions during immersion. Such behavior, however, is not expected in the neutral

bis-sulfur silane system. Furthermore, the result shown in Table 4.2 also implies that the inferior corrosion behavior of the bis-amino silane is related to its nature of attracting detrimental anions.

Table 4.2. EDX results (in wt.%) for bis-amino silane film on AA 2024-T3 before and after immersed in 0.5M K₂SO₄

| Element | Before immersion | Immersion for 40 min | Immersion for 20 days | AA 2024-T3 [96] |
|----------------|-----------------------------|---------------------------------|----------------------------------|----------------------------|
| C | 21.67 | 17.32 | 17.38 | -- |
| O | 9.01 | 13.12 | 14.51 | -- |
| Mg | 2.19 | 1.12 | 0.79 | 1.2-1.8 |
| Al | 56.78 | 56.29 | 54.48 | Balance |
| Si | 7.53 | 7.75 | 8.74 | 0.5 |
| S | -- | 0.63 | 1.08 | -- |
| Mn | 0.26 | 0.58 | 0.36 | 0.3-0.9 |
| Cu | 3.08 | 3.19 | 2.66 | 3.8-4.9 |

Table 4.3. EDX results (in wt.%) for bis-amino and bis-sulfur silane films on AA 2024-T3 after 15 days of immersion in a 0.6 M NaCl solution (pH 6.5)

| Element | Bis-amino silane | Bis-sulfur silane | AA 2024-T3 [96] |
|---------|------------------|-------------------|-----------------|
| O | 6.86 | 13.31 | -- |
| Mg | 1.41 | 1.00 | 1.2-1.8 |
| Al | 77.16 | 70.82 | Balance |
| Si | 5.45 | 8.48 | 0.5 |
| S | 3.90 | -- | -- |
| Cl | -- | 1.62 | -- |
| Cu | 5.06 | 4.77 | 3.8-4.9 |

4.3. Conclusions

1. In order to obtain a sufficient amount of silanols for the formation of a crosslinked siloxane network, a minimum hydrolysis time is required for both bis-sulfur and bis-amino silane water/alcohol solutions: at least 50 hrs for a 5% bis-sulfur silane solution at its natural pH (6.5); and 4 hrs for a 5% bis-amino silane solution at pH 7.5.

2. The bis-amino silane hydrolyzes much faster than bis-sulfur silane. This may be caused by the secondary amino groups contained in the bis-amino silane, which act as a catalyst for the silane hydrolysis.

3. A further crosslinking occurs in both silane treated AA 2024-T3 systems upon curing at 100°C in the ambient. As a result, the outmost silane film becomes dense; and an interfacial layer as a reaction product between the silanes and the Al oxide is formed. The interfacial layer is very likely comprised of SiOSi and SiOAl units, which may play a critical role in the corrosion protection process. The existence of the interfacial layer can be detected by EIS but not by IR.

4. The formation of carbamates and bicarbonates in a long-time aged bis-amino silane film was detected in both IR and EIS measurements. These compounds are formed by the reaction between the secondary amines, carbon dioxide and moisture absorbed from the atmosphere.

5. The low-frequency impedance of bis-sulfur silane treated AA 2024-T3 system is much higher than that of bis-amino system. This is because the positively charged bis-amino silane film promotes the diffusion of conducting SO_4^{2-} ions by electrostatic attraction during EIS measurements. The conductivity of the bis-amino silane in the K_2SO_4 solution is hence increased, as reflected by a low impedance value in EIS plots. In the neutral bis-sulfur silane system, on the contrary, such phenomenon is not expected.

Chapter 5. Surface Modification of Metals by Silanes¹

Abstract Two important effects, i.e., the effect of type of organic solvents and the effect of metal substrates, on bis-sulfur silane film structures were investigated using FTIR-RA. The results showed that: (a) The structure of the bis-sulfur silane film is affected by the solvent type. The silane hydrolysis in the bis-sulfur silane solution approaches to completion when dioxane rather than ethanol is used as the solvent. With more silanols generated in the solution, the dioxane-based film is characteristic of longer siloxane chains in comparison with the ethanol-based film. Nevertheless, the resulting corrosion performance of these two types of films is comparable. This indicates that complete silane hydrolysis is not require from a good corrosion protection perspective. (b) Metal substrates on which the bis-sulfur silane film deposited have a significant effect on the film structures. In addition, an interfacial layer at the silane/AA 2024-T3 interface was investigated using far-IR technique. This interfacial layer is thought to play a key role in the corrosion protection of AA 2024-T3 by silane films.

5.1. Introduction

In addition to the effects of processing parameters discussed earlier, some other effects are also of practical importance. Such effects are the effect of the type of organic solvents used in silane solutions and the effect of metal substrates. In this chapter, these

¹ The chapter is included in a paper which is to be published in the proceedings of ‘Adhesion Aspects of Polymeric Coatings’, held May 25-26, Newark, NJ, 2000, (in press), 2002

two effects on bis-sulfur silane film structures were studied using FTIR-RA. A 5% bis-sulfur silane solution was used here. In addition, an interfacial layer observed in the previous EIS studies (discussed in Chapters 3 and 4) was further studied using a far-IR technique.

5.2. Results and Discussion

5.2.1. Effect of organic solvents on the film structure of bis-sulfur silane on AA 2024-T3

It has been reported [3] that the hydrolysis of silanes in protic solvents, such as water and ethanol, approach equilibrium rather than completion, due to the competition between silane hydrolysis and alcoholysis. The hydrolysis process in non-protic solvents such as dioxane, on the contrary, tends to completion. In the case of the bis-sulfur silane, we also observed a similar phenomenon [24, 90]. In this work, one critical issue is whether or not the solvent type would further affect the corrosion performance of the resulting bis-sulfur silane films through influencing the hydrolysis process in the silane solution. To clarify this, FTIR-RA and salt immersion test were employed.

Two types of solvents studied here were ethanol and dioxane. The former is a commonly-used solvent for the bis-sulfur silane solution. Two kinds of bis-sulfur silane films were deposited on AA 2024-T3 from 5% ethanol-based and dioxane-based bis-sulfur silane solutions (aged for 8 days), followed by curing at 100°C for 10 min, to make the films sufficiently crosslinked. The FTIR-RA measurements were then conducted on

these two silane-coated AA 2024-T3 specimens, and the results are shown in Figure 5.1. The IR peak assignments are given in Table 5.1. In Figure 5.1, a broad band at around 3300 cm^{-1} appears for both silane films, indicating that there still exist a considerable amount of hydrogen-bonded SiOH groups in the films after curing at 100°C for 10 min [24]. Two peaks, 2974 cm^{-1} and 953 cm^{-1} , correspond to the unhydrolyzed ester groups ($-\text{SiOC}_2\text{H}_5$). One at 2974 cm^{-1} is due to the CH stretching vibration in the ester groups, and the other at 953 cm^{-1} is attributed to the SiO deformation bending mode in the ester groups. It is noted that for the ethanol-based bis-sulfur silane film, these two peaks are pronounced. In the case of the dioxane-based bis-sulfur silane film, however, the peak at 2974 cm^{-1} has totally disappeared and that at 953 cm^{-1} has diminished. This difference indicates that the ester groups have been converted completely to silanols in the dioxane-based solution but not in the ethanol-based solution. In other words, a complete hydrolysis of the bis-sulfur silane can be obtained using dioxane as a solvent instead of ethanol. As also shown in Figure 5.1, only one broad and strong band is seen for the ethanol-based silane film at around 1130 cm^{-1} , which corresponds to SiOSi bonds. In the case the dioxane-based film, two intensive peaks are observed at 1130 cm^{-1} and 1030 cm^{-1} for SiOSi bonds. As reported [88,89], the appearance of double peaks for SiOSi bonds is associated with long SiOSi chains in silane films. Obviously, a film structure with long SiOSi chains can be obtained from a completely-hydrolyzed silane solution where a large number of SiOH groups are available for crosslinking. These results allow the conclusion that the type of organic solvents used in the bis-sulfur silane solutions significantly affects the resulting film structures.

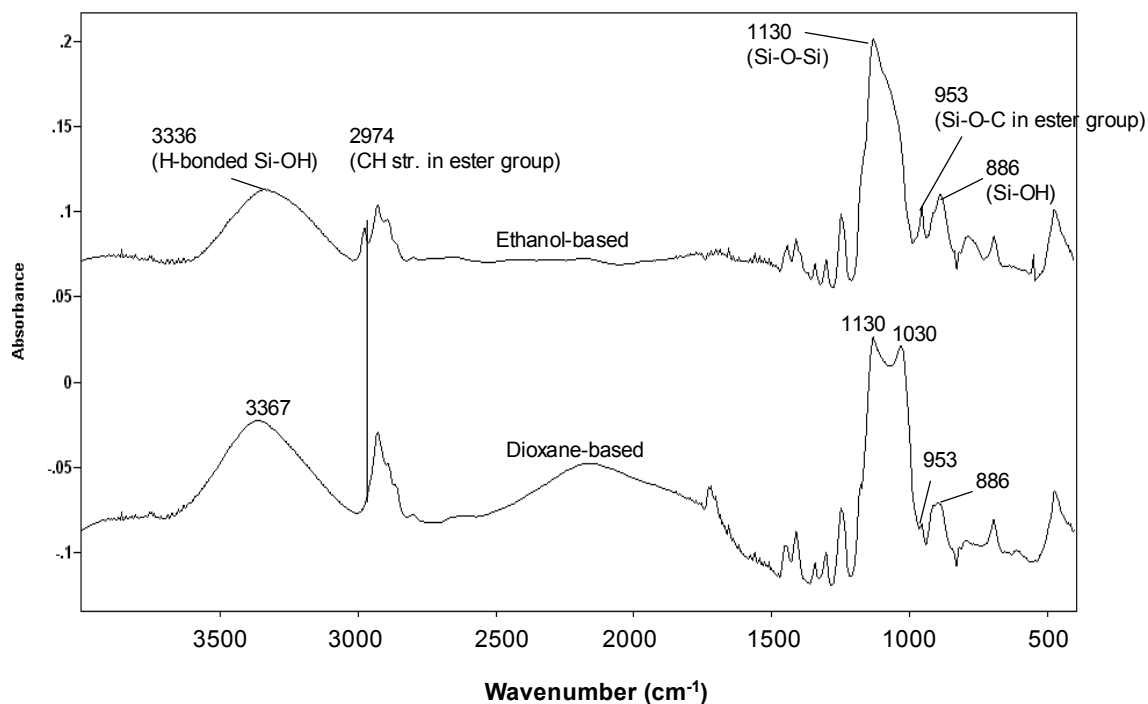


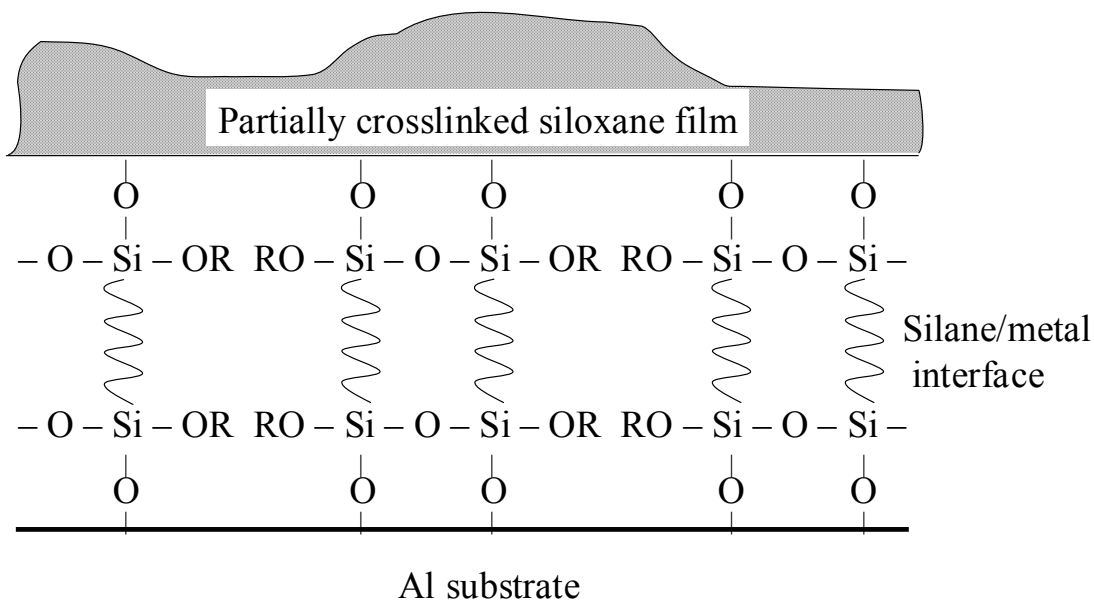
Figure 5.1. FTIR-RA spectra of ethanol- and dioxane-based bis-sulfur silane films on AA 2024-T3

Table 5.1 Assignments of absorption bands for bis-sulfur silane films [88,89]

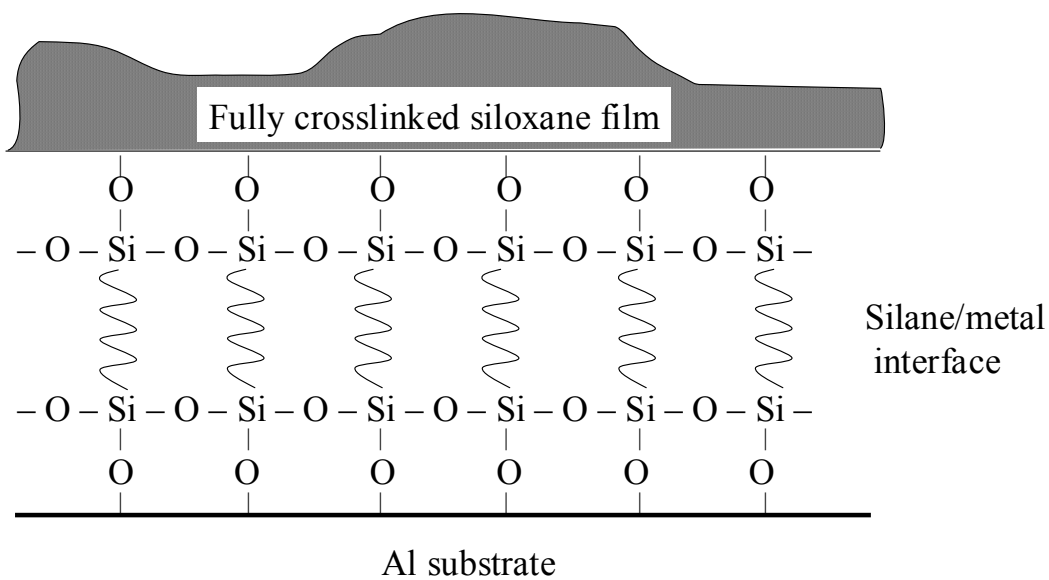
| Absorption band (cm^{-1}) | Assignment |
|--------------------------------------|---|
| 3336, 3367 | SiOH (H-bonded) |
| 2974, 2924, 2886 | SiOC ₂ H ₅ (C-H str.) |
| 1130, 1030 | SiOSi (Si-O asym. str.) |
| 953 | SiOC (Si-O asym. str.) |
| 886 | SiOH (H-bonded) |

Based upon the IR spectra discussed above, Figures 5.2(a) and (b) schematically illustrate the molecular structures of these two types of bis-sulfur silane films on AA 2024-T3. In the ethanol-based bis-sulfur silane film (Figure 5.2(a)), there still exist considerable amount of unhydrolyzed ester groups (OR). The generated SiOH groups in the interfacial region react with the Al oxide layer forming AlOSi bonds and condense within themselves forming SiOSi bonds. As a result, an extensively crosslinked interfacial layer is developed, the structure of which is mostly likely a three-dimensional AlOSi and SiOSi network.

Figure 5.2(b) gives a possible structure of the dioxane-based bis-sulfur silane film on Aa 2024-T3. Since the hydrolysis in the dioxane-based silane solution is completion, unhydrolyzed ester groups are not expected in the film. As a consequence of complete condensation of SiOH groups, more linear or longer SiOSi chains are formed in the film and in the interfacial layer. This is clearly reflected by the double peaks at 1130 cm^{-1} and at 1030 cm^{-1} . In contrast, such structure cannot be formed in the ethanol-based bis-sulfur silane film due to the lack of sufficient SiOH groups generated in the ethanol-based silane solution.



(a)



(b)

Figure 5.2. Schematic of the structures of two types of bis-sulfur silane films on AA 2024-T3; (a) ethanol-based, and (b) dioxane-based

Corrosion protection performance of these two types of bis-sulfur silane films on AA 2024-T3 was evaluated in a salt immersion test (i.e., 0.6 M NaCl, pH 6.5). After 7 days of immersion, no significant difference was seen between these two types of silane films, as shown in Figure 5.3. This indicates that different organic solvents do not have a noticeable effect on the corrosion performance, although they do affect the film structures by influencing the hydrolysis of the bis-sulfur silane in a different way. Based upon this result, an interesting conclusion can be drawn here that, a completely hydrolyzed silane solution is not necessary for optimum corrosion protection of AA 2024-T3, although a sufficiently-hydrolyzed solution is required to form a solid rather than oily film, as discussed in Chapter 4.

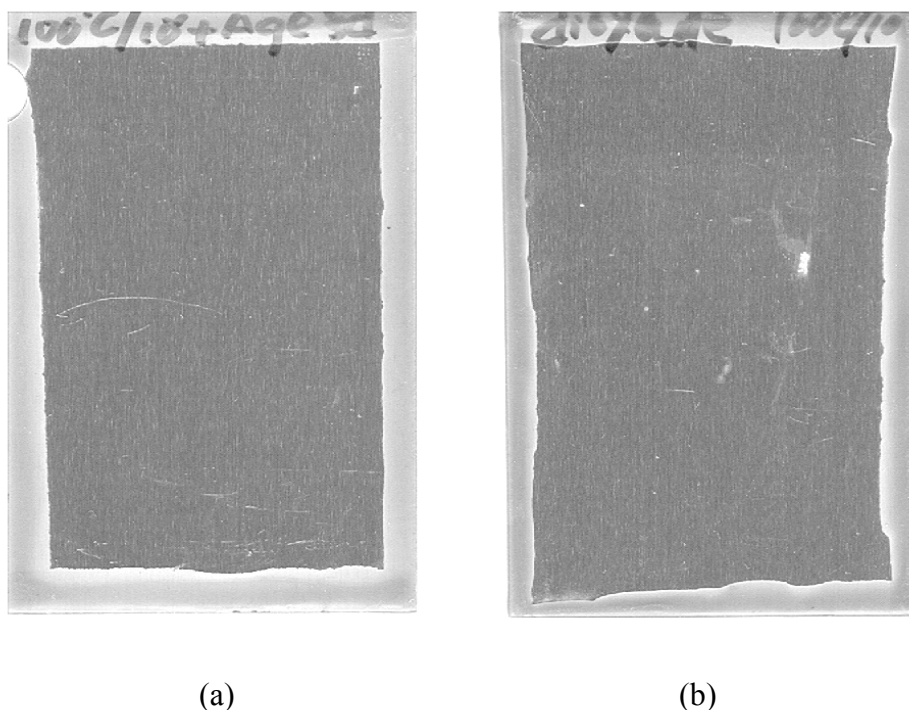


Figure 5.3. 7-day immersion test for AA 2024-T3 treated with different types of bis-sulfur silanes; (a) ethanol-based, and (b) dioxane-based

5.2.2. Effect of metal substrates on the film structure of bis-sulfur silane

In this section, we are attempting to understand this phenomenon by characterizing the bis-sulfur silane film on 4 different metal substrates. The metals selected for this study were, AZ 91B (Mg alloy), CRS (Fe alloy), AA 2024-T3 (Al alloy) and HDG (Zn-coated steel). The silane films were deposited on the metals from a 5% bis-sulfur silane water/ethanol solution, followed by curing at 100°C for 10 min before FTIR-RA measurements. The IR spectra are shown in Figure 5.4. The IR peak assignments are similar to those given in Table 5.1.

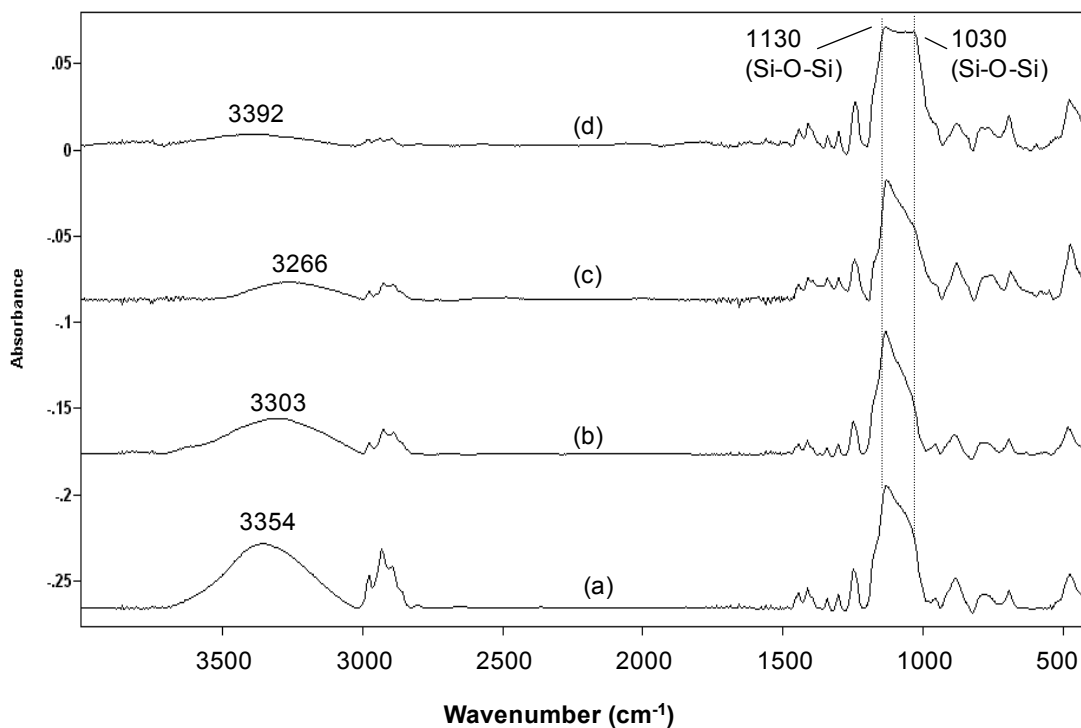


Figure 5.4. FTIR-RA spectra of ethanol-based bis-sulfur silane films on different metals; (a) HDG, (b) AA 2024-T3, (c) CRS, and (d) AZ 91B

In the SiOH region (3500-3000 cm^{-1} in Figure 5.4), a broad band is shown around 3300 cm^{-1} , indicating H-bonded SiOH groups still exist in the bis-sulfur silane films formed on all the alloys. The intensity of the band, however, depends strongly on the metal substrate. The intensity of SiOH groups on AZ 91B is the smallest, while that on HDG (Zn-coated steel) is the greatest. Obviously, the film on AZ 91B has almost been fully crosslinked after cured at 100°C for 10 min, as a broad band at 3392 cm^{-1} has diminished compared with the others. The film on HDG, on the contrary, is the least crosslinked because a considerably intensive SiOH band is still seen at 3350 cm^{-1} . Furthermore, one broad and intensive band around 1130 cm^{-1} due to SiOSi is observed for the silane films on CRS, AA 2024-T3 and HDG, whereas double peaks at 1030 cm^{-1} and at 1130 cm^{-1} are shown for the film on AZ 91B. As discussed earlier, the appearance of double peaks for SiOSi is associated with long chain of SiOSi bonds [88,89]. Apparently, the structure of the bis-sulfur silane film deposited on AZ 91B with longer or more linear SiOSi bonds in comparison with the others. A possible explanation is given as follows, by taking into account the highly basic nature of magnesium oxide (MgO) on AZ 91 B.

It is known that MgO is very basic, with an equilibrium pH of ~11 [97]. In other words, at $\text{pH} < 11$, MgO undergoes acidic dissolution according to the reaction,



As a result, magnesium ions (Mg^{2+}) and hydroxide ions (OH^-) are generated. In this case, when the AZ 91 B sample were dipped into the silane water/ethanol solution work, the

MgO layer was very likely to dissolve to a certain extent. A high pH region would be formed along the metal surface, as schematically illustrated in Figure 5.5(a). Both hydrolysis and condensation would be accelerated and eventually be completed in this high pH region by a base-catalyzed mechanism [3]. As a result, long SiOSi chains are formed in the silane films, similar to the case of the dioxane-based silane film. Grubb also observed a similar effect caused by alkali metal hydroxides [98]. He stated that the condensation of trimethylsilanol in methanol was catalyzed by alkali metal hydroxides. The rate of condensation was dependent on the concentration of hydroxide anion, but not on the alkali metal cation.

In contrast with MgO, the other oxides, i.e., Al₂O₃, ZnO, and FeO, are stable during a neutral pH range. Oxide dissolution is therefore not expected on the other metals. In the case of AA 2024-T3, for example, only Al hydroxyls (AlOH) are formed on the surface when in contact with water or moisture (Figure 5.5(b)). Subsequently, these AlOH groups would react with SiOH groups from the silane solution, forming Al-siloxane (AlOSi).

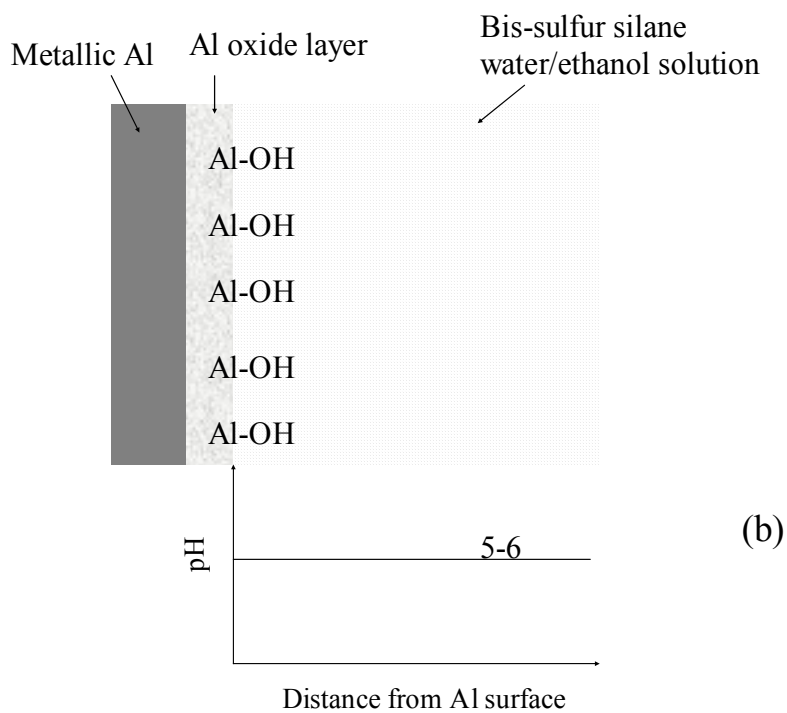
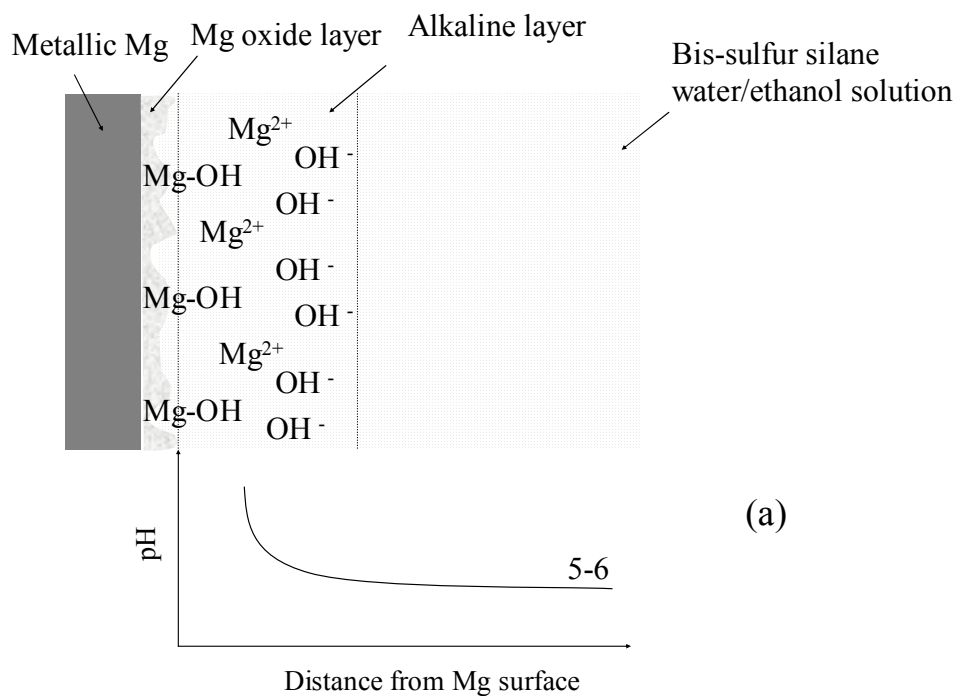
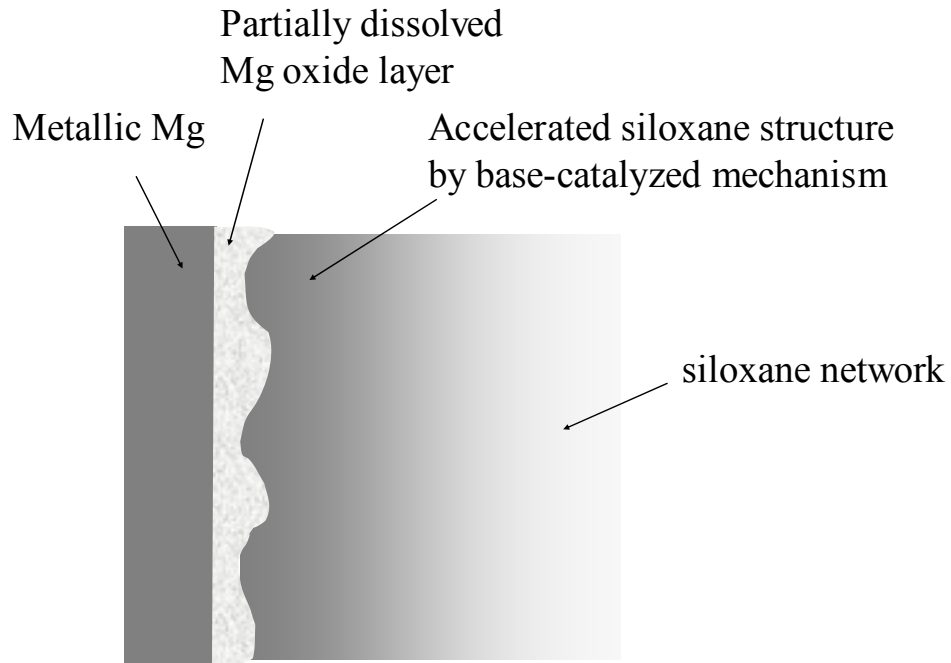


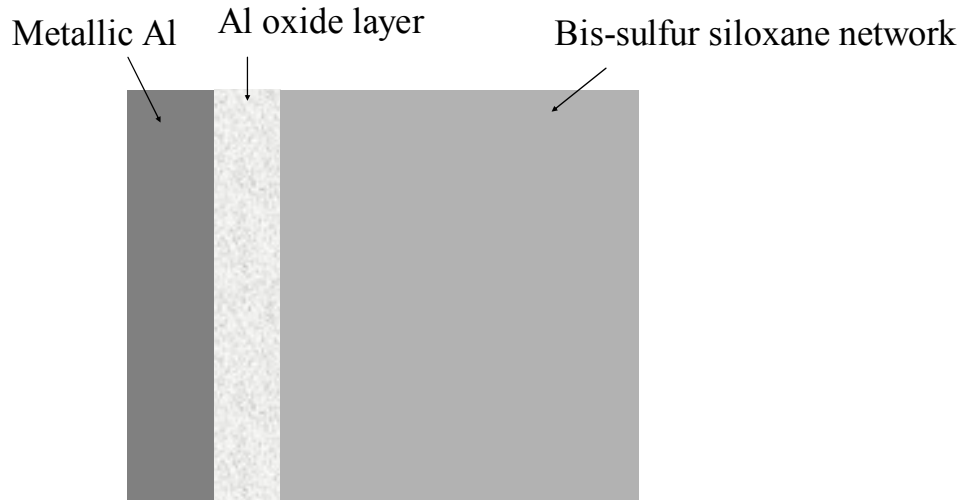
Figure 5.5. Schematic of the interfaces of metals and bis-sulfur silane water/ethanol solution; (a) Mg/silane-solution, and (b) Al/silane-solution

Figures 5.6(a) and (b) show schematically the interfacial structure of silane/metal systems, based upon the structural information extracted from the FTIR-RA spectra in Figure 5.4. Figure 5.6(a) illustrates that the interfacial structure of the bis-sulfur silane-treated Mg system. The basic MgO layer on the surface is likely to dissolve to a certain degree during immersion in the silane water/ethanol solution. This would result in a local alkalization adjacent the metal surface. Such local alkalization would further influence the film structure by accelerating silane hydrolysis and condensation. The SiOSi peak at 1030 cm^{-1} in Figure 5.4 clearly indicates this effect on the structure.

Figure 5.6(b) depicts the interfacial structure of the bis-sulfur silane-treated Al system. Unlike MgO, Al oxide is stable with the silane solution at a neutral pH. Therefore, the resulting silane film structure would not be affected. [1].



(a)



(b)

Figure 5.6 Schematic of the interfacial regions between metals and bis-sulfur silane film;
(a) Mg /silane film, and (b) Al/silane film

5.2.3 Observation of the interfacial layer of silane/metal systems

It was found that there existed three time constants in the EIS spectra for a bis-sulfur silane coated AA 2024-T3 system (Chapter 3). These three time constants were assigned to, from outside to inside, the outermost silane film, the interfacial layer, and the inner oxide layer. FTIR-RA measurements also showed some evidence which supported this suggestion. The formation of this interfacial layer is very much likely through the condensation reactions (1) between AlOH groups on the AA 2024-T3 surface and the SiOH groups in the silane film, and (2) among the SiOH groups in the interfacial region.

To further clarify this inorganic interfacial layer, the FTIR-RA spectra of two types of silane films on AA 2024-T3 were obtained in the far-IR range (2000 cm^{-1} to 200 cm^{-1}), as shown in Figure 5.7. The silane films were deposited on AA 2024-T3 from 5% silane solutions of bis-amino and bis-sulfur silanes, respectively. The silane films were cured at 100°C for 10 min before the IR measurements.

In Figure 5.7, two broad but weak bands in the region from 1200 cm^{-1} to 800 cm^{-1} are observed for the untreated AA 2024-T3, which are associated with the Al oxide layer on the surface. The AA 2024-T3 substrate coated with the bis-amino silane film shows a strong and broad band in the region from 1200 cm^{-1} to 1000 cm^{-1} , known as the SiOSi region, and a medium one around 500 cm^{-1} . The AA 2024-T3 sample coated with the bis-sulfur silane film exhibits similar results: one intensive peak at 1100 cm^{-1} indicating SiOSi bonds and one medium peak around 500 cm^{-1} . As no peaks were observed for the untreated AA 2024-T3 at 500 cm^{-1} , the peak around 500 cm^{-1} for both silane films on AA 2024-T3 is thus attributed to the silane films. Since few peaks are normally observed

for polymeric materials below 600 cm^{-1} , the peaks at around 500 cm^{-1} are probably due to an inorganic region formed in the silane film and/or at the silane/metal interface [99].

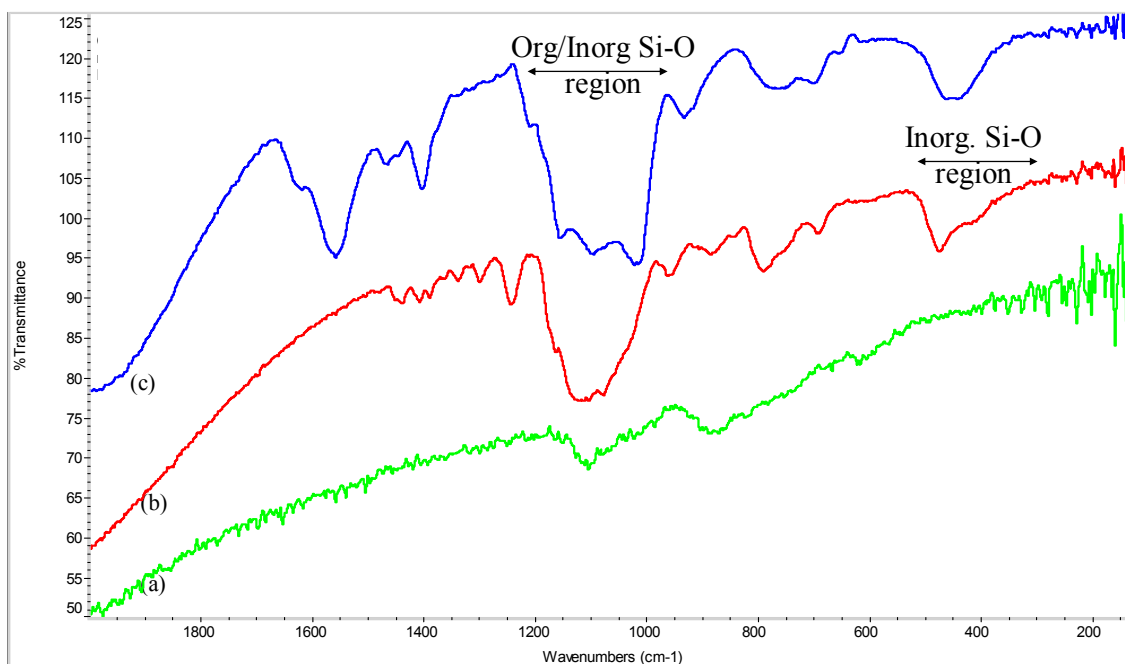


Figure 5.7. FTIR-RA spectra of untreated and silane-treated AA 2024-T3; (a) untreated, (b) treated with bis-sulfur silane (5%, natural pH 6.5), and (c) treated with bis-amino silane (5%, pH 7)

The authors in Ref. 33 assumed that some bands corresponding to metallo-siloxane (MeOSi) bonds also appeared in the region from 1200 cm^{-1} to 1000 cm^{-1} . It is, however, difficult to extract such information from Figure 5.7, as the $1200\text{-}1000\text{ cm}^{-1}$ region is dominated by several bands corresponding to SiOSi bonds. In order to extract the information about the interfacial region, one possible way is to deposit a thin silane film on AA 2024-T3. Since it is known that the silane film thickness is exclusively

determined by the corresponding solution concentration, the 5% bis-sulfur silane solution was further diluted down to different lower concentrations, i.e., 1%, 0.5% and 0.1%.

Figure 5.8 compares the FTIR-RA spectra of bis-sulfur silane films on AA 2024-T3 alloy corresponding to the concentrations of 5%, 1%, 0.5%, and 0.1%. It is seen that some weak peaks in the case of 5% can be distinguished clearly at low concentrations (1–0.1%). In the region from 550 cm^{-1} to 400 cm^{-1} , three medium peaks become distinct with decreasing concentrations. These peaks may be associated with the inorganic layer at the silane/metal interface. The peaks are attributed to SiO deformation bending mode for SiOSi in inorganic silica or silicates [99]. We thus tentatively postulate an interfacial structure of the organic/inorganic silicates of the type $[\text{Al}_2\text{O}_3 \bullet \text{XSiO}_2]$ where X is organic/inorganic substitutions such as $-(\text{CH}_2)_2-$ and $-\text{S}_4-$.

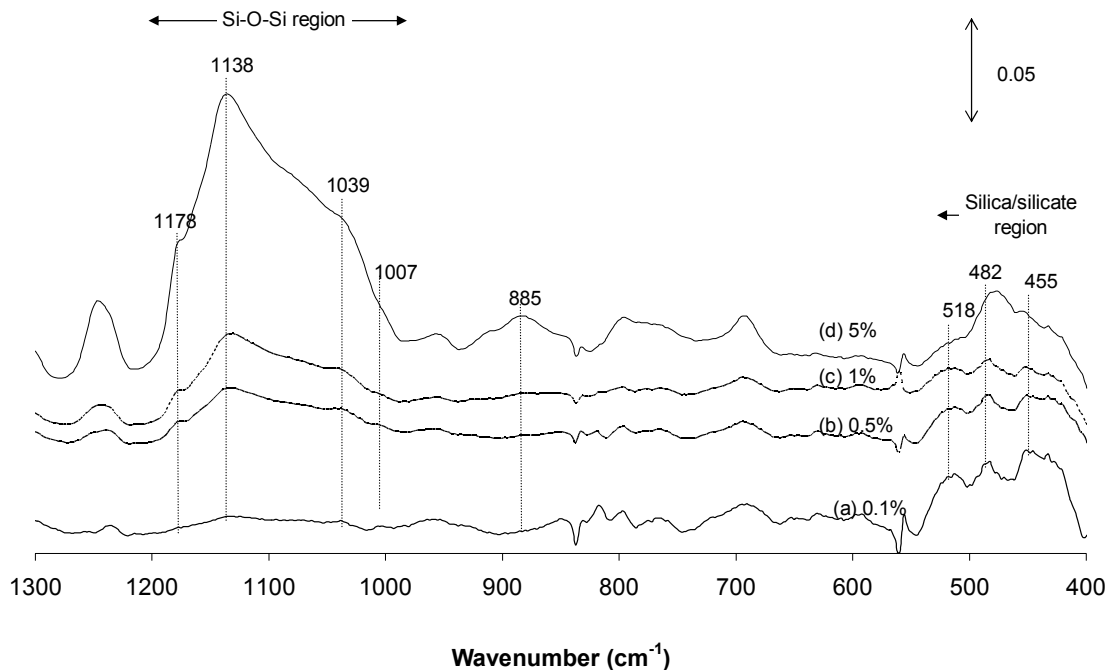


Figure 5.8. FTIR-RA spectra of bis-sulfur silane films on AA 2024-T3 from silane solutions with different concentrations; (a) 0.1%, (b) 0.5%, (c) 1%, and (d) 5%

5.3. Conclusions

1. The structure of the bis-sulfur silane films was influenced by the solvent type used in the bis-sulfur silane solution. The ethanol-based silane film shows only a partly crosslinked structure due to the incompleting hydrolysis in the ethanol-based solution, while that of dioxane-based film has a fully crosslinked structure as a result of the complete hydrolysis in the dioxane-based solution. The difference in anticorrosive behavior of these two types bis-sulfur silane films on AA 2024-T3, however, was insignificant. This indicates that a complete silane hydrolysis in the silane solution is not necessary from a good corrosion protection of metals perspective.

2. Metal substrates, on which the bis-sulfur silane film is deposited, have a significant effect on the film structure. In the case of the Mg alloy (AZ 91B), the basic MgO dissolves partly in the bis-sulfur silane water/alcohol solution. The as-generated OH^- ions increase the local pH close to the alloy surface. As a result, both hydrolysis and condensation of the bis-sulfur silane are accelerated in the high pH region by a base-catalyzed mechanism. The less basic oxide layers on the other alloys, i.e., AA 2024-T3, HDG, and CRS, only form hydroxide layers in the presence of water or moisture, which do not vary the pH nearby the alloy surfaces. Therefore, the bis-sulfur silane films formed on these alloys are similar in structure.

Chapter 6. Corrosion Inhibition of AA 2024-T3 by Bis-[triethoxysilylpropyl]tetrasulfide in Neutral Sodium Chloride Solution – Part 1: Early Corrosion of AA 2024-T3¹

Abstract Corrosion of 2024-T3 aluminum alloy (AA 2024-T3) was studied using Scanning Electron Microscopy (SEM) and Energy-Dispersive X-ray spectroscopy (EDX). The results showed that anodic S phase (Al_2CuMg) particles dealloyed Al and Mg during the 3.5 hrs of immersion in a neutral 0.6 M sodium chloride (NaCl) solution, with the dealloying of Mg being the most severe. Simultaneously, a heavy dissolution was also observed for the surrounding Al matrix of the S phase particles. This Al dissolution is likely to be caused by a local alkalization resulting from the coupled cathodic reaction (water and/or oxygen reduction). Such corrosion in AA 2024-T3, however, can be effectively inhibited after the treatment of bis-[3-(triethoxysilyl)propyl]tetrasulfide (bis-sulfur silane). The associated mechanistic studies on bis-sulfur silane treated AA 2024-T3 will be presented in the second part in Chapter 7.

6.1. Introduction

AA 2024-T3 is extensively used in aerospace industries due to its excellent mechanical properties. Such mechanical properties are achieved by the strengthening of the alloy matrix with a number of second-phase particles. Some particles, however, are

¹ The chapter has been accepted by Corrosion Science, 2002

not desirable from a corrosion prevention perspective. Anodic S phase particles (Al_2CuMg), for example, cause severe pitting of the alloy when exposed to a chloride-containing environment [59–62, 65]. Chromating processes, such as the Alodine[®] process, are therefore used as an anticorrosive surface treatment for AA 2024-T3.

Recently, the use of chromates has been heavily restricted by environmental legislations and regulations due to the high toxicity and carcinogenicity of hexavalent chromium ions (Cr(VI)). A need for an alternative anticorrosion surface treatment has thus evolved. Various inorganic and organic corrosion inhibitors have been proposed and studied. Among them, silane surface treatment is a promising alternative that has attracted a lot of attention from industries in the recent years. In general, this technology includes attractive benefits such as environmental compliance, economical application, and good corrosion inhibition as well as paint adhesion to a variety of metals.

Before extending the study of clarifying the roles of silanes playing in the corrosion protection of AA 2024-T3, the corrosion behavior of bare AA 2024-T3 during immersion in a neutral NaCl solution was studied, and the results are reported here. The second part of the report will be presented in Chapter 7, which involves the investigation of the anticorrosion mechanism of bis-sulfur silane-treated AA 2024-T3 system.

AA 2024-T3 panels were cut into coupons with dimensions of 2.5 cm × 2.5 cm, polished mechanically using SiC polishing papers with different grades, and finished with a 5- μm alumina paste. The polished mirror-like surfaces were then cleaned ultrasonically for 5 min in ethanol. A polished AA 2024-T3 coupon was immersed in a 0.6 M NaCl aqueous solution (pH 6.5) for various times to initiate pitting in AA 2024-T3. The alloy

surface was examined using scanning electron microscopy (SEM) and energy-dispersive X-ray spectrometry (EDX) before and after the test.

6.2. Results

6.2.1. Identification of second-phase particles in AA 2024-T3

Figure 6.1 shows a uniform distribution of the second-phase particles in the matrix of AA 2024-T3. This area was randomly chosen on a freshly polished alloy surface. These particles serve to strengthen the alloy matrix giving it excellent mechanical properties. According to the literature [59–61,65], two major groups of second-phase particles are often observed in AA 2024-T3. One is Al-Cu-Mg-containing (or Al_2CuMg , S phase) particles and the other is Al-Cu-Fe-Mn-containing particles. The former is anodic towards the Al matrix and the latter is cathodic with respect to the Al matrix.

By examining the alloy studied in this work, 4 types of second-phase particles were found with chemical compositions: Al-Cu-Mg-containing (S phase), Al-Cu-Fe-Mn-Si-containing, Al-Si-containing and Al-Cu-containing (θ phase). It is noted that the latter two were seldom reported in the literature [59–62]. The corresponding SEM images of these particles are shown in Figures 6.2(a)–(d).

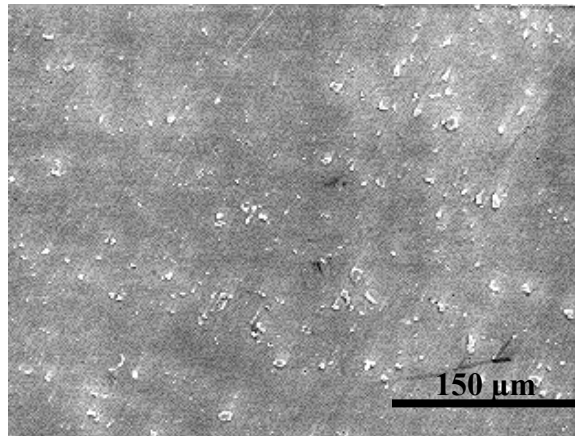


Figure 6.1. Distribution of second-phase particles on the matrix of AA 2024-T3

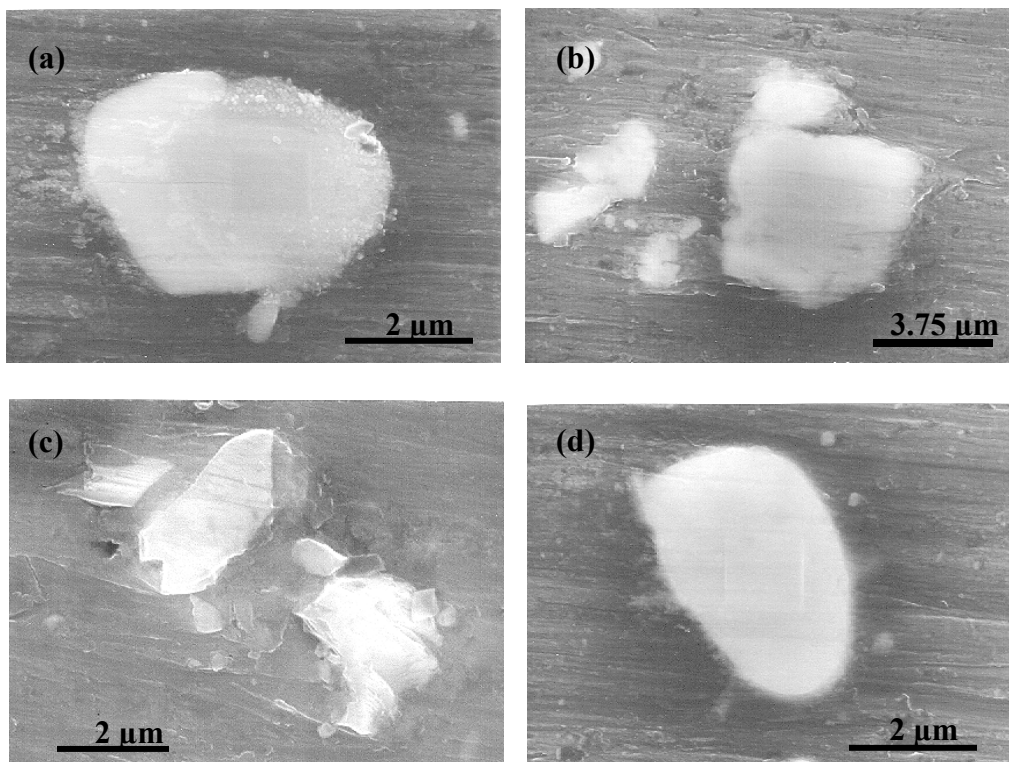


Figure 6.2. SEM images of 4 types of second-phase particles in AA 2024-T3; (a) Al-Cu-Mg, (b) Al-Cu-Fe-Mn-Si, (c) Al-Si, and (d) Al-Cu

It is seen that both S and θ have a round shape (Figures 6.2(a) and (d)), while the other two are much more irregular-shaped (Figures 6.2(b) and (c)). The chemical compositions of these particles were determined by EDX and are listed in Table 6.1. On the average, 4 particles of each kind ($> 1 \mu\text{m}$) were examined. Only the S phase contains a high amount of Mg, about 14 at%.

Table 6.1. Chemical composition (in at. %) of second-phase particles in AA 2024-T3

| Element | Al-Cu-Mg- containing | Al-Cu-Fe-Mn- containing | Al-Si- containing | Al-Cu- containing |
|---------|-------------------------|----------------------------|----------------------|----------------------|
| Al | 76.38 | 77.14 | 27.29 | 75.16 |
| Cu | 13.40 | 6.82 | -- | 24.84 |
| Mg | 10.23 | -- | -- | -- |
| Fe | -- | 8.51 | -- | -- |
| Mn | -- | 4.80 | -- | -- |
| Si | -- | 2.73 | 72.10 | -- |

6.2.2. SEM/EDX observation of corrosion of AA 2024-T3 during immersion in a neutral NaCl solution

Before immersion, an arbitrary area on the polished alloy surface was selected, as shown in Figure 6.3(a). The compositions of some of the large particles were identified with SEM/EDX. The particles marked as “A₁” and “A₂” contain Al-Cu-Mg and are designated as S phase; those labeled as “B₁” and “B₂” contain Al-Cu-Fe-Mn-Si; and the

particles “C₁” and C₂” contain Al-Si. θ phase particles were not detected in this area. This may be due to their low area fraction.

The polished coupon was immersed into a stagnant 0.6 M NaCl aqueous solution (pH 6.5). The solution was open to air throughout the entire test period. During the immersion, the alloy surface was found to corrode gradually. After 3.5 hrs, the coupon was taken out and rinsed with tap water. The same area shown in Figure 6.3(a) was re-examined with SEM/EDX, as shown in Figure 6.3(b). It is seen that only the regions around the S phase particles (i.e., “A₁” and “A₂”) corroded heavily. The Al matrix around the S phase particles at site “A₁” dissolved substantially, while the S phase particle at “A₂” fell out or decomposed into nano-particles spreading over the pit edge. No corrosion is actually visible in the vicinities of particles “B₁”, “B₂”, “C₁” and “C₂”. This observation indicates that the onset of pitting corrosion of AA 2024-T3 is indeed associated with the S phase particles. After the SEM observation, the sample was then re-immersed into the NaCl solution until the end of the test, i.e., 72 hrs of immersion. Figure 6.3(c) shows the SEM image of the sample surface corresponding to after 72 hrs of immersion. The alloy surface is similar to the one shown in Figure 6.3(b), except that a large quantity of nano-particles are distributed uniformly all over the surface.

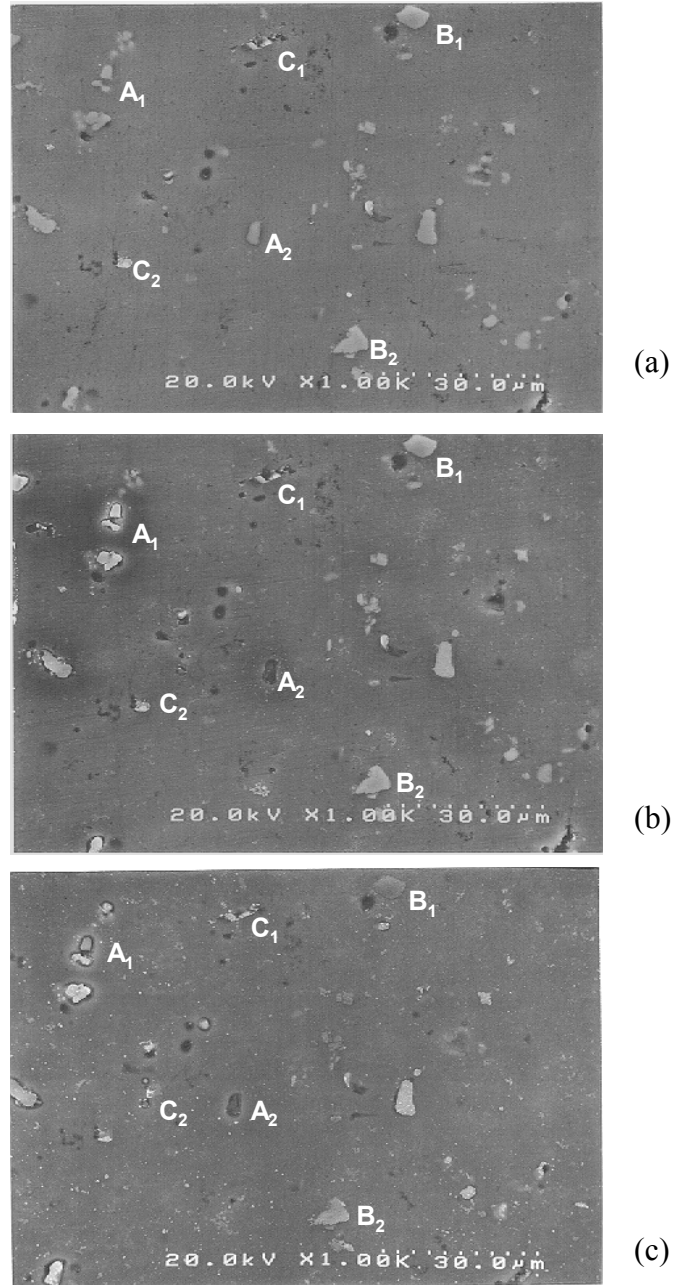


Figure 6.3. SEM images of AA 2024-T3 sample immersed in a neutral 0.6M NaCl solution; (a) before immersion, (b) 3.5 hrs of immersion, and (c) 72 hrs of immersion

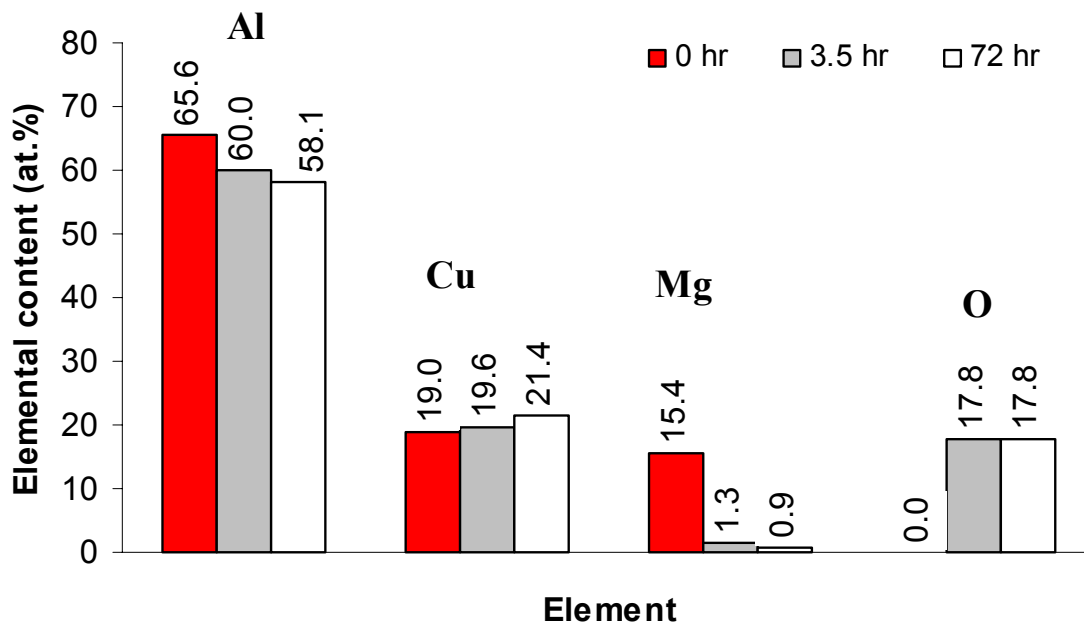


Figure 6.4. Composition of elements of the S phase particle at site “A₁”

Figure 6.4 shows the changes in the composition of the S phase particle located at site “A₁” in Figure 6.3 as a function of immersion time. In Figure 6.4, the contents of both Al and Mg are seen to decrease continuously during immersion. The atomic percent of Mg drops sharply from 15.4 % to 1.3 % in the first 3.5 hrs, and continuously decreases to 0.9 % after 72 hrs. The percent of Al also decreases to some extent, from 65.6 % to 58.1 % after 72 hrs. The Cu content in the remnant, however, remains almost constant at around 19.0% in the first 3.5 hrs, and increases slightly up to 21.4 % after 72 hrs. These changes indicate that the S phase particle experienced dealloying of Mg and Al during immersion, with the dealloying of Mg being the most severe in the first 3.5 hrs. As a result, a remnant enriched with Cu was left behind. 17.8% of O detected after testing is from the corrosion products. The SEM images of two adjacent S phase remnants at site “A₁” corresponding to 3.5 hrs and 72 hrs of immersion are presented in Figures 6.5(a)

and (b), where no significant changes in the pit morphology are observed after 72 hrs. This implies that severe pitting corrosion of AA 2024-T3 occurred mainly in the very early stages (e.g., 3.5 hrs), exhibiting as the dealloying of S phase and the dissolution of the surrounding Al matrix.

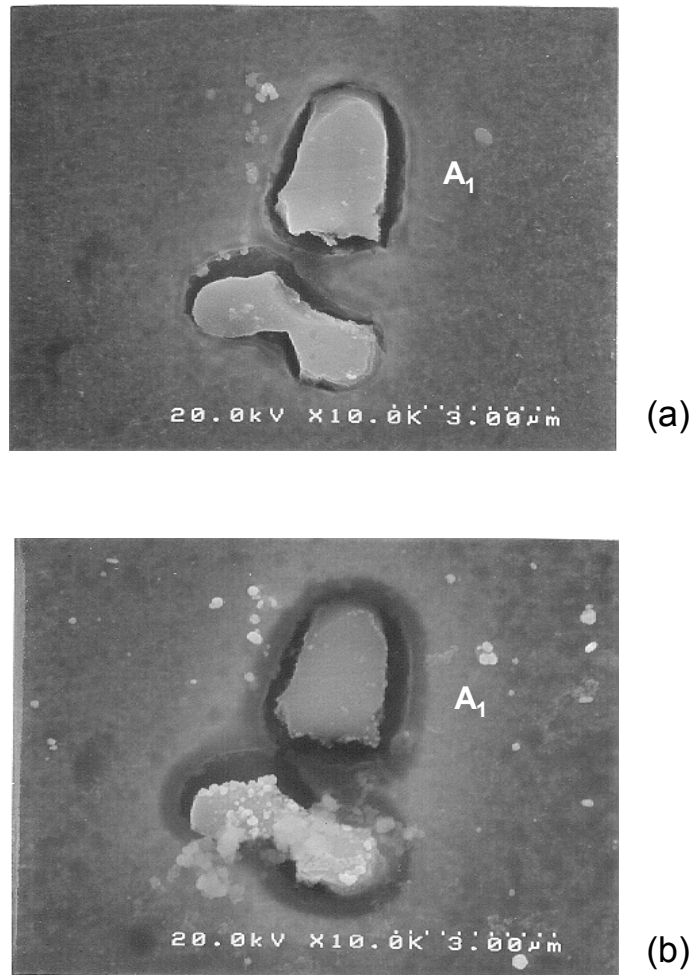


Figure 6.5. SEM images of two adjacent S phase remnants at “A₁” after immersion in 0.6M NaCl solution (pH 6.5) for various times; (a) 3.5 hrs, and (b) 72 hrs (Note: the compositions of the top one are reported in Figure 6.4)

The particles labeled as “B₁” (Al-Cu-Mn-Fe-containing) and “C₁” (Al-Si-containing) in Figure 6.3 are both cathodic towards the Al matrix [59-62, 65]. After 3.5 hrs of immersion, these two particles and their surrounding Al matrix remained intact without showing any corrosion sign. Some noticeable morphological changes are observed after 72 hrs of immersion, as displayed in Figures 6.6(a) and (b). In Figure 6.6(a), a micro-crack is seen along the Al-Cu-Mn-Fe-containing particle. Moreover, nodular particles spread uniformly over the entire particle surface. This micro-crack possibly resulted from a slight anodic dissolution of the Al matrix. In Figure 6.6(b), a similar distribution of nodular particles is seen on the Al-Si particle surface after 72 hrs. However, no micro-crack is observed along the Al-Si-containing particle.

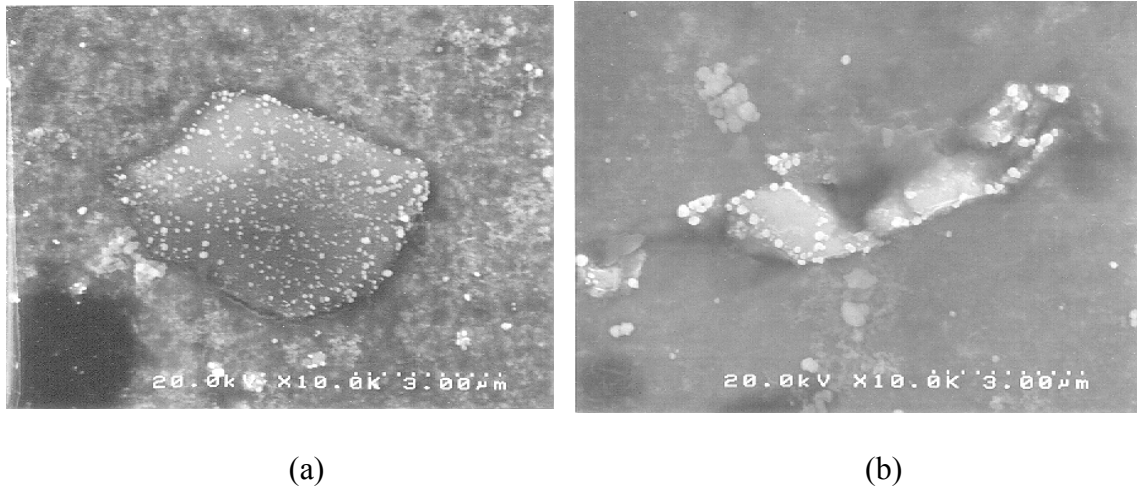


Figure 6.6. SEM images of the cathodic particles after 72 hrs of immersion in 0.6 M NaCl solution (pH 6.5) ; (a) Al-Cu-Fe-Mn-containing particle (at “B₁” in Figure 6.3), and (b) Al-Si-containing particle (at “C₁” in Figure 6.3)

Similar observation for nodular particles was also reported by others [60,65]. According to these studies [60,65], the nodular particles found on both cathodic second phase particles are pure Cu. Chen et al [65] stated that the Al-Cu-Mn-Fe-containing particles function as cathodic sites, which favors cupric ions (Cu^{2+}) dissolved in the NaCl solution to be reduced as nodular Cu deposits on the particles. Obispo et al [60] studied Cu deposition on AA 2024-T3 using TEM/EDX along with a replica-based lift-off technique to enhance the particle and surface debris resolution. They observed large Cu clusters deposited on Fe-rich or Fe-containing areas when AA 2024-T3 was immersed in NaCl solutions. They suggested that the reduction of copper from solution is an electrochemical displacement reaction which is very likely to occur on cathodic particles by oxidization or dealloying of electroactive elements such as iron (Fe) out of the particles. As might be noted in Figure 6.5(b), a cluster of nodular particles are also displayed on the surface of the dealloyed S phase remnant (the bottom one). This might indicate that after dealloying to a certain extent, the S phase remnant becomes so cathodic towards the Al matrix that it turns into a favorable place for Cu reduction, as the other two cathodic particles do.

An alternative explanation given by Buchheit et al [59] to the distribution of Cu nodular particles on the AA 2024-T3 surface is as follows. The appearance of these Cu nano-particles is most likely a result of the decomposition of porously-structured Cu-rich remnants. The Cu-rich remnants decompose into nano-particles, and later on they are transported away from the original sites by mechanical motion of growing corrosion product or solution movement, spreading over the alloy surface.

6.3. Discussion

6.3.1. Pitting associated with anodic S phase particles

The mechanism for pitting associated with S phase particles in AA 2024-T3 has been proposed earlier [59]. In summation, corrosion of AA 2024-T3 starts from the dealloying of anodic S phase particles as a result of galvanic corrosion driven by the galvanic couple of anodic S phase and cathodic Al matrix. This was also confirmed in this work.

As for the dissolution of the surrounding Al matrix along the S phase particles, the explanation in reference [59] is as follows. As dealloying continues, the S phase remnants become Cu-rich and finally turn into cathodes towards the adjacent Al matrix. Consequently, the opposite galvanic couple of the anodic Al matrix and the cathodic Cu-rich S phase remnant is established. This would lead to another galvanic corrosion, causing dissolution of the surrounding Al matrix [59]. However, this explanation is not fully supported by the experimental evidence in this work.

If the above explanation were the case, then we would have expected to observe a much more severe dissolution of the Al matrix in the later stages (i.e., 72 hrs), as the S phase remnants would become more cathodic towards the surrounding Al matrix in the later stages due to the completion of the dealloying. As opposed with what was expected, the Al matrix around the S phase particles was only observed to dissolve heavily within the first 3.5 hrs (Figure 6.5(a)) along with the dealloying of the S phase particles. Further dissolution of the Al matrix seemed to cease or to slow down in the later stages even

when the S phase remnant became more cathodic towards the Al matrix (Figure 6.5(b)). A question hence arises here: is the galvanic corrosion suggested in reference [59] the primary cause for the several Al dissolution around the S phase particles? We will further discuss this issue in consideration of some other possibilities in Section 6.3.3.

6.3.2. Corrosion behavior of cathodic Al-Cu-Fe-Mn-containing and Al-Si-containing phase particles

The other two cathodic particles (i.e., Al-Cu-Fe-Mn-containing and Al-Si-containing particles) did not corrode within the first 3.5 hrs (Figure 6.3(b)). After 72 hrs, only a slight trench or a micro-crack was formed around the Al-Cu-Mn-containing particle (Figure 6.6(a)), but no corrosion activity was seen in the vicinity of the Al-Si-containing particle (Figure 6.6(b)). Al-Cu-Fe-Mn-containing phase, for example, has a corrosion potential of -0.35V/SCE in chloride-containing solutions [100], 0.2 V/SCE positive towards AA 2024-T3 matrix (-0.65 V/SCE). In principle, a galvanic couple of anodic Al matrix/cathodic Al-Cu-Fe-Mn-containing phase should be developed, inducing the dissolution of the surrounding Al matrix. In reality, however, we did not observe a severe dissolution of the Al matrix along the particle throughout immersion. This phenomenon is understandable by taking into account the effect of the cathode-to-anode area ratio on galvanic corrosion.

It is known that galvanic corrosion can either be accelerated by increasing the cathode-to-anode area ratio, or be weakened by reducing the ratio. In the former case, galvanic corrosion concentrates on a small anode, causing a severe damage of the anode.

This actually explains the extensive dealloying of the anodic S phase particles in the first 3.5 hrs. The S phase particles as small anodes suffered intensive galvanic corrosion, when surrounded by the large cathodic Al matrix. In the latter case, the initiated galvanic attack spreads over a greater anodic area. The corrosion activity on the anode is therefore weakened. This is exactly the case for these two cathodic particles. Compared to the surrounding Al matrix, these two cathodic particles are relatively small. The galvanic attack induced by these two small cathodic particles would readily spread over a large area of the anodic Al matrix. As a result, a severe dissolution of the Al matrix is avoided, as shown in Figures 6.6(a) and (b).

By the use of this area ratio effect, the corrosion behavior of the dealloyed S phase remnants in the later stages can also be explained. In the later stages, the dealloyed S phase remnants serve as small cathodes like the other two cathodic particles. Such small cathodic S phase remnants, however, are unlikely to induce severe Al dissolution at the peripheries.

6.3.3. Alternative mechanism of Al dissolution in the vicinity of S phase particles

As discussed in Section 6.3.1, the SEM/EDX observation in this work does not support the suggested mechanism for the severe dissolution of the Al matrix in the vicinity of the S phase remnants [59]. In this section, we give an alternative explanation to this phenomenon in consideration of some other possibilities.

Figure 6.7 illustrates schematically the pitting corrosion of AA 2024-T3 in a naturally-aerated neutral chloride-containing solution. The overall corrosion starts with

the dealloying of the anodic S phase particle. The corresponding anodic and cathodic reactions are given by,

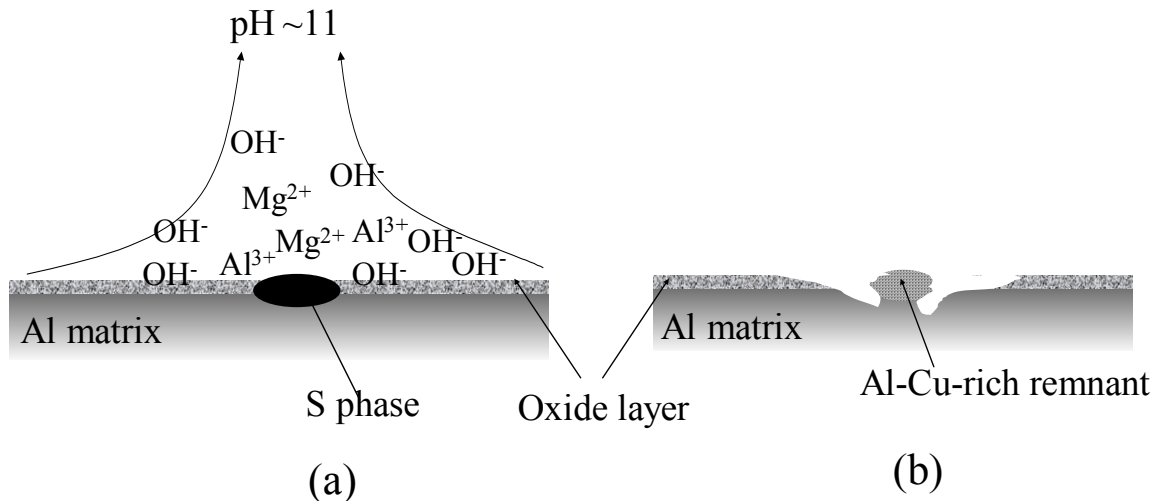
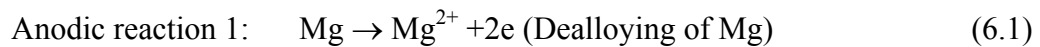
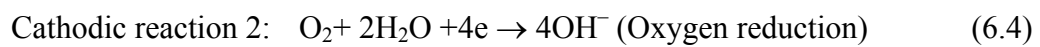
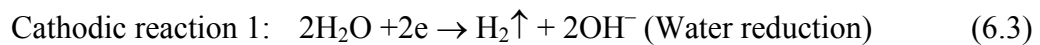


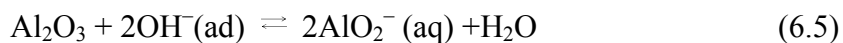
Figure 6.7. Schematic of early corrosion process of AA 2024-T3 in 0.6M NaCl solution; (a) dealloying and local alkalization, and (b) cathodic dissolution of the surrounding Al matrix



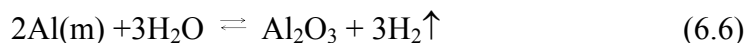
And,



The above anodic reactions (i.e., dealloying of Mg and Al) occur at the surface of the S phase particles. The accompanying cathodic reactions, water reduction and oxygen reduction, are most likely to take place on the Al matrix at the periphery of the S phase particles. It should be noted that along with the S phase dealloying, the coupled cathodic reactions (6.3) and (6.4) would also generate hydroxide ions (OH^-) by reducing water and/or oxygen molecules. The rate of water reduction and the amount of OH^- ions is obviously determined by the rates and the extent of the anodic reactions (6.1) and (6.2). Since Mg dissolved so vigorously within the first 3.5 hrs from the S phase particles, it is reasonable to expect a considerably high amount of OH^- ions generated from the coupled water and oxygen reductions. Accordingly, a local alkalization is likely to be formed around the S phase remnant in a stagnant solution (Figure 6.7(a)). Once the local pH exceeds 9 (i.e., the equilibrium pH of Al oxide), the surrounding Al oxide layer on the Al matrix would no longer survive and would dissolve according to,



Simultaneously, the bare Al matrix underneath would be oxidized to form a new layer of Al oxide, releasing hydrogen gas by the reaction,



where $\text{OH}^-(\text{ad})$ = the adsorbed hydroxide ion; $\text{AlO}_2^- (\text{aq})$ = the aluminate ion in the aqueous solution; $\text{Al} (\text{m})$ = the Al atom in the Al lattice. It should be noted that the dissolution of Al oxide (6.5) is simply a chemical dissolution (i.e., without electron transfer), whereas the formation of the Al oxide (6.6) is an electrochemical process in which an electron transfer (or metal oxidation) is involved [57]. The Al dissolution in an alkaline medium in Figure 7(b) is known as cathodic corrosion of Al.

The local pH around the S phase particle is possibly raised up to 11 without forming stable Mg hydroxides. pH 11 is the equilibrium pH of $\text{Mg}(\text{OH})_2$, below which $\text{Mg}(\text{OH})_2$ is not stable and tends to dissolve acidically. In the presence of chloride ions (Cl^-), the formation of $\text{Mg}(\text{OH})_2$ may be further delayed, as Cl^- ions are known to destabilize $\text{Mg}(\text{OH})_2$ [97].

A similar mechanism for corrosion of AA 5085 and AA 6061 in a neutral NaCl solution was proposed by Elboujdaini and Ghali [101,102]. They stated that a high content of electroactive Mg in the second-phases in both alloys increases the cathodic activity (i.e., hydrogen evolution at the Mg-rich particle surfaces). As a result, an alkaline diffusion layer located along the particles is formed, which leads to the dissolution of the matrix around the particles and final removal of Mg-rich particles from the surface. When the cathodic activity ceases, a protective oxide film is reformed on the surface of the pit in place of the removed particle. Other similar works have also been documented [103–105].

In the case of AA 2024-T3, a likely mechanism can be applied to the dissolution of the Al matrix around S phase. That is, the surrounding Al matrix undergoes cathodic corrosion caused by a high local pH environment, rather than galvanic corrosion driven

by the opposite galvanic relationship developed between S phase remnants and the surrounding Al matrix [59]. The overall cathodic dissolution of the surrounding Al matrix consists of the following two simultaneous processes: (1) chemical dissolution of the Al oxide layer; and (2) electrochemical formation of a new layer of Al oxide by the oxidation of the bare Al matrix. The slowing down of the Al dissolution in the vicinity of the S phase remnant in the later stages is attributable to the small cathode-to-anode area ratio (i.e., S phase remnant-to-Al matrix), which mitigates the corrosion by spreading the induced galvanic attack over the great area of the Al matrix.

6.4. Conclusions

The corrosion study of AA 2024-T3 in a neutral NaCl solution showed that, (1) pitting initiates around the anodic S phase particles, exhibiting as the dealloying of elements Al and Mg and the severe dissolution of the surrounding Al matrix; and (2) Al dissolution in the vicinity of S phase remnants is likely to be caused by the local alkalization resulting from the coupled cathodic reactions (water/oxygen reduction), rather than by the galvanic corrosion induced by the galvanic couple of the Cu-rich S phase remnants (cathode) and the surrounding Al matrix (anode) [59]. Such corrosion can be efficiently inhibited by a bis-sulfur silane treatment, as demonstrated in Chapter 7.

Chapter 7. Corrosion Inhibition of AA 2024-T3 by Bis-[triethoxysilylpropyl]tetrasulfide in Neutral Sodium Chloride Solution – Part 2: Mechanism of Corrosion Protection¹

Abstract The corrosion protection of AA 2024-T3 by the film of bis-[3-(triethoxysilyl)propyl]tetrasulfide (bis-sulfur silane) was studied in a neutral 0.6 M NaCl solution using potential transient, potentiodynamic polarization and Electrochemical Impedance Spectroscopy (EIS) techniques. The results showed that a highly crosslinked interfacial layer that developed between the silane film and the aluminum oxide is a major contribution to the corrosion protection of AA 2024-T3. This interfacial layer tightly anchors to the metal surface by the formation of Al-siloxane (AlOSi) covalent bonds at the interface. In this way, hydrophilic Al hydroxyls (AlOH) at the metal surface are consumed. This leads to a hydrophobic metal surface which is not favorable for water/moisture adsorption. The corrosion tendency of the metal is thus reduced. Additionally, a highly crosslinked film structure (i.e., a small porosity) with a number of hydrophobic SiOSi units and sulfur chains of bis-sulfur silane film enhances water resistance of the film, which effectively postpones water penetration into the system. Corrosion control of AA 2024-T3 is hence secured by preventing hydrolysis of AlOSi bonds at the interface.

¹ The chapter has been accepted by Corrosion Science, 2002

7.1. Introduction

In Chapter 6, the corrosion mechanism of bare AA 2024-T3 was studied. In summary, it was found that the corrosion of this alloy starts from the dealloying of anodic S phase particles (Al_2CuMg), followed by severe dissolution of the surrounding Al matrix due to the local alkalization formed around the particles. Such corrosion in AA 2024-T3, however, can be inhibited efficiently by silanes. In this chapter, we investigated anticorrosion mechanism of the bis-sulfur silane-treated AA 2024-T3 system using electrochemical tests, such as potentiodynamic polarization tests and EIS measurements. SEM/EDX was also used to characterize the silane-treated alloy surfaces before and after the corrosion tests. On the basis of these results, a mechanism for corrosion protection of AA 2024-T3 by the bis-sulfur silane was proposed. A 5% bis-sulfur silane water/ethanol solution was used in this work. The silane-treated panels were cured at 100°C for 24 hrs in order to obtain an extensively crosslinked film structure.

7.2. Results and discussion

7.2.1. Electrochemical tests

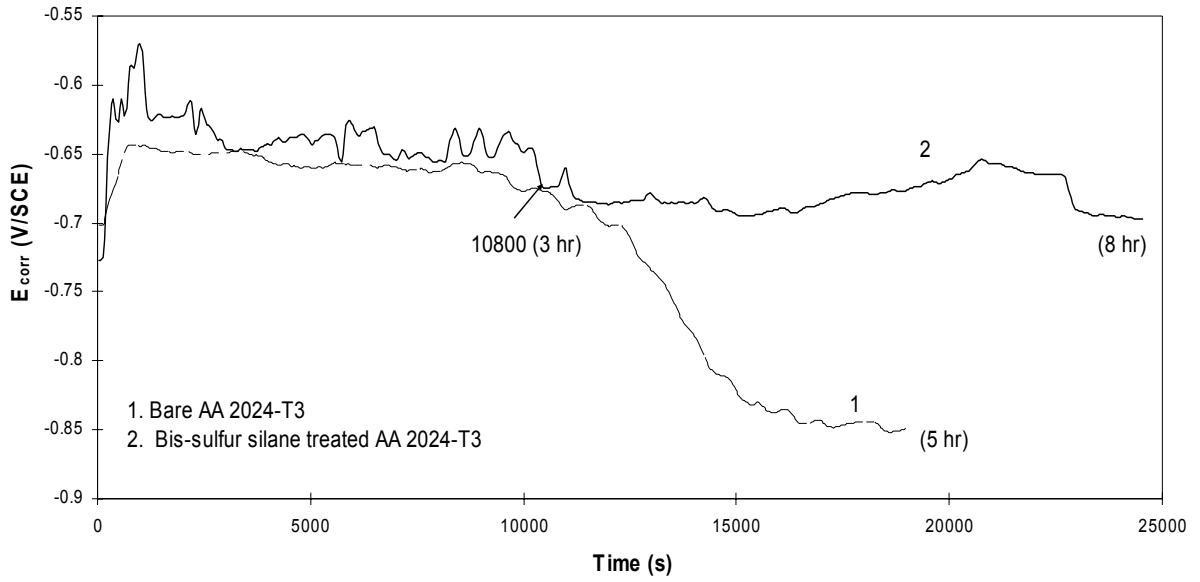
7.2.1.1. Potential transient measurements in a neutral 0.6 M NaCl solution

Figure 7.1(a) compares the E_{corr} values as a function of immersion time of the AA 2024-T3 panels treated with and without the bis-sulfur silane in a 0.6 M NaCl solution. It

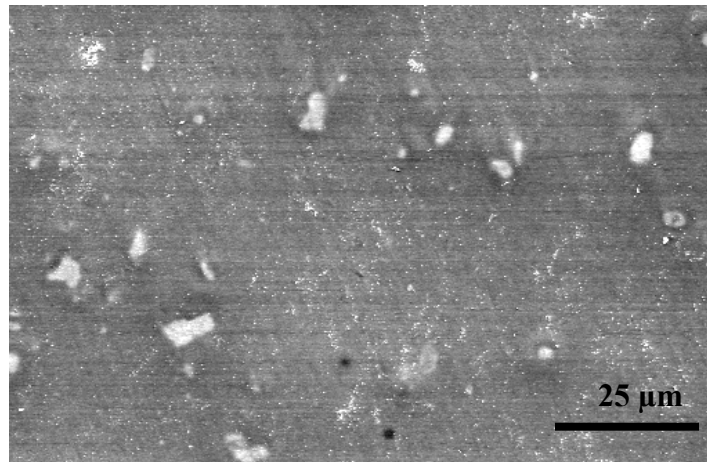
is seen that the potential curve of the silane-treated AA 2024-T3 fluctuates around -0.65 V/SCE in the first 3 hrs, and then becomes smooth and stable at around -0.68 V/SCE afterwards. This suggests that a steady state is achieved for an extensively-crosslinked bis-sulfur silane treated AA 2024-T3 system after 3 hrs of immersion in the electrolyte.

The E_{corr} of the bare AA 2024-T3 (curve 1 in Figure 7.1 (a)) decreases during immersion. The overall process can be divided into two stages in terms of the decreasing rate of E_{corr} . The first stage is from 0 hr – 3 hrs, during which E_{corr} decreases slowly from the initial value of -0.65 V/SCE to more cathodic potentials. In combination with the SEM/EDX results obtained in Chapter 6, the slow decrease in E_{corr} may reflect the initial dealloying of the S phase particles. The local pH during this period increased continuously, yet might have not exceeded 9. Thus, the surrounding Al oxide was still stable, which prevented the bare Al matrix from dissolution. When the immersion enters the second stage, i.e., after 3 hrs, the E_{corr} of the bare AA 2024-T3 drops abruptly from above -0.7 V/SCE down to around -0.85 V/SCE. The sharp drop in E_{corr} in the second period may suggest that the Al matrix in the vicinity of the S phase remnants started to experience a significant dissolution caused by the high pH (>9) developed there. A similar phenomenon was also reported on cathodic corrosion of Al coupled with Mg components [97,106]. It was stated that the shift of the Al potential in the active direction is in accordance with the Al dissolution in alkaline seawaters [106].

The sample surfaces were examined with SEM/EDX after testing. The surface of the bare AA 2024-T3 after 5 hrs of testing was corroded heavily, while for the silane treated AA 2024-T3, all second-phase particles remained intact under the bis-sulfur silane film without visible corrosion after 8 hrs of exposure (Figure 7.1(b)).



(a)



(b)

Figure 7.1. Potential transient curves of AA 2024-T3 treated with and without bis-sulfur silane (a), SEM images of bis-sulfur silane treated AA 2024-T3 after 8 hrs of immersion in a neutral 0.6 M NaCl solution (b)

7.2.1.2. Anodic and cathodic polarization tests of bis-sulfur silane-treated AA 2024-T3 in a neutral 0.6 M NaCl solution

Figure 7.2 displays anodic polarization curves of AA 2024-T3 treated with and without the bis-sulfur silane, measured in a naturally-aerated 0.6 M NaCl solution (pH 6.5). The bis-sulfur silane treated AA 2024-T3 panels were immersed in the electrolyte for 8 hrs before data collection. In Figure 7.2, the anodic current density of AA 2024-T3 has been significantly reduced after the silane treatment (curve 2) at higher applied voltages with respect to that of the bare AA 2024-T3 (curve 1). The pitting potential of this alloy is difficult to identify on curve 1 in Figure 7.2, as the test was running under aerated conditions. Under such conditions, the Al oxide layer is very thin and not stable. The film breakdown is thus not obvious and the corresponding pitting potential is not well-defined on curve 1 in Figure 7.2.

It is also noted in Figure 7.2 that curve 2 for the silane-treated sample becomes “zig-zag” when the voltages increase above 0 V/SCE. This is probably related to the onset of breakdown of the silane film. Further discussion on this aspect will be done in Section 7.2.3.

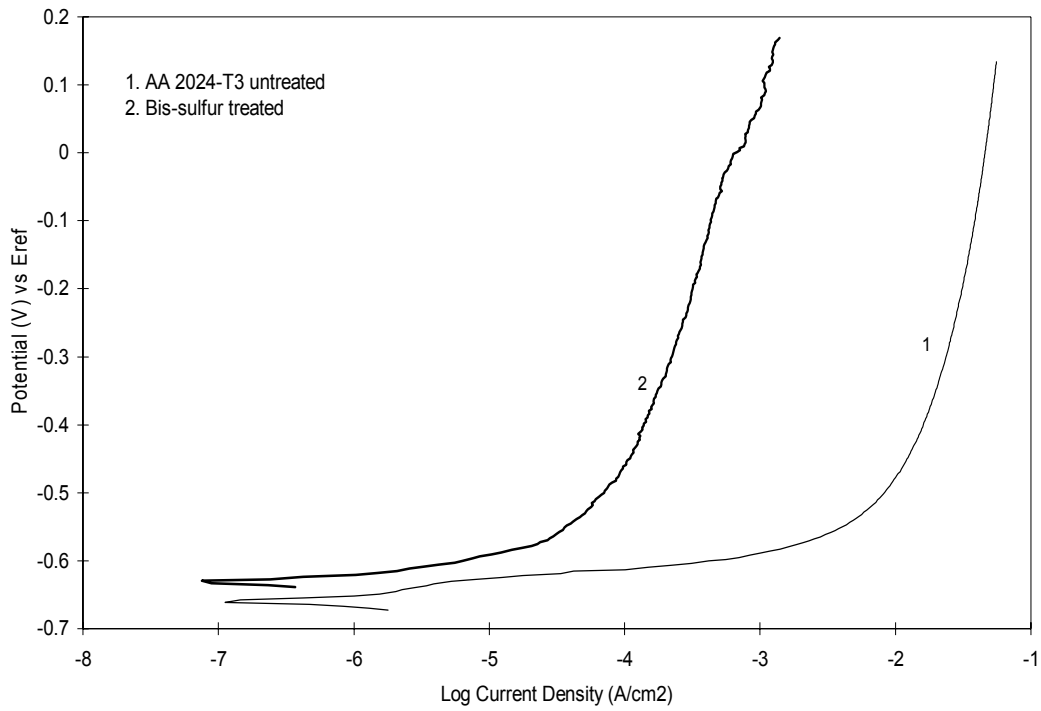


Figure 7.2. Anodic polarization curves of AA 2024-T3 treated with and without bis-sulfur silane

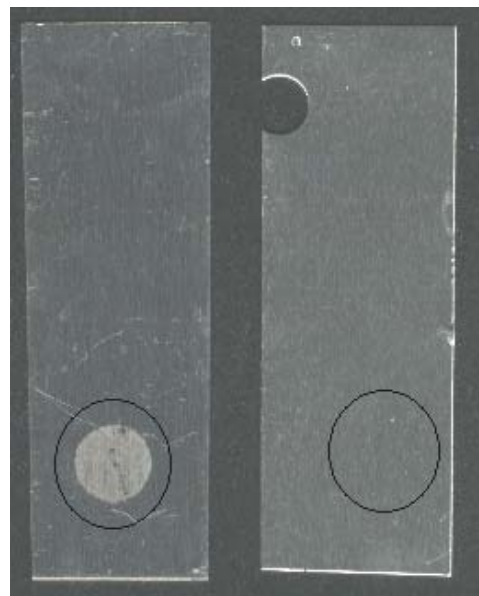


Figure 7.3. Scanned images of AA 2024-T3 with and without bis-sulfur silane after anodic polarization ending at 0.1 V/SCE; (a) untreated, and (b) silane-treated

The samples were examined visually after the test ending at 0.1 V/SCE. The scanned images are shown in Figure 7.3. The untreated surface (Figure 7.3(a)) corroded thoroughly, while the silane-treated surface only shows a few tiny pits after (Figure 7.3(b)).

Figure 7.4 compares the cathodic behavior of the silane-treated AA 2024-T3 and that of the bare alloy. Similarly, the silane-treated samples were immersed in the electrolyte for 8 hrs prior to the test. In Figure 7.4, the cathodic current density of AA 2024-T3 had been reduced appreciably after the silane treatment (curve 2). The current density at voltages lowers than -0.7 V/SCE, for example, has been reduced by more than one decade.

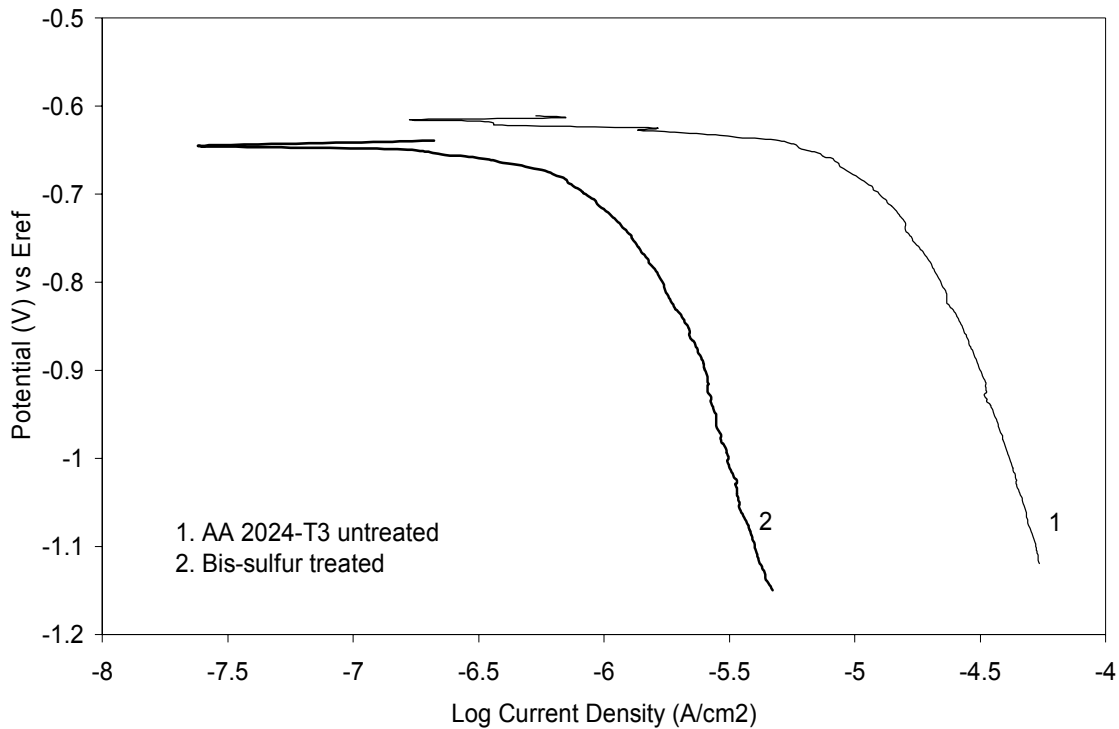
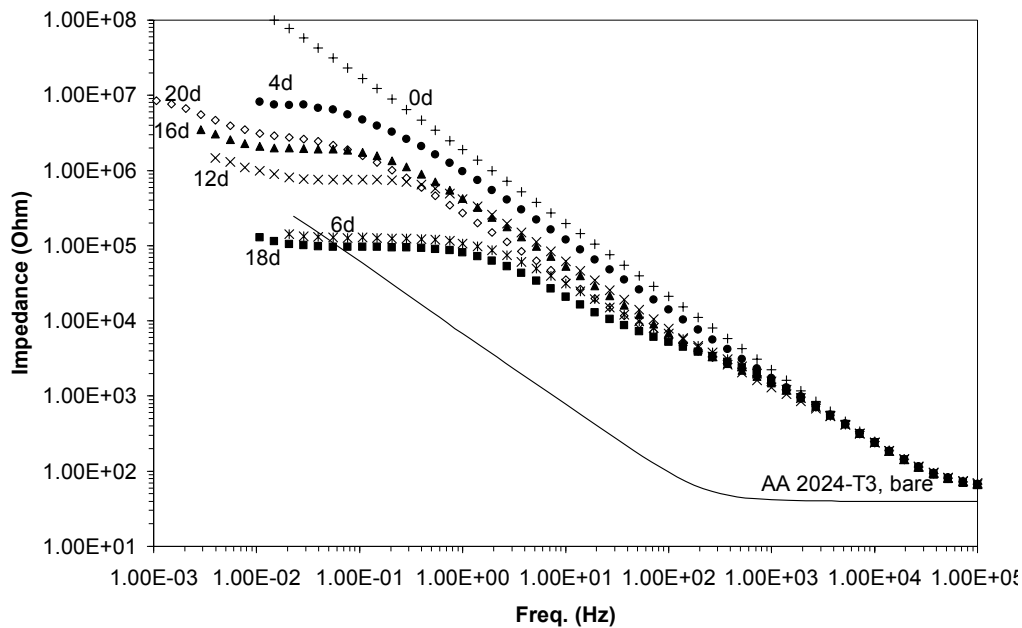


Figure 7.4. Cathodic polarization curves of AA 2024-T3 treated with and without bis-sulfur silane

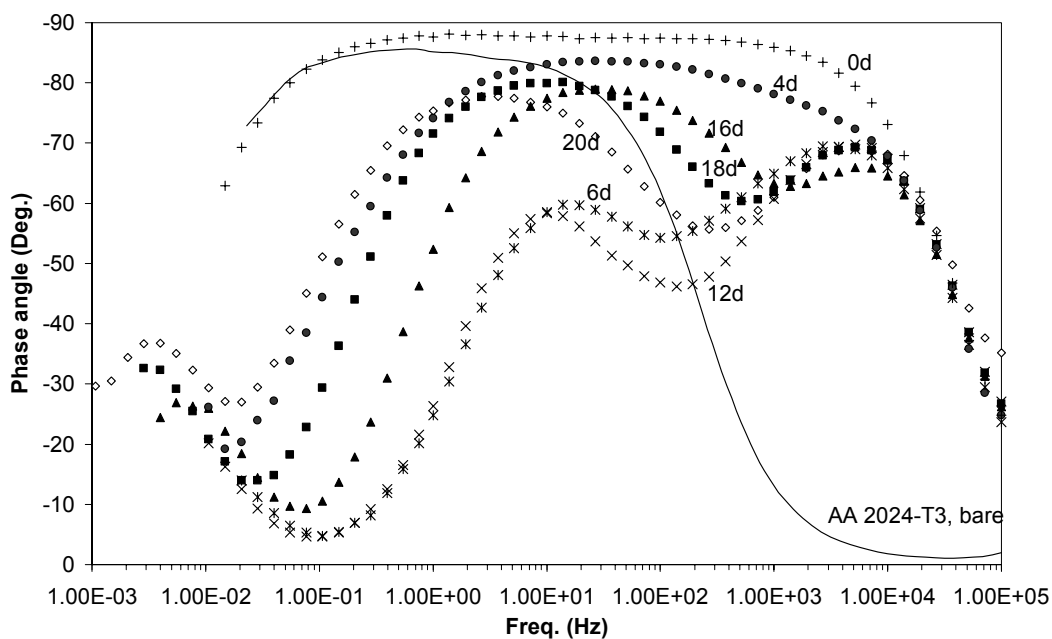
From the above anodic and cathodic polarization tests, it is clear that the silane treatment indeed inhibits corrosion of AA 2024-T3. On the other hand, it is also noted that both E_{corr} and curve slopes in Figures 7.2 and 7.4 are not altered by the silane deposition. This indicates that the bis-sulfur silane film behaves as a physical barrier, but not a chemical barrier like a chromate layer. It is well known that the latter inhibits corrosion of Al by altering electrochemical properties of the Al oxide layer [107-110]. Further discussion on anti-corrosion mechanism of the bis-sulfur silane will be presented later in Section 7.2.3.

7.2.1.3. EIS measurements in a neutral 0.6 M NaCl solution

The corrosion behavior of the bis-sulfur silane-treated AA 2024-T3 was monitored by EIS for 30 days as a function of immersion time in a naturally-aerated 0.6 M NaCl solution (pH 6.5). Figures 7.5(a) and (b) present Bode plots of the bis-sulfur silane treated AA 2024-T3 system during immersion. Significant variations in impedance at low frequencies are seen. The curves of bare AA 2024-T3 are also shown in Figure 7.5 as references. Within the first 4 days, only one broad time constant is observed with a decrease in the low-frequency impedance on the 4th day. No corrosion was visually observed in this period. This indicates that the major event occurring in this period was the water/ion penetration into the silane film, resulting in the film saturated with the electrolyte. After 6 days, two time constants become obvious with a small tail forming at low frequencies in Figure 7.5. Still, no corrosion was visually observed on the surface.



(a)

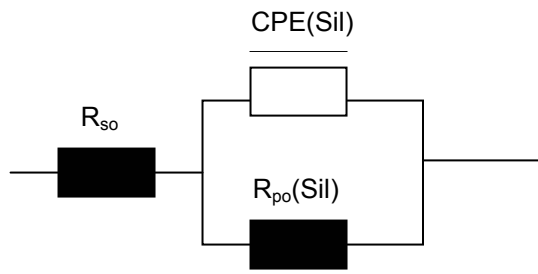


(b)

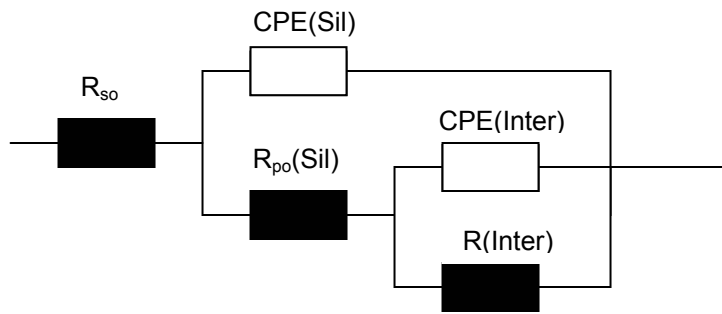
Figure 7.5. Bode plots of bis-sulfur silane treated AA 2024-T3 during immersion in a neutral 0.6 M NaCl solution for 30 days (exposed area: 3.14 cm²); (a) impedance plot, and (b) phase angle plot

On the basis of the previous characterization works in Chapters 3 and 4, the bis-sulfur silane-treated AA 2024-T3 system is made up of three different regions. They are, from the outside to the inside, a crosslinked outermost bis-sulfur silane film enriched with SiOSi bonds, an extensively crosslinked or dense bis-sulfur interfacial layer dominant with SiOSi and SiOAl bonds, and the inner Al oxide layer on the alloy substrate, as illustrated in Figure 4.5 (in Chapter 4). Referring to this structure, the high-frequency time constant centered at 10^4 Hz is due to the outermost silane film; the mid-frequency one at 10 Hz is the response of the interfacial layer; and the small tail appearing below 0.1 Hz may be related to the Al oxide layer. As the immersion continued, one pit was observed clearly on the alloy surface after 10 days, and correspondingly one small time constant centered at 0.01 Hz is formed in Figure 7.5. This time constant is thus assigned to the pitted Al oxide layer.

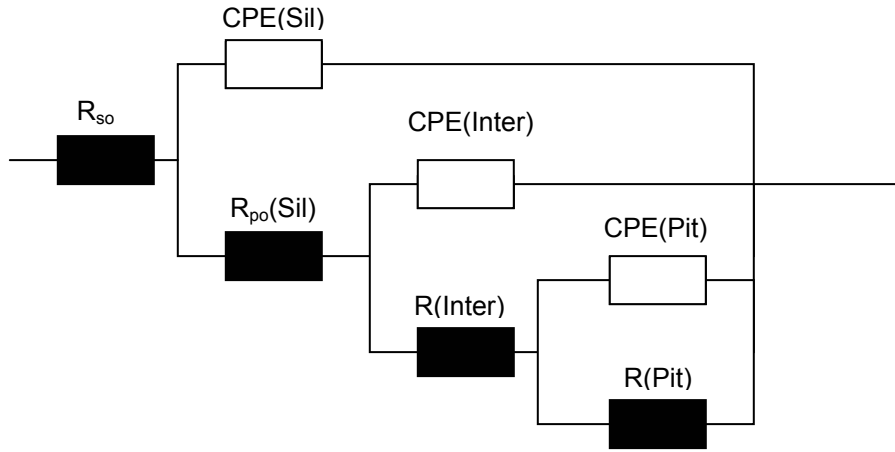
Several configurations of equivalent electric circuit models (ECM) were tested, in order to fit the experimental EIS data. Figure 7.6 shows 4 ECMs constructed for this purpose. These ECMs have been successfully used in our previous EIS work (see Chapter 3) as well as in the studies of other polymer-coated metal systems [71,77,79,80]. Figures 7.7(a) to (d) give some examples of the fitted EIS plots by using the ECMs in Figure 7.6. It is evidenced that the experimental EIS data in this study are fitted very well with these ECMs. It should be mentioned that both 3-time-constant models in Figures 7.6(c) and (d) were used for the data fitting after pitting occurred, which gave similar EIS parameters.



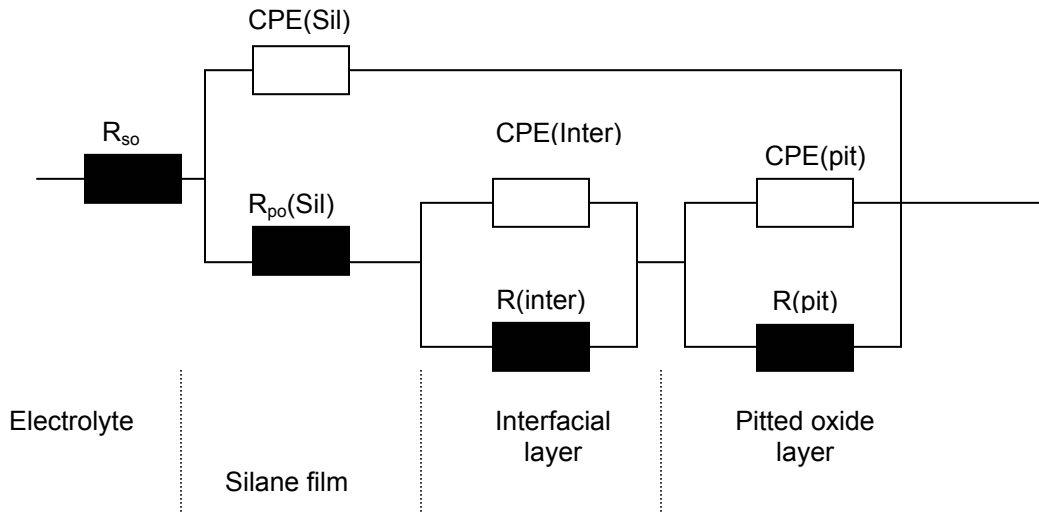
(a)



(b)

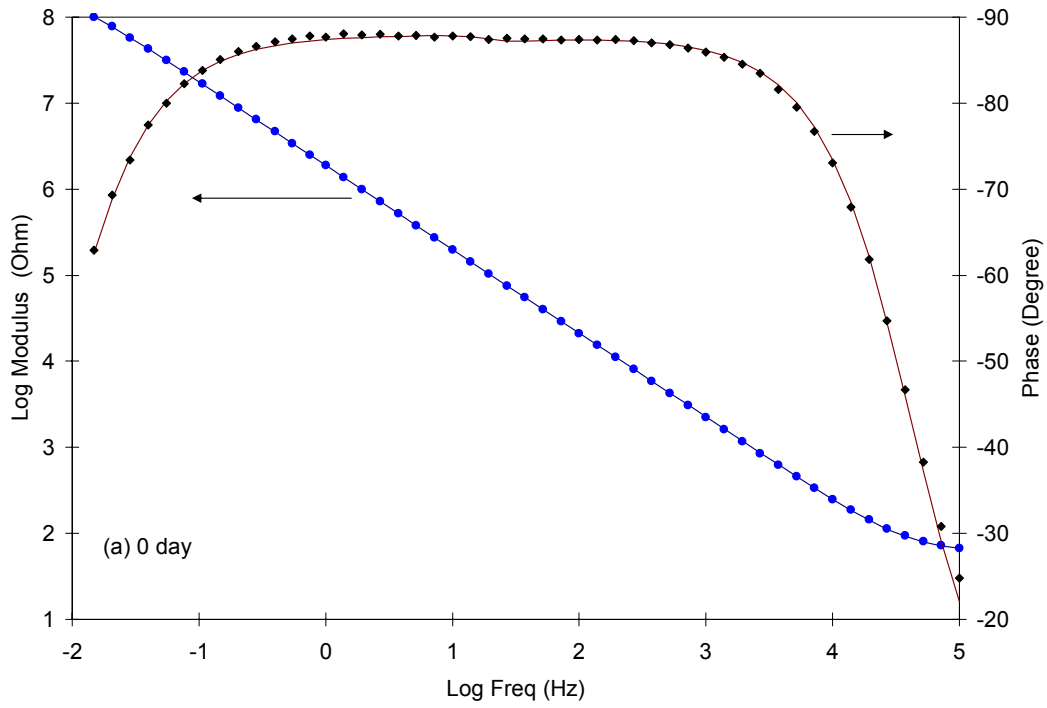


(c)

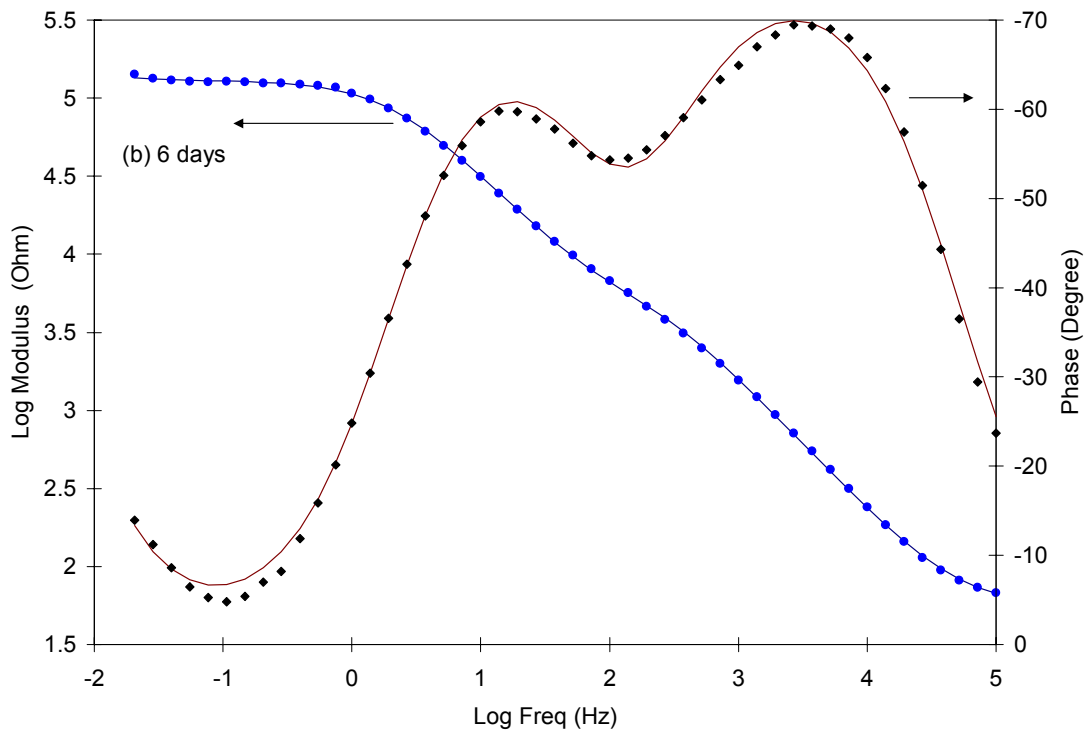


(d)

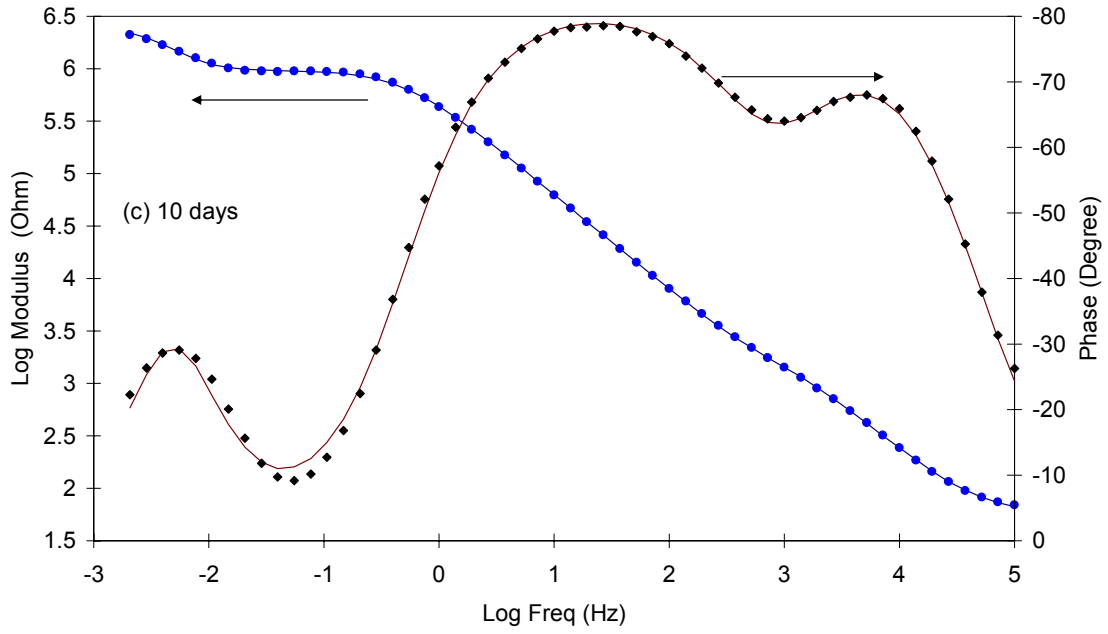
Figure 7.6. ECMs for EIS data fitting for bis-sulfur silane treated AA 2024-T3 after 30 days of immersion in 0.6 M NaCl; (a) before water penetration into the film, (b) after water saturation of the film, (c) after pit formation-model 1, and (d) after pit formation – model 2



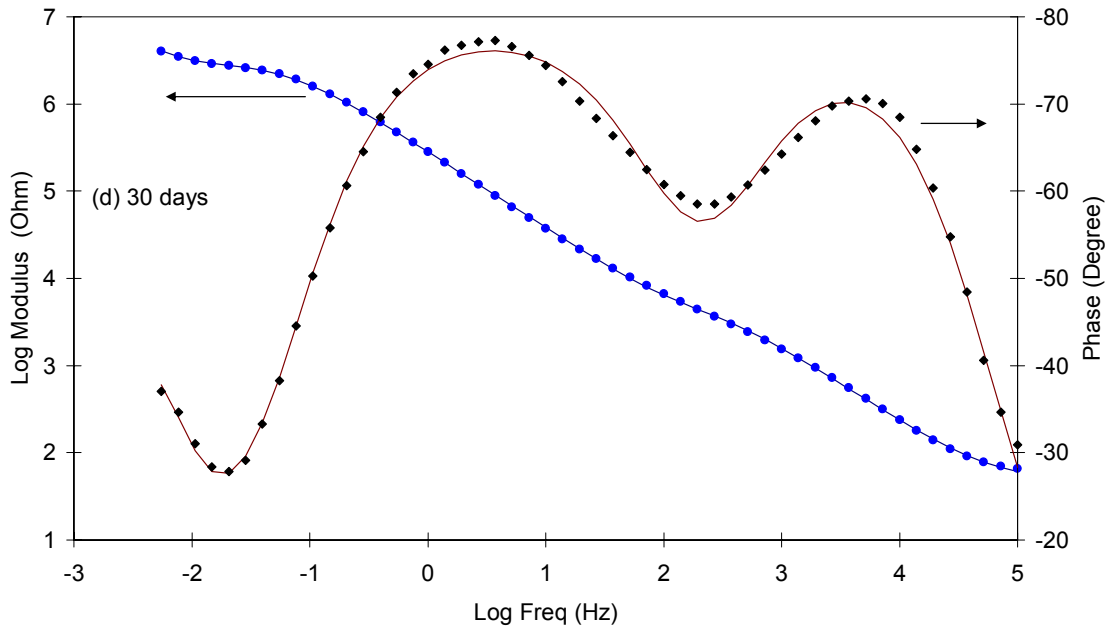
(a)



(b)



(c)



(d)

Figure 7.7. Fitted EIS plots for different immersion time with the ECMs in Figure 7.6, (a) 0 day, (b) 6 days, (c) 10 days, and (d) 30 days

The resistance, obtained from the above data fitting, of each region in the bis-sulfur silane treated system is shown in Figure 7.8 as a function of immersion time. All resistance values have been normalized to the exposed area of 3.14 cm^2 . In Figure 7.8, it is shown that the pore resistance (R_{po}) of the outermost bis-sulfur silane film decreases significantly after 4 days of immersion, from about $10^6 \Omega\text{-cm}^2$ to $10^3 \Omega\text{-cm}^2$. The value remains constant at around $10^3 \Omega\text{-cm}^2$ afterwards. This indicates that the outermost film has been progressively saturated with the electrolyte within the first 4 days. The resistance of the interfacial layer (R_{inter}) drops by 2 orders of magnitude after 6 days, from $4 \times 10^6 \Omega\text{-cm}^2$ to $4 \times 10^4 \Omega\text{-cm}^2$, and increases again to $5 \times 10^5 \Omega\text{-cm}^2$ after 8 days. The initial decrease in R_{inter} may reflect the fact that the electrolyte penetrated into the interfacial layer, and consequently corrosion occurred at the metal surface. The as-formed corrosion products later on intruded into the interfacial layer causing “pore blocking”, which leads to the increase in R_{inter} afterwards. After 10 days, a stable pit was visually seen on the silane-treated surface. The resistance of the pitted oxide layer (R_{pitt}) is consistent with that of the interfacial layer since then, showing that pitting behavior is intimately associated with that of the interfacial layer.

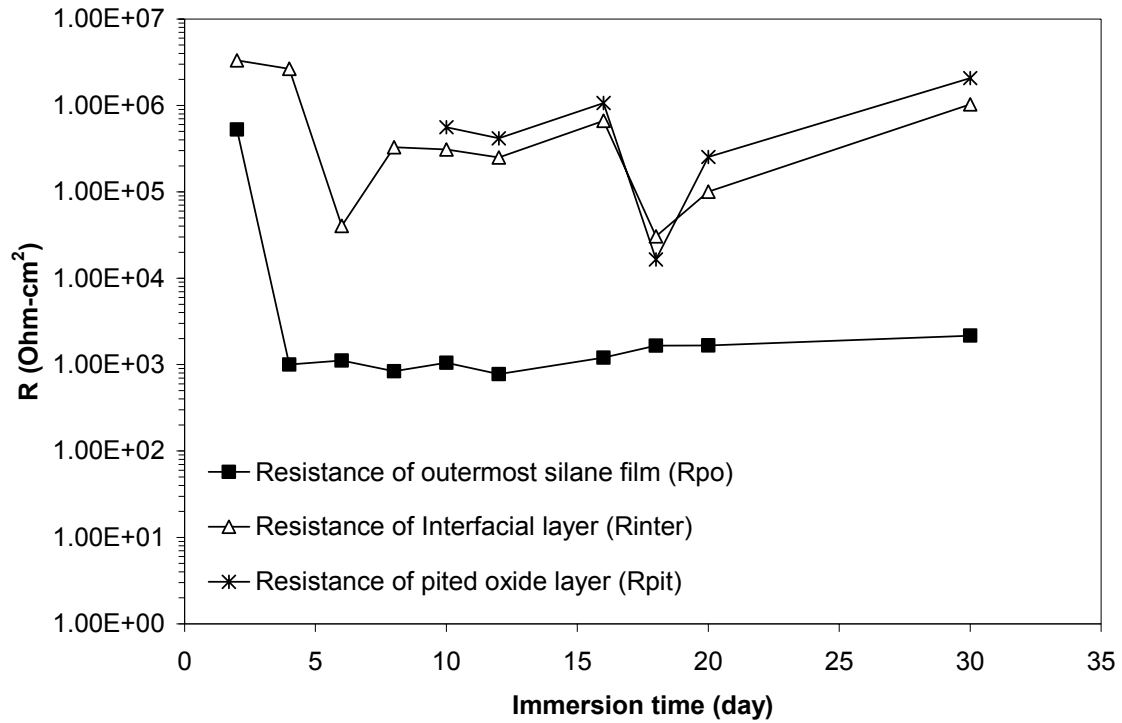
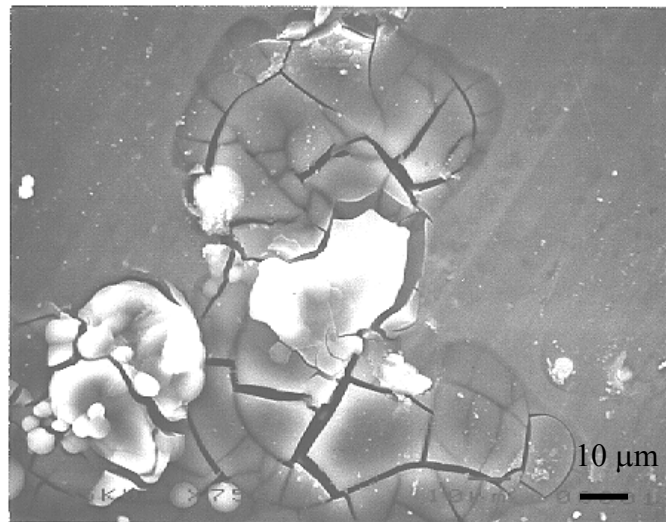


Figure 7.8. Resistances of silane film, interfacial layer, and pit as a function of immersion time in a neutral 0.6 M NaCl solution of the bis-sulfur silane treated AA 2024-T3 system

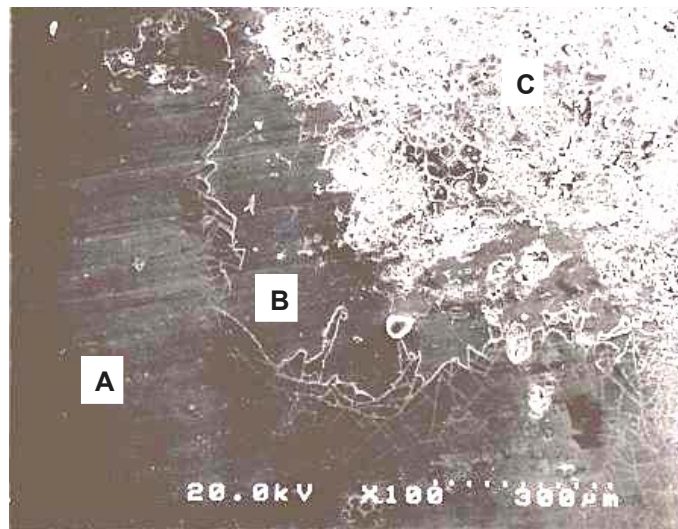
7.2.2. SEM/EDX observation

SEM and EDX were performed on the silane-treated alloy surface after immersion of 15 days in a 0.6 M NaCl solution (pH 6.5). Two pits were observed after the immersion test. The SEM images of these two pits are shown in Figures 7.9(a) and (b). Figure 7.9(a) shows the morphology of the younger pit, where the topside silane film starts to crack. Moreover, local film delamination is observed around the pit. In Figure 7.9(b), the older pit is present with some important morphological features. In general, three different regions indicated as regions A, B and C are clearly seen in the figure. Region A is the topside silane film, with some micro-cracks formed in the area adjacent

to region B. Region C is the pitting center, where the alloy has been severely eaten away. The corresponding compositions detected by EDX of these three regions are listed in Table 7.1. The composition of bare AA 2024-T3 is also shown here as a reference [96].



(a)



(b)

Figure 7.9. SEM image of the pits formed on the bis-sulfur silane treated AA 2024-T3 surface after 15 days of immersion in 0.6 M NaCl; (a) younger pit, and (b) older pit

Table 7.1. Comparison of chemical compositions (in wt %) of regions A, B and C in Figure 7.9, and bare AA 2024-T3

| Element | Region A | Region B | Region C | AA 2024-T3 [96] |
|----------------|-----------------|-----------------|-----------------|------------------------|
| O | 6.86 | 5.02 | 45.33 | -- |
| Mg | 1.41 | 1.15 | -- | 1.2-1.8 |
| Al | 77.16 | 82.18 | 37.79 | Rem. |
| Si | 5.45 | 3.59 | 1.35 | 0.5 |
| S | 3.90 | 2.11 | 1.59 | -- |
| Cl | -- | 0.26 | 6.24 | -- |
| Cu | 5.06 | 5.86 | 7.60 | 3.8-4.9 |

It is seen in Table 7.1 that region A contains high amounts of elements Si (5.5 wt %) and S (3.9 wt %). Both are the characteristic elements in the bis-sulfur silane film. 1.4 wt % of Mg (i.e., the regular content for AA 2024-T3 alloy) was also detected in region A, indicating that the AA 2024-T3 substrate is still protected effectively by the silane film in region A where dealloying of Mg is inhibited.

Region B is the area where the topside film has been delaminated. The composition of region B is analogous to that of region A. It should be noted that region B is not simply the AA 2024-T3 substrate exposed after film delamination, as both Si and S detected in region B are not the major alloying elements in AA 2024-T3. The nominal Si content of bare AA 2024-T3 is relatively low, i.e., only 0.5 wt %, and no S content is given in the source [96]. The abnormally high amount of Si and S in region B is therefore strong indication that region B is indeed a new region developed in the system. In combination with the previous EIS results in Chapters 3 and 4, it is concluded that region

B is very likely the interfacial layer illustrated in Figure 4.5. In the previous the EIS measurements in Chapters 3 and 4, this interfacial layer was first detected as an additional time constant (RC3) gradually appearing in the middle of the frequency range during various curing processes, (e.g., curing at 100°C or immersion in water). The formation of this interfacial layer is suggested as a result of the condensation reactions in the interfacial region during different curing processes. The substrate under the interfacial layer in region B is also protected, as evidenced by the regular amount of Mg (1.2 wt %) detected in this region.

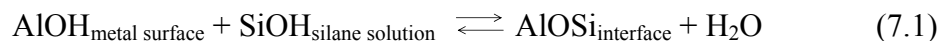
The composition of region C is featured by high contents of O (45.3 wt %) and Cl (6.2 wt %), and low amounts of Al (37.8 wt %). This is indicative of the formation of the corrosion products, most likely aluminum oxychlorides [$\text{Al}(\text{OH})\text{Cl}_2$ and $\text{Al}(\text{OH})_2\text{Cl}$] [48]. It is also noted in Table 7.1 that 7.6 wt % of Cu in region C exceeds its regular amount in AA 2024-T3 (i.e., 3.8 – 4.9 wt %) [96]. Furthermore, no Mg was detected in region C. This observation confirms that corrosion of AA 2024-T3 indeed starts with significant dealloying of Mg from S phase. This consequently causes Cu enrichment of the S phase remnants. Details were discussed in Chapter 6 as well as in the studies by others [59,61,65]. The amount of Si (1.4 wt %) and S (1.6 wt %) is also noticeable in region C, which stems from the residues of the interfacial layer (shown in region C in Figure 7.9(b) as small pieces).

7.2.3. General discussion

7.2.3.1. Mechanism for corrosion protection of AA2024-T3 by bis-sulfur silane

In the initial immersion period, the outermost silane film acts as a physical barrier to retard the electrolyte penetration. Such function, however, is lost once the film has been saturated with the electrolyte after 4 days (Figure 7.8). The interfacial layer therefore plays a critical role in the subsequent corrosion inhibition process.

It is known that in ambient, a bare metal surface is commonly covered with a hydroxide layer with a number of hydrophilic metallic hydroxyl groups (MeOH, Me stands for metals), i.e., AlOH groups in the case of Al. These hydrophilic hydroxyl groups are the favorable sites for the adsorption of water molecules from aqueous media or moisture. After the silane treatment, a number of AlOH groups are consumed in the condensation reaction with SiOH groups from silane solutions, forming AlOSi covalent bonds at the interface according to the following reaction equilibrium



Apparently, a number of favorable sites for water adsorption are blocked due to the loss of hydrophilic AlOH groups. The tendency of aqueous corrosion on the metal surface is therefore effectively reduced. This is actually physical inhibition rather than chemical inhibition, as no changes are seen in E_{corr} and the slopes of the curves in the DC polarization curves (Figures 7.2 and 7.3).

As also noticed above, the “zig-zag” region observed at higher voltages on curve 2 in Figure 7.2 is probably related to the breakdown of the silane film. This phenomenon can be explained as follows. Unlike the bare AA 2024-T3 where the corrosion products generated at lower applied voltages can readily transport away from the original corrosion sites and thus leads to continuous metal dissolution, the corrosion products generated under the interfacial is difficult to diffuse away from the original corrosion sites due to a good adhesion between the metal and the interfacial layer. The corrosion products would thus accumulate in-situ. This obviously hinders pit growth underneath. In time, the accumulated corrosion products would cause tensile stresses in the silane film due to the mismatch in the densities of the silane film and the corrosion products. This would eventually break the film down (interfacial layer + outermost silane film), as reflected as a “zig-zag” region in Figure 7.2.

In summation, the interfacial layer inhibits corrosion of AA 2024-T3 in the following two ways: (1) blocking favorable sites for water adsorption by the formation of AlOSi at the metal surface which effectively reduces the tendency of aqueous corrosion; and (2) restricting transportation of the existing corrosion products away from their original sites which hinders the pit growth.

It should be pointed out here that although the formation of AlOSi bonds effectively reduce the corrosion tendency at the metal surface, the bonds themselves are not hydrolytically stable [1]. That is, AlOSi bond tends to hydrolyze back reforming AlOH and SiOH groups when encountering a large amount of water according to reaction equilibrium (7.1). Obviously, such hydrolysis is detrimental from a corrosion protection

point of view. Therefore, effective methods to prevent this hydrolysis should be searched for. A more detailed discussion on this aspect will be given later.

As the immersion continues, pits were eventually observed (see Figures 7.9(a) and (b)). It is very likely that pitting starts at certain defective sites where are poorly covered by the silane film. The electrolyte is thus relatively easy to intrude into the metal surface. When a sufficient amount of water arrives, AlOSi bonds are hydrolyzed locally. The metal surface underneath again becomes hydrophilic and is then a favorable place for adsorption of water molecules. As a result, the silane film delaminates and corrosion occurs. Over time, the amount of corrosion products increases in situ which would eventually break down the interfacial layer forming visible pits like those shown in Figure 7.9.

It is also observed in Figure 7.9(b) that the micro-cracks formed in region A (i.e., outermost silane film) is never seen in region B (i.e., the interfacial layer). This is most likely the result of film swelling of the outermost silane film. Since film swelling is usually caused by severe water uptake in the film, this observation actually implies that the outermost silane film is porous-structured and is highly permeable to water. In contrast, the interfacial layer (i.e., region B) does not exhibit such cracking in Figure 7.9(b), indicating that the interfacial layer is denser and therefore is not favorable to water penetration.

In summary of the above discussion, it is clear that the formation of AlOSi covalent bonds at the interface is highly desirable from a good corrosion protection perspective. The more AlOSi bonds formed, the more AlOH groups consumed, and eventually the more hydrophobic the treated metal surface will be. Following this

concept, bis-silanes have been extensively employed in practice, as bis-silanes are capable of forming a high density of AlOSi bond at the interface. A detailed discussion is given as follows.

7.2.3.2. Enhancement of interfacial adhesion: bis-silanes vs. mono-silanes

As shown in Figure 7.10, each bis-silane molecule contains 6 hydrolyzable OR groups (Figure 7.10(b)), which doubles the number of that of mono-silane molecule (Figure 7.10(a)). Assuming that both silanes are completely hydrolyzed in their solutions, then each bis-silane molecule would generate 6 SiOH groups available for the subsequent condensation reactions while each mono-silane molecule only has 3 SiOH groups. After the Al substrate treated with the silane solutions, AlOSi covalent bonds are formed at the interface and SiOSi bonds in the silane films.

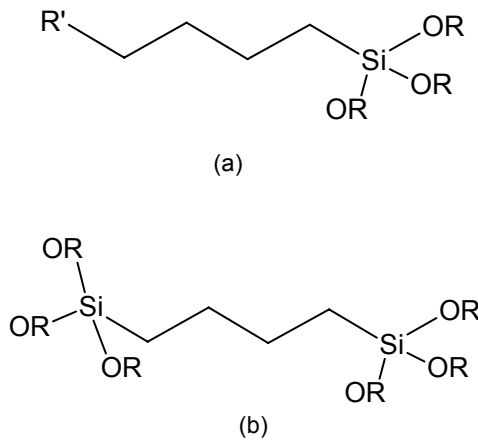
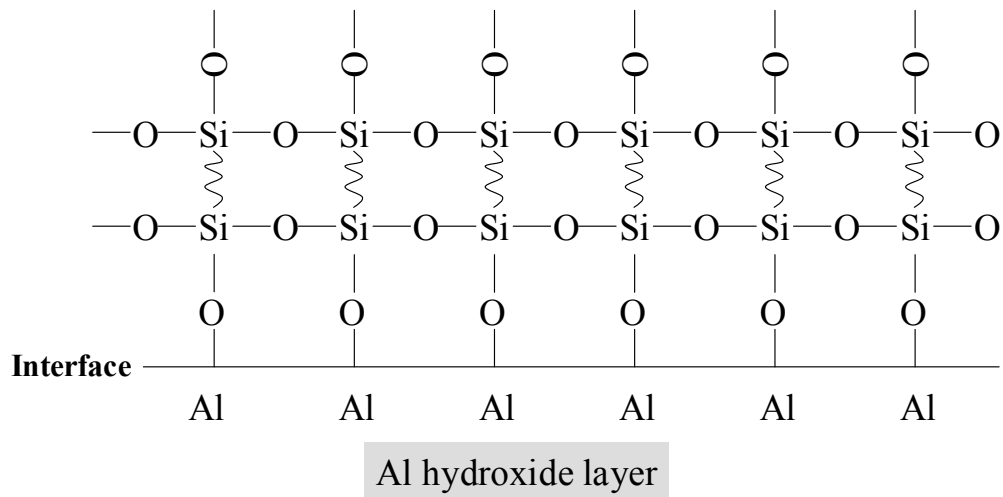
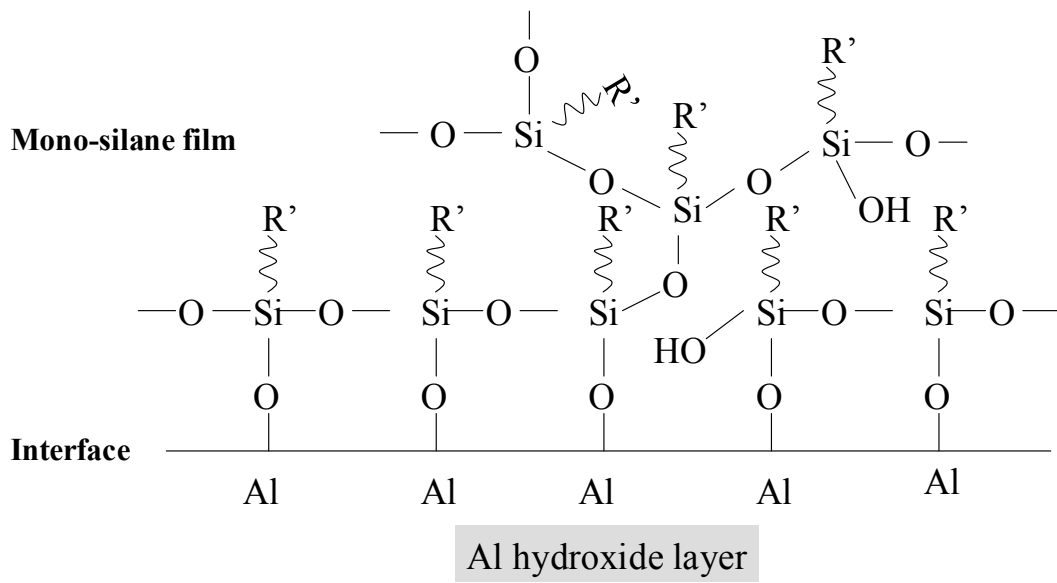


Figure 7.10. Structures of bis-silane molecule (a), and mono-silane molecule (b)

Since the number of SiOH groups of bis-silane molecules doubles that of mono-silane molecules, bis-silane molecules are therefore more reactive than mono-silane molecules. On one hand, bis-silane molecules are capable of reacting with more AlOH groups on the Al substrate forming an interface with a high density of AlOSi bonds. On the other hand, the remaining SiOH groups condense with themselves building up a crosslinked silane film (i.e., SiOSi network) of an appreciable thickness on the top. Mono-silane molecules, however, cannot achieve this. A comparison of possible interfacial regions formed in these two systems is given in Figure 7.11. It is clearly seen that the interfacial region developed between a bis-silane film and the Al substrate (Figure 7.11(a)) contains a higher density of AlOSi bonds than that of a mono-silane film (Figure 7.11(b)). In addition, the mono-silane film structure developed on the Al substrate is porous due to the lack of SiOH groups. Thus, we can expect that the use of bis-silanes leads to a more hydrophobic metal surface than mono-silanes. In the case of bis-sulfur silane, sulfur (S) atoms in the bis-sulfur silane are not highly affinity to Al, therefore the preferential reaction in the interface is the condensation of AlOH and SiOH groups.



(a)



(b)

Figure 7.11. Schematic of bonding mechanism in mono-type silane/Al system; (a) bonding of bis-silane to Al, and (b) bonding of mono-silane to Al

7.2.3.3. *Enhancement of water resistance of silane films*

As mentioned above, AlOSi bond suffers hydrolysis when encountering a large amount of water. To prevent hydrolysis of AlOSi bond, it is necessary to minimum water uptake in the film. In other words, water resistance or hydrophobicity of the silane film is essential in this regard. A common way to improve the water resistance of a silane film is to form an extensively crosslinked structure. In this way, the film porosity is reduced. Moreover, a number of hydrophobic SiOSi units as a product of film crosslinking would also enhance the intrinsic film hydrophobicity. Additionally, in the case of bis-sulfur silane film, sulfur chains ($-S_4-$) carried by bis-sulfur silane molecule are hydrophobic. These sulfur chains would also contribute the film hydrophobicity. Thus, water penetration would be difficult in such an extensively crosslinked bis-sulfur silane film. AlOSi bonds at the interface are therefore secured and furthermore, a good corrosion protection of the metal is guaranteed.

7.3. **Conclusions**

1. The results from the corrosion study of bis-sulfur silane-treated AA 2024-T3 system showed that the highly crosslinked interfacial layer developed in the system is an important contributor in the corrosion protection of AA 2024-T3. This interfacial layer inhibits corrosion in the following two ways: (1) blocking favorable sites for water adsorption by the formation of AlOSi bonds at the interface which effectively reduces the

tendency of aqueous corrosion; and (2) restricting transportation of the existing corrosion products away from their original sites which hinders the pit growth.

2. Bis-silanes are highly desirable from a corrosion protection perspective, as bis-silanes are capable of forming a high density of AlOSi bond at the interface. This would effectively reduce the number of favorable sites for water adsorption.

3. High water resistance of silane films is required in order to prevent hydrolysis of AlOSi bonds at the interface. Two major ways can be employed to achieve this: (1) highly crosslinking of the film to form as many as hydrophobic SiOSi units which in the meantime reduces the film porosity; and (2) employing silanes with hydrophobic substitution, such as hydrophobic sulfur chains in bis-sulfur silane, to enhance the intrinsic film hydrophobicity. Such film structure is expected to greatly delay water penetration. As a result, AlOSi bonds are secured and therefore corrosion control of AA 2024-T3 is guaranteed.

Chapter 8. Enhanced Corrosion Resistance of AA 2024-T3 and HDG Using A Silane Mixture of Bis-[triethoxysilylpropyl]-tetrasulfide and Bis-[trimethoxysilylpropyl]amine¹

Abstract The corrosion resistance of AA 2024-T3 and Hot-dip Galvanized steel (HDG) was studied after treatment with bis-[3-(triethoxysilyl)propyl]tetrasulfide (bis-sulfur silane), bis-[trimethoxysilylpropyl]amine (bis-amino silane) and their mixture. Electrochemical tests in a neutral 0.6 M NaCl solution as well as SEM/EDX were performed. The results showed that: (1) Hydrophilic bis-amino silane did not offer good corrosion protection on either of the metals. This is because the bis-amino silane film tends to be positively charged. This promotes ingress of anions like Cl⁻ ions as well as water into the film by electrostatic attraction. As a result, corrosion readily proceeds at the metals. (2) Hydrophobic bis-sulfur silane performed very well on AA 2024-T3, but failed on HDG. The failure stems from non-uniform film coverage on HDG owing to an insufficient wetting of bis-sulfur silane solution on the Zn oxide on HDG. Local corrosion initiates at defective sites where are poorly covered by the silane film. (3) The bis-sulfur/bis-amino mixture at the ratio of 3/1 greatly enhanced the corrosion resistance of both AA 2024-T3 and HDG. This substantial improvement is achieved by selectively overcoming the major shortcomings of the above individual silanes.

¹ The chapter is submitted to Acta Eelectrochim for publication

8.1. Introduction

As previously reported, some of bis-silanes perform very well on metals in terms of their corrosion protection. However, it was also found that the performance of these bis-silanes is highly dependent upon metals. The bis-sulfur silane, for example, exhibited good corrosion protection of Al alloys, but it failed when applied to hot-dip galvanized steel (HDG). This is surely not desirable for industries where metallic assemblies or structures are made up of more than one metal. Therefore, our efforts were made to develop a universal silane system that should provide protection for more than one metal. Preliminary studies on a number of promising bis-silanes showed that a mixture based on bis-sulfur and bis-amino silanes performed extraordinarily well on AA 2024-T3 and HDG. Unlike the individual silanes, the mixture of bis-sulfur and bis-amino silanes at a volume ratio of 3 to 1, survived a 0.6 M NaCl immersion tests very well for AA 2024-T3 during 32 days of exposure, and HDG during 8 days of exposure. The individual silanes, on the contrary, did not survive on both metals. Obviously, a certain synergic effect is generated by mixing these two individual silanes at the ratio of 3/1. This chapter is devoted to understand this synergic effect of the silane mixture on the corrosion protection of AA 2024-T3 and HDG by using electrochemical tests and SEM and EDX. 5% of bis-sulfur and bis-amino silane solutions were prepared according to the experimental details in Chapter 2. The mixture solution of bis-sulfur and bis-amino silanes was made simply by mixing the above individual silane solutions at a bis-sulfur/bis-amino ratio of 3/1. The measured pH of the mixture solution was 7.5. The

silane-treated panels were cured at 100°C for 24 hrs to obtain a highly cross-linked silane film.

8.2. Results and Discussion

8.2.1. Silane film thickness measurements

Table 8.1 reports the film thickness of three silanes studied here. The silane films were deposited on a mirror-like stainless steel (SS) surface from their 5% silane solutions, and were cured at 100 °C for 1 hr and aged in the ambient condition for two weeks. It is seen that the bis-amino silane film has the greatest film thickness value, i.e., 798.5 nm, among the three silanes, while the bis-sulfur silane film is the thinnest with the value of 440 nm. The mixture film has the thickness of 698.7 nm between the two individual silane films. It is also noted that the bis-sulfur silane film gives the highest non-uniformity value of 10%, suggesting that the bis-sulfur silane film does not cover the substrate very homogenously, as compared to the others. Both bis-amino silane and the mixture films offer better film coverage on the substrate, as evidenced by the smaller non-uniformity values, i.e., 7% and 5%.

Table 8.1. Film thickness of three silanes deposited on SS

| Silane | Thickness (nm) | Non-uniformity (%) |
|--------------------------------|----------------|--------------------|
| Bis-sulfur silane (5%, pH 6.5) | 440.0 | 10 |
| Bis-amino silane (5%, pH 7.5) | 798.5 | 7 |
| Mixture (5%, 3/1, pH 7.5) | 698.7 | 5 |

8.2.2. Electrochemical studies of silane-treated AA 2024-T3 and HDG in a neutral 0.6 M NaCl solution

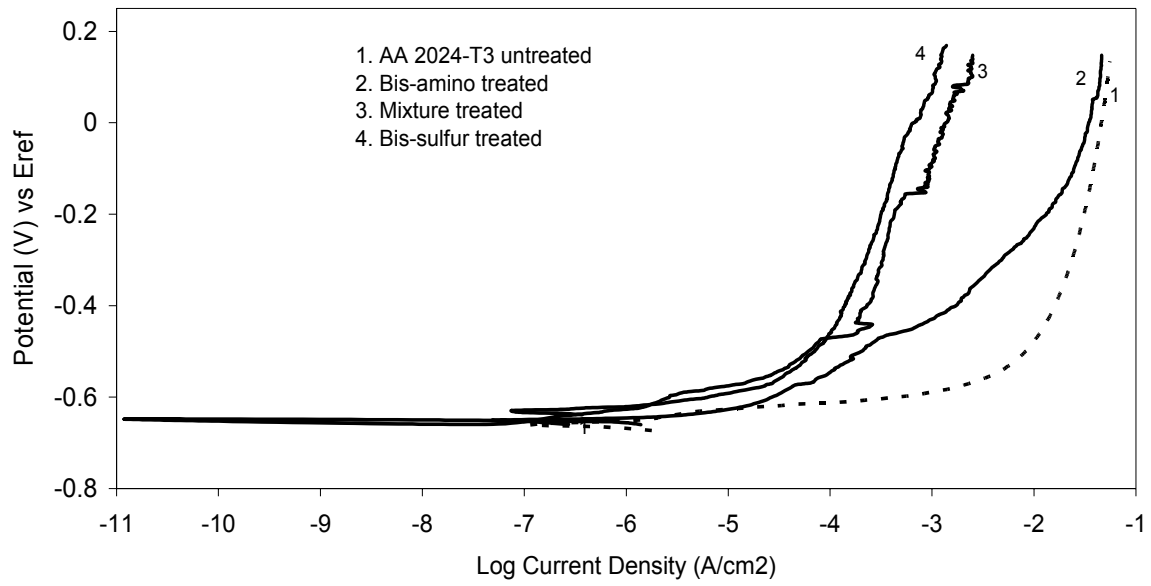
(a) AA 2024-T3

Figures 8.1 (a) and (b) display the anodic and cathodic polarization behaviors of AA 2024-T3 treated with and without silanes measured in 0.6 M NaCl (pH 6.5) after 8-hr exposure. It is seen in Figure 8.1(a) that the current density for the untreated panel (curve 1) increases rapidly with applied voltages until the value of 10^{-2} A-cm² is reached, which reflects fast metal dissolution. After treated with bis-sulfur silane and the mixture (curves 3 and 4), the increase in the anodic current densities is largely slowed down. A nearly-potential-independent region is formed after 10^{-5} A-cm². This indicates that the extent of metal dissolution has been reduced by the silane deposition. The mechanism concerning this inhibitive effect is attributed to the formation of AlOSi covalent bonds between an interfacial layer and the substrate, as detailed in Chapter 7. A “zig-zag” region is again seen for the bis-sulfur and the mixture at higher voltages (curves 3 and 4). It has been stated in Chapter 7 that such “zig-zag” behavior is actually related to silane film

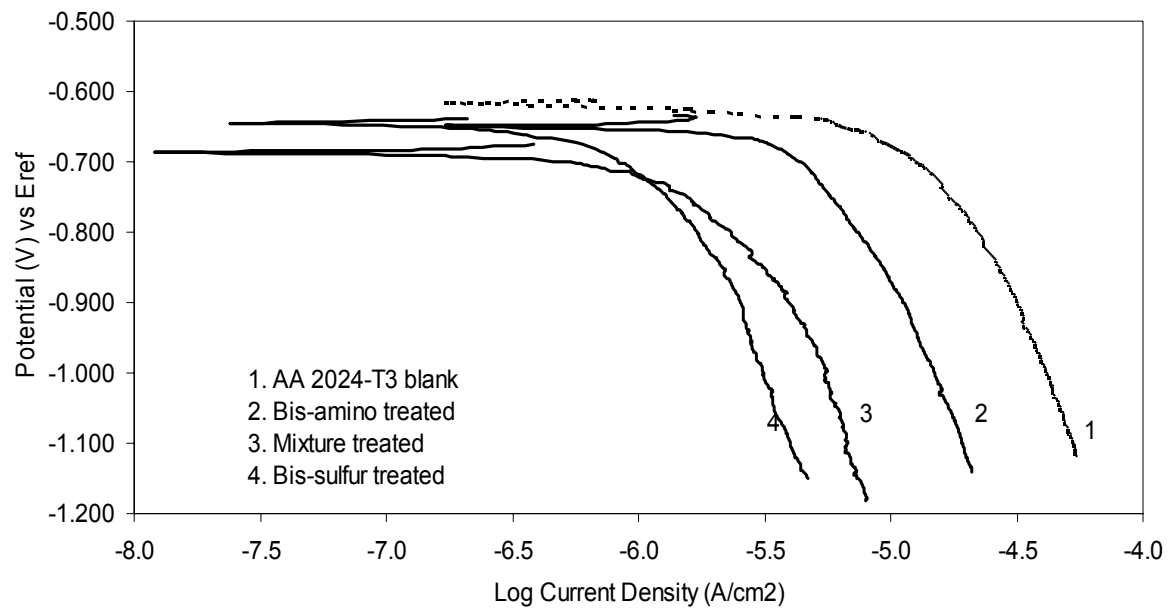
breakdown. The bis-amino silane, in contrast with the two above silanes, shows no suppression in the anodic current density (curve 2). This indicates that the bis-amino silane film cannot provide sufficient corrosion protection for AA 2024-T3. The tested panel surfaces were visually inspected after the test ending at 0.2 V/SCE. Both untreated and bis-amino silane treated surfaces extensively corroded, while the other two surfaces treated with the bis-sulfur silane and the mixture only showed a few tiny pits. This further supports that both bis-sulfur silane and the mixture offer good corrosion protection for AA 2024-T3, but not the bis-amino silane.

The cathodic behaviors of the three silanes shown in Figure 8.1(b) have a similar trend. The current densities for all silane-treated AA 2024-T3 panels shift to lower values compared to that for the untreated AA 2024-T3 (curve 1), with the shifts for the bis-sulfur and the mixture being the greatest extent (curves 3 and 4). The performance of the bis-amino silane, again, is inferior with respect to the other two silanes.

Since changes are not obviously seen in the curve shapes and E_{corr} values for all samples in Figures 8.1(a) and (b), it is thus concluded that the silanes deposited on the AA 2024-T3 primarily perform as a physical barrier rather than a chemical barrier like a conventional chromate layer [107–110]. That is, the formation of AlOSi bonds at the interface effectively blocks a number of active anodic as well as cathodic sites for redox reaction.



(a)



(b)

Figure 8.1. DC polarization curves of the silane-treated AA 2024-T3 panels, measured in a neutral 0.6 M NaCl solution; (a) anodic polarization, and (b) cathodic polarization

The long-term corrosion performance of the silane-treated AA 2024-T3 system in 0.6 M NaCl was examined using EIS. The EIS plots were obtained at the OCPs after 32 days of immersion, as shown in Figures 8.2(a) and (b). The impedance behavior of the bis-sulfur and the mixture-treated AA 2024-T3 is comparable, with a high low-frequency impedance (Z_{lf}) values above $10^5 \Omega$ (exposure area: 5.06 cm^2). The bis-amino silane, again, shows a poor performance. Its Z_{lf} value is nearly one order of magnitude lower than those of the bis-sulfur silane and the mixture. In the corresponding phase angle plot (Figure 8.2(b)), two-time-constant behavior is observed for both bis-sulfur silane and mixture-treated AA 2024-T3 systems (curves 3 and 4), while only one time constant is seen for the bis-amino silane-treated and the bare AA 2024-T3 (curves 1 and 2). This two-time-constant-behavior for the bis-sulfur silane-treated AA 2024-T3 system was discussed in detail in Chapters 3, 4 and 7. According to these studies, the time constant at high frequencies ($\sim 10^4 \text{ Hz}$) is attributed to the outermost bis-sulfur silane film, while the one at middle frequencies (10 Hz) is due to the interfacial layer formed in the bis-sulfur silane-treated AA 2024-T3. The existence of this interfacial layer has been consistently confirmed in the previous EIS measurements as well as SEM/EDX observations (Chapters 3 and 7). The mixture shows an EIS behavior similar to that of the bis-sulfur silane, suggesting that the mixture has a comparable performance and an analogous structure on AA 2024-T3 as the bis-sulfur silane. In the case of the bis-amino silane, one time constant centered at middle frequencies in Figure 8.2 is possibly due to its interfacial layer. The lack of impedance response for the outermost bis-amino silane film is most likely related to its hydrophilic nature that highly promotes water/ion penetration. More details regarding this aspect will be discussed later.

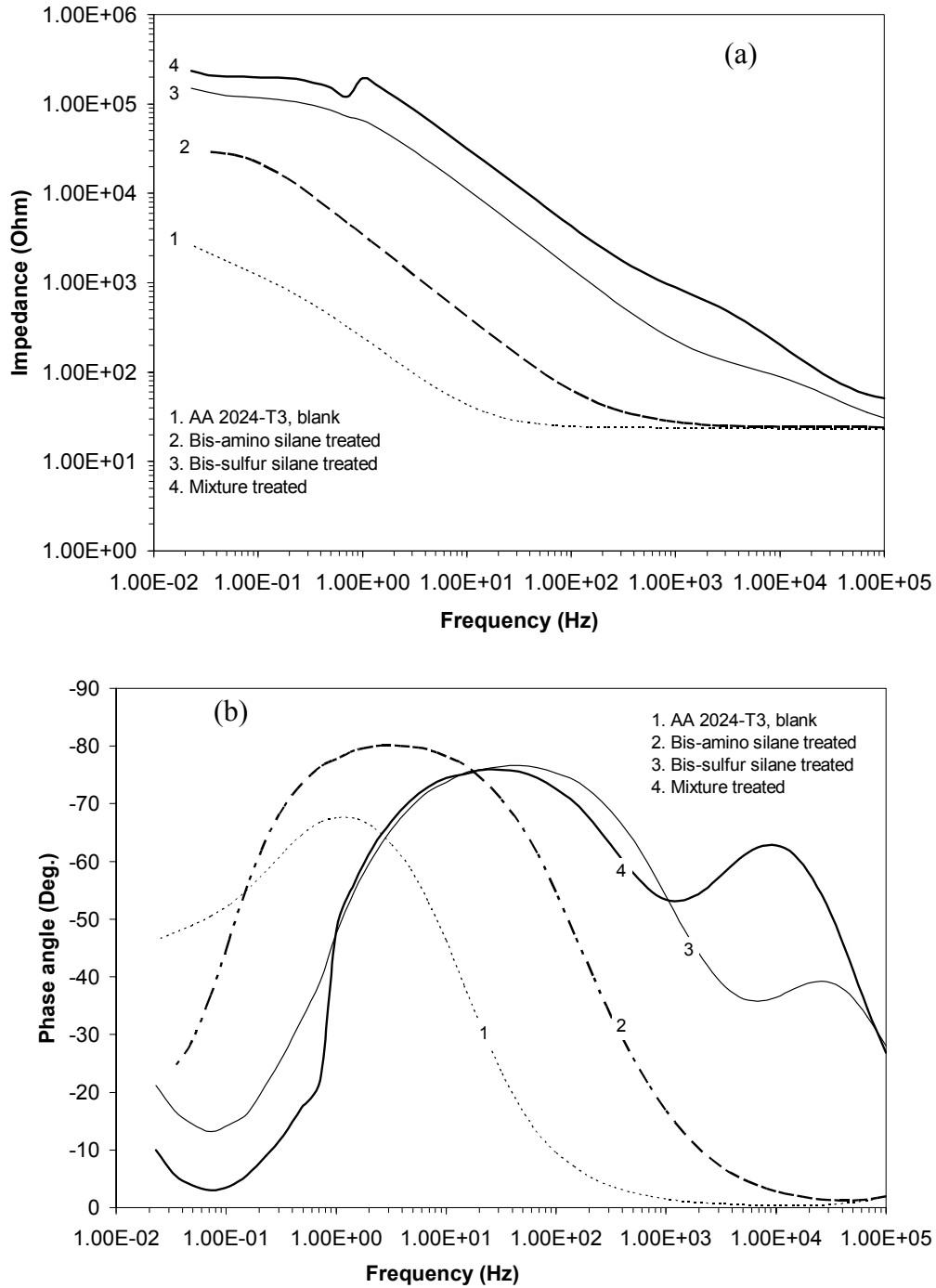
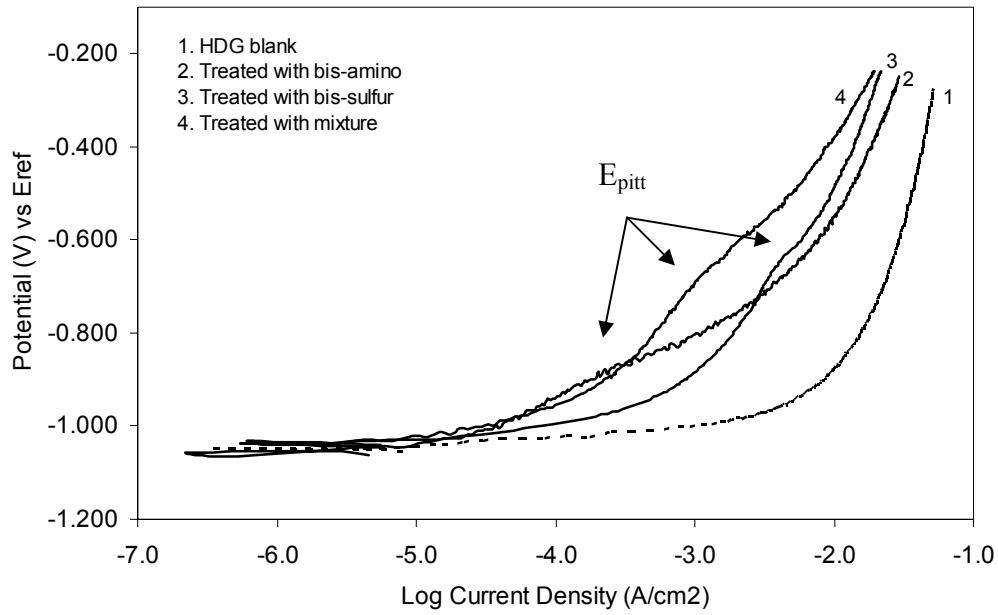


Figure 8.2. Bode plots of silane-treated AA 2024-T3 panels in a neutral 0.6 M NaCl solution after 32 days of exposure; (a) impedance plot, and (b) phase angle plot (exposed area: 5.06 cm²)

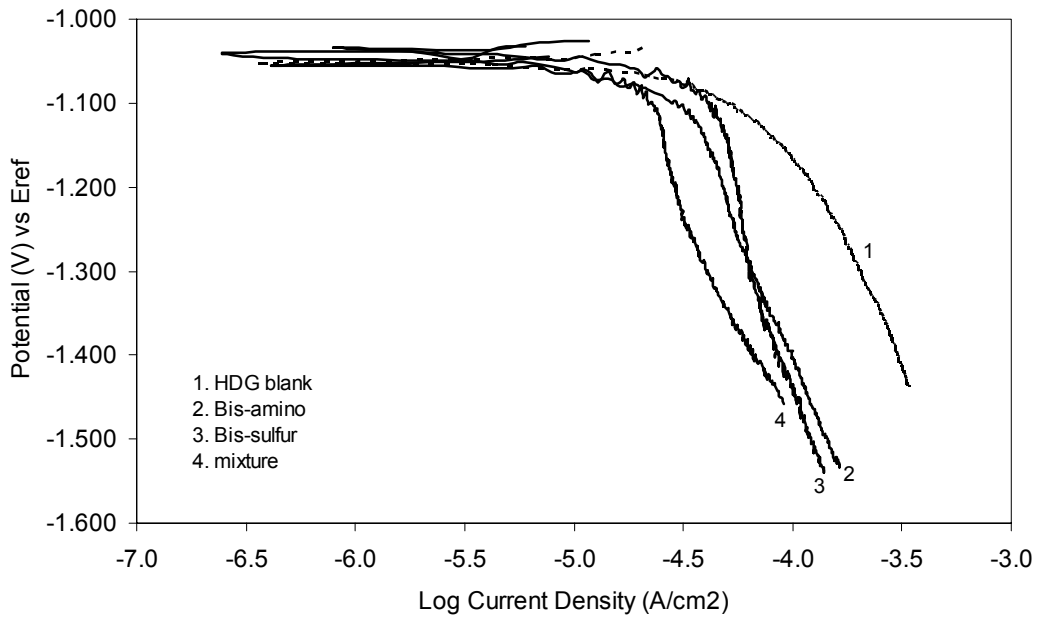
(b) HDG

Figures 8.3(a) and (b) exhibit the anodic and cathodic polarization curves of HDG treated with and without the silanes, obtained in 0.6 M NaCl after 3 hrs of exposure to the electrolyte. In Figure 8.3(a), the anodic current density for the bare HDG increases rapidly at its OCP at around -1.05 V/SCE, followed by a nearly potential-independent region after achieving 10^{-2} A-cm² (curve 1). This indicates that the Zn coating on HDG initially experiences heavy dissolution. The further dissolution slows down after 10^{-2} A-cm², due to the hindrance effect of the corrosion products built up in-situ. The anodic current densities for all silane-treated samples have been reduced to different extents. The mixture performs the best among them, giving considerable suppression (curve 4) soon after the value of 10^{-4} A-cm² is reached. Both bis-sulfur and bis-amino silanes show a certain degree of inhibition (curves 2 and 3), yet their inhibitive effect is not as appreciable as that of the mixture (curve 4).

Interestingly, pitting potentials (E_{pit}) are noticeable on the curves for the silane-treated samples (curves 2 to 4), but not for the curve without the silane treatment (curve 1). It is known [111,112] that Zn corrosion proceeds in the form of general corrosion, therefore E_{pitt} is not expected to see for the bare sample (curve 1). The appearance of E_{pitts} for the silane-treated HDG samples reflects the fact that the silane films formed on the Zn oxide behave as insulating or protective layers till the silane films are broken down at their E_{pitts} .



(a)



(b)

Figure 8.3. DC polarization curves of silane treated HDG panels, measured in 0.6 M NaCl solution; (a) anodic polarization, and (b) cathodic polarization

Cathodic behaviors of the above HDG panels after exposed for 3 hrs in the same electrolyte are presented in Figure 8.3(b). Again, the mixture (curve 4) among all three silanes exhibits the best corrosion protection performance by reducing the cathodic current density to the greatest extent. Bis-sulfur and bis-amino silanes perform similarly in this case (curves 2 and 3), i.e., inferior compared to the mixture.

EIS results after 8-day immersion are compared in Figures 8.4(a) and (b). It is seen in Figure 8.4(a) that, among all silanes, only the mixture-treated HDG system remains a much higher Z_{lf} value than the others after 8 days of immersion. The Z_{lf} values for both bis-sulfur and bis-amino silanes are similar, i.e., approximately one order of magnitude lower than that of the mixture. This is consistent with the result from the above DC polarization tests, showing that the mixture is a better solution for corrosion protection of HDG than the individual silanes. It is also noted that in the corresponding phase angle plot (Figure 8.4(b)), the mixture shows a pronounced time constant with its maximum peak located at about -75° at high frequencies, while the phase angle plots for the others are almost flattened after 8 days of immersion, showing little protectiveness for HDG. Unlike the mixture-treated AA 2024-T3 system which exhibits two time constants (in Figure 8.2(b)), only one time constant is shown for the mixture-treated HDG. This indicates that, rather than forming two distinct layers (i.e., outermost silane layer and interfacial layer) as in the case of AA 2024-T3, the mixture only forms one single structure with HDG that is detectable to EIS.

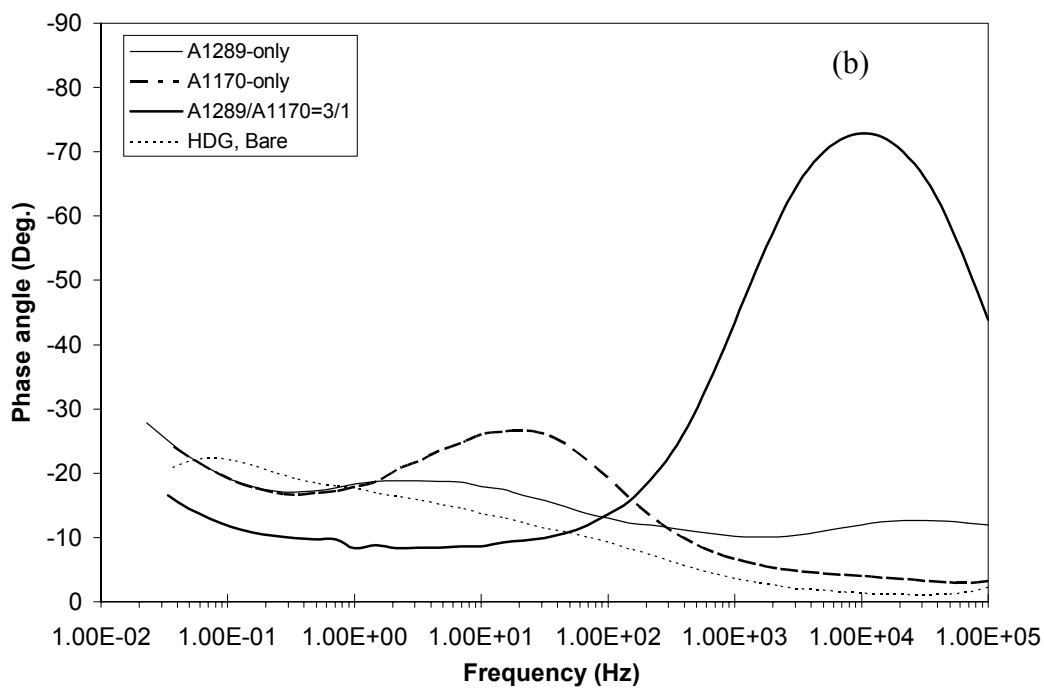
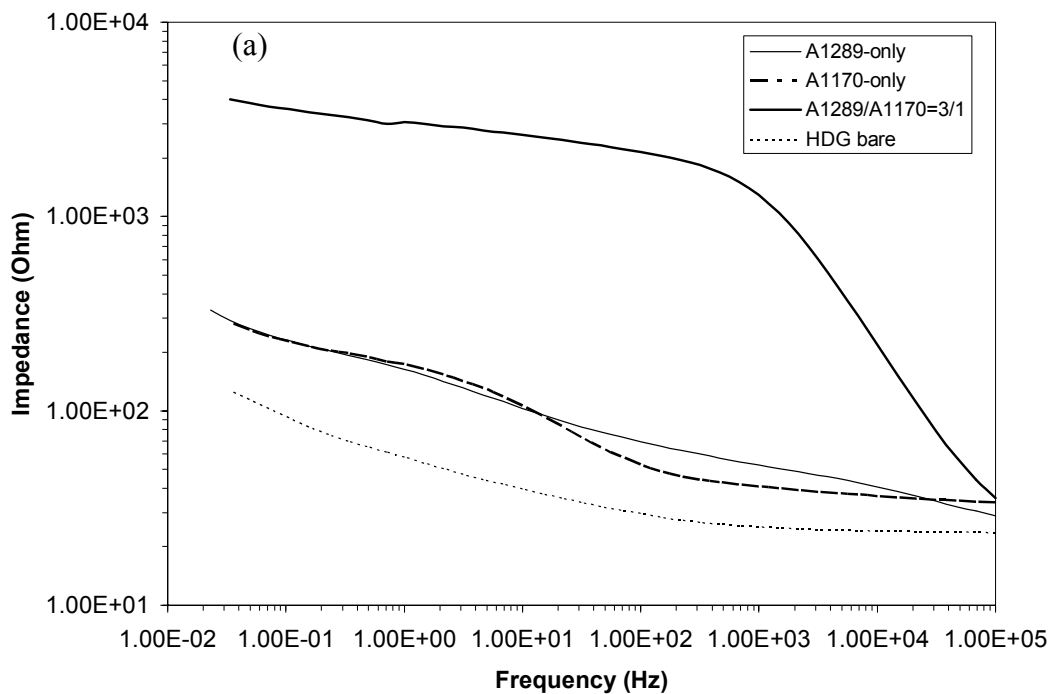
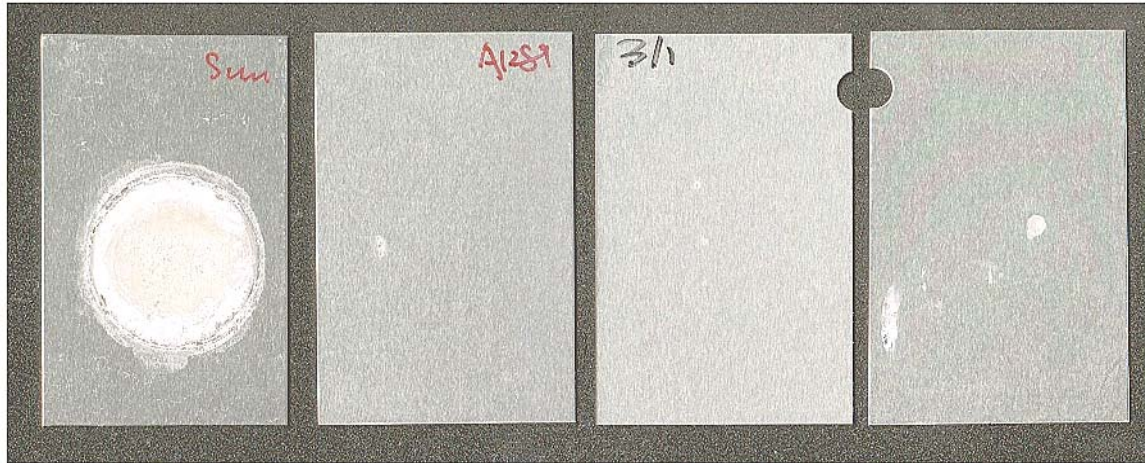


Figure 8.4. Bode plots of silane-treated HDG panels measured in 0.6 M NaCl solution (pH 6.5) after 8 days of exposure; (a) impedance plot, and (b) phase angle plot (exposed area: 5.06 cm²)

Figures 8.5 and 8.6 present the scanned images of both silane-treated AA 2024-T3 and HDG panels after the EIS measurements. It is clearly seen that no corrosion is shown on both mixture-treated AA 2024-T3 and HDG panels (Figures 8.5(c) and 8.6(c)), indicating that the mixture provides good corrosion protection for both metals. The bis-sulfur silane, although performs similarly as the mixture on AA 2024-T3 (Figure 8.5(b)), its performance on HDG is very poor (Figure 8.6(b)). The bis-amino silane consistently exhibits its poor corrosion performance on both alloys, i.e., large pitting patches on AA 2024-T3 (Figure 8.5(d)) whilst uniform corrosion on HDG (Figure 8.6(d)). Based upon the above results, the silanes can thus be ranked as follows in terms of their protective efficiency on AA 2024-T3 and HDG (from the best to the worst): mixture (bis-sulfur/bis-amino = 3/1) > bis-sulfur silane > bis-amino silane.

8.2.3. SEM observation of silane-treated AA 2024-T3 and HDG surfaces after immersion in a neutral 0.6 M NaCl solution

In this section, we are attempting to understand the corrosion mechanisms for all silane-treated systems from a microstructure point of view. Prior to SEM and EDX examination, all samples were exposed to a neutral 0.6 M NaCl solution for various times to initiate pits, i.e., 15 days for AA 2024-T3 and 5 days for HDG.



(a)

(b)

(c)

(d)

Figure 8.5. AA 2024-T3 panels after 32 days of immersion in 0.6 M NaCl solution; (a) untreated, (b) bis-sulfur silane treated, (c) mixture-treated, and (d) bis-amino silane-treated



(a)

(b)

(c)

(d)

Figure 8.6. HDG panels after 8 days of immersion in 0.6 M NaCl solution; (a) untreated, (b) bis-sulfur silane treated, (c) mixture-treated, and (d) bis-amino silane treated

(a) AA 2024-T3

The SEM images of pitting areas on the silane-treated AA 2024-T3 surfaces after immersion shown in Figures 8.7(a), (b) and (c). Similar features are seen for all pitted areas on these three silane-treated surfaces. Three distinct regions are identified for all the samples, indicated as regions A, B and C in the figures. Obviously, region A is the silane-coated area where the substrate is still covered continuously with the intact silane film. Region B is the unattacked area from which the topside silane film has been delaminated. It is noted that some micro-cracks are formed in region A that is adjacent to region B. The formation of these micro-cracks was primarily caused by film swelling during immersion, as discussed in Chapter 7. Region C shows a heavily corroded area, where the metal has been eaten away. EDX identification of these three regions for all silane-treated AA 2024-T3 panel surfaces is listed in Table 8.2.

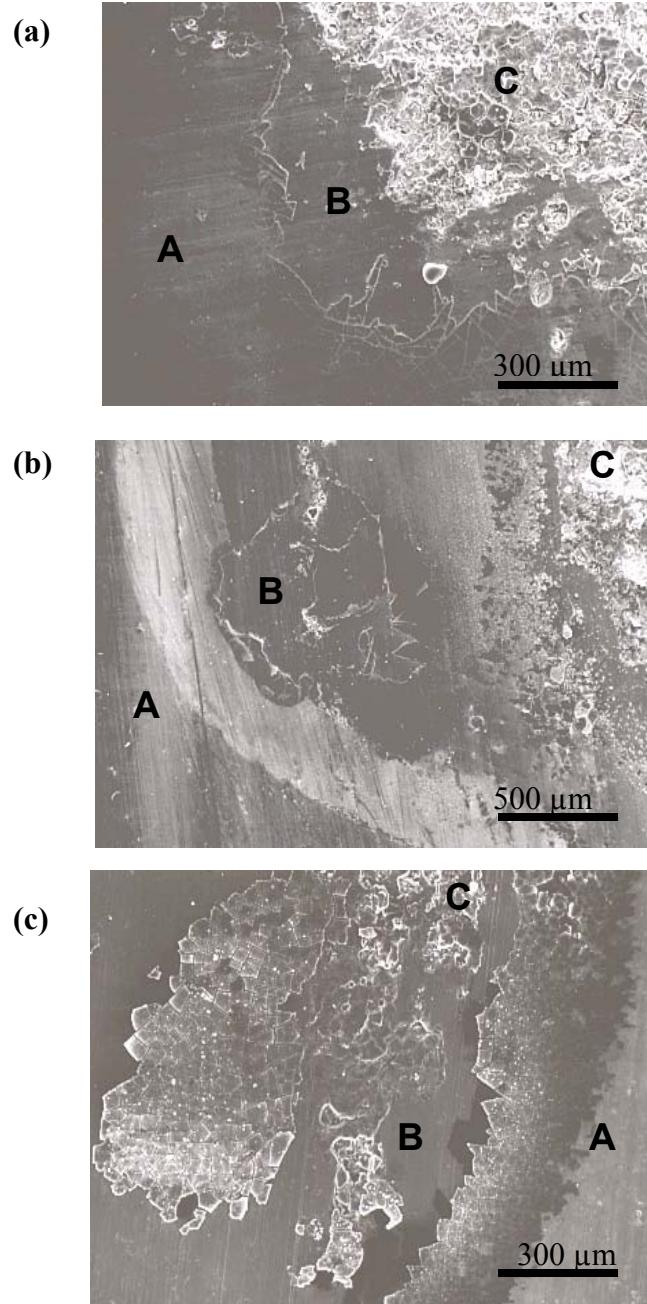


Figure 8.7. SEM images of silane-treated AA 20240T3 surfaces after 32 days of immersion in a neutral 0.6 M NaCl solution; (a) bis-sulfur silane-treated, (b) bis-amino silane-treated, and (c) mixture-treated

Table 8.2. Compositions (wt. %) of three regions in silane-treated AA 2024-T3 systems

| Elem. | Region A | | | Region B | | | Region C | | | AA |
|-------|------------|-----------|------|------------|-----------|------|------------|-----------|------|--------------|
| | Bis-sulfur | Bis-amino | Mix | Bis-sulfur | Bis-amino | Mix | Bis-sulfur | Bis-amino | Mix | 2024-T3 [96] |
| O | 8.0 | 13.3 | 12.3 | 6.7 | 9.6 | 5.1 | 43.0 | 34.3 | 22.4 | -- |
| Mg | 1.3 | 1.0 | 1.5 | 1.2 | 1.0 | 0.9 | -- | -- | -- | 1.2-1.8 |
| Al | 81.4 | 70.8 | 71.5 | 74.2 | 74.8 | 77.4 | 28.5 | 53.3 | 67.5 | Rem |
| Si | 2.7 | 8.5 | 6.6 | 7.1 | 8.8 | 8.0 | -- | 4.4 | 0.7 | 0.5 |
| S | 2.3 | -- | 4.4 | 6.2 | -- | 4.6 | -- | -- | -- | -- |
| Cl | -- | 1.6 | -- | 0.5 | 1.2 | -- | 0.8 | 1.0 | -- | -- |
| Cu | 4.3 | 4.8 | 3.7 | 4.1 | 4.6 | 3.9 | 27.5 | 6.7 | 9.0 | 3.8-4.9 |

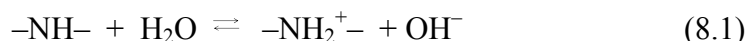
It is seen in Table 8.2 that the compositions of regions A and B are analogous for all silanes: both regions are featured with a higher amount of Si, varying from 2.3 to 8.8 wt %, with respect to bare AA 2024-T3. Such a high content of Si detected in region B strongly suggests that region B is not simply the bare AA 2024-T3 substrate (nominally contains 0.5 wt % of Si [96]) exposed after the delamination of the topside silane film, but is probably a new structure, the so-called interfacial layer, formed between the bis-sulfur silane and the substrate. Indeed, this interfacial layer was first detected as an additional time constant (RC3) appearing in various curing processes in the previous EIS studies (see Chapters 3 and 4). This interfacial layer is thought to consist of SiOSi and SiOAl bonds formed via condensation reactions. A schematic of a silane-treated Al system is illustrated in Figure 4.5 in Chapter 4. It was further stated in Chapter 7 that the highly crosslinked interfacial layer rather than the outermost silane film is a major

contributor in corrosion protection of AA 2024-T3. The interfacial layer anchors tightly to the AA 2024-T3 substrate due to a high density of AlOSi bonds formed at the interface. AlOSi bonds are formed by the consuming of hydrophilic AlOH groups at the metal surface. As a consequence, the resulting metal surface becomes so hydrophobic that water adsorption is different. Without the participation of water, corrosion of the metal is inhibited.

As also discussed in Chapter 7, although corrosion inhibition of the metal is intimately related to AlOSi bond, the bond itself is not hydrolytically stable [1]. When encountered a large amount of water, AlOSi bond is hydrolyzed back to reform hydrophilic AlOH groups and SiOH groups. This obviously weakens the hydrophobicity of the metal surface. Therefore, suppression of water uptake in a silane film is of virtual importance in terms of maintaining a good adhesion between the silane film and the substrate. As stated in Chapter 7, there are two major methods which can be employed to enhance water resistance of the film. (1) Fully crosslinking of silane films. On one hand, film porosity is reduced by crosslinking; on the other hand, a hydrophobic SiOSi network is built up by consuming hydrophilic SiOH groups. (2) Enhancing intrinsic film hydrophobicity by introducing hydrophobic organic/inorganic substitutions into the silane film. With the enhancement of water resistance of the silane film, water uptake in the film is suppressed and hydrolysis of AlOSi bond is prevented. The corrosion protection of the metal is therefore guaranteed.

Another important finding in Table 8.2 is that a noticeable amount of chloride was detected for regions A and B in the bis-amino silane treated AA 2024-T3 system, i.e., 1.6 wt% in region A and 1.2 wt% for region B. Such a high amount of chloride, however,

was not found for the bis-sulfur silane and the mixture treated AA 2024-T3 surfaces. This finding reveals the cause behind the inferior performance of the bis-amino silane film. It is commonly known that the secondary amino groups ($-\text{NH}-$) in the bis-amino silane tend to protonate in the presence of water. The protonation can be expressed as below [113]:



$-\text{NH}_2^+$ groups are formed, releasing hydroxide ions (OH^-) as the byproduct. This actually explains why the bis-amino solution is highly alkaline, with a natural pH ~ 10.8 . Since the silane solution tends to gel at such high pH in a few minutes, acetic acid (HAc) is added into the bis-amino solution to reduce the pH to 7 to stabilize the solution. When a metal is treated with the bis-amino silane water/alcohol solution, these $-\text{NH}_2^+$ groups along with the bis-amino silane molecules are deposited on the metal surface, forming a positively-charged silane film. Upon exposing to a NaCl solution, this positively-charged bis-amino silane film will electrostatically attract anions like Cl^- ions as well as water into the film, as illustrated in Figure 8.8. Apparently, corrosion occurs at the metal surface once a sufficient amount of Cl^- ions/water arrives. A similar observation for γ -APS was discussed elsewhere [27,32]. In Chapter 4, the electrostatic attraction of SO_4^- ions by the bis-amino silane film was also noted.

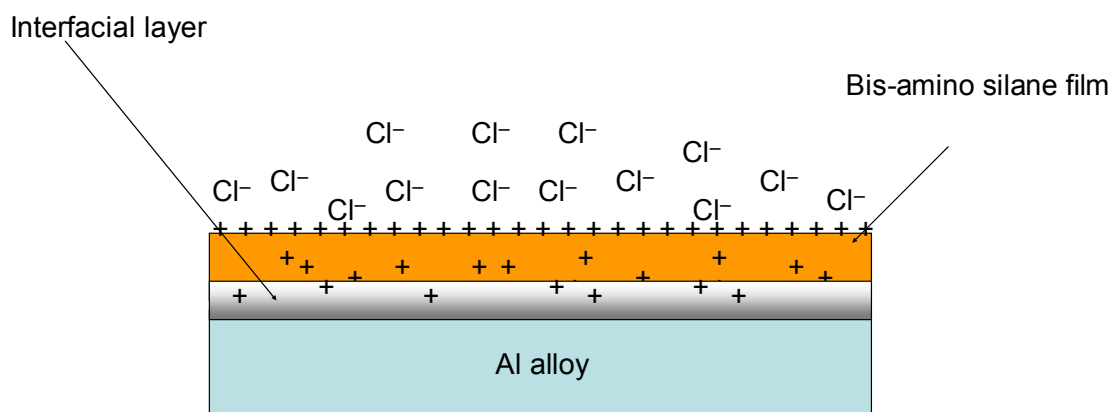
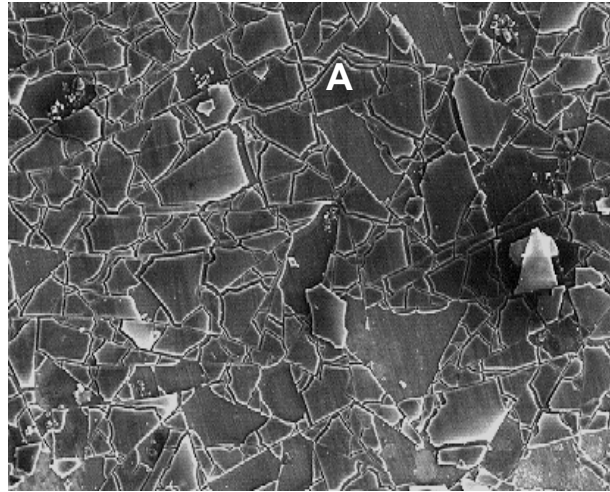


Figure 8.8. Attraction of Cl^- ions in the electrolyte by a positively-charged bis-amino silane film on Al alloy

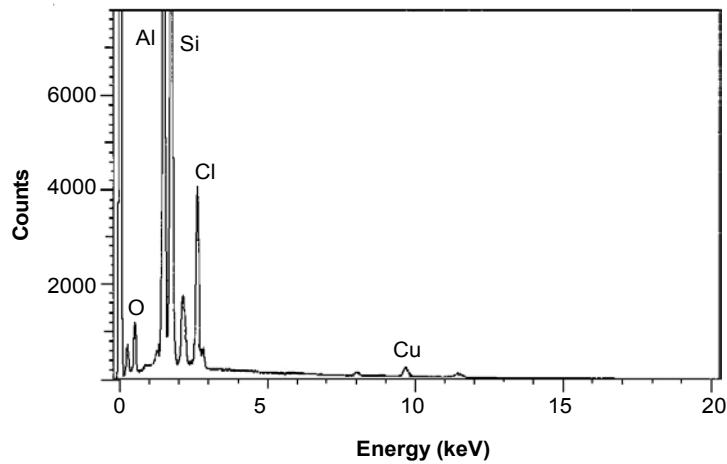
Indeed, the absence of the time constant at high frequencies for the bis-amino silane film in Figure 8.2(b) is also related to this hydrophilic structure. That is, electrolyte intrusion into the hydrophilic outermost bis-amino silane film is so readily that the corresponding impedance response is not detectable to EIS.

Another evidence exists which strongly supports the above view. When further neutralizing OH^- ions with HAc in the bis-amino silane solution (i.e., further decreasing the solution pH), reaction equilibrium (8.1) is driven to the right. More $-\text{NH}_2$ groups are expected to be protonated. As a result, the as-formed bis-amino silane film should be more positively-charged or more hydrophilic as compared to the one from pH 7. Figure 8.9(a) shows the SEM image of an AA 2024-T3 sample treated with a 5% bis-amino silane solution at pH 4, after 4 days of immersion in neutral 0.6 M NaCl. Unlike the bis-amino silane film in Figure 8.7 (b), the entire bis-amino silane film has uniformly cracked into small pieces, spreading all over the alloy surface. Figure 8.9(b) gives the EDX

spectrum of the piece “A” in Figure 8.9(a). Again, a high amount of Cl is observed here, indicating a strong attraction to Cl^- ions of the film. Apparently, the bis-amino silane film was heavily swollen by the electrolyte intrusion during immersion, which resulted in the severe film cracking shown in Figure 8.9(a).



(a) 300 μm



(b)

Figure 8.9. Bis-amino silane-treated AA 2024-T3 (in 5% bis-amino silane solution at pH 4), after immersion in a neutral 0.6 M NaCl solution for 4 days; (a) SEM image, and (b) EDX spectrum of bis-amino silane piece (site A in Figure 8.9(a))

The bis-sulfur silane film, on the contrary, is neutral and is not expected to promote ingress of Cl^- ions/water. Therefore, no chloride content was detected. As for the mixture (bis-sulfur/bis-amino=3/1), although it also contains some amount of $-\text{NH}_2^+$ groups, no chloride signal was detected in the EDX analysis. This suggests that the number of $-\text{NH}_2^+$ in the mixture film is so low that its attraction to Cl^- ions can be negligible. In other words, the film of the mixture is hydrophobic enough to avoid promoting the transportation of Cl^- ions/water, which behaves similar to the bis-sulfur silane. Thus, both bis-sulfur silane and the mixture films provide equally good protectiveness on AA 2024-T3.

(b) HDG

Figure 8.10 shows the SEM images of silane-treated HDG surfaces after immersed in a neutral 0.6 M NaCl solution for 5 days. The EDX results are present in Tables 8.3, 8.4 and 8.5. It is clearly seen in Figure 8.10 that the morphologies of all three silane treated HDG surfaces are distinctly different.

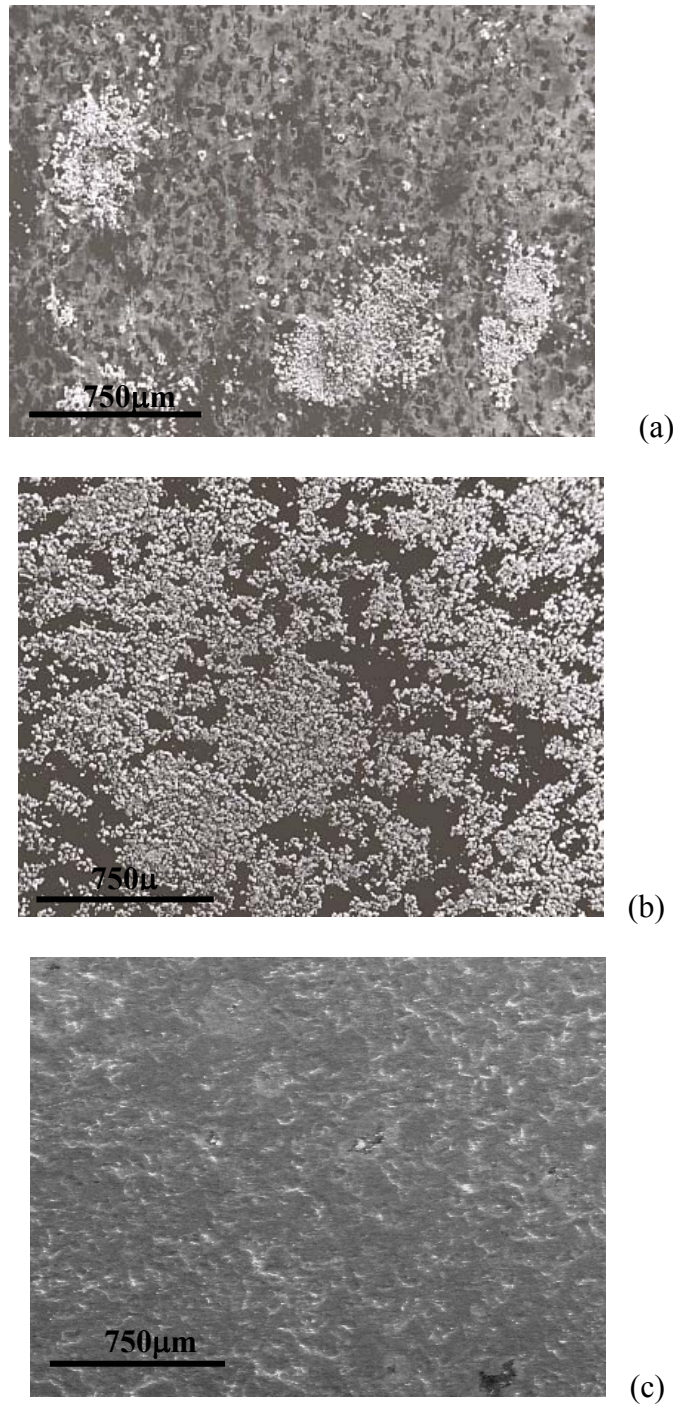


Figure 8.10. SEM images of silane-treated HDG surfaces after 8 days of immersion in a neutral 0.6 M NaCl solution; (a) bis-sulfur silane-treated, (b) bis-amino silane-treated, and (c) mixture-treated

Table 8.3. Compositions of bis-sulfur silane-treated HDG, shown in Figure 8.10 (a)

| Element | Grey region | Dark patch | Corroded region |
|----------------|--------------------|-------------------|------------------------|
| O | 6.7 | 8.7 | 35.8 |
| Si | 5.2 | 17.8 | 0.7 |
| S | 5.4 | 24.1 | -- |
| Cl | -- | -- | 1.4 |
| Zn | 82.7 | 49.1 | 62.0 |

Table 8.4. Compositions of bis-amino silane-treated HDG, shown in Figure 8.10 (b)

| Element | Intact region | Corroded region |
|----------------|----------------------|------------------------|
| O | 8.9 | 39.8 |
| Si | 11.6 | 0.6 |
| Cl | 1.7 | 3.2 |
| Zn | 77.8 | 56.3 |

Table 8.5. Compositions of mixture silane-treated HDG, shown in Figure 8.10(c)

| Element | Region 1 | Region 2 |
|----------------|-----------------|-----------------|
| O | 6.2 | 5.8 |
| Si | 8.3 | 9.0 |
| S | 5.6 | 6.8 |
| Cl | -- | -- |
| Zn | 79.8 | 78.3 |

In Figure 8.10(a), clusters of corrosion products are observed here and there on the bis-sulfur silane treated HDG surface, along with irregular dark patches distributed uniformly over the surface. The EDX results of these dark patches in Table 8.3,

compared to the other regions or “grey region”, show markedly high amounts of S (24.1 wt %) and Si (17.8 wt %) and relatively low content of Zn (49.1 wt %). It is also noted that the S/Si ratio is similar for both dark patches and the other regions in Figure 8.10(a). Therefore, the dark patches are very likely the areas of thicker bis-sulfur silane films. In other words, HDG surface is not uniformly covered with the bis-sulfur silane film. Such phenomenon, however, was not observed for the bis-sulfur treated AA 2024-T3 surface. This difference could be explained in light of different wettabilities of aluminum and zinc oxides. It is known that aluminum oxide has a higher surface energy, wetting of Al oxide by the bis-sulfur silane solution is not a problem. However, the same bis-sulfur silane solution seems too hydrophobic to the Zn oxide that has a lower surface energy. This obviously leads to an insufficient wetting of the Zn oxide. As a result, a non-homogeneous bis-sulfur silane layer is formed on HDG, as shown schematically in Figure 8.11. Local corrosion hence initiates at those defective sites where are poorly covered by the bis-sulfur silane film.

As opposed to the bis-sulfur silane, the bis-amino silane is more hydrophilic and should wet the Zn oxide readily, forming a uniform silane film on HDG. Nevertheless, the hydrophilic nature of the bis-amino silane film still leads to heavy corrosion on HDG (Figure 8.10(b)). This is indeed confirmed by a noticeable amount of Cl (1.7%) detected in the bis-amino silane film on HDG (Table 8.4).

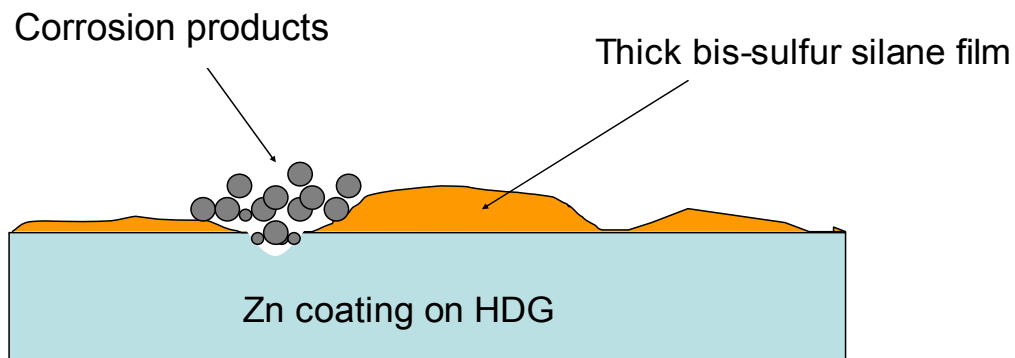


Figure 8.11. Poorly-coated HDG surface with the bis-sulfur silane, and local corrosion occurring at defects

Figure 8.10(c) shows the SEM image of an intact mixture-treated HDG surface where no corrosion was observed after 5 days of immersion. Neither dark patches nor chloride signal are discerned on this sample. Two regions were chosen randomly on the surface for compositional identification by EDX. The EDX results are shown in Table 8.5. The compositions of both regions can be considered as the same within the experimental variations, indicating that the mixture gives a uniform film coverage on HDG as the bis-amino silane does. Apparently, with the addition of a small amount of bis-amino silane, the solution of the bis-sulfur/bis-amino silane mixture becomes hydrophilic enough to wet the Zn oxide and further form a homogeneous film. It is evidenced in Figure 8.10(c) that such film still offers good corrosion protection on HDG, inferring that the as-formed mixture film is hydrophobic enough from a corrosion protection perspective. The hydrophobicity of the mixture film is obviously attributed to the large amount of bis-sulfur silane in the mixture. In all, the mixture film provides a universal protection on both AA 2024-T3 and HDG by selectively overcoming the major drawbacks of the two individual silanes.

8.3. Conclusions

1. Hydrophilic bis-amino silane film consistently showed an inferior corrosion protection performance on AA 2024-T3 and HDG. This is because that the bis-amino silane film is positively-charged due to the protonation of secondary amino groups. This positively-charged bis-amino silane film strongly attracts anions such as Cl^- ions as well as water from outside, eventually leading to corrosion of metals.

2. Hydrophobic bis-sulfur silane performed very well on AA 2024-T3, but failed on HDG. It was found that the major cause behind this failure is the insufficient wetting of the bis-sulfur silane solution towards the Zn oxide on HDG, which results in non-uniform film coverage on HDG. Corrosion starts at defective sites where are poorly covered by the film.

3. A mixture at the bis-sulfur/bis-amino ratio of 3/1 enhances the corrosion resistance of both AA 2024-T3 and HDG. This improvement is achieved for the mixture by selectively overcoming the major drawbacks of the two individual silanes. A small portion of bis-amino silane makes the mixture solution hydrophilic enough to wet Zn oxide on HDG, which facilitates the formation a homogenous film on HDG. On the other hand, a large portion of bis-sulfur silane enhances the hydrophobicity of the mixture film, which is the basis for good protective performance of the mixture.

Chapter 9. Development of Water-based Silanes for Corrosion Protection of Metals¹

9.1. Introduction

The silanes that have been studied can be divided into two groups in terms of their hydrophobicity: alcohol-based and water-based. The former is highly immiscible with water. Therefore, a large amount of organic solvents like ethanol is required when preparing silane solutions. Examples of such silanes are bis-[triethoxysilyl]ethane (BTSE) and bis-[triethoxysilylpropyl]tetrasulfide (bis-sulfur silane). Despite of their confirmed corrosion protective performance, the requirement of alcohol for silane solution preparation still poses a major obstacle in the transfer of this technology into existing industrial systems, as a reduction of Volatile Organic Compounds (VOC) is also a mandate in industry for the sake of flammability and human safety concern. Therefore, a demand has been made for developing water-based silane surface treatments.

In this chapter, several newly-developed water-based silanes are presented. In general, the major advantages of this group of silanes can be summarized as follows. (1) Alcohol-free, i.e., only de-ionized (DI) water is needed for silane solution preparation. (2) Instantaneous and complete hydrolysis. It requires less time to prepare water-based silane solutions than that of the alcohol-based. Besides, the hydrolysis of water-based silanes approaches completion rather than equilibrium as alcohol-based silanes do. (3) Good

¹ Part of this chapter has been submitted to Progress in Organic Coatings as a manuscript of “Corrosion Protection of Metals by Water-based Silane Mixtures of Bis-[trimethoxysilylpropyl]amine and vinyltriacetoxysilane”

corrosion protection performance, especially with topcoats. (4) Some water-based silane mixtures provide broader paint compatibility. A good example is the silane mixture of bis-amino and (vinyltriacetoxysilane) VTAS. As the mixture carries two organofunctional groups (i.e., amino groups of bis-amino silane and vinyl groups of VTAS), it is therefore expected to be compatible to more paint systems.

The process of silane solution preparation is simple. Take bis-amino/VTAS mixture as an example. First, mix the as-received bis-amino and VTAS silanes together at a certain ratio, e.g., 3/1, and then dilute the mixture simply with DI water. For making a 2% by volume mixture solution at a total amount of 100 ml, for instance, simply add 2 ml silane mixture into 98 ml deionized (DI) water and stir the solution until it becomes clear. Figure 9.1 shows individual bis-amino and VTAS silanes, their mixture, and the resulting 2% silane mixture solution.

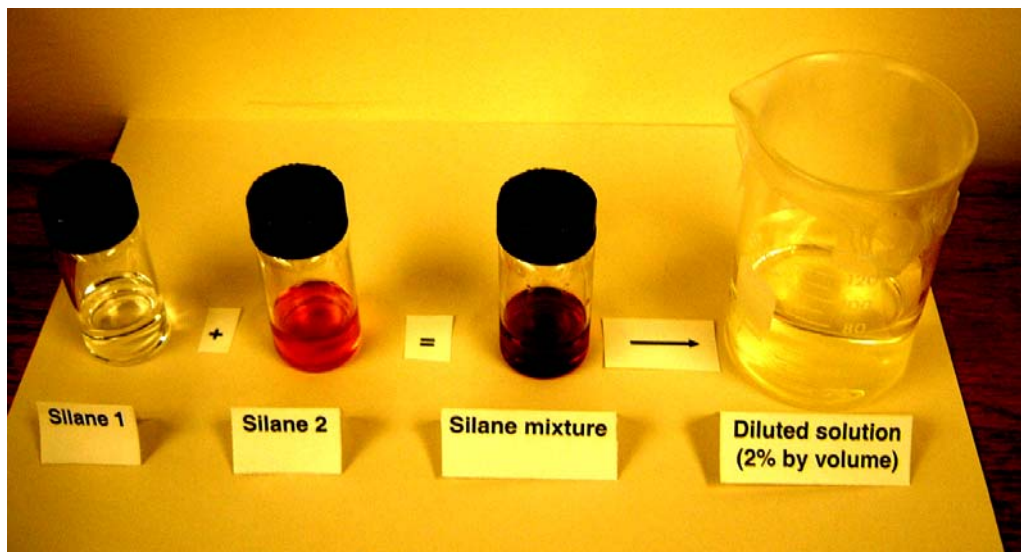


Figure 9.1. Individual silanes, silane mixture, and diluted aqueous silane solution used in this work (Note: silane 1 = unhydrolyzed bis-amino silane, silane 2 = unhydrolyzed VTAS, silane mixture = unhydrolyzed mixture at the bis-amino/VTAS ratio of 3/1 (v/v))

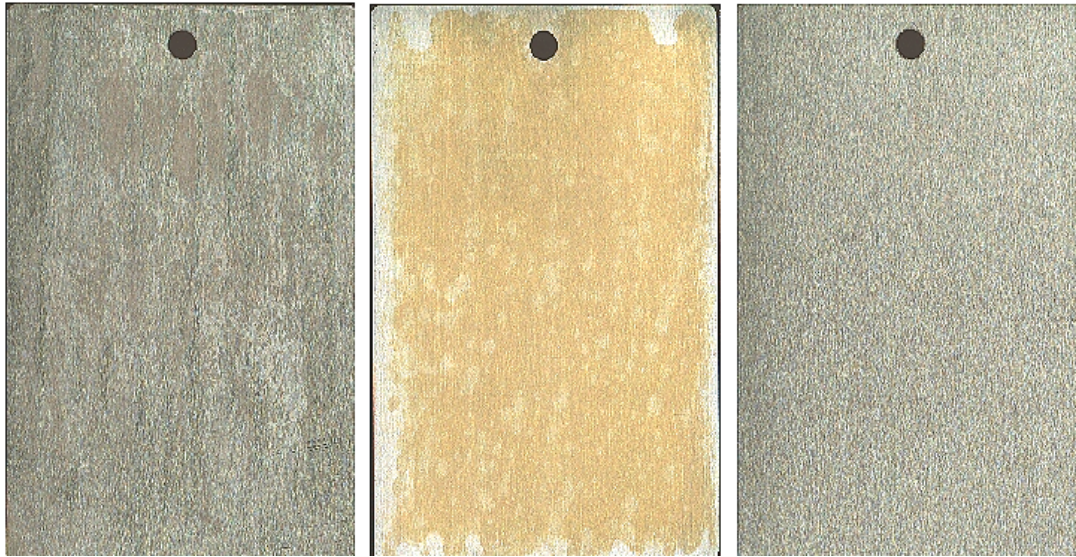
It is seen in Figure 9.1 that when two individual silanes mixed together, the color of the mixture changes with time, becoming darker than that of the individual ones. The reason behind this color change is possibly related to the interaction between VTAS and bis-amino silane during mixing, which will be discussed later in this chapter.

9.2. Results and discussion

9.2.1. Corrosion performance of metals treated with bis-amino/VTAS silane mixtures

9.2.1.1. Bare corrosion protection

Figures 9.2 and 9.3 display the salt spray testing (SST) results of two types of Al alloys, i.e., AA 6061 and AA 2024-T3, with different surface treatments. It is seen in Figure 9.2, the silane-treated AA 6061 surface (Figure 9.2(c)) does not show any corrosion sign after 336 hrs of SST, while the chromated surface (Figure 9.2(b)) exhibits a certain degree of discoloration. The bare AA 6061 surface (untreated, Figure 9.2(a)) has corroded heavily after 20 hrs of exposure, showing a uniform corrosion on the surface.



(a)

(b)

(c)

Figure 9.2. AA 6061 panels after 336 hrs of SST; (a) untreated (20 hrs of exposure), (b) chromated (Alodine-series), and (c) silane-treated (Bis-amino/VTAS=1.5/1, 5%, pH 3.7)



(a)

(b)

(c)

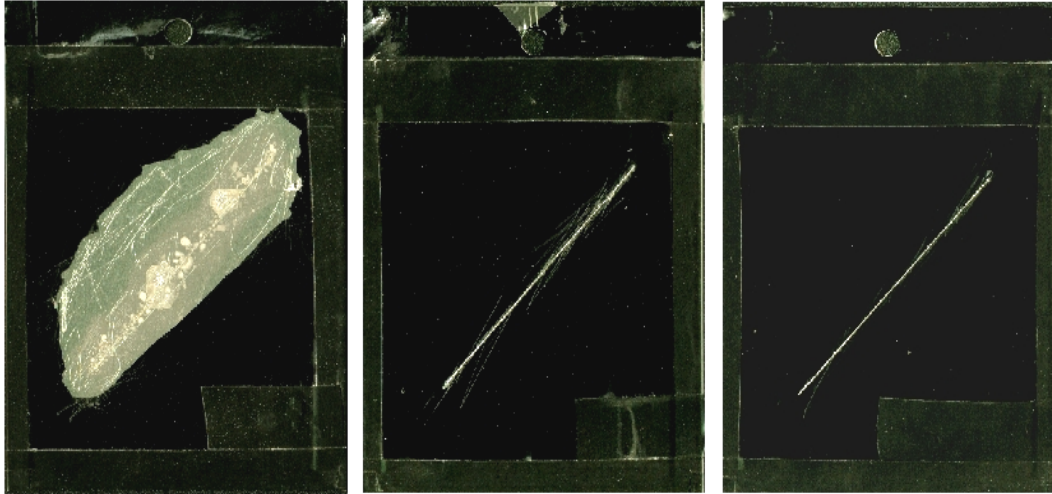
Figure 9.3. AA 2024-T3 panels after 168 hrs of SST; (a) untreated, (b) chromated (CHEM-CODE 105[®]), and (c) silane-treated (bis-amin/VTAS = 1.5/1, 5%, pH 3.7)

In Figure 9.3, the same tendency is seen. The major part of the silane-treated AA2024-T3 surface still retains shiny after 168 hrs of SST (Figure 9.3(c)), except for slight corrosion shown at the edges. The chromated surface (Figure 9.3(b)) shows a little heavier corrosion as compared with the silane-treated one. The bare AA 2024-T3 surface (Figure 9.3(a)), however, has heavily corroded by showing a large amount of white rust over the surface.

9.2.1.2. Corrosion protection and paint adhesion

In addition to bare corrosion protection, these silane mixtures have also demonstrated both excellent corrosion protection and paint adhesion with different paints. The paints to which the mixtures are compatible include: polyurethane-based (PU), polyester-based (PET), epoxy-based, acrylic-based, and rosin-based. Some examples are shown as follows.

Figures 9.4 and 9.5 present 1008-hr SST results of AA 2024-T3 painted with PU and PET, respectively. It is clearly seen that, in both cases, the performance of the silane mixture is comparable to that of the chromated, i.e., no paint delamination and corrosion sign is seen along the scribe line (Figures 9.4(c) and 9.5(c)). The untreated AA 2024-T3 panels (Figures 9.4(a) and 9.5(a)), on the contrary, exhibit a large degree of paint delamination as well as corrosion activity along the scribe lines.

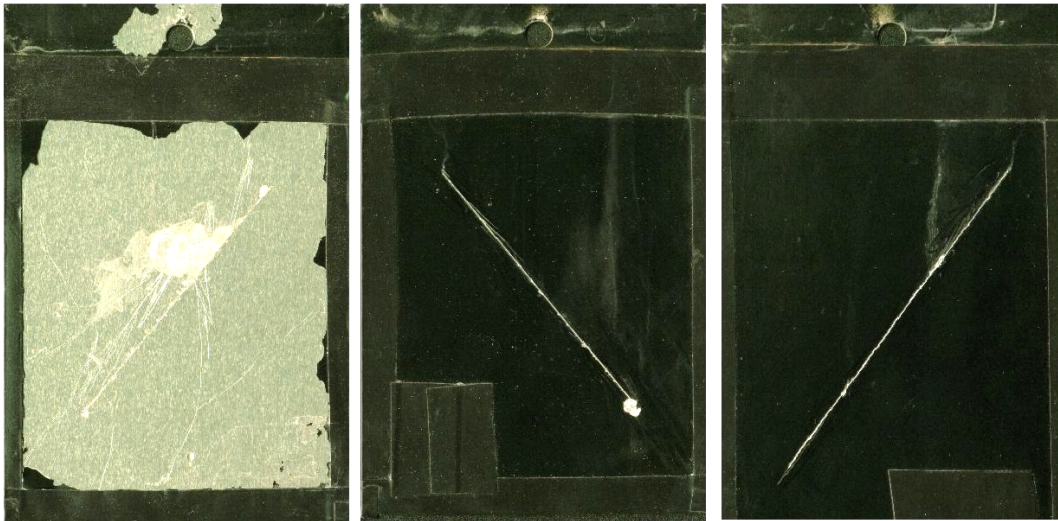


(a)

(b)

(c)

Figure 9.4. PU powder-painted AA2024-T3 after 1008 hrs of SST; (a) untreated, (b) chromated (CHEM CODE 105[®]), and (c) silane-treated (bis-amino/VTAS=1.5/1, 2%)



(a)

(b)

(c)

Figure 9.5. PET powder-painted AA2024-T3 after 1008 hrs of SST, (a) untreated, (b) chromated (CHEM CODE 105[®]), and (c) silane-treated (bis-amino/VTAS =1.5/1, 2%)

After 240-hr exposure to a copper-accelerated acetic acid salt spray test (CASST), both silane-treated and chromated AA 5005 panels painted with PU and PET panels exhibit no any paint delamination and corrosion along the scribe line, as seen in Figures 9.6 and 9.7. The untreated AA 5005 surfaces (Figures 9.6(a) and 9.7(a)), in contrast, display severe paint delamination and corrosion in the delaminated areas.

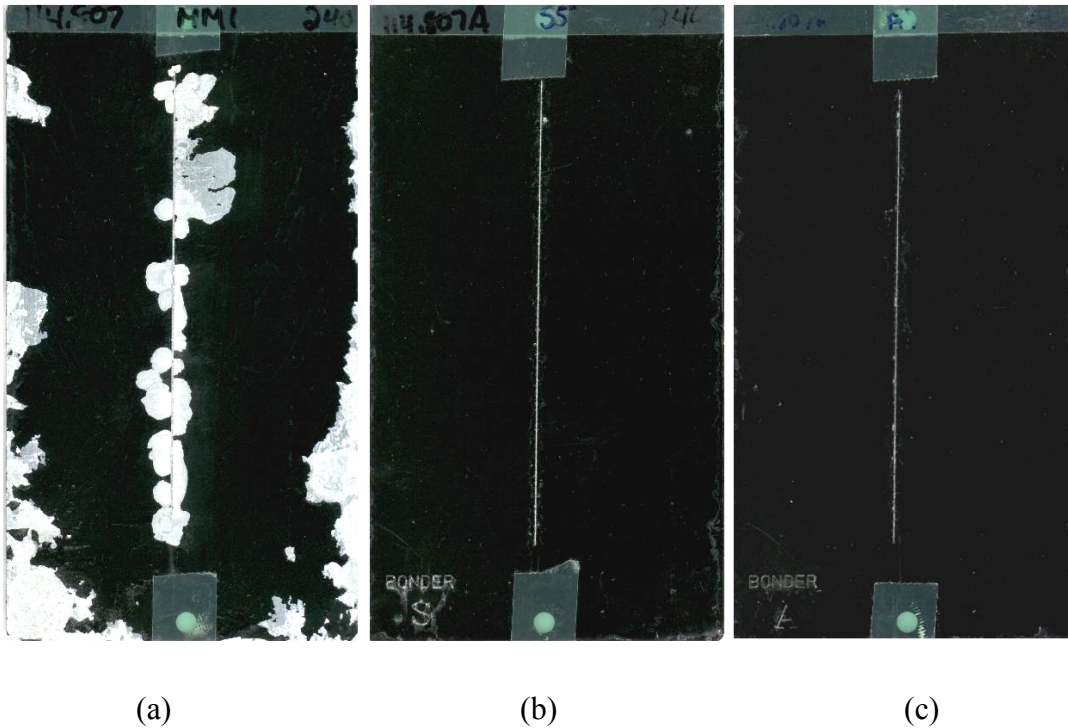
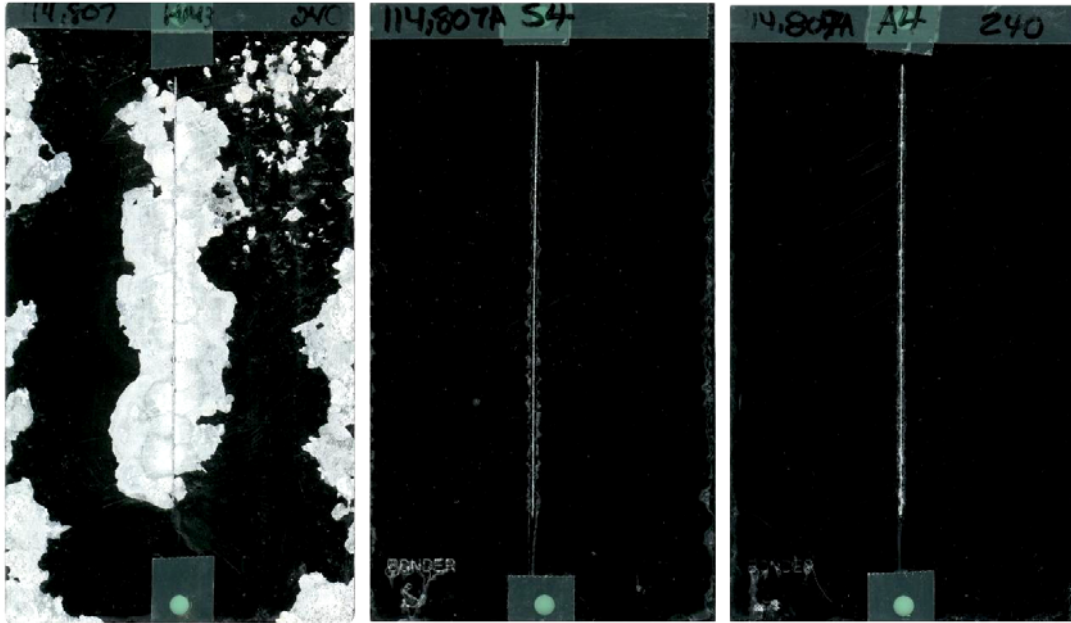


Figure 9.6. PET-powder-painted AA 5005 after 240 hrs of CASST; (a) untreated, (b) chromated (Chromicoat 103[®]), and (c) silane-treated (bis-amino/VTAS = 1.5/1, 2%, pH 4)



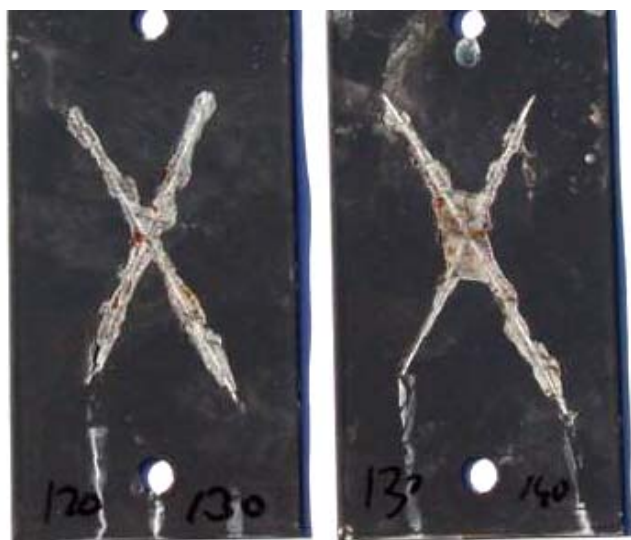
(a)

(b)

(c)

Figure 9.7. PU-powder-painted AA 5005 after 240 hrs of CASST; (a) untreated, (b) chromated (chromicoat 103[®]), and (c) silane-treated (bis-amino/VTAS =1.5/1, 2%, pH 4)

Besides Al alloys, these silane mixtures have also found their uses for other metals. Figure 9.8 shows the 1000-hr SST result for PET-painted delta Zn steel (i.e., batch hot-dip galvanized steel at 560 °C). Both silane mixture and chromate performed equally well, achieving the criterion of less than 5 mm paint delamination along the scribe lines.

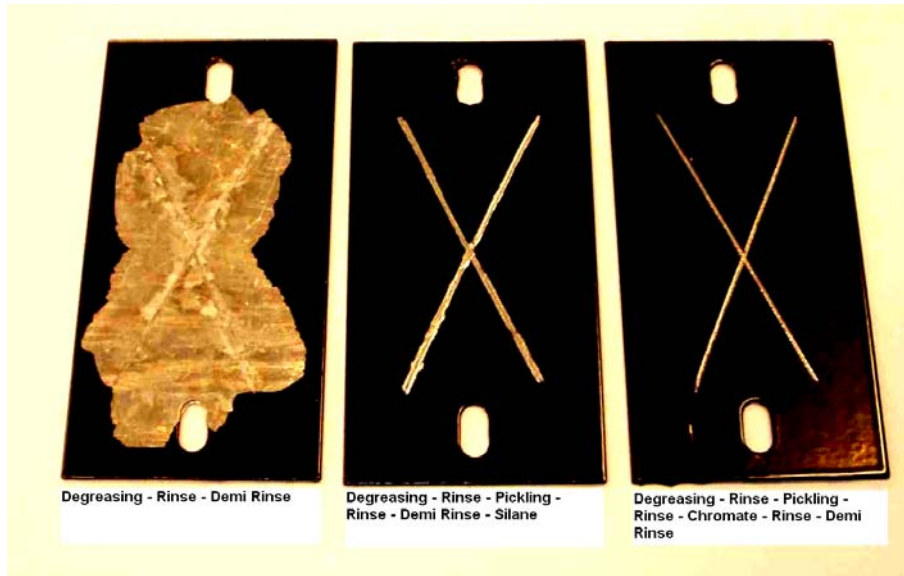


(a)

(b)

Figure 9.8. 1000-hr exposure of PET powder painted delta Zn panels; (a) silane-treated (bis-amino/VTAS = 5/1, 2%, pH 6), and (b) chromated (Granodine 108B[®])

As shown in Figure 9.9, Machu test [114] results of HDG exhibit the same trend: the behaviors of the silane mixture and the chromated are comparable, i.e., no paint delamination and corrosion has been observed after testing (Figures 9.9(c) and (d)), whereas the untreated panel (Figure 9.9(a)) shows a large extent of paint loss and some amount of corrosion along the scribe line.



(a)

(b)

(c)

Figure 9.9. Machu testing results of PET-painted HDG panels, (a) untreated, (b) silane-treated (bis-amino/VTAS = 5/1, 2%, pH 6), and (c) conventional chromate-treated (Granodine 108B[®])

Austenitic AL6XN stainless steel (20Cr-24Ni-6Mo) is one of the selected materials for non-magnetic ship hull construction. After painted with an epoxy topcoat, this alloy is unfortunately prone to crevice corrosion at the metal/epoxy interface. The larger the portion of bare alloy, the more severe the crevice corrosion at the metal/epoxy interface. An existing solution to prevent crevice corrosion is Zn-rich primer/epoxy system. Nevertheless, one concern about the use this system is the potential for liquid metal embrittlement of the stainless steel should the need for repair welding or high temperature cutting arises [115-119]. Therefore, a better pretreatment system was searched for to mitigate crevice corrosion and to replace Zn-rich primer/epoxy system.

Silane systems including the bis-amino/VTAS silane mixture (2%, bis-amino/VTAS=5/1, pH 6) were hence tested with AL 6XLN stainless steel panels. Various portions of the panels were pretreated with the silanes (i.e., 20%, 80% and 100%) and topcoated with a rosin-based Cu-antifouling paint. The painted panels were then continuously immersed in fresh-filtered (5-10 μ m) natural seawater (Wrightsville, NC) for 9 months. Figure 9.10 shows the panels after the first 3-month of immersion. Clearly, crevice corrosion has already formed at the metal/epoxy interface (Figure 9.10(a)). The silane-pretreated and Cu-antifouling topcoated panel (Figure 9.10(c)), however, does not show any crevice corrosion at the metal/paint interface. A final report after 9-month also confirmed that no corrosion activity was observed for the silane-treated panels [120].

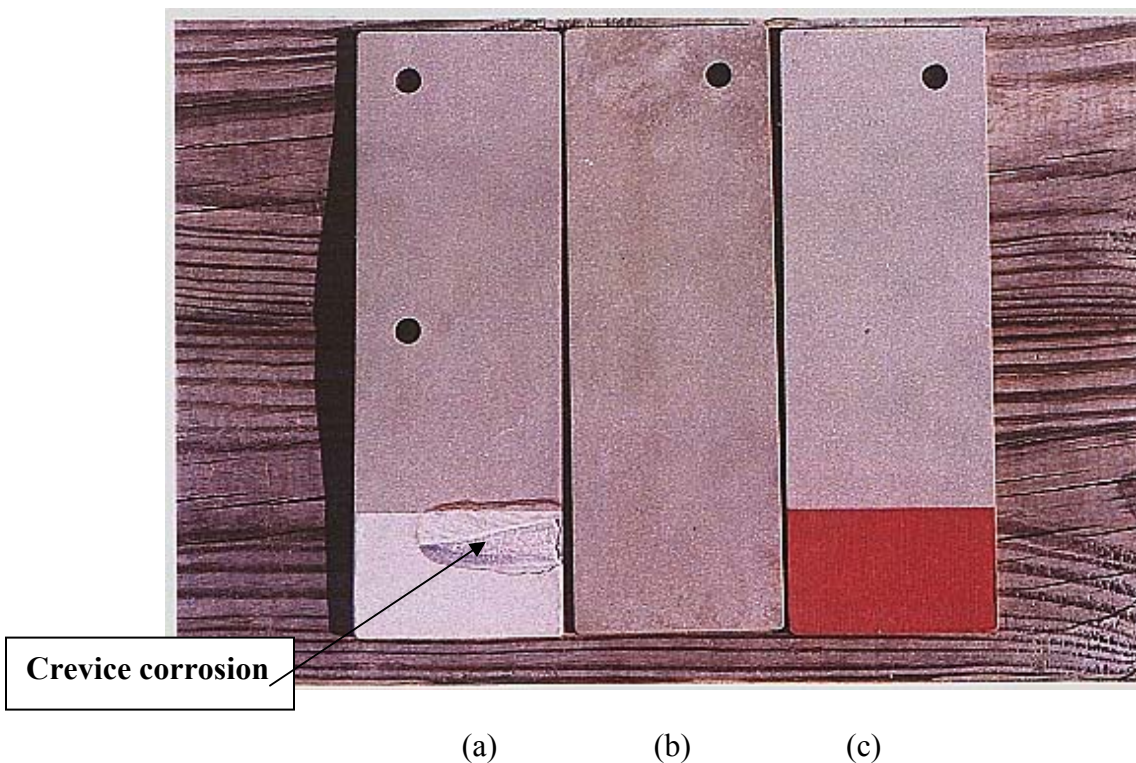


Figure 9.10. Representative view of 3-month immersed panels; (a) epoxy-coated only, (b) silane-treated only, and (c) silane-pretreated (bis-amino/VTAS = 5/1, 2%, pH 6), followed by Cu-antifouling painted

9.2.2. Characterization of silane mixtures of bis-amino and VTAS systems

Based upon the above performance tests, it can be concluded that the bis-amino/VTAS silane mixtures do have a great potential to replace chromating in industries. In the following section, characterization work has been conducted on this system in order to obtain a better understanding of the system. This is essential if one wishes to use the system judiciously. This work includes silane hydrolysis, solution stability, film thickness measurement, electrochemical testing as well as structural characterization of the silane films are reported.

9.2.2.1. Hydrolysis of silane mixtures of bis-amino and VTAS

As was mentioned earlier, the bis-amino/VTAS silane mixtures are simply prepared by mixing the individual bis-amino and VTAS silanes together at certain ratios, e.g., 3/1 (Figure 9.1). It was found in practice that, when mixing these two silanes together, the temperature of the mixtures is normally raised, indicating that there is an exothermic reaction occurring during the mixing process. This exothermic reaction is possibly the hydrolysis reaction of VTAS catalyzed by bis-amino silane, as suggested in Figure 9.11.

9.2.2.2 Solution stability of silane mixtures of bis-amino and VTAS

In practice, it is consistently noticed that solution pH and solution stability of the bis-amino/VTAS mixtures are strongly dependent upon the ratios of bis-amino and VTAS, regardless of the solution concentration. Table 9.1 shows the measured silane mixture solution pH and the observed solution stability corresponding to various bis-amino and VTAS ratios. All bis-amino/VTAS silane solutions were 5%. A criterion for judging solution stability is whether a solution remains clear. A clear solution is considered stable, while a solution loses its stability when it becomes hazy due to condensation of silanols [7].

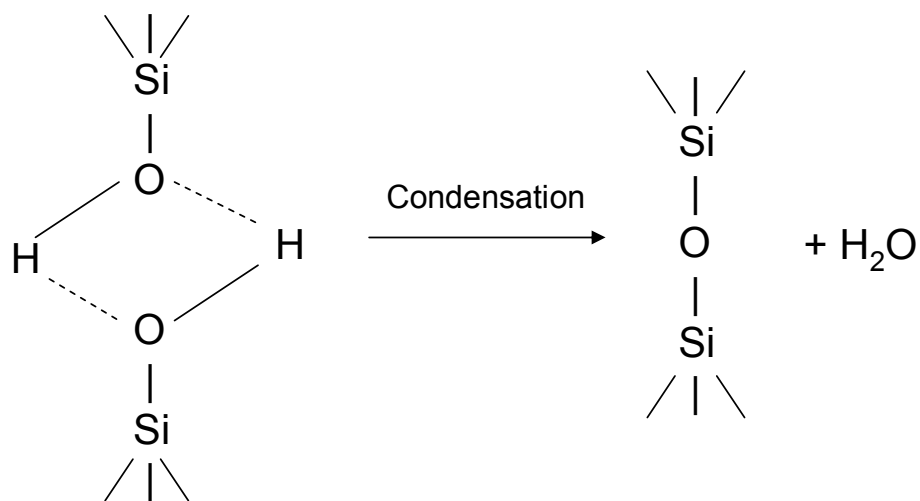
It is seen in Table 9.1 that the solution pH and the solution stability increase with the content of basic bis-amino silane in the mixtures. A continuous visual inspection found that the silane solutions stayed clear when the amount of bis-amino silane in the mixture exceeds 50%, while those with the bis-amino silane less than 50% readily became hazy within the first week. Clearly, the bis-amino silane plays an essential role in stabilizing the silane mixture solutions. An explanation regarding the effect of the bis-amino silane is given as below.

According to [7], the appearance of haze or onset of phase separation in a silane solution is coincident with the occurrence of branching or cyclic formation (i.e., tetramer) due to the condensation among SiOH groups in the solution. Scheme 9.1 illustrates the process of condensation of SiOH groups in a silane solution. However, such condensation can be inhibited with the addition of a small amount of bis-amino silane, as shown in Scheme 9.2. It is because SiOH groups are weakly acidic whilst the secondary amine (–

NH-) groups strongly basic, and therefore the H-bond formed between –NH– and SiOH is more stable than that between SiOH groups. As a result, the VTAS silane solution is stabilized by means of the addition of bis-amino silane. A similar work on the solution stability of γ -APS was reported elsewhere [8].

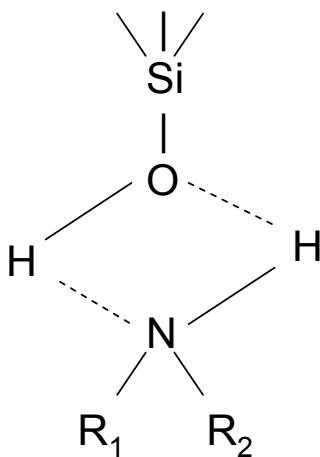
Table 9.1. pH and stability of 5% bis-amino/VTAS mixture solutions as a function of the content of bis-amino silane in the bis-amino/VTAS silane mixture

| Bis-amino/VTAS | Content of bis-amino silane (%) | pH | Solution stability |
|-----------------------|--|-----------|-----------------------------|
| VTAS-only | 0.0 | 2.8 | Hazy (within a few minutes) |
| 1/5 | 16.7 | 3.0 | Hazy (within a week) |
| 1/2 | 23.3 | 3.3 | Hazy (within a week) |
| 1/1.5 | 40.0 | 3.3 | Hazy (within a week) |
| 1/1 | 50.0 | 3.5 | Hazy (within a week) |
| 1.5/1 | 60.0 | 3.8 | Clear (over a year) |
| 2/1 | 66.7 | 4.0 | Clear (over a year) |
| 3/1 | 75.0 | 4.4 | Clear (over a year) |
| 4/1 | 80.0 | 4.8 | Clear (over a year) |
| 5/1 | 83.3 | 5.8 | Clear (over a year) |
| 6/1 | 85.7 | 7.5 | Clear (over a year) |
| 7/1 | 87.5 | 7.9 | Clear (over a year) |
| Bis-amino only | 100.0 | 10.8 | Hazy (within a few minutes) |



Hydrogen bonded

Scheme 9.1.



Hydrogen bonded

Scheme 9.2.

9.2.2.3. Thickness measurement of silane mixture of bis-amino and VTAS

The film thickness of the silane mixture of bis-amino and VTAS (1.5/1) was measured on stainless steel substrate using ellipsometry technique. The result is plotted as a function of solution concentration shown in Figure 9.12. It is clearly seen that the silane film thicknesses are proportional to their corresponding solution concentrations. That is, the higher the solution concentration, the greater the resulting silane film thickness. This result supports the conclusion that silane film thickness can be exclusively controlled by adjusting the concentration of the corresponding silane solution but not by the contact time. Such observation has also been confirmed in our previous works [29, 121].

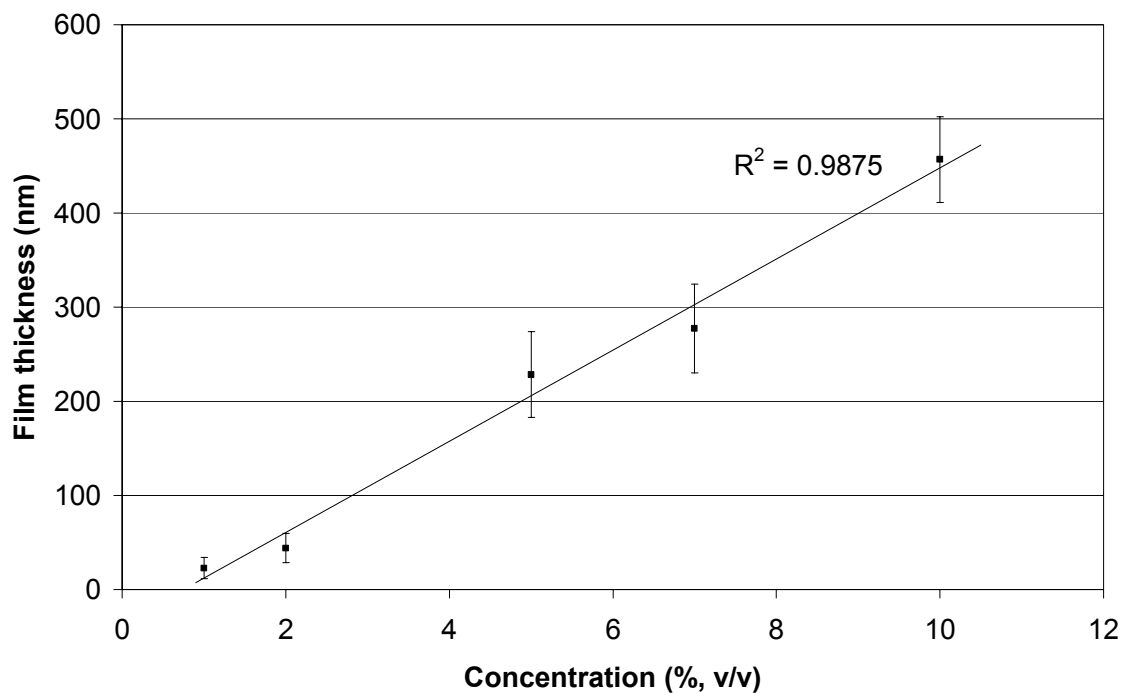


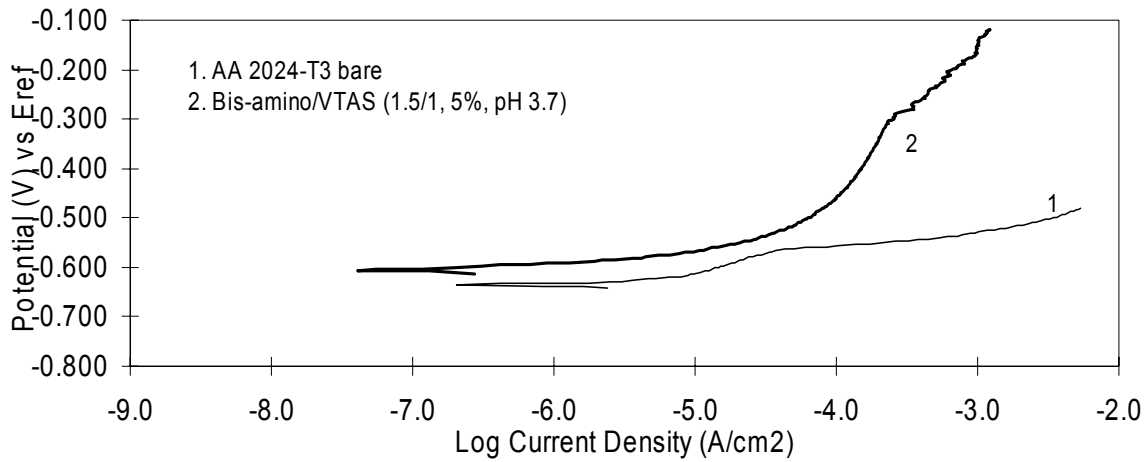
Figure 9.12. Film thicknesses of silanes as a function of the corresponding silane solution concentrations

It should be noted that in comparison with conventional chromate layers (> 1000 nm thick), commonly-used bis-amino/VTAS silane films, such as the films corresponding to 5% and 2%, are much thinner. As mentioned previously, 5% is used for the purpose of bare corrosion protection of metals whilst 2% is typically used for surface pretreatment to improve paint adhesion of metals before painting. It is seen in Figure 9.12 that a silane film corresponding to 5% has the thickness of less than 250 nm, while the film thickness for a 2% silane solution is only around 50 nm. Hence, it is safe to say that silane films outperform conventional chromates per a per weight basis.

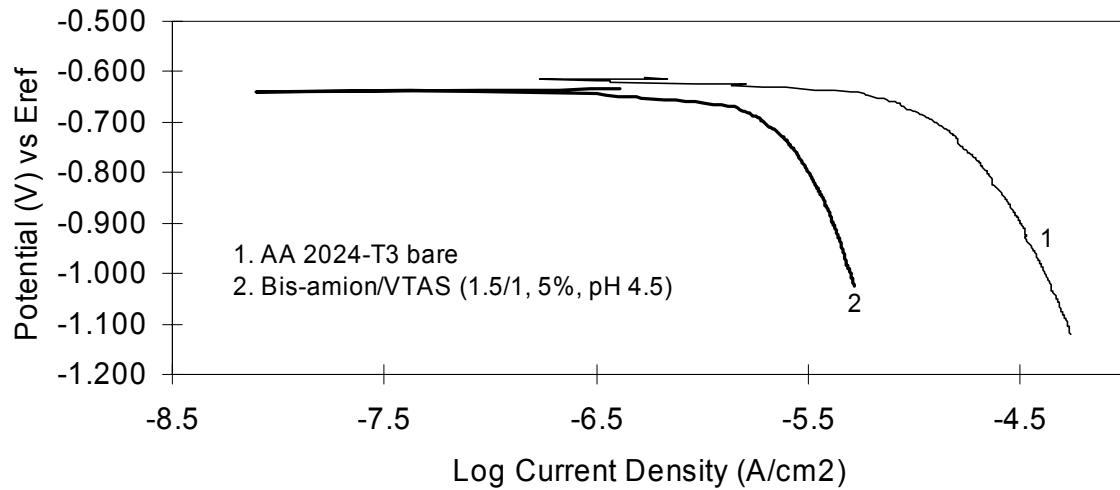
9.2.2.4. DC polarization tests of bis-amino and VTAS mixtures on AA 2024-T3

The DC polarization tests were conducted on the bis-amino/VTAS treated AA 2024-T3 panels in a 0.6 M NaCl solution (pH 6.5). The results are presented as anodic and cathodic polarization curves as shown in Figures 9.13 (a) and (b), respectively. It is seen that both anodic and cathodic current densities for AA 2024-T3 has been largely reduced after the silane deposition (curve 2) compared to the bare AA 2024-T3 (curve 1). More detailed discussion regarding corrosion inhibitive action of silane films was given in Chapters 7 and 8. In general, a silane film performs as a physical barrier to inhibit corrosion process at the metal. This attribute is directly associated with the interfacial layer formed in the system. On one hand, a number of AlOSi bonds are formed between the interfacial layer and the metal which effectively blocks favorable sites for water adsorption; on the other hand, a good adhesion between the interfacial layer and the substrate restricts corrosion products diffusing away from original corrosion sites which

hinders pit growth underneath. Suppression of water uptake is essential for maintaining this interfacial adhesion by preventing hydrolysis of AlOSi bonds. This can be achieved by reducing film porosity via highly crosslinking the film and by enhancing the hydrophobicity of the film via introducing hydrophobic components into the film.



(a)



(b)

Figure 9.13. DC polarization of AA 2024-T3 treated with and without silane; (a) anodic polarization, and (b) cathodic polarization

Nevertheless, it is also observed that bare corrosion protection performance of bis-amino/VTAS mixtures, in most cases, is inferior with respect to hydrophobic silane films such as bis-sulfur silane and bis-sulfur/bis-amino silane mixture. This is understandable, as the mixture contains a considerable amount of hydrophilic bis-amino silane. Although the addition of the bis-amino silane is essential for enhancing the solution stability of the mixtures, an extra amount of the bis-amino silane would obviously make the mixture film hydrophilic, which is detrimental to its corrosion protective performance. Most recently, it was found that, with the loading of a small amount of hydrophobic tetraethoxysilane (TEOS) into mixture solutions, the hydrophobicity of the bis-amino/VTAS silane film can be enhanced. This new system gave a comparable performance as the bis-sulfur silane and BTSE. Detailed studies will be continued.

9.2.2.5. Structural characterization of bis-amino and VTAS silane mixtures on AA 2024-T3 and HDG by FTIR-RA

As seen in Table 9.1, the water-based bis-amino/VTAS solution pH varies with the ratio of bis-amino silane and VTAS. On the other hand, it is also known that different metal oxides have their own passive pH regions. For instance, Al oxide is passive in the pH range between 4 to 9, while Zn oxide is safe if the pH is from 6 to 12 [36]. Therefore, the issue arisen here is whether or not the structure of silane films would be affected by metal substrates where the metal oxides are prone to dissolution in silane solutions with a low pH. To clarify this issue, the FTIR-RA technique was used here. Three bis-

amino/VTAS silane solutions (5%) with different pHs, i.e., bis-amino/VTAS =1/2 (pH 3.3), 1.5/1 (pH 3.7), and 5/1 (pH 5.8) were applied onto AA 2024-T3 and HDG surfaces. The silane treated panels were then cured at 100°C for 10 min to crosslink the silane films before the FTIR-RA measurements.

The silane mixtures with three different bis-amino/VTAS ratios (5%, 1/2, 1.5/1, 5/1) were deposited on AA 2024-T3. Similar IR spectra for these three silane mixtures are observed in Figure 9.14. The peak at 1622 cm^{-1} is due to NH in the mixtures [87]. The peaks at 1147 and 1046 cm^{-1} are attributed to SiO asymmetric stretching in SiOSi [87,88]. Small variations in intensity are also seen in the region below 1700 cm^{-1} , which are caused by the different ratios of bis-amino and VTAS in the films.

Figure 9.15 display the IR spectra of the same silane mixtures deposited on HDG. Unlike the IR spectra on AA 2024-T3, some distinct differences are shown between these silane mixtures. It is noted that the solution pHs at the bis-amino/VTAS ratios of 1/2, and 1.5/1 are below 5. As a result, the Zn coating on HDG dissolves in the solution at pH less than 5, forming zinc hydroxide ($\text{Zn}(\text{OH})_2$) on the surface. The peaks shown in Figure 9.16 at 1575, 1149, 1016 and 903 cm^{-1} are due to zinc carbonates formed through the reactions between $\text{Zn}(\text{OH})_2$ and CO_2 in the atmosphere [122]. In the case of bis-amino/VTAS ratio of 1.5/1, dissolution of Zn is not that severe, as the pH is 6. Correspondingly, the peaks for the zinc carbonates are not pronounced in the spectrum (c) in the Figure 9.15. The peak at 1618 cm^{-1} is due to NH in the silane mixture.

On the basis of the above IR results, it appears that the bis-amino/VTAS silane mixture solution at the bis-amino/VTAS ratio of 5/1 (pH 5.8) is passive enough for both metal oxides, as no IR peaks due to metal dissolution is observed in the corresponding IR

spectra (spectra (c) in Figures 9.14 and 9.15). Another noticeable feature is that the wave numbers for the IR peaks due to SiOSi bonds are different for both AA 2024-T3 and HDG, i.e., 1147 cm^{-1} for AA 2024-T3 whilst at 1120 cm^{-1} for HDG. This indicates that metal substrates indeed have a significant influence on the structure of the silane films. A similar work on the effect of metal substrates on the structure of bis-sulfur silane film was discussed in Chapter 5.

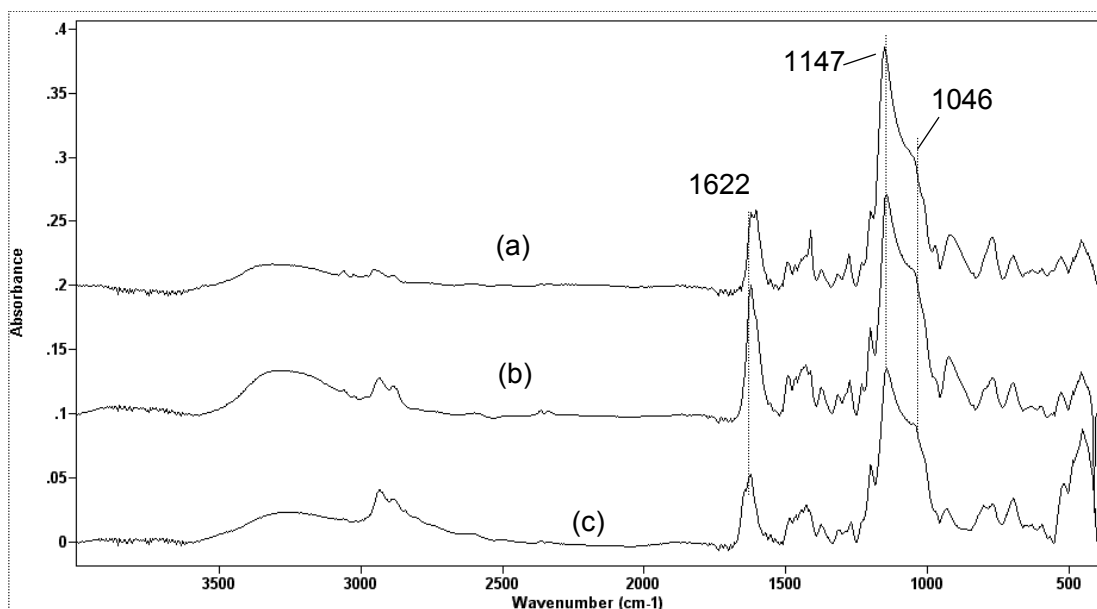


Figure 9.14. FTIR-RA spectra of bis-amino/VTAS silane films on AA2024-T3; (a) bis-amino/VTAS (5%, 1/2, pH 3.0), (b) bis-amino/VTAS (5%, 1.5/1, pH 3.7), and (c) bis-amino/VTAS (5%, 5/1, pH 6)

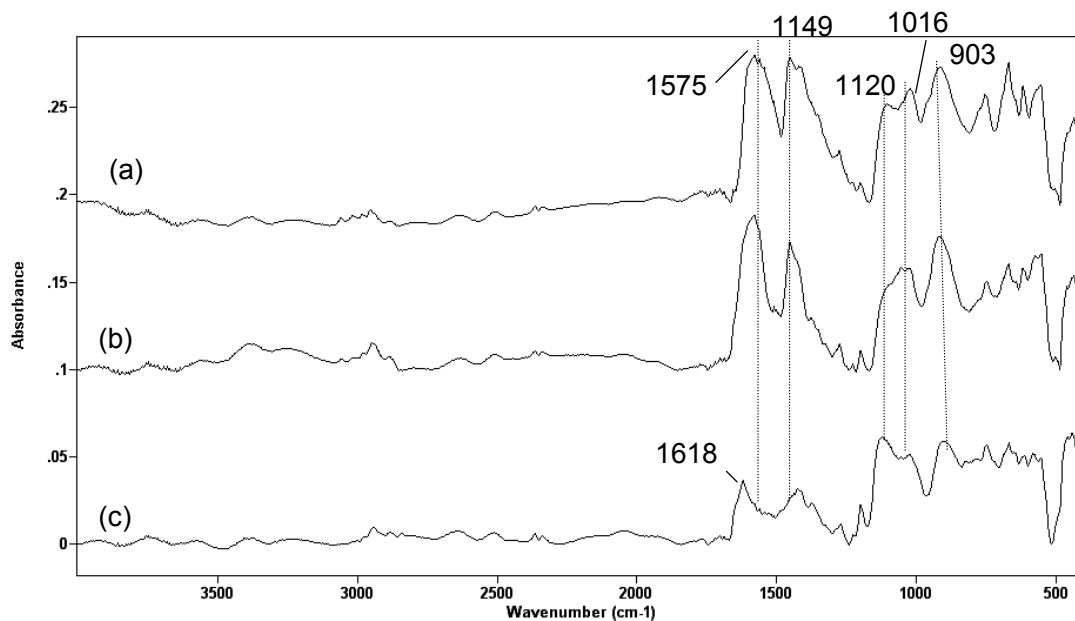


Figure 9.15. FTIR-RA spectra of silane films on HDG (a) bis-amino/VTAS (5%, 1/2, pH 3.0), (b) bis-amino/VTAS (5%, 1.5/1, pH 3.7), and (c) bis-amino/VTAS (5%, 5/1, pH 6)

9.2.3. Other water-based silane systems

Besides the silane mixtures of bis-amino and VTAS, some other water-based silane systems have also been developed recently. In this section, a brief summary on the preliminary work on these silanes is given.

9.2.3.1. Salt immersion test for silane-treated metals

Figure 9.16 shows a 7-day salt immersion test result of AA 2024-T3 treated with silanes A and B. It is seen that the bare AA 2024-T3 surface has heavily corroded (Figure 9.16(a)), while the panels after the treatment of these two silane mixtures do not display any corrosion on the surfaces (Figures. 9.16(b) and (c)). HDG panels were also tested with these silane systems. However, no protection was seen. The reason is probably that the natural pH of these silane mixtures is less than 5, which is too low for HDG. As was demonstrated in Figure 9.15, HDG dissolves at low pH. Apparently, a protective silane layer is not able to form on the dissolved Zn oxide on HDG.

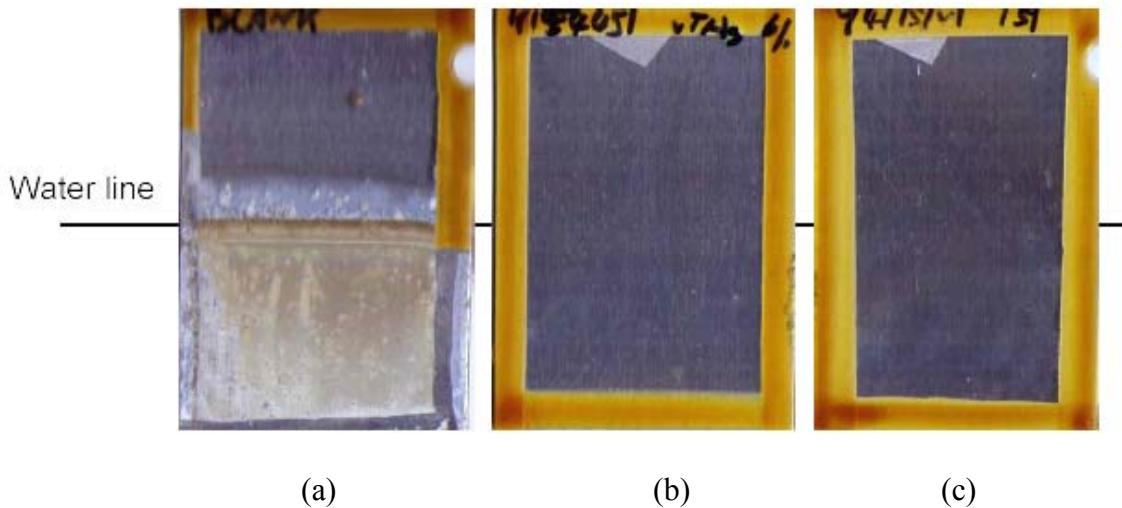


Figure 9.16. A 7-day immersion test in 0.6M NaCl solution (pH 6.5, open to air); (a) untreated, (b) treated with silane A and (c) treated with silane B

9.2.3.2. Improved adhesion of silane-treated metals to adhesives and paints

Three different metal parts, i.e., Galvanized steel (GS), stainless steel (SS) and Al alloy, were pretreated with a series of water-based silanes. A pair of silane-treated metal parts were bonded together using polyurethane-based (PU) adhesive. The bonded pairs were then subjected to an accelerated corrosion test: three cycles at 60°C and 100% relative humidity (RH) for 140 hrs and -10°C for 2 hrs. The adhesion strength of the tested pairs was then measured using a tensile tester. The results are shown in Table 9.2. All silane-treated metals survived the test, showing high adhesion strength and a cohesive failure mode.

Table 9.2. Adhesion strength of silane-treated metals

| Metal | Silane | Adhesion strength (kg) | Failure mode |
|--------------|---------------|-------------------------------|-----------------------|
| GS | A (2%, pH 9) | 610 | 90% cohesive failure |
| Al | A (5%, pH 6) | 600 | 100% cohesive failure |
| SS | C | 555 | 100% cohesive failure |

Zn-phosphate pretreatment is currently used for carbon steel in order to offer efficient corrosion protection and paint adhesion. However, the use of Zn-phosphating is also under pressure due to environmental concerns. The alloy used here was sand-blasted high-strength carbon steel. The steel coils were treated with a number of water-based silanes, followed by painted with epoxy. The results from a 1000-hr salt spray test and a

GM 9505 environmental cycle J – 5 cycles test indicated that two silanes survived very well. These two silanes were, (1) mixture of bis-amino and VTAS (2%, bis-amino/VTAS=5/1 (v/v), pH 8.5, adjusted by KOH) and (2) silane D (1%, pH 10). The results are shown in Table 9.3. It is seen that the silane-treated coil springs exhibit a comparable behavior (i.e., corrosion protection and paint adhesion) as that of Zn-phosphated. It is also noted that since the silane solution pH is as high as 8-9, the negative effect caused by acidic Zn-phosphating (i.e., etching effect) on fatigue life of coil springs can be avoided.

Table 9.3. Testing result for carbon epoxy-painted steel after GM 9505P Environmental Cycle J-5 cycles

| Pretreatment | Delamination degree (mm) |
|---|---------------------------------|
| Bis-amino/VTAS silane mixture (2%, 5/1, pH 8, adjusted by 5.5wt.% KOH) | 8.4 |
| D | 7.8 |
| Zn-phosphate (Control 1) | 8.4 |
| Alkaline-cleaned, untreated (Control 2) | 18.4 |

Cobalt-chromium (CoCr) alloy is a popular biomaterial used for dental repairing. This alloy serves by bonding with a specific acrylic-based adhesive mixture in dental devices. The scientists in this field are now searching for a new surface treatment to improve the adhesion between the CoCr alloy and the adhesive mixture and to replace conventional processes. The CoCr samples were pre-treated with the bis-amino/VTAS

silane solution (1%, 1/1, pH 4), and then bonded with the adhesive. The samples were then subjected to 5000 thermal cycles between 5°C to 55°C. After that, the tensile strength of the samples was determined using a Zwick tensile tester. The result is shown in Table 9.4. It is seen that the bis-amino/VTAS silane mixture highly outperforms the two conventional processes, namely A' and B', showing the greatest tensile (or adhesion) strength after testing, i.e., 26.7 MPa. The two conventional treatments, however, only gave the values of 13.7 MPa for A and 7.4 MPa for B.

Table 9.4. Adhesion strength of acrylic-adhered CoCr samples, after subjection to various pretreatments and followed by 5000 thermal cycles between 5°C to 55°C

| Pretreatment | Adhesion strength (MPa) |
|--|-------------------------|
| Bis-amino/VTAS silane mixture (1%, 1/1, pH 4.0) | 26.7 |
| Conventional process A' (Control 1) | 13.2 |
| Conventional process B' (Control 2) | 7.4 |

9.3. Conclusions

1. Water-based silane mixtures of bis-amino and VTAS as well as other newly-developed silane systems provide both corrosion protection and paint adhesion to a variety of metals, as conformed in industrial tests.

2. The bis-amino/VTAS film thickness is proportional to the corresponding silane solution, suggesting that the film thickness control can be achieved exclusively by adjusting the corresponding silane solution concentration.

3. The bis-amino/VTAS silane solution pHs and the solution stability increase with the bis-amino content in the mixtures. The higher the content of basic bis-amino silane, the higher the solution pH, and the better the solution stability. The reason behind this is most likely that the secondary amine group in the bis-amino silane forms more stable H-bond with silanol group than the one between silanols themselves. In the way, the condensation of silanols is prevented.

4. Metal oxides of the metal substrates experience dissolution during silane treatment if the bis-amino/VTAS solution pHs are beyond the passive pH ranges of the metal oxides. The dissolution of the metal oxides would consequently affect the structure and performance of the bis-amino/VTAS films deposited onto it. Severe dissolution of Zn oxide occurs in the acidic silane solution with a pH below 6, whereas the Al oxide is fairly stable at pH slightly lower than 4, as conformed by the FTIR-RA measurements.

Chapter 10. Other Properties of Silane Films

Besides the excellent corrosion performance of silanes on metals, several other properties, such as electrical properties, mechanical properties and thermal stabilities etc., are also of great importance in industrial applications. In this chapter, these properties were measured, and the results are summarized here.

10.1. Resistivity/conductivity of silane films on AA 2024-T3 and Cold Rolled Steel

In the automotive industry, cathodic electro-coating (e-coat) is the standard coating process for car bodies. Silane-pretreated metals, such as hot-dip galvanized steel (HDG), carbon steel, and aluminum alloys, are thus required to possess a conducting surface.

The previous work [29] on the e-coatability of the silane-treated metals showed that in most cases silane treated metals, i.e., aluminum alloys, HDG, electro-galvanized steel (EGS), and cold-rolled steel (CRS), performed very well in e-coating of ED 5000[®] (epoxy-based), in comparison with the references (i.e., chromated and phosphated). The above metals treated with 2% bis-amino silane or bis-sulfur/amino silane mixture solutions had a conducting surface which enabled e-coat in a similar way as phosphated metals did. That is, the epoxy paint covered uniformly on the silane-treated surfaces with the paint thickness no less than 25 μm .

In this section, the measurement of specific resistivities of silane-treated metal surfaces was carried out in accordance with the specifications of ASTM A717M-95 (Standard Test Method for Surface Insulation Resistivity of Single-Strip Specimens, or “Franklin Test”) [72]. Two metals were selected as the substrates for silane deposition, i.e., AA 2024-T3 and CRS. The tested silanes are listed in Tables 10.1 and 10.2, along with the corresponding curing conditions and the values of resistivity (R_j in $\Omega\bullet\text{cm}^2/\text{surface}$) and conductivity (I in A). Some important effects on resistivity of silane treated metal surfaces are discussed as follows.

Effect of high-temperature curing It is seen in Tables 10.1 and 10.2 that R_j values for all silane films increase invariably after curing at 100°C for 10 min regardless of the substrates, as compared with those without curing. In Table 10.1, R_j of the bis-sulfur silane film on AA 2024-T3 from its 5% solution increases from $3.6 \Omega\bullet\text{cm}^2$ (not cured) to $4.4 \Omega\bullet\text{cm}^2$ ($100^\circ\text{C}/10\text{min}$), while that of the bis-amino silane film from its 5% solution on AA 2024-T3 increases from $28.0 \Omega\bullet\text{cm}^2$ to $36.0 \Omega\bullet\text{cm}^2$ after curing. This result indicates that the silane films become more insulating after curing. This is understandable, as a curing process leads to the formation of a highly crosslinked structure within the silane film. Apparently, a crosslinked silane film is more insulating compared to the one lack of crosslinking.

Table 10.1. Conductivities and resistivities of silanes films on AA 2024-T3

| Silanes | Curing condition | Franklin parameters | |
|-------------------------------|------------------|---------------------|--|
| | | I (A) | R_j ($\Omega \cdot \text{cm}^2/\text{surface}$) |
| Bis-amino silane | --- | 0.687 | 1.469 |
| (2%, pH=8) | 100°C/10min | 0.656 | 1.691 |
| Bis-amino silane | --- | 0.103 | 28.090 |
| (5%, pH=8) | 100°C/10min | 0.082 | 36.100 |
| Bis-sulfur silane | --- | 0.926 | 0.258 |
| (2%, pH=6.5) | 100°C/10min | 0.845 | 0.592 |
| Bis-sulfur silane | --- | 0.471 | 3.637 |
| (5%, pH=6.5) | 100°C/10min | 0.421 | 4.435 |
| Mix(bis-sulfur +bis-amino) | --- | 0.596 | 2.186 |
| (5%+2%, 1:1, pH=7) | 100°C/10min | 0.423 | 4.399 |
| Mix(bis-sulfur +bis-amino) | --- | 0.741 | 1.127 |
| (5%+2%, 1:3, pH=7) | 100°C/10min | 0.658 | 1.676 |
| Mix(bis-sulfur +bis-amino) | --- | 0.539 | 2.758 |
| (2%+2%, 1:1, pH=7) | 100°C/10min | 0.545 | 2.692 |
| Mix(bis-sulfur +bis-amino) | --- | 0.861 | 0.521 |
| (2%+2%, 1:3, pH=7) | 100°C/10min | 0.835 | 0.637 |
| AA 2024-T3 | --- | 0.993 | 0.045 |
| (Untreated, alkaline cleaned) | | | |

Table 10.2 Conductivities and resistivities of silanes films on CRS

| Silanes | Curing condition | Franklin parameters | |
|--|------------------|---------------------|--|
| | | I (A) | R_j ($\Omega \cdot \text{cm}^2/\text{surface}$) |
| Bis-amino silane (2%, pH=8) | --- | 0.977 | 0.076 |
| | 100°C/10min | 0.964 | 0.120 |
| Bis-amino silane (5%, pH=8) | --- | 0.277 | 8.719 |
| | 100°C/10min | 0.231 | 10.778 |
| Bis-sulfur silane (2%, pH=6.5) | --- | 0.984 | 0.054 |
| | 100°C/10min | 0.975 | 0.085 |
| Bis-sulfur silane (5%, pH=6.5) | --- | 0.957 | 0.145 |
| | 100°C/10min | 0.938 | 0.213 |
| Mix(bis-sulfur +bis-amino) (5%+2%, 1:1, pH=7) | --- | 0.643 | 1.791 |
| | 100°C/10min | 0.562 | 2.513 |
| Mix(bis-sulfur +bis-amino) (5%+2%, 1:3, pH=7) | --- | 0.811 | 0.752 |
| | 100°C/10min | 0.778 | 0.920 |
| Mix(bis-sulfur +bis-amino) (2%+2%, 1:1, pH=7) | --- | 0.467 | 3.681 |
| | 100°C/10min | 0.405 | 4.738 |
| Mix(bis-sulfur +bis-amino) (2%+2%, 1:3, pH=7) | --- | 0.940 | 0.206 |
| | 100°C/10min | 0.917 | 0.292 |
| CRS Untreated, alkaline cleaned) | --- | 0.986 | 0.085 |

Effect of silane type As might be noted in Tables 10.1 and 10.2, after the same curing process (e.g., 100°C/10 min), R_j for the bis-sulfur silane film is still much lower than that of the bis-amino silane film on the metals. R_j of the cured bis-amino silane film on AA 2024-T3 from a 5% solution is $36.1 \Omega \cdot \text{cm}^2$, while that of the cured bis-sulfur silane film is only $4.4 \Omega \cdot \text{cm}^2$ (Table 10.1). Such substantial difference can also be

explained in light of their different film structures. As is known, the bis-amino silane contains basic secondary amines that function as auto-catalytic species for silane hydrolysis. As a result, a larger number of SiOH groups are generated in the solution in comparison with the bis-sulfur silane which has no auto-catalytic species. With more SiOH groups available, the bis-amino silane film is thus expected more crosslinked than the bis-sulfur silane film. Correspondingly, the bis-amino silane film more insulating than the bis-sulfur silane film, as reflected by the greater R_j value of the bis-amino silane film.

It is also noticed that the values of R_j for the mixtures of bis-sulfur and bis-amino silanes are of the same order of magnitude as that for the bis-sulfur silane film, i.e., lower in comparison with that for the bis-amino silane film. This result may infer that the structures of the mixtures are similar to that of the bis-sulfur silane film rather than to the bis-amino silane film. After 10 min of curing at 100°C, the silane mixture films were still not able to extensively crosslink. Low R_j values were thus expected and measured.

Effect of silane solution concentration When increasing the silane solution concentration, i.e., from 2% to 5%, R_j of the corresponding silane films has also improved, as clearly shown in Tables 10.1 and 10.2. In Table 10.1, the cured bis-sulfur silane film deposited from a 5% solution has the R_j of 4.4 $\Omega\cdot\text{cm}^2$; while that from a 2% solution has only $\sim 0.6 \Omega\cdot\text{cm}^2$. Similarly, that of the cured bis-amino silane film corresponding to 5% is 36.1 $\Omega\cdot\text{cm}^2$, whereas that to 2% is only $\sim 0.6 \Omega\cdot\text{cm}^2$. It was found from the previous studies [26,29] that film thickness of silanes is nearly proportional to their corresponding solution concentration. In other words, the higher the solution concentration, the thicker the deposited silane film. The above difference hence shows the thickness-dependence of R_j , and also indicates that resistivity is an extrinsic quantity.

Effect of metal substrate Another effect of great importance shown in Tables 10.1 and 10.2 is that the metal substrates influenced the resistivity of the deposited silane films significantly. In general, the R_j values measure on AA 2024-T3 are greater than those on CRS. The cured bis-sulfur silane film from the 5% solution, for example, has R_j of $4.4 \Omega \cdot \text{cm}^2$ on AA 2024-T3 (Table 10.1), whereas that on CRS only is $0.2 \Omega \cdot \text{cm}^2$ (Table 10.2). Clearly, the silane films deposited on AA 2024-T3 seem to be more insulating than those on CRS. This infers that the silane structures formed on AA 2024-T3 is different from those on CRS.

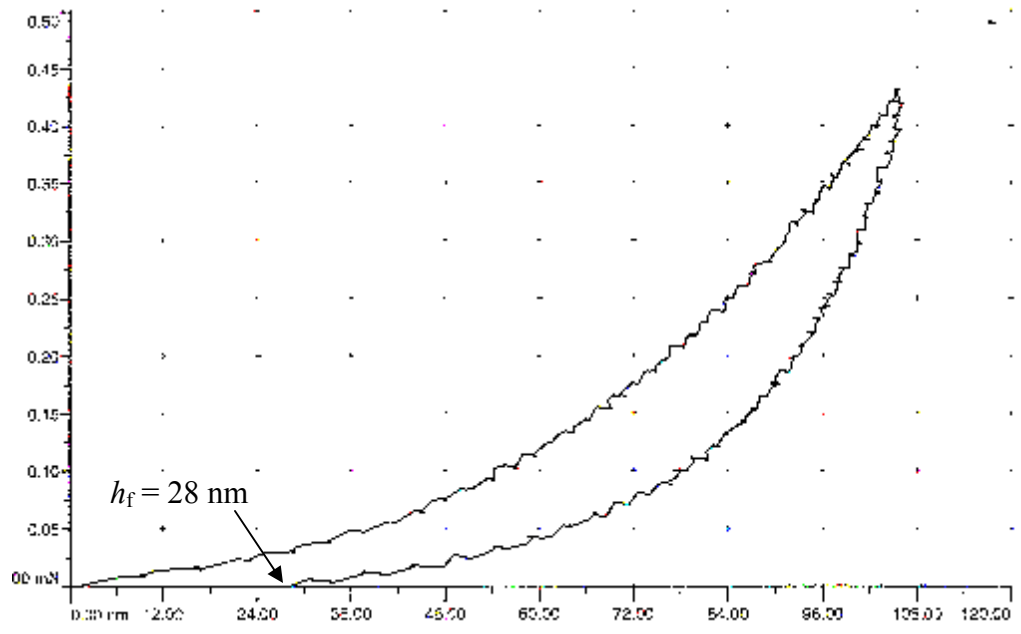
The effect of metals substrates on the bis-sulfur silane film structure was studied in Chapter 5. Indeed, the work confirmed that metal substrates or metal oxides do have a significant influence on the film structure. The difference in the R_j values of the bis-sulfur silane film for AA 2024-T3 and for CRS may also be considered as another evidence for the effect of metals on silane film structures.

10.2. Measurements of mechanical properties of silane films

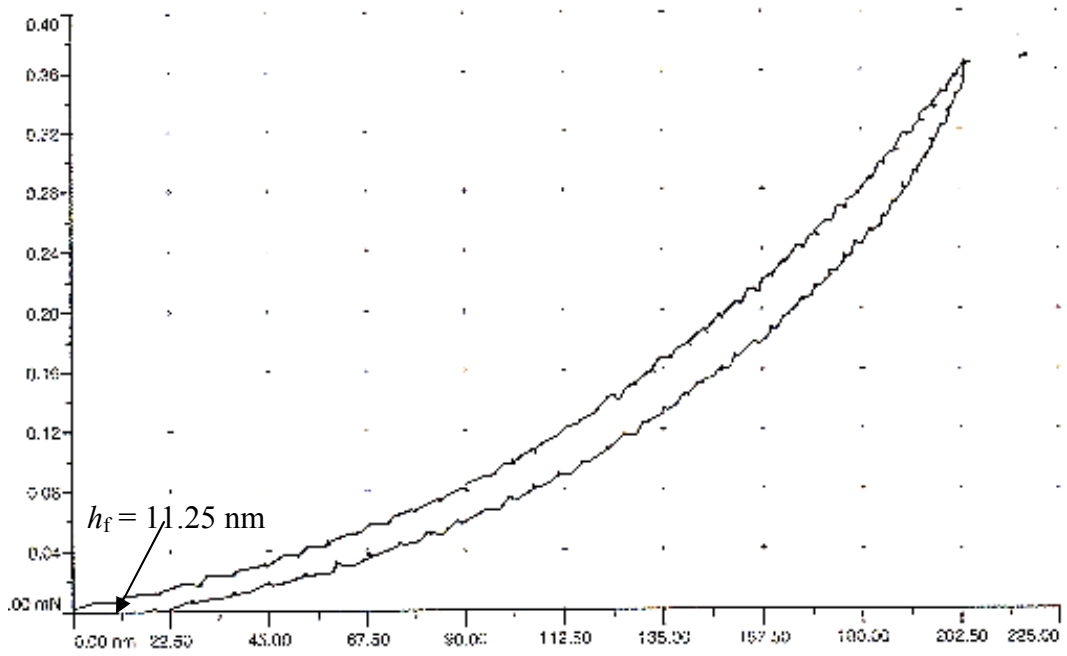
Some silanes, such as bis-sulfur silane and the bis-sulfur/amino silane mixtures, have shown a great potential for their use as stand-alone corrosion protective coatings in the unpainted state. For this reason, such mechanical properties as hardness and wear resistance of silane films are essential. In this section, nano-hardness tester (NHT, or nano-indentation tester) and pin-on-disk tribometer were used for the measurements of hardness, modulus and friction coefficient of the selected silane films. All silane films were deposited on mirror-like surfaces of bright stainless steel (BSS).

10.2.1. Nano-indentation testing: Hardness and Modulus

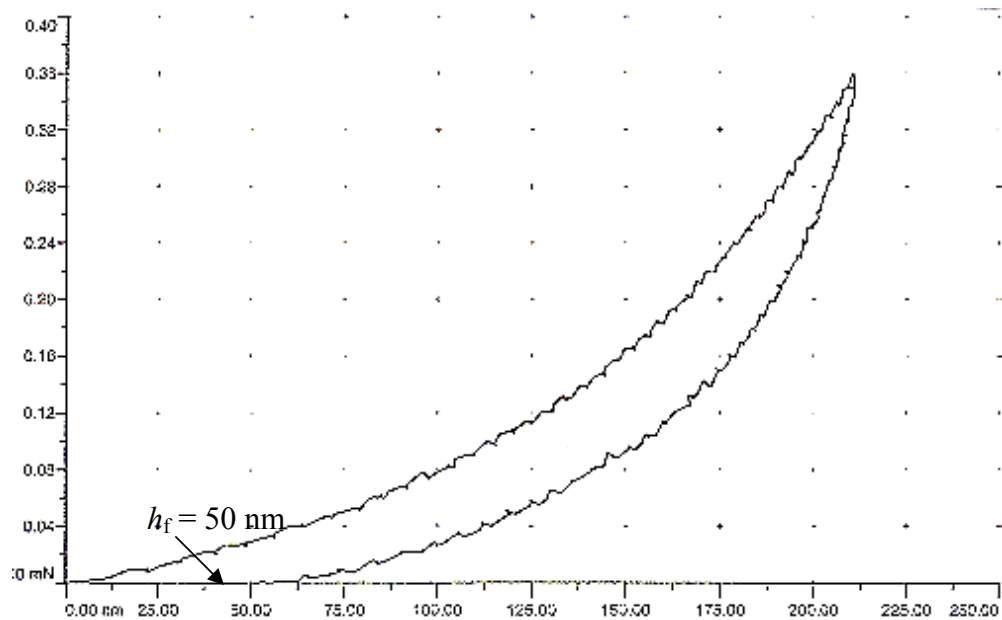
The indentation hysteresis curves for the respective silane films are shown in Figure 10.1(a)-(d), from which the values of H and E were derived and listed in Table 10.3. H and E for the bare BSS substrate (untreated) are also presented as references. More experimental details were given in Chapter 2. It is seen from the table that H for the bis-amino silane film obtained from a 2% solution (200 nm thick) is the greatest, 1630.7 MPa, while those for the bis-sulfur silane for a 5% solution (350 nm) and the bis-amino/sulfur mixture silane films are fairly low, i.e., 717.0 MPa and 549.1 MPa. The values of E shown in Table 10.3 have the same trend as the values of H . It should be pointed out that both H and E are intrinsic quantities, i.e., they are only determined by film structure but independent of film thickness. Thus, the differences in H and E of the tested silane films are explained as follows in terms of their film structures. For the cured bis-amino silane film, a high H value is expected since its film structure is extensively crosslinked after curing at 100°C for 10 min. In contrast with the bis-amino silane film, the much lower values of H and E for both the bis-sulfur and bis-sulfur/amino mixture silane films are obviously due to the lack of extensive crosslinking in the films upon curing.



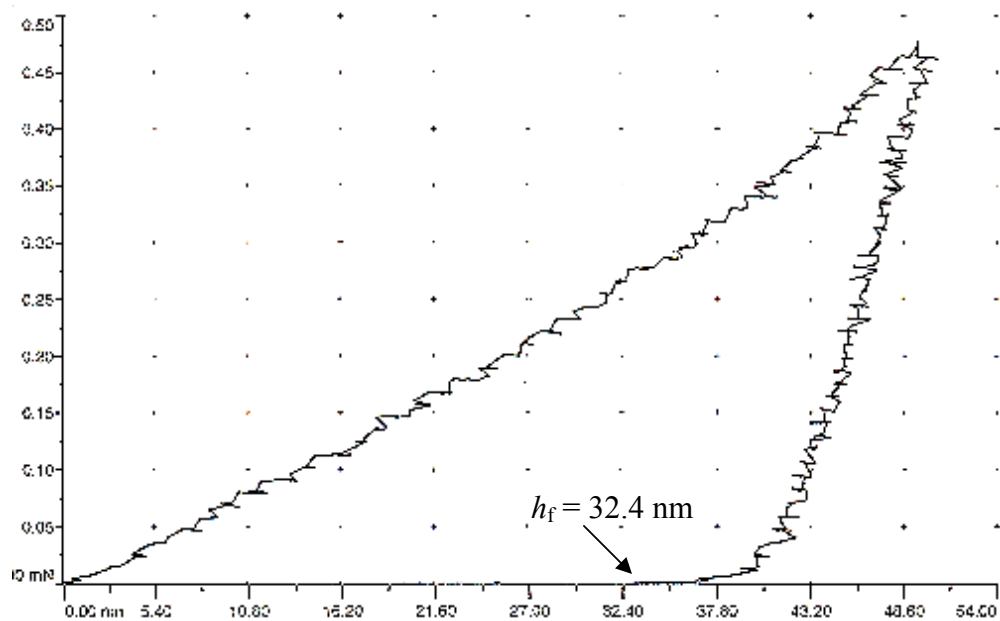
(a)



(b)



(c)



(d)

Figure 10.1. Loading-depth curves of silane films deposited on BSS; (a) bis-amino silane film; (b) bis-sulfur silane film, (c) bis-sulfur/amino mixture silane film, and (d) uncoated BSS substrate (reference)

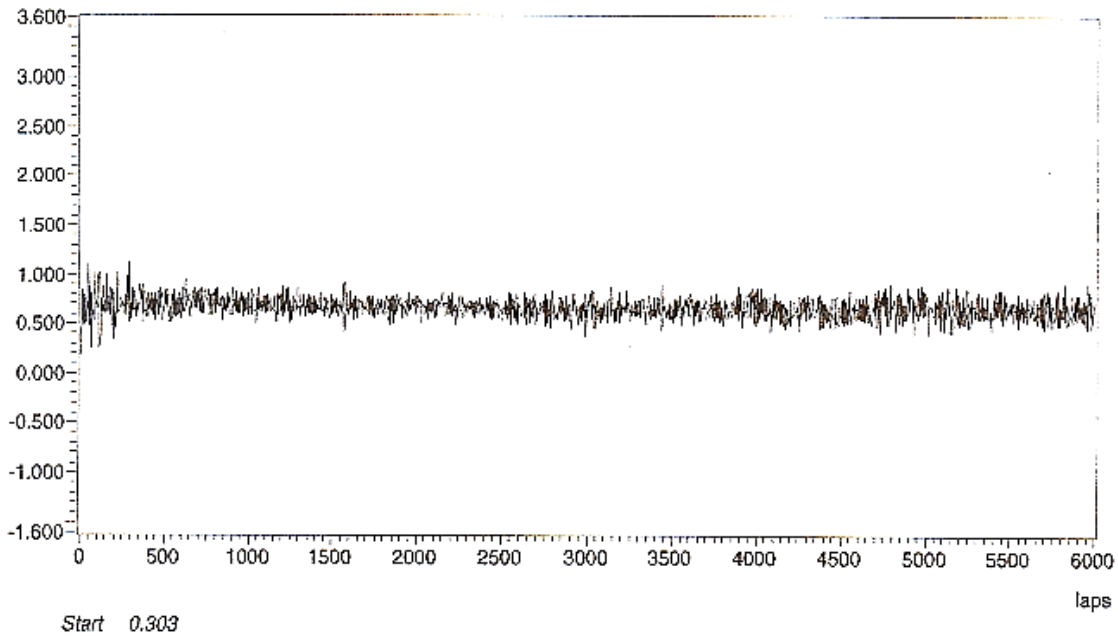
Table 10.3 Berkovich Hardness and Young's modulus of silane films on BSS

| Silanes | Curing condition | <i>H</i> (MPa) | <i>M</i> (GPa) |
|---|-------------------------|-----------------------|-----------------------|
| Bis-amino silane (2%, pH=7) | 100°C/10min | 1630.69 | 29.97 |
| Bis-sulfur silane (5%, pH=6.5) | 100°C/10min | 716.99 | 5.14 |
| Mix(bis-amino+bis-sulfur) (2%+5%, 1:1, pH=7) | 100°C/10min | 549.11 | 6.47 |
| BSS (untreated) | --- | 3256.49 | 131.97 |

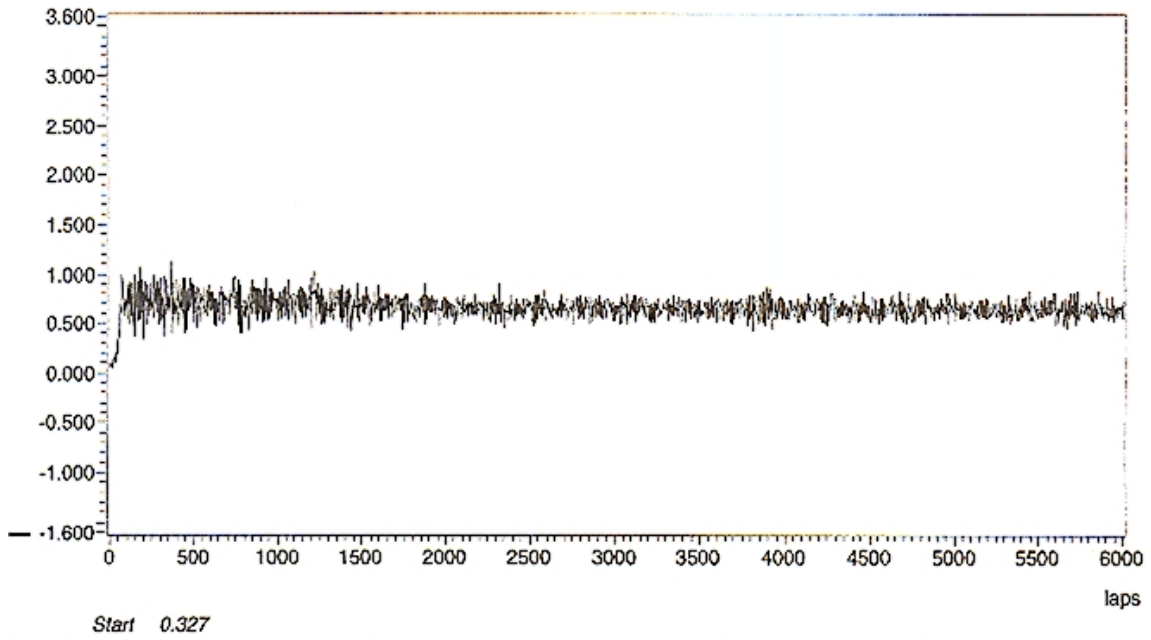
Besides H and E , deformability is also an important property in some practical cases where a certain degree of impacting or bending is unavoidable. The values of final indentation depth (h_f) in Figures 10.1(a)-(d) can be taken as a rough measure of the film deformability. In indentation measurements, h_f is the degree of permanent deformation of a coating after unloaded. Therefore, the greater the value of h_f , the more plastic or less deformable the coating. Comparing the values of h_f for all silane films shown in Figures 10.1(a) to (d), it is obvious that the bis-sulfur silane film has the lowest h_f value of 11.25 nm; which means that this silane film is the most elastic or deformable. In fact, it was observed that deformed bis-sulfur silane film could protect Galvalume[®] (GVL[®], i.e., steel substrate coated with a Zn-55% Al layer) and HDG panels from corrosion, surviving 48 hrs of salt spray test without corrosion ign on the surfaces [25], but not for the other silane-treated panels. The h_f of bis-sulfur/amino silane mixture film, on the contrary, is 50.00 nm, which is the greatest among all silane films. This suggests that the mixture film is less deformable, and as a result, maybe prone to cracking during deformation. The premature formation of cracks leads to the loss of protectiveness of the silane film.

10.2.2. Pin-on-Disk testing: Friction coefficient

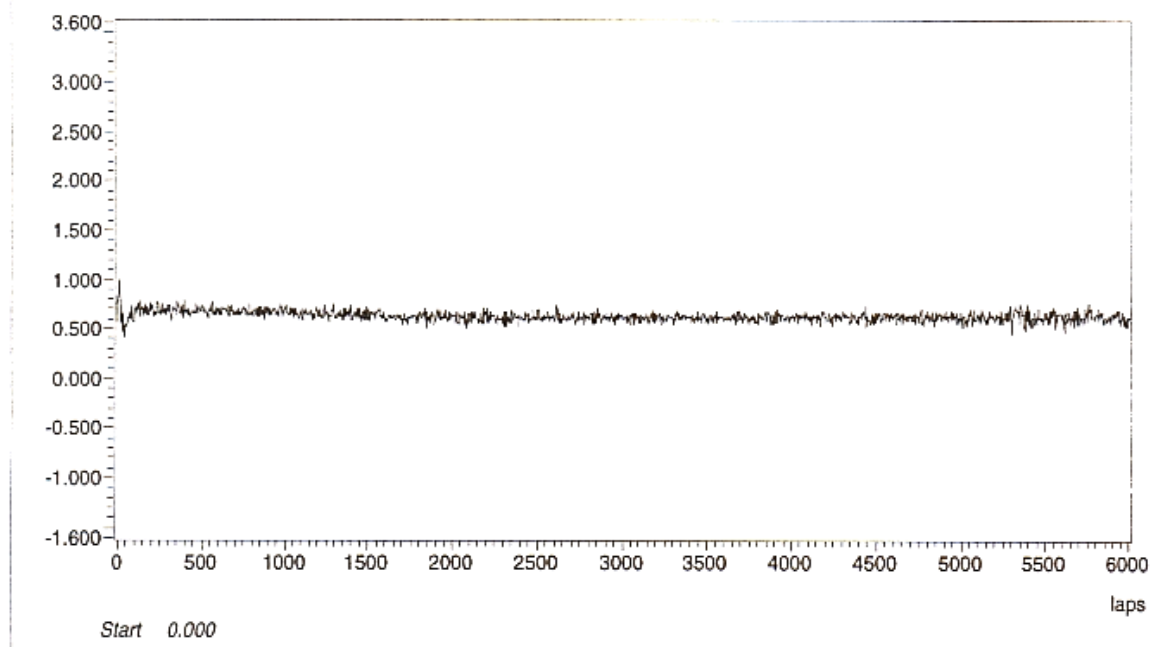
Another important mechanical property of silane films is their friction and wear resistance, which is also a critical concern on moving machine parts in manufacturing industry. A Pin-on-Disk tribometer is usually used to determine friction coefficient (μ) and wear resistance of materials. The friction coefficients for the samples were plotted as a function of distance (lap) shown in Figure 10.2(a)-(d). The values of μ of the silane films were obtained based on these curves and the results are listed in Table 10.4. It is seen in the table that the μ values of the bis-amino silane and bis-sulfur silane films are on the same order of magnitude, ~ 0.09 , while μ of the bis-sulfur/amino silane mixture film is lower, ~ 0.05 than the former individual silanes.



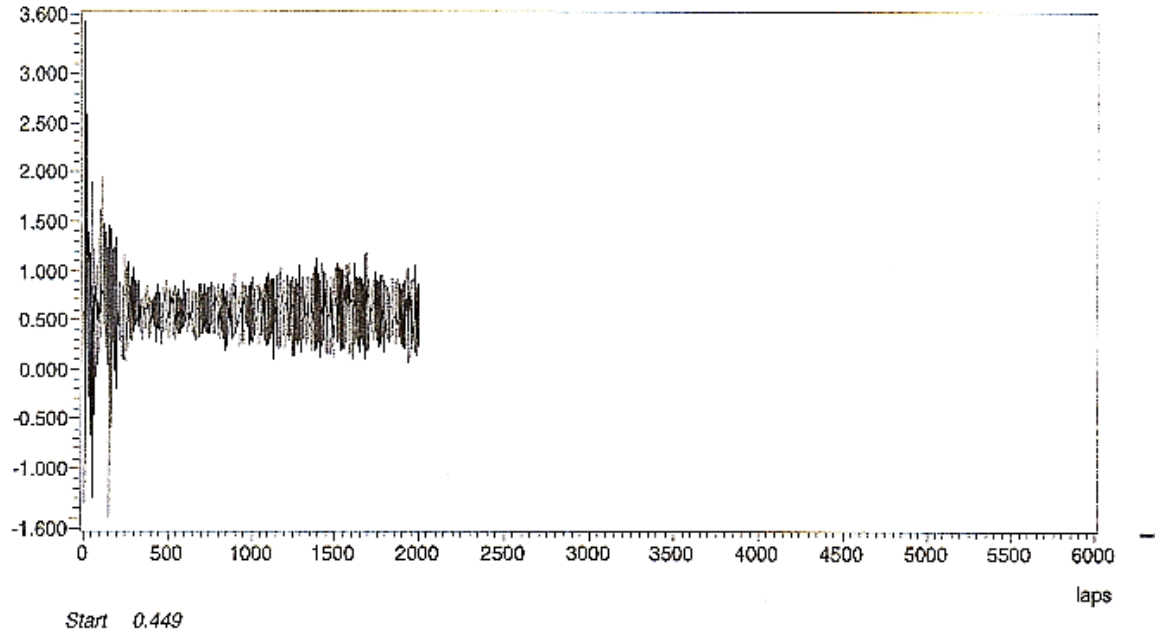
(a)



(b)



(c)



(d)

Figure 10.2. Friction curves of silane films deposited on BSS; (a) bis-amino silane film, (b) bis-sulfur silane film, (c) bis-sulfur/amino mixture silane film, and (d) uncoated BSS substrated (reference)

Table 10.4. Frictional coefficient and distance before failure of silane films on BSS

| Silanes | Curing condition | Distance before failure (m) | μ |
|---|------------------|-----------------------------|--------|
| Bis-amino silane (2%, pH=7) | 100°C/10min | 13.36 | 0.0910 |
| Bis-sulfur silane (5%, pH=6.5) | 100°C/10min | 47.88 | 0.0999 |
| Mix(bis-amino+bis-sulfur) (2%+5%, 1:1, pH=7) | 100°C/10min | 2.36 | 0.0488 |
| BSS (untreated) | -- | -- | 0.2111 |

It is noted that the bis-sulfur/amino silane mixture consistently show unpredictable values in all the above measurements. In the NHT measurements, the silane mixture has the H value of 549.1 MPa, far below those of the individual silanes, i.e., 1630.7 MPa for the bis-amino silane and 717.0 MPa for the bis-sulfur silane. Moreover, the same trend is also shown in the μ values obtained from the Pin-on-Disk measurements. μ of the silane mixture is 0.05, half less than those of the individual silanes. All these observations indicate that there is a synergistic effect of mixing the two silanes. That is, a mixture of bis-sulfur and bis-amino silane may have a relatively different structure from those of the individual silanes.

10.3. Stability of bis-sulfur silane film in water and ethanol

Immediately after treated with silane solutions, the treated metals need to be dried for a certain period at either RT or an elevated temperature to obtain a stable crosslinked film structure. Such structure is required to resist the negative impacts in possible subsequent processes, such as further DI-water-rinsing and/or alcohol-cleaning in practice. In addition, from a reduction of manufacturing cost point of view, quick acquisition of a stable silane/metal structure is also highly desirable. This test was designed to obtain the knowledge of stabilities of silane films in water as well as organic solvents such as ethanol. The structural changes in the bis-sulfur silane film on AA 2024-T3 upon drying and the changes in the subsequent immersion were monitored using FTIR-RA.

10.3.1. Stability of bis-sulfur silane film in DI water

The AA 2024-T3 panels were treated with a 5 vol.% bis-sulfur silane solution, followed by drying in the ambient for various times (i.e., 0 to 60 min). The dried panels were then immersed in DI water or ethanol for 30 min. FTIR-RA measurements were carried out to examine the silane films after immersion.

Figure 10.3 presents the FTIR-RA spectra of the bis-sulfur silane films on AA 2024-T3 after drying in the ambient for various times and followed by immersed in DI water for 30 min. The IR spectrum for a freshly deposited film (spectrum (e) in Figure 10.3) is also shown as reference. It can be seen in spectrum (e) that the intensities of both bands at 3300 cm^{-1} and 881 cm^{-1} due to hydrogen-bonded (H-bonded) SiOH are pronounced. This indicates that the freshly deposited film still contains a considerable amount of SiOH groups which are not condensed without further drying. Such silane films were found to be porous and highly permeable to water, as discussed in Chapter 3.

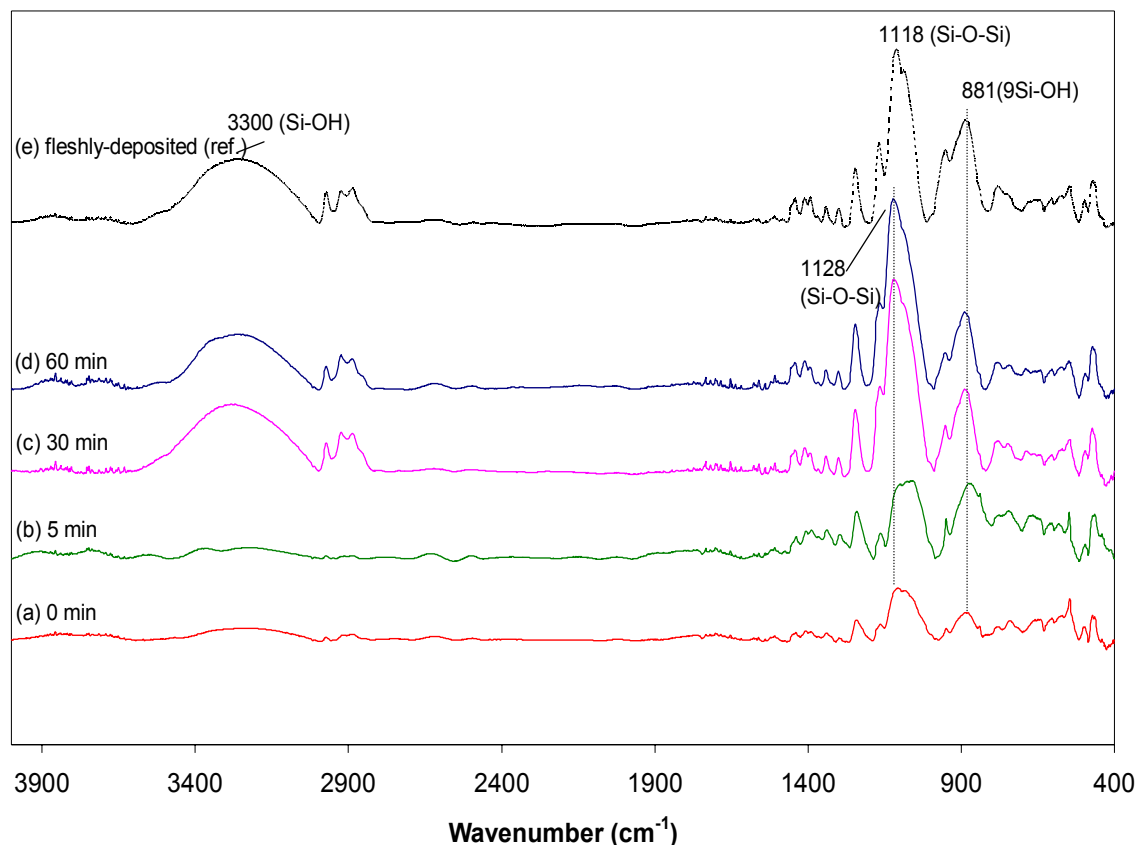


Figure 10.3. FTIR-RA spectra of bis-sulfur silane film on AA 2024-T3 after dried in the ambient for various times and followed by immersed in DI water for 30 min

After immersing the above freshly silane treated AA 2024-T3 panel into DI water for 30 min, all the IR peaks decrease remarkably, as shown in spectrum (a) in Figure 10.3. Apparently, a large number of hydrophilic SiOH groups in the film lead to the most part of this freshly deposited silane film dissolves during DI water immersion.

When extending the drying time to 5 min, the water resistance of the bis-sulfur silane treated AA 2024-T3 panel improves, as evidenced by the IR spectrum (b) in Figure 10.3. The IR peaks below 1400 cm^{-1} are more pronounced in spectrum (b) than in spectrum (a). This indicates that during the 5-min drying process, the silane film has been

further crosslinked forming more hydrophobic SiOSi units. In other words, the film becomes more hydrophobic or water resistant than the one without drying. It is also noted that at this point, H-bonded SiOH band at 880 cm^{-1} is obvious and the broad H-bonded SiOH band at 3300 cm^{-1} is not seen.

After 30 min of drying, the water resistance of the system has been further improved, as evidenced by the IR spectrum (c) in Figure 10.3. No significant decreases in the intensities of the IR bands are observed, suggesting that a stable silane film has finally established. In addition, it is noted that the strongest SiOSi band has shifted from 1118 cm^{-1} to 1128 cm^{-1} . This shift is indicative of the further crosslinking in the system [88,89]. The broad band at 3300 cm^{-1} for H-bonded SiOH is noticeable, along with the SiOH band at 881 cm^{-1} . It should be pointed out that compared with the SiOH band at 3300 cm^{-1} , the one at 881 cm^{-1} seems to more stable. The latter is already pronounced even after 5 min of drying (spectrum (c) in Figure 10.3). A possible explanation to this is that SiOH groups reflected by the 881 cm^{-1} band may locate inside the silane film (e.g., the interfacial region). Thus, these SiOH groups would not be easily washed away during immersion.

The IR spectrum for 60 min of drying (spectrum (d) in Figure 10.3) shows no difference as compared with that for 30 min. This again indicates that 30 min of drying in the ambient is enough to develop a stable and water-resistant bis-sulfur silane film on AA 2024-T3.

It should be noted that critical drying time for the formation of a stable silane film can be significantly shortened if increasing drying temperature. A drying (or curing) process of 10 min at 100°C , for example, is commonly used in the laboratory. This curing

process is sufficient enough to crosslink silane films and to drive the most of solvents (i.e., alcohol or water) out of the films. A temperature above 300°C, however, is not recommended, since some silane films begin to decompose above 300°C. The results obtained from TGA measurements will be presented in Section 10.4.

10.3.2. Stability of bis-sulfur silane film in ethanol

Figure 10.4 compares the FTIR-RA spectra for the bis-sulfur silane films on AA 2024-T3 after dried in the ambient for various times and followed by immersed in ethanol for 30 min. Compared with Figure 10.4, a similar trend for the IR spectra is also shown in Figure 10.4. In general, 30 min of drying is needed for establishing an alcohol-resistant bis-sulfur silane film on AA 2024-T3, as intensive SiOSi bands remain after 30 min of immersion in ethanol (spectrum (d) in Figure 10.4). Furthermore, it is also observed in Figures 10.3 and 10.4 that the freshly-deposited bis-sulfur silane film on AA 2024-T3 tends to dissolve more readily in ethanol than in DI water, as the SiOSi region between 1200 cm^{-1} to 1000 cm^{-1} is more pronounced for the one in Figure 10.3 than in Figure 10.4.

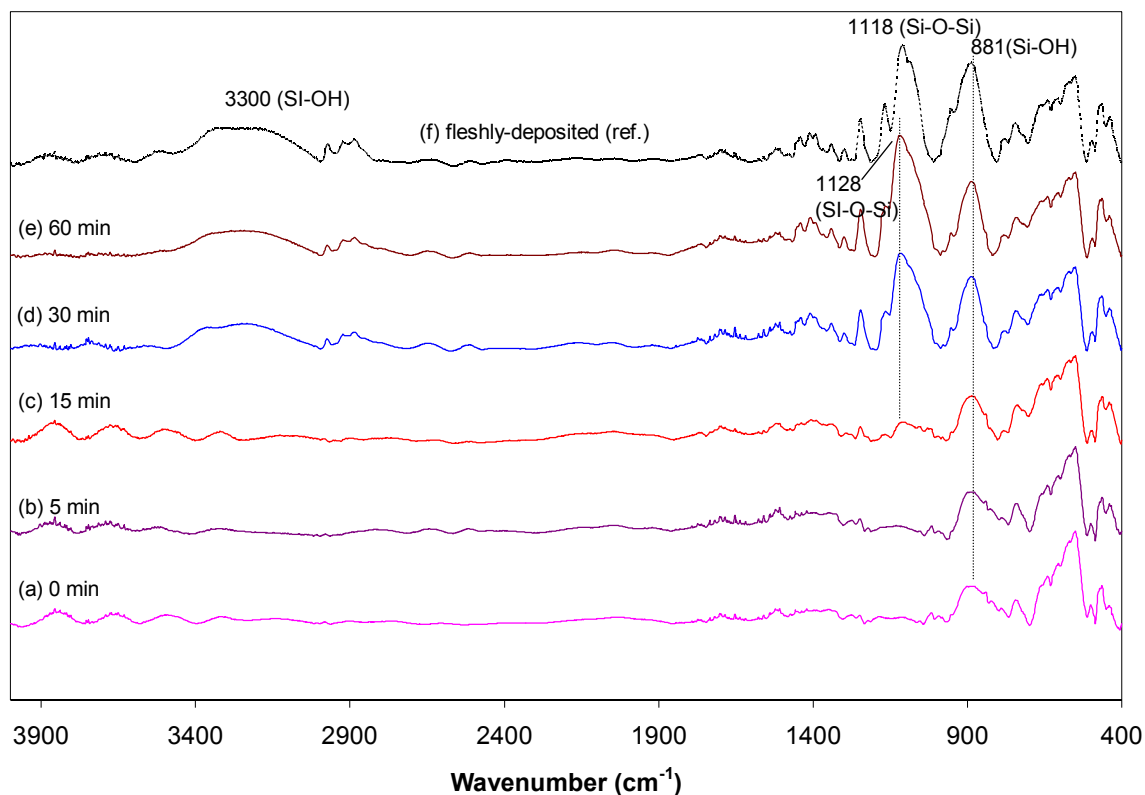


Figure 10.4. FTIR-RA spectra of bis-sulfur silane film on AA 2024-T3 after drying in the ambient for various times and followed by immersed in ethanol for 30 min

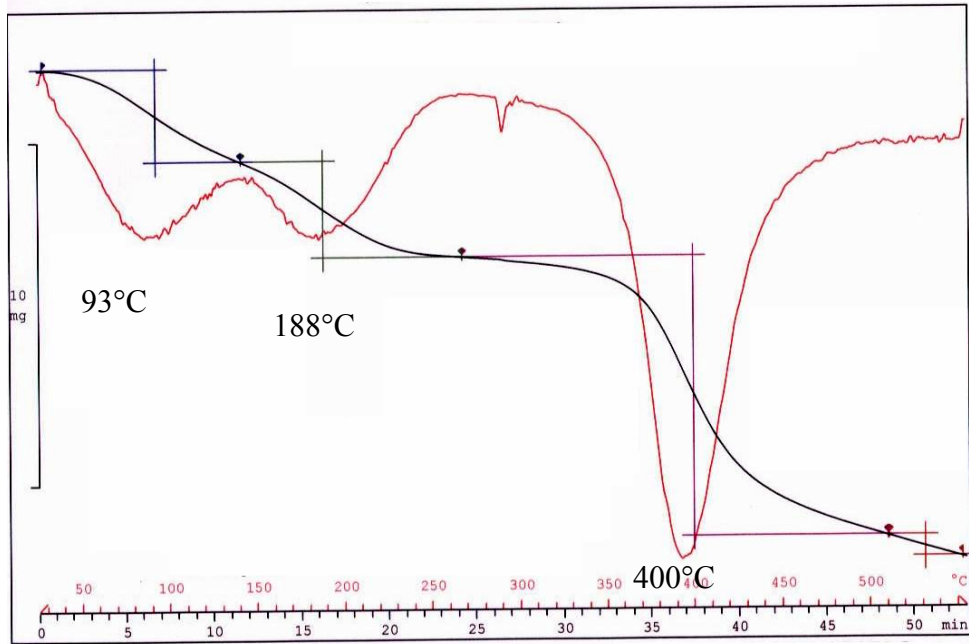
10.4. Thermal stability of silane films

10.4.1. TGA measurements of free silane films

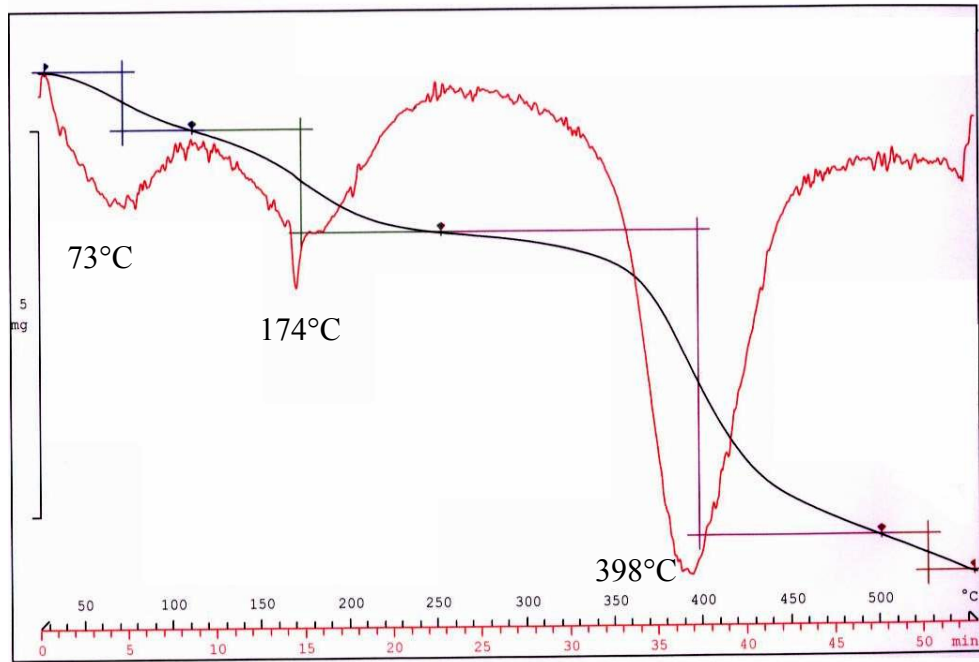
The knowledge of the thermal stability of silane films is of great industrial importance, as silane films are expected to be used at different temperatures. The thermal stability of free silane films (i.e., without substrates) was investigated on a METTER TOLEDO STAR[®] System. The silanes selected here were bis-amino silane, bis-sulfur

silane, bis-sulfur/amino silane mixture (bis-sulfur/bis-amino=9/1), and bis-amino/VTAS silane mixture (bis-amino/VTAS=1.5/1). The plastic dishes that contained a small amount of these 5% silane solutions were placed in a hood for 1 day to obtain crosslinked silane films by driving the solvents out of the solutions. The obtained silane films were further ground to fine powders for the TGA measurements. The results are shown in Figures 10.5(a) to (d). It is seen that the bis-amino silane and the bis-amino/VTAS silane mixture behave similarly in the TGA measurements (Figure 10.5(a) and (b)), i.e., two small “humps” appear below 200 °C, and a significant change exhibits around 400 °C. The former two are related to free water evaporation (< 100°C) and water release in further crosslinking (< 200°C); whereas the latter dip may be associated with the major decomposition of the silane compounds (< 400°C).

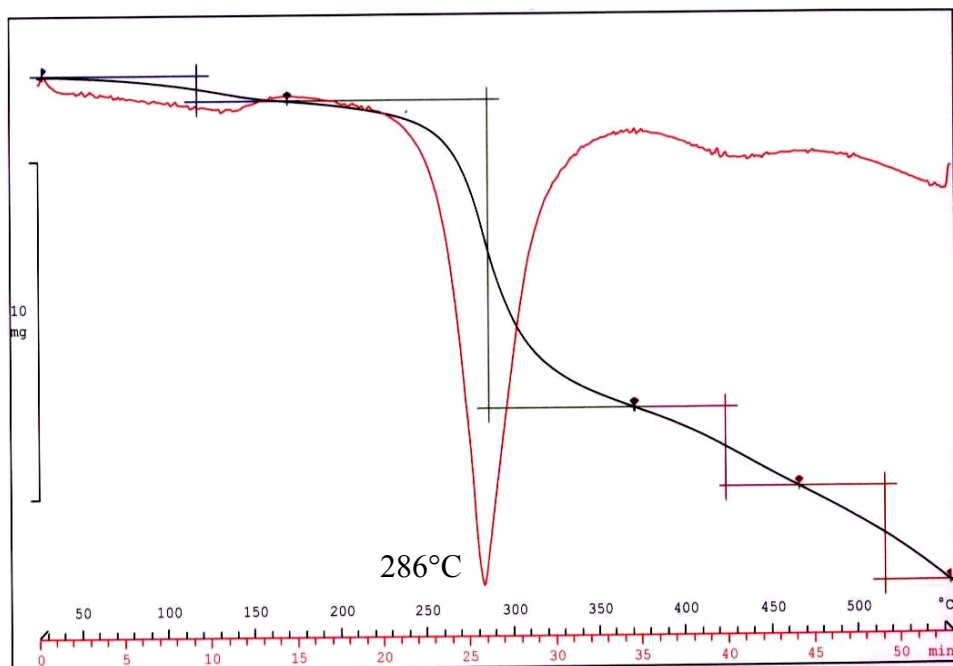
In Figures 10.5(c) and (d), both bis-sulfur silane and bis-sulfur/amino silane mixture perform similarly. No change is observed below 100°C, indicating that both silane films do not tend to entrap free water like the bis-amino silane and bis-amino/VTAS silane films do. This further suggests that the bis-sulfur and bis-sulfur/amino mixture silane films are more hydrophobic than the bis-amino and bis-amino/VTAS. This is understandable. Unlike the former two silane films, the latter two silane films lack hydrophilic groups like –NH– groups and thus do not entrap free water in the films. A small hump around 150°C may indicate a further crosslinking in both bis-sulfur and bis-sulfur/amino silane films. Apparently, the degree of the crosslinking is small as compared to the former two silanes. A major change shown around 300 °C indicates the decomposition of the silane compounds.



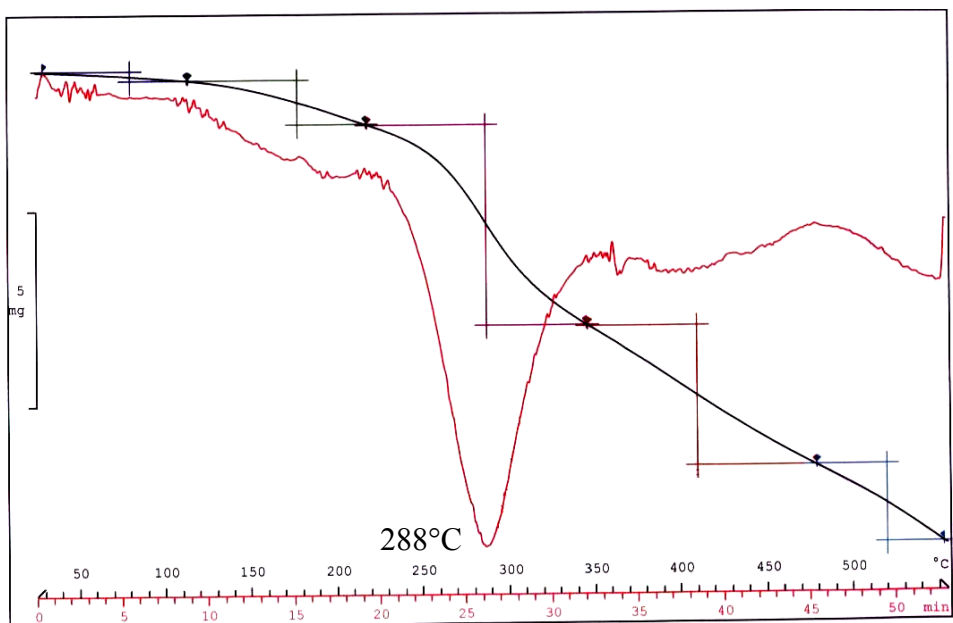
(a)



(b)



(c)



(d)

Figure 10.5. TGA curves of free silane films; (a) bis-amino silane film, (b) bis-amino/VTAS (1.5/1) mixture silane film, (c) bis-sulfur silane film, and (d) bis-sulfur/bis-amino (9/1) silane film

Based on the above results, it can be concluded here that, (1) a further crosslinking occurs for in all silane films near to 200°C in the TGA measurements, and the produced water subsequently evaporates from the silanes showing a weight loss in the TGA curves; (2) the decomposition temperature for bis-amino silane and bis-amino/VTAS silane mixture is around 400 °C, which is 100°C higher than that of bis-sulfur silane and bis-sulfur/amino silane mixture, indicating that the thermal stability of the former two is greater than the latter two; and (3) both bis-amino silane and bis-amino/VTAS silane mixture films tend to entrap free water due to their hydrophilic nature, while hydrophobic bis-sulfur and bis-sulfur/amino (9/1) silane films do not.

10.4.2. Corrosion performance of silane-treated metals at different temperatures

10.4.2.1. Effect of 200°C-curing on the corrosion performance of silane-treated CRS

The silane-treated CRS panels were heated up to 200°C for various time periods. DC polarization tests were conducted in a 0.6 M NaCl solution (pH 6.5), in order to evaluate the effect of elevated temperatures on the corrosion performance of silane films. Figure 10.6 displays corrosion rates (I_{corr}) values for the silane-treated CRS panels as a function of curing time.

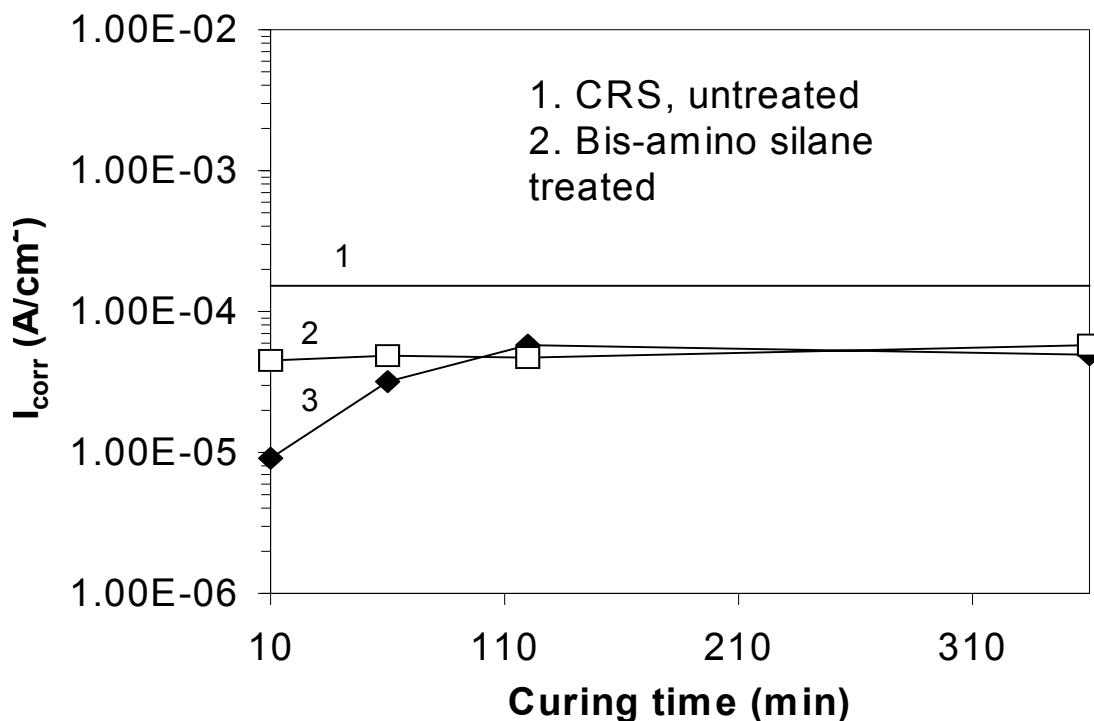


Figure 10.6. I_{corr} of silane-treated CRS panels as a function of curing time at 200°C

It is clearly seen that I_{corr} for the bis-amino silane-treated CRS remains constant in the curing period (curve 2). In other words, the corrosion performance of the bis-amino silane-treated CRS is independent of the curing time. This indicates that the bis-amino silane film is stable at 200°C. On the contrary, the I_{corr} value for the bis-sulfur silane-treated CRS gradually increases with increasing curing time (curve 3). After only 10 min of curing, the bis-sulfur silane has the I_{corr} value around 10^{-5} A/cm², lower than that of the bis-amino silane. This suggests that the bis-sulfur silane at this moment still protects the CRS substrate effectively. After 120 min of curing at 200°C, I_{corr} for the bis-sulfur silane-treated CRS increases distinctively, indicating the degradation of the corrosion performance of the bis-sulfur silane. This degradation of the bis-sulfur silane film is apparently associated with its low decomposition temperature (286°C in Figure 10.5(c)).

10.4.2.2. Effect of -70°C -cooling process on the corrosion performance of silane-treated AA 2024-T3

The effect of low temperature on corrosion behavior of bis-amino and bis-sulfur silane-treated AA 2024-T3 was evaluated using DC polarization tests after cooled at -70°C using dry ice. The silane-treated AA 2024-T3 panels were cured at 100°C for 10 min and then remained at -70°C for 2 hrs. After that, DC polarization tests were conducted on these panels. I_{corr} values for the AA 2024-T3 panels treated with and without silanes are compared in Figure 10.7.

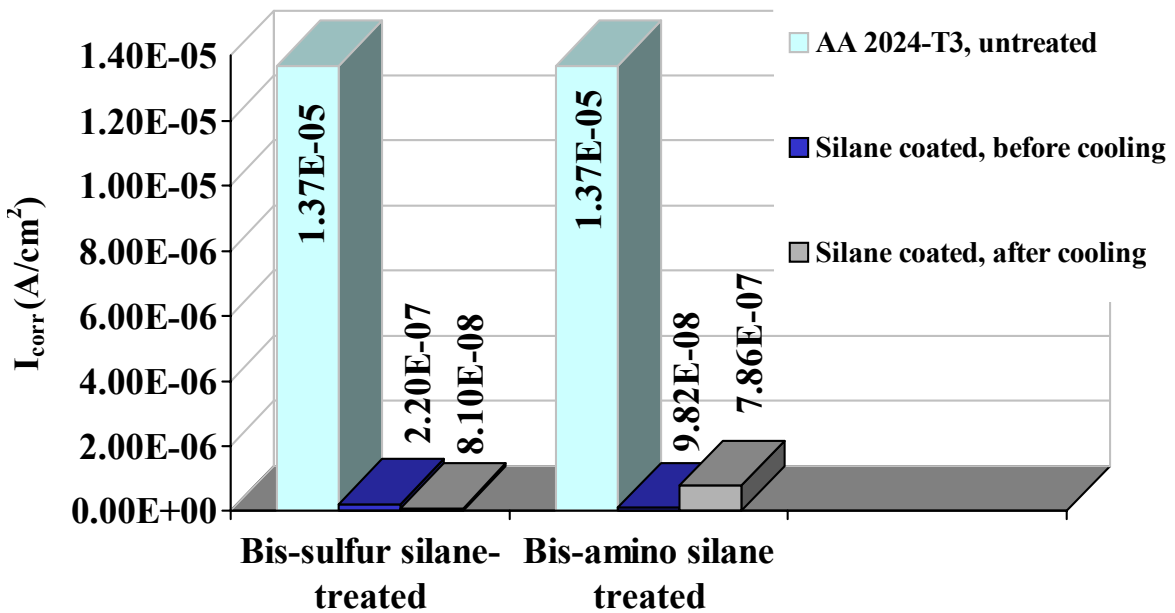


Figure 10.7. Corrosion rates (I_{corr}) of AA 2024-T3 treated with and without silanes

In Figure 10.7, no distinct change is seen for I_{corr} values of the bis-sulfur silane-treated AA 2024-T3 before and after cooling. However, I_{corr} for the bis-amino silane-

treated AA 2024-T3 increases about one order of magnitude after cooling, from 9.8×10^{-8} A/cm² to 7.8×10^{-7} A/cm². The degradation of the bis-amino silane may be caused by micro-cracking occurring at -70°C , due to its brittle nature. The good performance of the bis-sulfur silane, on the other hand, implies that this silane film is more flexible than the bis-amino silane film at low temperatures. As a result, micro-cracks are not easily formed in the bis-sulfur silane film. AA 2024-T3 is thus protected by the intact bis-sulfur silane film.

10.5. Conclusions

1. Bis-amino silane film deposited on both AA 2024-T3 and CRS has a higher resistivity value than bis-sulfur silane and bis-sulfur/amino mixture silane. This is because the bis-amino silane film can easily obtain an extensively crosslinked structure during curing due to a large number of SiOH groups available in the corresponding bis-amino silane solution. Metal substrates significantly affect the resistivity of the silane films. In general, the same silane films on AA 2024-T3 are more insulating than those on CRS.

2. The bis-amino silane film has higher hardness and modulus values than the bis-sulfur silane and bis-sulfur/amino silane mixture films. The friction coefficient of the bis-amino silane and the bis-sulfur silane films is similar, while that of the bis-sulfur/amino silane mixture film is much lower.

3. The bis-sulfur silane film needs to be dried at the ambient over 30 min to obtain a stable crosslinked structure on AA 2024-T3. The as-formed structure is stable

enough to resist the dissolution in water and ethanol. Increasing drying/curing temperature is an efficient way to shorten the drying time for silane films. A temperature greater than 300°C is not recommended, since some silane films begin to decompose above 300°C.

4. TGA measurement results showed that both bis-amino and bis-amino/VTAS mixture silanes have a higher thermal stability than bis-sulfur and bis-sulfur/amino mixture silanes. The decomposition temperature of the former two is around 400 °C, while that of the latter two is less than 300°C.

Chapter 11. General Conclusions and Suggested Future Work

11.1. General conclusions

1. Effects of different curing conditions on bis-sulfur silane film structures on AA 2024-T3 were studied using EIS and FTIR-RA (Chapter 3). The results showed that further hydrolysis and crosslinking occurs in the applied bis-sulfur silane films in the presence of water or moisture. This is because the bis-sulfur silane is difficult to hydrolyze completely in its water/ethanol solution, as a result, the remaining ester groups would hydrolyze to SiOH groups when water or moisture presents (e.g., in the processes of curing in the atmosphere and immersion in an aqueous solution). The as-formed SiOH groups would further condense either with themselves or with AlOH groups at the alloy surface, forming SiOSi and AlOSi bonds.

2. Hydrolysis time of silane solutions significantly affects the resulting silane film structures (Chapter 4). A sufficiently hydrolyzed silane solution is required, in order to obtain a solid silane film which is necessary from a corrosion protection perspective. It was also found that the type of organic solvents (i.e., protic solvents such as ethanol and non-protic solvents such as dioxane) used in bis-sulfur silane solution affects the resulting film structure (Chapter 5). This is because hydrolysis of bis-sulfur silane approaches to completion when using dioxane as a solvent. As a consequence, the film obtained from a dioxane-based solution is extensively crosslinked and is characteristic of longer (or more linear) SiOSi chains than the one from an ethanol-based solution where bis-sulfur silane cannot be fully hydrolyzed. Nevertheless, no big difference was observed for the

corrosion performance of these two types of films. This leads to the conclusion that sufficient rather than complete silane hydrolysis is needed from a corrosion protection point of view.

3. Both EIS and SEM/EDX studies indicated that three different regions are formed in the bis-sulfur silane-treated AA 2024-T3 system. These three regions were detected as three distinct time constants in the EIS measurements (Chapter 3), and were further observed in the SEM/EDX studies (Chapters 7 and 8). They are, from outside to inside, outermost silane film dominated with SiOSi bonds, interfacial layer with both SiOSi and AlOSi bonds, and innermost aluminum oxide, as schematically shown in Figure 11.1. The likely composition of the interfacial layer is $[Al_2O_3]_x \cdot [XSiO_2]_y$.

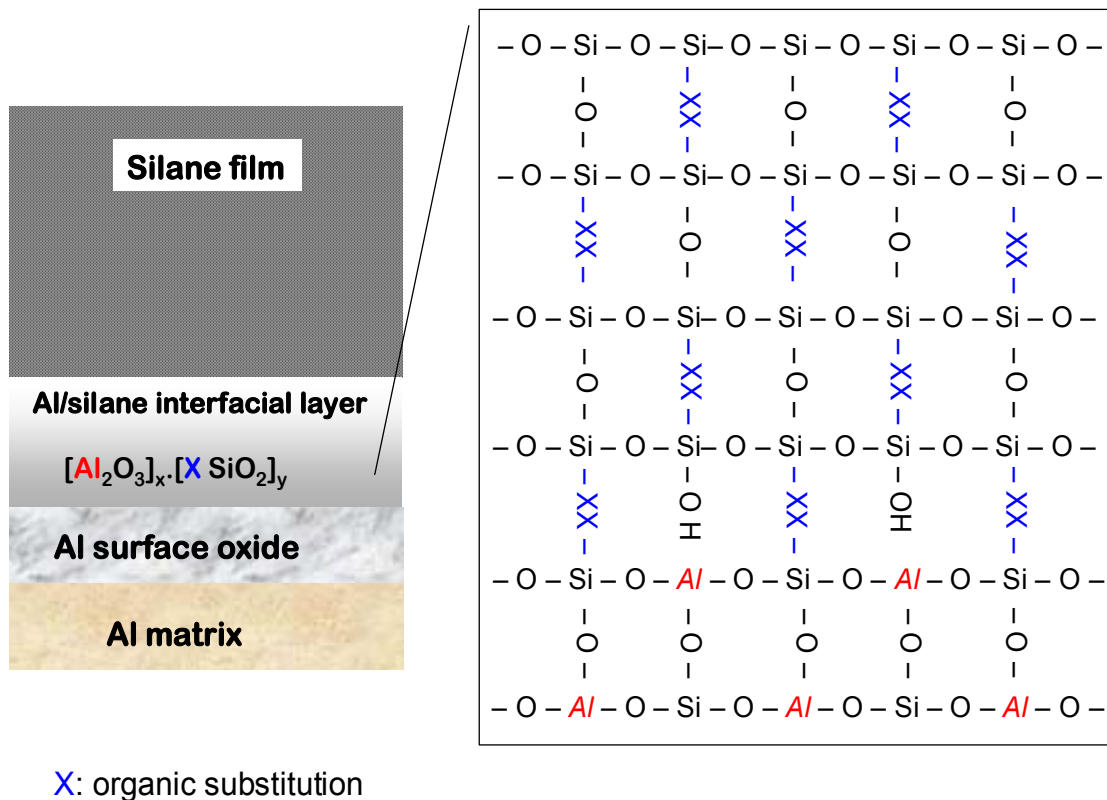


Figure 11.1. A schematic of the interfacial layer formed in a silane-treated Al system

4. On the basis of the corrosion studies (Chapters 7 and 8), it is believed that the following factors play key roles in the corrosion protection of AA 2024-T3.

- ***The formation of a highly-crosslinked interfacial layer.*** This interfacial layer inhibits corrosion in the following two ways: (1) blocking favorable sites for water adsorption by the formation of AlOSi bonds at the interface which effectively reduces the tendency of aqueous corrosion; and (2) bonding tightly to the metal and thus restricting transportation of the existing corrosion products away from their original sites which hinders pit growth. It should be noted that a high density of AlOSi bonds can be obtained by employing bis-silanes rather than mono-silanes (Chapter 7).

- ***High water resistance of silane films.*** It is known that as-formed SiOAl covalent bonds are the major basis for a good adhesion between silane films and the substrate. Nevertheless, SiOAl bond is not hydrolytically stable [1]. The bond tends to hydrolyze back reforming AlOH group and SiOH group when in contact with a large quantity of water. To prevent this detrimental hydrolysis, reduction of water amount in silane films is required. There are, in general, two major ways to achieve this. (1) Fully crosslinking of silane films. On one hand, film porosity is reduced by crosslinking; on the other hand, a hydrophobic SiOSi network is built up by consuming hydrophilic SiOH groups. (2) Employment of silanes with hydrophobic organic/inorganic substitutions, such as sulfur chains ($-\text{S}_4-$) in bis-sulfur silane and alkyl substitution ($-(\text{CH}_2)_2-$) in BTSE, to enhance intrinsic film hydrophobicity. Indeed, the above two methods are all efficient to make the films more water resistant. With the enhanced water resistance of silane films, the interfacial adhesion is secured and the corrosion protection is therefore guaranteed.

5. Hydrophilic bis-amino silane can not provide a desirable corrosion protection for metals (Chapter 8). This is because the bis-amino silane film tends to be positively charged due to the protonation of hydrophilic amino groups. As a result of electrostatic attraction, the transportation of anions like Cl^- ions as well as water is promoted in the film. Corrosion thus readily occurs at the alloy surface. Without sufficient water resistance of the film, AlOSi bonds at the interface are readily hydrolyzed. The interfacial adhesion is consequently lost. Corrosion thus readily proceeds at the alloy surface.

6. Although bis-sulfur silane performs well on Al alloys, it fails on HDG. This is caused by poor film coverage on HDG due to the insufficient wetting of Zn oxide by bis-sulfur silane solution. A mixture at the bis-sulfur/bis-amino ratio of 3/1 enhances the corrosion resistance of both AA 2024-T3 and HDG (Chapter 8). This success is achieved by overcoming the major drawbacks of the two individual silanes. A small portion of bis-amino silane makes the mixture solution hydrophilic enough to wet Zn oxide on HDG, which facilitates the formation of a homogenous film on HDG. On the other hand, a large portion of bis-sulfur silane enhances the hydrophobicity of the mixture film, which is the basis for good protective performance of the mixture.

7. Water-based silane systems have been developed as a response of VOC reduction (Chapter 9). These silane systems are highly miscible with water, which makes them more industrial acceptable than alcohol-based silanes. Test results demonstrated that these silanes can provide excellent corrosion protection as well as paint adhesion on a variety metals including, Al alloys, Zn-coated steels, carbon steels, stainless steels, and CoCr alloy.

8. Resistivity/conductivity of silane films was measured (Chapter 10). The results showed that, (1) a highly crosslinked silane film is more insulating than poorly-crosslinked one; (2) metal substrates affect the film resistivity of the same silane film, e.g., the film deposited on AA 2024-T3 is more insulating than that on CRS.

9. The results from the measurements of mechanical properties of silane films showed that (Chapter 10), (1) bis-sulfur silane film is more flexible than the bis-amino and the mixture of bis-amino and bis-sulfur silane films, and a deformed bis-sulfur silane film is still able to protect metals from corrosion; and (2) the friction coefficient of the mixture is much lower than the bis-sulfur and bis-amino silane films.

10. TGA measurements showed that both bis-amino and bis-amino/VTAS mixture have a higher thermal stability than bis-sulfur silane (Chapter 10). The decomposition temperature of the formers is around 400°C, 100°C higher than that of bis-sulfur silane.

11.2. Suggested future work

The following areas are suggested for the future work on silane surface treatment of metals.

11.2.1. Study on silane/metal interface

It is clear from this work that the interfacial layer that formed between silane and AA 2024-T3 plays a critical role in the process of corrosion protection. Although this interfacial layer has been consistently observed in EIS and SEM/EDX studies, its chemistry is still open to further study. Therefore, a more detailed study on silane/metal interface is definitely expected with the aim of powerful characterization tools such as XPS, ToF-SIMS and Auger spectroscopy, etc.

11.2.2. Transferring silane technology into existing industrial systems

11.2.2.1. In-line quality control of silane solution

This issue is of importance in the process of transferring silane technology into existing industrial systems. So far, no systematic work has been done on this aspect. The aim of this work is to find a method which can be easily used in service to monitor changes in silane solutions used in line. Some potential methods include: (1) titration, (2) X-ray fluorescence spectrometer (XRF), (3) UV-vis spectrometer, and (4) liquid FTIR.

Another related issue is to clarify the effect of metal ions on the efficiency of in-line silane solutions. Unfortunately, this issue has always been ignored on the laboratory scale.

11.2.2.2. In-line detection of silane films on metals

This issue is equally important as the above one. Although XRF has been tested with satisfactory results, some other simpler methods, such as coloring silane films using colorants, are still worthy of a try.

11.2.3. “Self-healing” silane-based systems

It is clear that intact silane films provide equally good corrosion protection for metals as chromates do. However, they will lose their protectiveness when the films are damaged. On the contrary, chromates have been distinguished for their “self-healing” effect [107,108]. When a chromated metal surface is damaged accidentally in service, the chromates are able to leach out and diffuse to the damaged area, reforming a protective film in-situ. The damaged area is thus protected. Development of “self-healing” silane systems is necessary in order to make the silane systems more powerful. In this case, both existing cathodic and anodic inhibitors are worthy of testing.

Appendix A. Comparison of Corrosivity of K_2SO_4 and NaCl

Potentiodynamic polarization tests were done on AA 2024-T3 blank and treated by sulfane silane in both 0.5 M K_2SO_4 and 0.5 M NaCl solutions at pH 6. The purpose of the tests was to evaluate the corrosivity of K_2SO_4 and NaCl solutions. The tested specimens were immersed in the electrolytes for 40 min before recording the data in an attempt to achieve a steady state. The results are presented in Figures A1 and A2. It is evident from Figure A1 that both cathodic and anodic currents reduce significantly in 0.5 M K_2SO_4 for AA 2024-T3 blank, compared with the case in 0.5M NaCl. In the case of bis-sulfur silane-treated AA 2024-T3 (Figure A2), although no difference between cathodic currents in both 0.5 M K_2SO_4 and 0.5 M NaCl solutions, the anodic reaction (or metal dissolution) is apparently inhibited in 0.5 M K_2SO_4 . Based on the comparisons above, 0.5 M K_2SO_4 has thus been chosen as a non-corrosive electrolyte in the EIS study here.

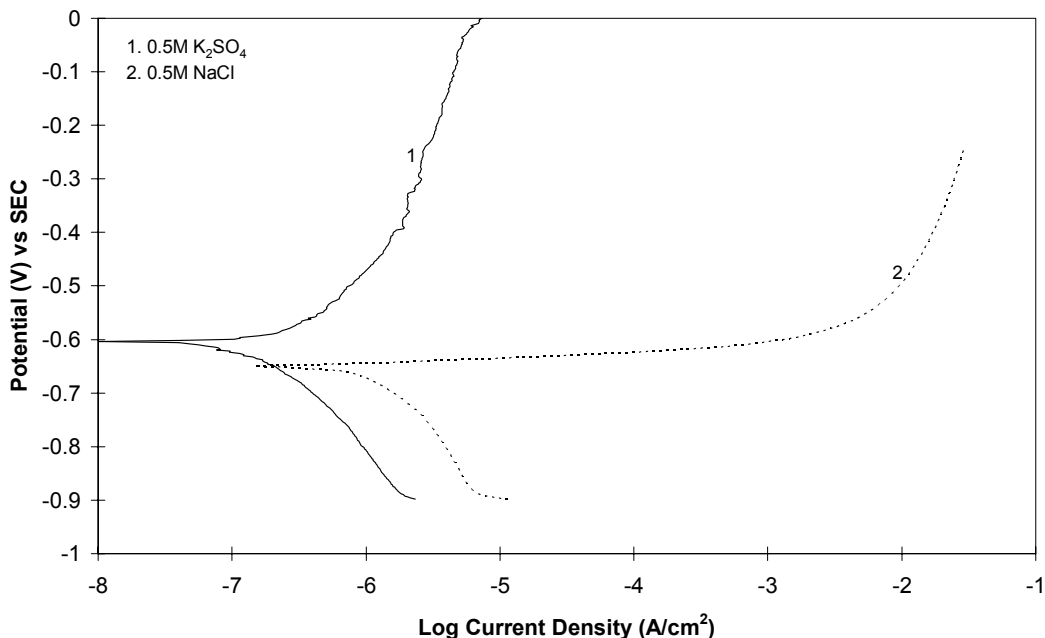


Figure A1. Potentiodynamic polarization curves of AA 2024-T3 blank in 0.5M K_2SO_4 and 0.5 M NaCl solutions at pH 6

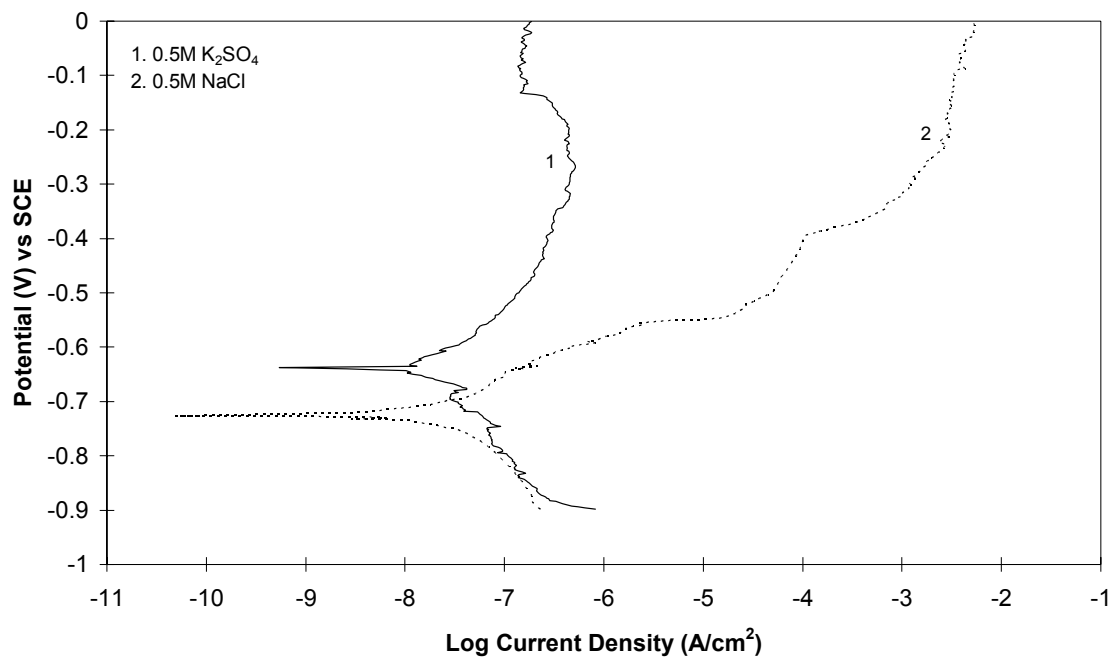


Figure A2. Potentiodynamic polarization curves of bis-sulfur-treated AA 2024-T3 in 0.5 M K₂SO₄ and 0.5 M NaCl solutions at pH 6

Appendix B: Fitted EIS data for the bis-sulfane silane treated AA 2024-T3 systems studied in Chapter 3

Table B1. Summary of fitted EIS data for the immersion process

| t | Silane film | | | | Unknown phase | | | | Oxide film | | $R_0 \pm dR_0$ |
|------|----------------------------|----------------------------|----------------------------|----------------------------|----------------------------|----------------------------|----------------------------|----------------------------|----------------------------|----------------------------|----------------------------|
| (h) | $Q_{sil} \pm dQ_{sil}$ | $n_{sil} \pm dn_{sil}$ | $R_{sil} \pm dR_{sil}$ | $C_{sil} \pm dC_{sil}$ | $Q_{un} \pm dQ_{un}$ | $n_{un} \pm dn_{un}$ | $R_{un} \pm dR_{un}$ | $C_{un} \pm dC_{un}$ | $Q_{ox} \pm dQ_{ox}$ | $n_{ox} \pm dn_{ox}$ | (Ohm) |
| | (Ohm) | | (Ohm) | (F) | (Ohm) | | (Ohm) | (F) | (Ohm) | | |
| 0.16 | 3.23E+06 $\pm 1.91E+05$ | 9.16E-01 $\pm 5.76E-03$ | 1.85E+03 $\pm 5.58E-01$ | 1.30E-07 $\pm 8.99E-11$ | N/A | N/A | N/A | N/A | 6.37E+04 $\pm 5.15E+02$ | 8.73E-01 $\pm 3.24E-03$ | 3.99E+01 $\pm 8.24E-01$ |
| 2 | 5.47E+06 $\pm 6.05E+05$ | 9.48E-01 $\pm 9.69E-03$ | 1.88E+04 $\pm 9.24E+03$ | 1.08E-07 $\pm 8.08E-08$ | 2.09E+06 $\pm 1.60E+06$ | 7.50E-01 $\pm 2.05E-01$ | 1.85E+04 $\pm 9.96E+03$ | 8.08E-08 $\pm 5.05E-08$ | 7.99E+04 $\pm 2.66E+03$ | 8.52E-01 $\pm 2.33E-03$ | 4.27E+01 $\pm 1.16E-01$ |
| 4 | 6.69E+06 $\pm 5.70E+05$ | 9.54E-01 $\pm 7.96E-03$ | 2.76E+04 $\pm 1.04E+04$ | 9.83E-08 $\pm 1.61E-09$ | 6.77E+06 $\pm 1.34E+06$ | 7.69E-01 $\pm 4.48E-02$ | 1.88E+05 $\pm 1.27E+04$ | 4.79E-08 $\pm 1.80E-09$ | 9.07E+04 $\pm 2.24E+02$ | 8.54E-01 $\pm 3.41E-03$ | 4.08E+01 $\pm 1.10E-01$ |
| 8 | 7.97E+06 $\pm 7.50E+04$ | 9.66E-01 $\pm 0.00E-00$ | 1.04E+05 $\pm 2.38E+04$ | 9.44E-08 $\pm 2.21E-09$ | 1.39E+07 $\pm 2.35E+06$ | 8.57E-01 $\pm 5.15E-02$ | 4.75E+05 $\pm 2.65E+04$ | 3.71E-08 $\pm 8.88E-10$ | 9.42E+04 $\pm 2.36E+03$ | 8.61E-01 $\pm 0.00E-00$ | 4.10E+01 $\pm 9.35E-01$ |

Table B2. Summary of fitted EIS data for the curing process

| t | Silane film | | | | Unknown phase | | | | Oxide film | | $R_0 \pm dR_0$ |
|------|------------------------|------------------------|------------------------|------------------------|----------------------|----------------------|----------------------|----------------------|----------------------|----------------------|----------------|
| (h) | $Q_{sil} \pm dQ_{sil}$ | $n_{sil} \pm dn_{sil}$ | $R_{sil} \pm dR_{sil}$ | $C_{sil} \pm dC_{sil}$ | $Q_{un} \pm dQ_{un}$ | $n_{un} \pm dn_{un}$ | $R_{un} \pm dR_{un}$ | $C_{un} \pm dC_{un}$ | $Q_{ox} \pm dQ_{ox}$ | $n_{ox} \pm dn_{ox}$ | (Ohm) |
| | (Ohm) | | (Ohm) | (F) | (Ohm) | | (Ohm) | (F) | (Ohm) | | |
| 0.16 | 2.17E+06 | 8.91E-01 | 3.69E+02 | 1.40E-07 | N/A | N/A | N/A | N/A | 4.74E+04 | 8.82E-01 | 3.67E+01 |
| | $\pm 3.27E+05$ | $\pm 1.39E-02$ | $\pm 7.23E+00$ | $\pm 1.11E-10$ | | | | | $\pm 5.23E+02$ | $\pm 3.56E-03$ | $\pm 1.15E-01$ |
| 1 | 5.46E+06 | 9.47E-01 | 6.53E+03 | 1.08E-07 | N/A | N/A | N/A | N/A | 7.58E+04 | 8.28E-01 | 3.95E+01 |
| | $\pm 2.95E+05$ | $\pm 5.43E-03$ | $\pm 1.01E+02$ | $\pm 1.35E-10$ | | | | | $\pm 8.13E+02$ | $\pm 4.77E-03$ | $\pm 1.01E-00$ |
| 2 | 8.39E+06 | 9.83E-01 | 4.61E+04 | 1.03E-07 | 6.23E+06 | 7.73E-01 | 4.22E+05 | 5.15E-08 | 1.24E+05 | 7.65E-01 | 4.12E+01 |
| | $\pm 7.30E+05$ | $\pm 8.40E-03$ | $\pm 1.94E+04$ | $\pm 3.03E-09$ | $\pm 1.17E+06$ | $\pm 5.13E-02$ | $\pm 3.09E+04$ | $\pm 2.87E-09$ | $\pm 7.11E+03$ | $\pm 2.00E-02$ | $\pm 1.26E-00$ |
| 3.3 | 1.04E+07 | 9.77E-01 | 1.35E+05 | 8.25E-08 | 2.14E+07 | 8.06E-01 | 3.61E+06 | 2.19E-08 | 2.49E+05 | 7.36E-01 | 4.32E+01 |
| | $\pm 8.00E+05$ | $\pm 7.42E-03$ | $\pm 8.63E+04$ | $\pm 1.33E-09$ | $\pm 4.47E+06$ | $\pm 4.44E-02$ | $\pm 1.84E+05$ | $\pm 1.03E-09$ | $\pm 3.09E+04$ | $\pm 3.80E-02$ | $\pm 1.42E-00$ |
| 5.3 | 8.75E+06 | 9.71E-01 | 2.12E+05 | 9.54E-08 | 3.48E+07 | 8.77E-01 | 7.45E+06 | 1.89E-08 | 4.15E+05 | 6.57E-01 | 4.32E+01 |
| | $\pm 1.07E+05$ | $\pm 0.00E+00$ | $\pm 9.22E+04$ | $\pm 1.10E-09$ | $\pm 5.35E+06$ | $\pm 5.15E-02$ | $\pm 3.79E+05$ | $\pm 3.97E-10$ | $\pm 1.11E+05$ | $\pm 6.39E-02$ | $\pm 1.22E-01$ |
| 6 | 1.14E+07 | 9.79E-01 | 8.73E+05 | 7.73E-08 | 4.17E+07 | 8.99E-01 | 2.62E+07 | 1.90E-08 | N/A | N/A | 4.17E+01 |
| | $\pm 2.89E+05$ | $\pm 2.95E-03$ | $\pm 0.00E+00$ | $\pm 3.70E-10$ | $\pm 4.89E+06$ | $\pm 0.00E+00$ | $\pm 4.61E+05$ | $\pm 2.23E-09$ | | | $\pm 1.16E-00$ |

Table B3. Summary of fitted EIS data for the aging process

| t | Silane film | | | | Oxide film | | $R_0 \pm dR_0$ |
|-----|--------------------------------------|--------------------------------------|--------------------------------------|--------------------------------------|------------------------------------|------------------------------------|-----------------------|
| (h) | $Q_{\text{sil}} \pm dQ_{\text{sil}}$ | $n_{\text{sil}} \pm dn_{\text{sil}}$ | $R_{\text{sil}} \pm dR_{\text{sil}}$ | $C_{\text{sil}} \pm dC_{\text{sil}}$ | $Q_{\text{ox}} \pm dQ_{\text{ox}}$ | $n_{\text{ox}} \pm dn_{\text{ox}}$ | (Ohm) |
| | (Ohm) | | (Ohm) | (F) | (Ohm) | | |
| 24 | 2.99E+06 | 8.93E-01 | 6.98E+02 | 1.97E-07 | 5.24E+04 | 9.16E-01 | 3.70E+01 |
| | $\pm 2.61\text{E}+05$ | $\pm 8.10\text{E}-03$ | $\pm 8.40\text{E}+00$ | $\pm 9.58\text{E}-09$ | $\pm 4.01\text{E}+02$ | $\pm 2.74\text{E}-03$ | $\pm 9.79\text{E}-01$ |
| 72 | 5.74E+06 | 9.30E-01 | 1.42E+04 | 1.25E-07 | 6.45E+04 | 8.99E-01 | 3.71E+01 |
| | $\pm 0.00\text{E}+00$ | $\pm 0.00\text{E}+00$ | $\pm 6.54\text{E}+02$ | $\pm 0.00\text{E}+00$ | $\pm 6.54\text{E}+02$ | $\pm 0.00\text{E}+00$ | $\pm 0.00\text{E}+00$ |
| 96 | 6.33E+06 | 9.56E-01 | 2.74E+04 | 1.28E-07 | 6.53E+04 | 9.09E-01 | 4.14E+01 |
| | $\pm 0.00\text{E}+00$ | $\pm 0.00\text{E}+00$ | $\pm 2.43\text{E}+02$ | $\pm 0.00\text{E}+00$ | $\pm 7.24\text{E}+02$ | $\pm 0.00\text{E}+00$ | $\pm 7.14\text{E}-01$ |
| 120 | 7.10E+06 | 9.60E-01 | 6.28E+04 | 1.16E-07 | 6.81E+04 | 8.97E-01 | 4.06E+01 |
| | $\pm 1.69\text{E}+05$ | $\pm 2.61\text{E}-03$ | $\pm 1.90\text{E}-02$ | $\pm 1.35\text{E}-09$ | $\pm 9.76\text{E}+02$ | $\pm 6.60\text{E}-03$ | $\pm 8.06\text{E}-01$ |

The values of capacitance in the Tables B1~B4 were calculated from the CPE parameters, Y_0 ($=1/Q$) and n , using equation (2) mentioned in the paper. The errors in capacitance were obtained using the error propagation method applied to Eq. (2) [85].

It should be noted that the fitted EIS data for aluminum oxide film could not be determined in some cases, due to the instrumental limitations (10^{-3} Hz). The time constant for the oxide film is located at low frequencies, and in most cases a complete time constant for the oxide film could not be obtained.

Table B4. Dielectric constants ϵ of sulfane silane film in the curing process at 80°C

| t | ϵ |
|------|------------|
| (h) | |
| 0.16 | 15.85 |
| 1 | 12.22 |
| 2 | 11.66 |
| 3.3 | 9.34 |
| 5.3 | 10.80 |
| 6 | 8.75 |

The calculations have been done with an assumption that the thickness of silane film is constant in the process. A calculated dielectric constant of 8.75, for example, is quite reasonable for the film with some water inside after 6 hrs of curing at 80°C, compared with some literature data, e.g., 3~5 for fully cured polymer, and 6.60 for $\text{Al}_2\text{O}_3 \cdot \text{Si}_2\text{O}_3$.

Appendix C. ToF-SIMS Mapping of Bis-[triethoxysilylpropyl]tetrasulfide Film on AA 2024-T3

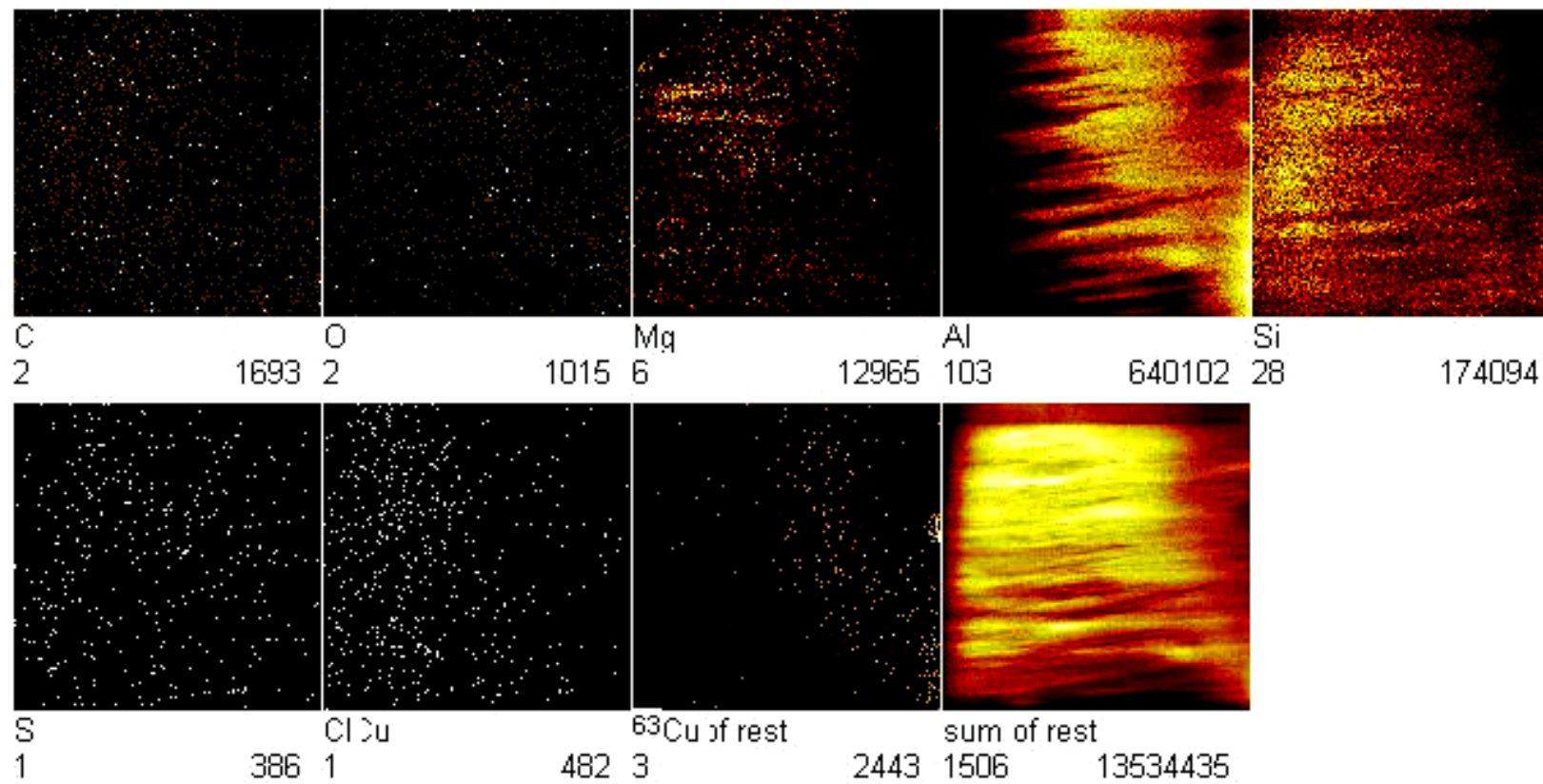


Figure C1. Positive mapping (resolution $1\mu\text{m} \times 1\mu\text{m}$)

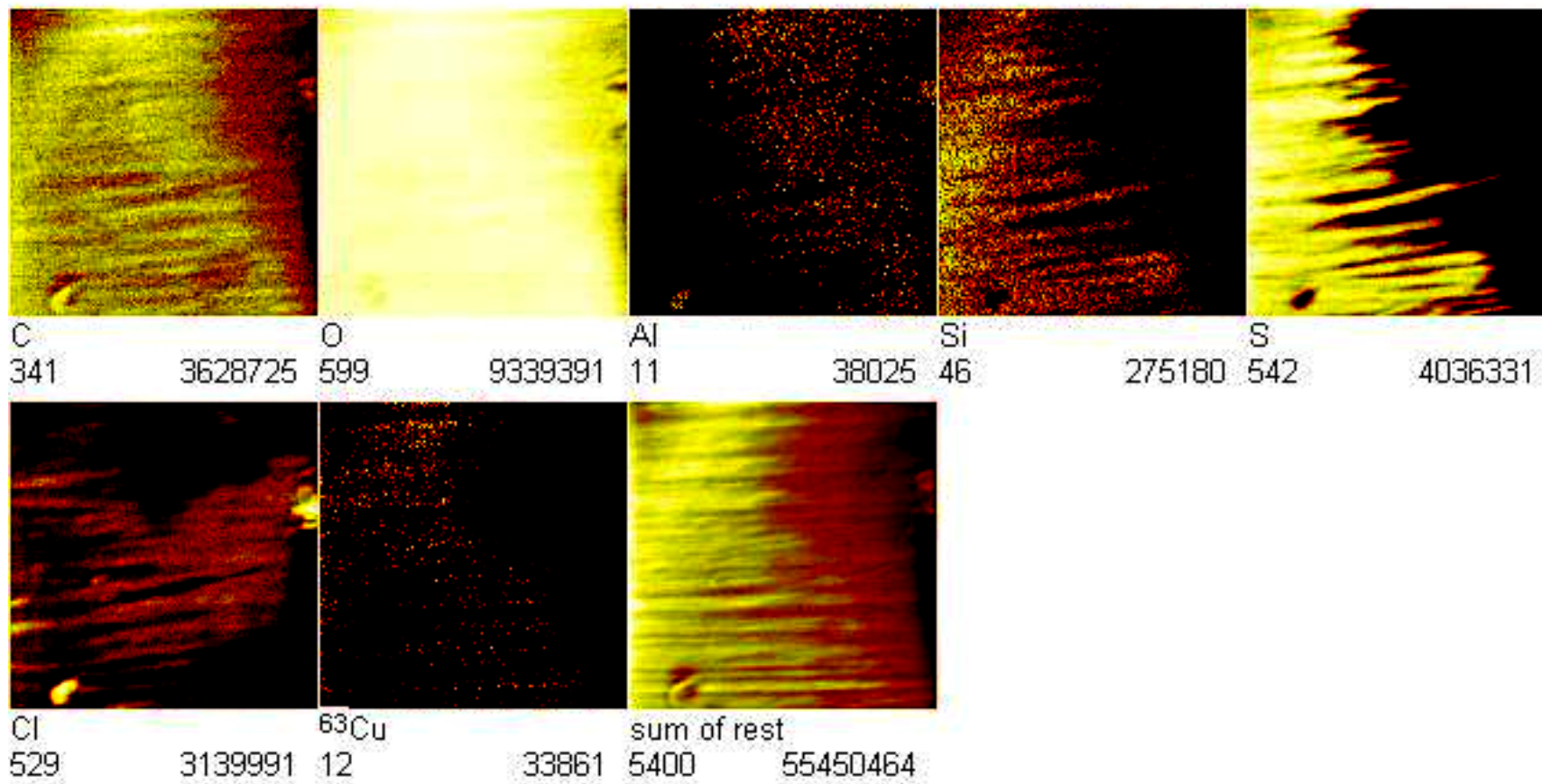


Figure C2. Negative mapping (resolution $1\mu\text{m} \times 1\mu\text{m}$)

References

1. E. P. Plueddenmann. "Silane Coupling Agents", 2nd edition, Plenum Press, New York, 1991
2. E. R. Pohl, A. Chaves, C. T. Danehey, A. Sussman and V. Bennett, In: "Silanes and Other Coupling Agents", Vol. 2, K. L. Mittal Ed., VSP, 15 (2000)
3. F. D. Osterholtz and E. R. Pohl, *J. Adhesion Sci. Technol.*, 6, 127 (1992)
4. E. R. Pohl. SPI, 38th Ann. Conf. Reinf. Plast. 40B (1983)
5. H. Ishida and J. L. Koenig. *Appl. Spectroscopy*, 32, 469 (1978)
6. E. R. Pohl and F. O. Osterholz. In "Silanes, Surfaces and Interfaces", Vol. 1, D. E. Leyden, Ed., Gordon & Breach, Amsterdam, 481 (1986)
7. B. Arkles, J. R. Steinmetz, J. Zazyczny and P. Mehta, *J. Adhesion Sci. Technol.*, 6, 193 (1992)
8. C. H. Chiang, H. Ishida, and J. Koenig. *J. Colloid Interface Sci.* 74, 396 (1980)
9. A. C. Zettlemyer. In "Chemistry and Physics of Interfaces", D. E. Gushee, Ed., Chapter XII, American Chemical Society, Washington, D.C. 1965
10. J. C. Bolger. In "Adhesion Aspects of Polymeric Coatings", K. L. Mittal, Ed., Plenum Press, New York, 3 (1983)
11. F. J. Boerio and R. G. Dillingham. In: "Adhesive Joints", K. L. Mittal, Ed., Plenum Press, New York, 541 (1984)
12. F. J. Boerio, R. G. Dillingham, and R. C. Bozian. SPI, 39th Ann. Tech. Conf. Reinf. Plast. 4-A. (1984)
13. P. Walker. *J. Coatings Technol.*, 52, 33 (1980)

14. Y. K. Lee and J. D. Craig. The Electrochemical Society 159th Meeting
Minneapolis, MN, Paper 141, 1981
15. E. P. Plueddemann. *Modern Plast.*, 54, 102 (1966)
16. M. A. Lutz and K. E. Palmanteer. *J. Coatings Technol.*, 51, 37 (1979)
17. E. P. Plueddemann. *Adhesives Age*, 18(36), June (1975)
18. E. P. Plueddemann and G. L. Stark. SPI, 35th Ann. Tech. Conf. Reinf. Plast. 13-A
(1980)
19. E. P. Plueddemann. In: “Surface and Colloid Science in Computer Technology”,
K. L. Mittal, Ed., p. 152, Plenum Press, New York, 1987
20. Gelest Inc., “Reactive Silicone: Forging New Polymer Links”, version 2.0.
21. M. Bethencourt, F. J. Botana, J. J. Calvino, M. Marcos, and M. A. Rodríguez-
Chacón, *Corros. Sci.*, 40, 1803 (1998)
22. N. N. Greenwood, and A. Earnshaw, “Chemistry of the Elements”, Pergamon
Press, Oxford, England, 1437 (1984)
23. C. M. Mustafa, S. M. Shahinoor Islam Dulal, *CORROSION*, 52, 16 (1996)
24. W. J. van Ooij and D. Zhu, *CORROSION*, 157, 413 (2001)
25. D. Zhu and W. J. van Ooij, ‘Surface Modification of Metals by Silanes’, to be
published in the proceedings of ‘Adhesion Aspects of Polymeric Coatings’, held
May 25-26, Newark, NJ, 2000
26. W. J. van Ooij and T. F. Child. *CHEMTECH*, 28, 26 (1998)
27. V. Subramanian, Ph. D. Dissertation, University of Cincinnati, Department of
Materials Science and Engineering, 1999

28. W. J. van Ooij, C. Zhang, J. Zhang, and W. Yuan, "Pretreatment of metals for painting by organofunctional silanes", presented at the International Symposium on "Advances in Corrosion Protection by Organic Coatings", Oct. 29-31, 1997, Science University of Tokyo, Noda, Japan
29. Guru Prasad Sundararajan, M. S. Thesis, University of Cincinnati, Department of Materials Science and Engineering, 2000
30. V. Subramanian and W. J. van Ooij, CORROSION, 54, 204(1998)
31. V. A. Ogarev, S. L. Selector. Prog. in Org. Coat., 21, 135 (1992)
32. M. A. Petrunic, A. P. Nazarov, and Yu. N. Mikhailovski, J. Electrochem. Soc. 143, 251 (1996)
33. A. M. Beccaria and L. Chiaruttini, Corros. Sci., 41, 885(1999)
34. P. R. Underhill and D. L. Duquesnay, "Silanes and Other Coupling Agents", Vol. 2, K. L. Mittal Ed., VSP, 149 (2000)
35. K. Aramaki, Corros. Sci., 42, 1975 (2000)
36. M. Pourbaix, Atlas of Electrochemical Equilibria in Aqueous Solutions, NACE, Houston, (1974)
37. Z. Szklarska-Smialowska, Corros.Sci., 41 (1999) 1743
38. A. Bezins, R. T. Lowson, and K. J. Mirns, Aust. J. Chem, 30 (1977) 1891
39. G. C. Wood, J. A. Richardson, abbo M. F. Abd, L. M. Mapa, and W. H. Sutton, in: "Proceedings of the Fourth International Symposium on Passivity", R. P. Frakenthl and J. Kruger (eds.), The Electrochem. Soc., Pennington, NJ, 973 (1978).

40. J. Augustynski, R. P. Franenthal, and J. Kruger (Ed.), "Proceedings of the Fourth International Symposium on Passivity", The Electrochem. Soc., Pennington, NJ, 997 (1978)
41. Z. Szklarska-Smialowska, in: NACE, "Pitting Corrosion of Metals", 347 (1986)
42. S. T. Pride, J. R. Scully, and J. L. Hudson, J. Electrochem. Soc., 141, 3028 (1994)
43. D. W. Buzz and R. C. Alkire, J. Electrochem. Soc., 142, 1104 (1995)
44. G. S. Frankel, L. Stockert, F. Humkeler, and H. Bohni, CORROSION, 43, 429 (1987)
45. J. R. Galvele, J. Electrochem. Soc., 123, 464 (1976)
46. H. P. Godard, Can. J. Chem. Eng, 21, 167 (1960)
47. F. Hunkeler and H. Boehni, CORROSION, 37, 645 (1981)
48. K. P. Wong and R. C. Alkire, J. Electrochem. Soc., 129, 464 (1982)
49. G. M. I. Hoch, in: NACE, R. Staehle, B. Brown, J. Kruger, A. Agrawal (Eds.), Houston, Texas, 134 (1974)
50. T. Hagyar, and J. Williams, Trans. Faraday Soc., 57, 2288 (1961)
51. E. McCafferty, "Surface Hydroxyl: The Outermost Layer of the Passive Film", in: Electrochemical Society Proceedings, Vol. 98-17, 42 (1998)
52. E. McCafferty and J. P. Wightman, J. Colloid Interface Sci., 194, 344 (1997)
53. C. L. McBee and J. Kruger in: Localized Corrosion, R. W. Staehle, B. F. Brown, J. Kruger, and Agrawahl, Eds., NACE, Houston, TX, 252 (1974)
54. L. F. Chin, C. Y. Chao, and D. D. Macdonald, J. Electrochem. Soc., 128, 1194 (1981)
55. S. -I. Pyun, and E. -J. Lee, Electrochimica Acta, 40, 1963 (1995)

56. E. P. G. T. van de Ven and H. Koelmans, *J. Electrochem. Soc.*, 123, 143 (1976)
57. S. -M. Moon and S. -I. Pyun, *Corros. Sci.*, 39, 399 (1997)
58. in: *Electrochem. Soc. Proceedings*, Vol. 98-17, 180 (1998)
59. R. G. Buchheit, R. P. Grant P. F. Hlava, B. Mckenzie, and G. L. Zender, *J. Electrochem. Soc.*, 144, 2621 (1997)
60. H. M. Obispo, L. E. Murr, R. M. Arrowood, E. A. Trillo, *J. of Mater. Sci.*, 35, 3479 (2000)
61. C. Blanc, B. Lavelle, and G. Mankowski, *Corros. Sci.*, 41, 421 (1999)
62. R. G. Buchheit, *J. Electrochem. Soc.*, 142, 3994 (1995)
63. M. J. Pryor and J. C. Fiste, *J. Electrochem. Soc.*, 131, 1230 (1984)
64. T. J. Warner, M. P. Schmidt, F. Sommer, and D. Bellot, *Z. Metallk.*, 86, 494 (1995)
65. G. S. Chen, M. Gao, and R. P. Wei, *CORROSION*, 52, (1996)
66. S. V. Kagwade, C. R. Clayton, et al. *J. of Electrochem. Soc.* 147, 4125 (2000)
67. M. Kendig and J. Scully, *CORROSION*, 46, 23 (1990)
68. W. S. Tait, "An Introduction to Electrochemical Corrosion Testing for Practicing Engineers and Scientists", PairODacs, Publications, Wisconsin, Racine, (1994)
69. M. D. G. Destreri, J. Vogelsang, L. Fedrizzi, and F. Deflorian, *Prog. Organic Coating*, 37, 69 (1999)
70. J. Ross MacDonald, ed., "Impedance Spectroscopy", John Wiley & Sons, New York, 1987
71. S.F. Mertens, C. Xhoffer, B.C. Cooman and E. Temmerman, *CORROSION*, 53, 381 (1993)

72. R.F. Allen and N.C. Baldini, eds., "1998 ASTM Annual Book of ASTM Standards", ASTM, West Conshohocken, Pennsylvania, 1998
73. A personal conversation with Sander of Weert Co. (Netherlands)
74. W. C. Oliver and G. M. Pharr, *J. Mater. Res.*, 7, 1564 (1992)
75. F. Mansfeld, S. Lin, S. Kim and H. Shin, *J. Electrochem. Soc.*, 137, 78 (1990)
76. C. Chen and F. Mansfeld, *Corros. Sci.*, 39, 1075 (1997)
77. F. Mansfeld, *J. Appl. Electrochem.*, 25, 187 (1995)
78. H. Shin and F. Mansfeld, *CORROSION*, 45, 610 (1989)
79. H. Xiao and F. Mansfeld, *J. Electrochem. Soc.*, 41, 2332 (1994)
80. H.P. Hack and J.R. Scully, *J. Electrochem. Soc.*, 138, 33 (1991)
81. E.P.M. van Westing, G.M. Ferrari and J.H.W. de Wit, *Corros. Sci.*, 36, 979 (1994)
82. M.D.G. Destreti, J. Vogelsang, L. Fedrizzi and F. Deflorian, *Progr. Org. Coat.*, 37, 69 (1999)
83. S. K. Jayaseelan, M.S. Thesis, University of Cincinnati, Department of Materials Science and Engineering, 2000
84. N.G. McCrum, B. E. Read, G. Williams, "Anelastic and Dielectric Effect in Polymeric Solids", Dover Publications Inc., New York, 1991
85. W.J. van Ooij, D. Zhu, G. Prasad, S. K. Jayaseelan, Y. Fu and N. Teredesai, *Surf. Engg.* 16, 386 (2000)
86. W. J. van Ooij, *Rubber Chem. Technol.*, 57, 421(1984)
87. E.P. M. van Westing, G.M. Ferrari and J.H.W. de Wit, *Corros. Sci.*, 34, 1511 (1993)

88. G. Socrates, "Infrared Characteristic Group Frequencies", John Wiley & Sons, New York, 1994.
89. M. W. Urban, "Vibrational Spectroscopy of Molecules and Macromolecules on Surfaces", John Wiley & Sons, New York, 1993.
90. Th. Van Schaftinghen, M.S. Thesis, Vrije Universiteit Brussel, Department of Materials Science and Electrochemistry, Brussels, Belgium, 1999
91. K. P. Battjes, A. M. Barolo and P. Dreyfuss, *J. Adhesion Sci. Technol.*, 5, 177 (1991)
92. F. J. Boerio, and J. W. Williams, *Proc. 36th Annu. Conf. Reinforced Plastics/Composites, Inst., Sect. 2-F* (1981)
93. S. R. Culler, M. S. Thesis, Case Western Reserve University, Cleveland, OH (1982)
94. N. B. Colthup, L. H. Daly and S. E. Wiberley, "Introduction to Infrared and Raman Spectroscopy", 3rd edition, Academic Press, Boston, 389 (1990)
95. S. Enfinger, Ph. D. Dissertation, University of Hannover, Germany, 1993
96. D. A. Jones, "Principles and Prevention of Corrosion", 2nd ed., Prentice-Hall Inc, 556 (1996)
97. E. Ghali, "Magnesium and Magnesium Alloys", in: R. W. Revie (Ed.), "Uhlig's Corrosion Handbook (2nd ed)", John Wiley & Son Inc, New York, 793 (2000)
98. W. T. Grubb. *J. Am. Chem. Soc.* 76, 3408 (1954)
99. Infrared Spectroscopy Committee of the Chicago Society for Paint Technology. "Infrared Spectroscopy. Its Use in the Coatings Industry". Federation of Societies for Coatings Technologies, Philadelphia, PA, 1969

100. G. O. Ilevbare and J. R. Scully, CORROSION, 57, 134 (2001)
101. M. Eleboujdaini and E. Ghali, Electrochim. Acta, 412 (1992)
102. M. Eleboujdaini, E. Ghali and R. G. Barrada and M. Firgis, Corros. Sci., 30 855 (1990)
103. K. Nisancioglu, K. Y. Davanger and O. Strandmylr, J. Electrochem. Soc., 127, 1325 (1980)
104. K. Nisancioglu, O. Lunder and H. Holtan, CORROSION, 41, 247 (1985)
105. B. Mazurkiewicz, Corros. Sci., 23, 687 (1983)
106. D. Hawke, A. Olsen, Proc., SAE, 79 (1993)
107. S. Prings, K. Woods, Met. Finish. 6, 49 (1981)
108. K. A. Korinek, "Chromate Conversion Coatings", in Metals Handbook, 9th ed., vol. 13, West Conshohocken, PA: ASTM, 392 (1987)
109. G. O. Ilevbare and J. R. Scully, Corrosion, 57, 134 (2001)
110. K. Asami, M. Oki, G. E. Thomason, G. C. Woods, V. Ashworth, Electrochim. Acta, 32, 337 (1987)
111. X. G. Zhang, "Zinc", in: R. W. Revie (Ed.), Uhlig's Corrosion Handbook, 2nd ed., John Wiley & Son, Inc, New York, 2000
112. F. C. Porter, "Corrosion Resistance of Zinc and Zinc alloys", P. A. Schweitzer (Ed.), Marcel Dekker Inc., 1994
113. M. Hein and L. Best, "College Chemistry: An Introduction to Inorganic, Organic and Biochemistry", 2nd ed. Brooks/Cole Publishing Co. , CA, 1990
114. W. Machu and L. Schiffman, Archiv. f.d. Eisenhüttenwesen 37, 679 (1966)
115. A. J. Sedriks and P. J. Dudt, CORROSION, 1, (2000) 84

116. M. H. Kasmdar, "Liquid Metal Embrittlement", ASTM Metals Handbook, 13, 1984
117. A. J. Sedriks, "Corrosion of Stainless Steels" 2nd edition, New York, J. Wiley & Sons, 418
118. W. G. Ashbaugh, Materials Performance, 32, 188 (1993)
119. A. J. Stavros, "Metals Handbook", Vol. 13, Corrosion, 9th edition, ASM International, Metals Park, OH, 432 (1987)
120. R. M. Kain, "Seawater Crevice Corrosion Resistance of Stainless Steels Coated with Silane and Antifouling Paint systems", final report under contract N00014-01-C-0177, August, 2002
121. C. Zhang, Ph. D. Dissertation, University of Cincinnati, Department of Materials Science and Engineering, 1997
122. R. A. Nyquist and R. D. Kagel, "Infrared Spectra of Inorganic Compounds", Academic Press, New York, 1971